University of Nottingham
*Department of Mechanical, Materials and Manufacturing Engineering*

THESIS SUBMITTED FOR THE DEGREE OF DOCTOR OF PHILOSOPHY

---

# Process induced distortions of composite structures

Doctoral Dissertation of:
**Neoklis Traiforos**

Principal Supervisor:
**Prof. Thomas Turner**

Secondary Supervisor:
**Asst. Prof. Mikhail Matveev**

---

*Declaration*

I confirm that this thesis presented for the degree of Doctor of Philosophy, has

i) been composed entirely by myself

ii) been solely the result of my own work except stated otherwise

iii) not been submitted for any other degree or professional qualification

Signed: Neoklis Traiforos

---

Date: Wednesday 7$^{\text{th}}$ June, 2023

---

# Dedication

*Dedicated to those rare unconventional individuals who, never say never, dream, dare, persist, do not compromise, love and travel, but most of all to those who sacrifice themselves for their ideals.*

# Abstract

A significant problem encountered during the manufacturing process of thermoset composite structures is the distortion of their shape from their Computer-Aided Design (CAD) nominal geometry.

In this research the effect of stacking sequence, specimen thickness, tooling material and curing cycle on Process Induced Distortion (PID) of L-shape composite structures is investigated experimentally and numerically. The specimens were manufactured from high temperature Vacuum Assisted Resin Transfer Moulding (VARTM) process with the EPIKOTE$^{TM}$ System 600 and IMS65 fibres. The spring-in angle of the parts was measured with a $3D$ scanner and a Coordinate Measuring Machine (CMM).

A thermo-chemo-mechanical simulation approach was developed to simulate the experiment, which is composed of a thermo-chemical and a chemo-mechanical part. The purpose of the thermo-chemical part, is to calculate at every time increment the temperature distribution across the structure. The calculated temperature field can then be used as input to the chemo-mechanical module, which purpose is to calculate the stress state of the material at every time increment of the curing history. Two chemo-mechanical modules were developed. The first one employs a modified Cure Hardening Instantaneously Linear Elastic (CHILE) material model, and the second one a linear viscoelastic material model. The material modelling developed is applicable from the gelation point of the resin, and is implemented using the ABAQUS Finite Element Analysis (FEA) software. The effect of various Boundary Conditions (BCs) on simulation results were investigated. Simulation results were compared against analytical results and the measured spring-in angles.

The spring-in angle of the parts predicted by the CHILE material model was found to be higher than that predicted by the viscoelastic model. The tool material significantly affects the distortion of the parts and contact boundary conditions should be employed for an accurate prediction of the part shape. Balanced, symmetric and thick laminates contribute to a reduction in part distortion, while elevated curing temperatures slightly affect the distortion level of the parts.

The chemo-mechanical modules developed were also applied to predict PID of a composite test frame from the door surround structure of $A350$ aircraft. The material systems and processes used to manufacture this part are the same as those of the L-shape structures studied. The $3D$ scanned geometry of the frame was compared against simulation results from the two chemo-mechanical modules (CHILE and viscoelastic material model).

It was found that manufacturing the product without any compensation will produce a part not meeting its manufacturing specifications. Furthermore, a tool geometry compensation approach based on the shape of the part after demolding will produce inaccurate results as the trimming operations release stresses and affect the distortion field of the structure. Finally, scripts were developed to automate the mirroring process of calculated distortions.

# Acknowledgements

A detailed reference to all the people who contributed to this result seems to be impossible. In ancient Greece the spearhead used to do the job in times of war between the contestant armies but that was only the tip of the iceberg. Here, I would briefly try to acknowledge those who directly contributed to this journey, which I embarked almost four years ago. I would like to apologize beforehand, to all those not explicitly mentioned, but substantially supported me, through my life to reach this outcome and redirect them to the dedication section of this thesis.

From the University of Nottingham (UK), I would like to thank especially my principal supervisor Prof. Thomas Turner for his continuous support to my research. His knowledge, experience and guidance were valuable assets throughout my PhD. Tom was always kind, patient, flexible and willing to help me, no matter where I was situated or what was the status of my research. Furthermore, I would like to thank Assoc. Prof. Dimitrios Chronopoulos from KU Leuven for being one of my supervisors during the first two years of the PhD and considering me, from the very beginning, as a suitable person to deliver research of this level. Moreover, I would like to thank Asst. Prof. Mikhail Matveev for supervising my research the last year of my studies. Mikhail on-boarded the project with ease, as if he was supervising me from the very beginning. Not only he shared with me his experience on composites manufacturing and facilitated my work in the laboratory, but also proofread and corrected my manuscripts in full detail.

From Hexion Germany GmbH, I would like to thank, Senior Global R&D Manager Composites, Dr. Tareq Hasson for providing the resin system necessary to conduct the experiment. Furthermore, I would like to acknowledge the contribution of Mr. Roland Bernicke, Sales Development Manager, and his team from Teijin Carbon Europe GmbH as well as the contribution of Ralf Trost from Premium AEROTEC GmbH that coordinated the shipment of the carbon fabric to the university. The experimental investigation I performed in the University of Nottingham would not be possible, if it wasn't the contribution of the people mentioned above, who provided

us with the right materials on time.

From Airbus Defence and Space GmbH in Manching, Germany, I would like to thank Dr. Gerd Schuchmacher for his supervision and his coordination to perform a 6-months placement in Premium AEROTEC GmbH, in order to enhance my knowledge in my research field. Special thanks goes to my manager in Airbus Dr. Fernaß Daoud, team leader of Stress Methods and Optimisation department. Fernaß is much more than a "cool" manager or supervisor to me. Starting his career as a football player in Syria to recently becoming a professor at the chair of aircraft design in Technical University of Munich (TUM), Fernaß is one of my role models. Many thanks also to Mr. Florian Glock, a passionate aeronautical engineer, always eager to help me and offer his advice.

Moreover, I would like to thank all of my colleagues from the Stress Methods and Optimisation team in Airbus for sharing their experiences with me during lunch and coffee breaks. Special thanks here, goes to Alessandro Gastaldi for being such a cool office-mate. A true European, a polyglot, a person to have in any office environment. I feel lucky to be placed in such international environment within Airbus and wish to have spent more time there.

From Premium AEROTEC GmbH in Augsburg, Germany, I would like to thank Dr. Daniel Hartung for hosting me in the Big Data/Advanced Analytics &AI department and supervising my work there. Special thanks goes to Mr. Patrik Runeberg for his continuous support and supervision to my research. Patrik spent numerous hours sharing his manufacturing and process simulation expertise with me. From solving IT related issues, to actively fighting bureaucracy and facilitating the shipment of the fabric, he shaped this research in a way that it would be different without his contribution. Here, I would like to thank also Premium AEROTEC GmbH for providing me the material data needed to develop and run the simulation framework presented afterwards.

From Optimisation of Multifunctional Aerospace Composite Structures (OptiMACS) project, which I am part of, I would like to thank my fellow Early Stage Researchers (ESRs) namely, George Ntourmas (ESR1), Giuseppe Corrado (ESR2), Massimo Sferza (ESR4) and Weijie Tan (ESR5) for being excellent collaborators, office mates and co-travelers across Europe, at various trainings, short courses and events. I would like to thank you all for supporting me whenever I needed you, research and administrative wise. When you are heading into a storm it is better not to be alone, but surrounded by skillful peers. And with this type of crew I would head into another one if necessary. Massimo, thank you for delivering me a Machiavelli short

course, when I needed it most.

Furthermore, I would like to thank Prof. Dimitrios Manolakos and Prof. Kyriakos Giannakoglou, from National Technical University of Athens not only for providing me with the necessary references to successfully apply for this project but actively motivating me to accomplish a PhD research, even when I was an undergraduate student in the university. I would also like to acknowledge the support of my ex-colleagues and friends from BETA CAE Systems that supported my decision to quit my job in the company and pursue this PhD offer.

A bit more personal now, I would like to thank my brother Agis for being my backup in Greece while I was abroad, for all those family related issues that need to be jointly dealt. Once again thank you Eleftheria for supporting me to follow this path and being a marvelous partner. Also, I would like to thank my friends Dimitrios Psarros and Michaela Hausova for facilitating my relocation to Germany, hosting me numerous times at their place in Munich and contributing in making my secondment in Germany a memorable one. On the other hand, Christos Kora is responsible for making my secondment in UK a wonderful one.

Last but certainly not least, I would also like to thank the European Union for funding the Horizon 2020 research and innovation programme. The OptiMACS project is an European Industrial Doctorate (EID) project, funded under the Marie Skłodowska-Curie grant agreement No 764650. Without this innovative programme chances are, that I wouldn't have applied for a PhD and have missed this wonderful experience.

# Contents

# List of Figures

# List of Tables

# List of Acronyms

**ABD** Stiffness matrix of a laminate
**AFP** Automated Fibre Placement
**AS** Antisymmetric
**ASTM** American Society for Testing and Materials
**ATL** Automated Tape Laying
**BC** Boundary Condition
**BF** Bending Flexible
**BS** Bending Stiff
**CAD** Computer-Aided Design
**CFD** Computational Fluid Dynamics
**CFRP** Carbon Fibre Reinforced Plastics
**CHILE** Cure Hardening Instantaneously Linear Elastic
**CLT** Classical Lamination Theory
**CMM** Coordinate Measuring Machine
**CNFs** Carbon Nanofibers
**CoF** Coefficient of Friction
**CPU** Central Processing Unit
**CSC** Chemical Shrinkage Coefficient
**CTE** Coefficient of Thermal Expansion
**CTO** Consistent Tangent Operator
**DSC** Differential Scanning Calorimetry
**DMA** Dynamic Mechanical Analysis
**DoF** Degrees of Freedom
**ECCA** Extended Concentric Cylinder Assemblage
**EID** European Industrial Doctorate
**ESR** Early Stage Researcher
**FEA** Finite Element Analysis
**FE** Finite Element
**FR** Frame

**GHG** Greenhouse Gas
**HLU** Hand Lay-up
**ICAO** International Civil Aviation Organization
**ISO** International Organization for Standardization
**KIT** Karlsruher Institut of Technology
**LCM** Liquid Composite Moulding
**MCL** Minimum Cut Length
**MDO** Multidisciplinary Design Optimisation
**MRCC** Manufacturer Recommended Curing Cycle
**NDT** Non Destructive Testing
**NCF** Non Crimp Fabric
**OEM** Original Equipment Manufacturer
**OML** Outer Mould Line
**OptiMACS** Optimisation of Multifunctional Aerospace Composite Structures
**PAN** Polyacrylonitrile
**PEEK** Polyetheretherketone
**PEI** Polyether imide
**PEKK** Polyetherketoneketone
**PID** Process Induced Distortion
**PPS** Polyphenylene sulphide
**PTFE** Polytetrafluoroethylene
**RFI** Resin Film Infusion
**RFT** Right First Time
**RTM** Resin Transfer Moulding
**SK** Skin
**SP** Spar
**ST** Stiffener
**TUM** Technical University of Munich
**UB** Unbalanced
**UD** Uni-Directional
**UV** Ultraviolet
**VARTM** Vacuum Assisted Resin Transfer Moulding
**VTP** Vertical Tail Plane
**WLF** Williams Landel Ferry

# List of Symbols

Definition of subscripts :

- $f$ : Fiber property
- $m$ : Matrix property
- $c$ : Composite lamina property
- $g$ : Glassy property
- $r$ : Rubbery property
- $1$ : Longitudinal direction of the lamina
- $2, 3$ : Transverse directions 2, 3 of the lamina respectively

Definition of superscripts :

- $T$ : Thermal
- $C$ : Chemical
- $0$ : Property at viscous state ($\alpha = 0$)
- $\infty$ : Property at fully cured state ($\alpha = 1$)
- $\overline{x}$ : Average value of $x$

Symbols :

$\alpha$ : Degree of cure
$\dot{\alpha}$ : Degree of cure rate
$\alpha^{gel}$ : The degree of cure at the gelation of the matrix
$\gamma$ : Spring-in angle
$\sigma$ : Population standard deviation
$s$ : Sample standard deviation
$\nu_s$ : Degree of freedom of the Student's test
$t_s$ : Student's test variable
$n$ : Sample size
$d_i$ : Distance of a point from the fitting plane
$R$ : Universal gas constant

$T$ : Temperature
$A_1, A_2$ : Arrhenius constants
$E_{1_a}, E_{2_a}$ : Activation energies of the autocatalitic models
$m_1, n_1, D, \alpha_{c0}, \alpha_{cT}, m_2, n_2$ : Material constants used by the cure kinetics equation
$T_g$ : Glass transition temperature
$\lambda$ : DiBenedetto material parameter
$\boldsymbol{\alpha}_m^{CTE}$ : CTE of the matrix second order tensor
$T^*$ : Temperature difference to the $T_g$
$T_{C_1}, T_{C_2}, C_2, C_3, C_4, \alpha_\alpha$ : Material constants used for the calculation of the matrix CTE
$\boldsymbol{V}_m^C$ : Volumetric chemical shrinkage of the matrix second order tensor
$B, \alpha_{c_1}, \alpha_{c_2}$ : Material constants used for the calculation of the volumetric chemical shrinkage of the matrix
$\alpha_c$ : Degree of cure fraction
$\boldsymbol{\varepsilon}_m^T$ : Matrix thermal strain second order tensor
$E$ : Young's modulus
$E_1, E_2, E_3, E_4, E_5, A, k_e, T_1, T_2, T_3, T_4, T_4, T_5$ : Material constants used by the CHILE material model
$a_T$ : Temperature shift factor
$a_x$ : Degree of cure shift factor
$a_{Tx}$ : Degree of cure-temperature shift factor
$C_{g1}, C_{g2}$ : Fitting parameters of the WLF equation
$T_{ref}$ : Reference temperature used for the temperature shift factor
$T_g^{ref}$ : Reference glass transition temperature used for the degree of cure shift factor
$E^{'}, E^{''}$ : DMA values of the storage and loss modulus respectively
$N$ : Total number of the Maxwell elements
$E_i$ : The relative stiffness of the $i^{th}$ Maxwell element
$\tau_i$ : Relaxation time of the $i^{th}$ Maxwell element
$\omega$ : The frequency of oscillation
$t$ : time
$t_{wall}, t_{corner}$ : Thickness of the flanges/corner of the specimens manufactured
$\nu$ : Poisson's coefficient
$G$ : Shear modulus
$k$ : Conductivity
$c_p$ : Specific heat capacity
$s_{r^0}, s_{r^\infty}, s_{g^0}, s_{g^\infty}, c_{r^0}, c_{r^\infty}, c_{g^0}, c_{g^\infty}, k_{fac}, D_{TC}$ : Material constants used for the calculation of matrix specific heat capacity
$V$ : Volume

$S$ : The surface bounding volume $V$

$\mathbf{t}$ : Surface traction at any point on $S$

$\mathbf{f}$ : Body force per unit of $V$

$\mathbf{x}$ : Position tensor

$\delta\mathbf{v}$ : "Virtual" velocity field

$\delta\mathbf{D}$ : "Virtual" strain rate

$U$ : Internal energy of the system

$\mathbf{q}$ : Heat flux per unit area of the body, flowing into the body

$\mathbf{z}$ : Heat supplied externally into the body per unit volume

$\mathbf{r}$ : Vector of the system's nodal displacements

$\mathbf{F}$ : Vector of nodal forces, representing external forces applied to the system's nodes

$\mathbf{F}^{\circ}$ : Vector of equivalent nodal forces

$V_m$ : Specific volume of the matrix

$V_{void}$ : Specific volume of the voids

$V_f$ : Fibre volume fraction

$\rho$ : Density

$K$ : Isotropic plane strain bulk modulus

$\boldsymbol{\beta}_c^{CSC}$ : Chemical Shrinkage Coefficient (CSC) of the lamina second order tensor.

$\boldsymbol{\varepsilon}_c^{NonMech}$ : Second order non-mechanical strain tensor of the lamina

$\boldsymbol{\varepsilon}_c^{Mech}$ : Second order mechanical strain tensor of the lamina

$\boldsymbol{\varepsilon}_c^{Total}$ : Second order total strain tensor of the lamina

$\dot{Q}$ : Exothermic heat reaction of the matrix

$H_m$ : Heat of reaction of the matrix

$h$ : Heat transfer coefficient

$\overrightarrow{\boldsymbol{n}}$ : Unit vector normal to surface

$\boldsymbol{\sigma}_{ij}$ : Second order stress tensor

$\boldsymbol{D}_{ijkl}$ : Fictitious creep stress second order tensor

$\boldsymbol{C}_{ijkl}^{\circ}$ : Elastic (glassy) fourth order stiffness tensor

$\tilde{\boldsymbol{C}}_{ijkl}$ : Relaxation fourth order stiffness tensor calculated using as input the transient decay of the Prony series Eq.(4.14)

Chapter

# 1

# Introduction

## 1.1 Context of the thesis

The research presented here is part of the Optimisation of Multifunctional Aerospace Composite Structures (OptiMACS) project. OptiMACS is an European Industrial Doctorate (EID), funded under the Marie Skłodowska-Curie actions.

As being an EID project, OptiMACS is inter-sectoral drawing from both academia and industry. The research is conducted by five Early Stage Researchers (ESRs) who spent at least 50% of their research time in one of the project's industrial beneficiaries. Those are Airbus Defence and Space GmbH in Manching, Germany and RISC Software GmbH in Linz, Austria. Also, the ESRs could perform a secondment in Premium AEROTEC GmbH, a subsidiary of Airbus headquartered in Augsburg in Germany. The University of Nottingham (UK) and the University of Porto are the two academic beneficiaries where the ESRs complemented their research and training activities.

The aim of OptiMACS is to develop, deliver and implement novel, accurate and efficient structural Multidisciplinary Design Optimisation (MDO) tools. More specifically, OptiMACS focuses on improving the accuracy and efficiency of the MDO platform and simulation tools currently employed by the Airbus Group. The project is multi-disciplinary combining expertise from mechanical, aerospace, manufacturing

and software engineering, as well as from the area of applied mathematics [2].

The ESRs worked on different but coupled research fields. ESR1 worked on the detailed sizing optimisation of industrial scale composite aeronautical structures [25–27], ESR2 conducted research on extended invariant failure criteria [28], ESR4 developed novel global/local approaches for the analysis and optimisation of composite structures [29] while ESR5 developed a methodology for facilitating digital data continuity and a seamless modular interaction of all tools and activities contributing to the complete composite development process. The work presented in this thesis contributes to the development of an efficient simulation framework for the prediction of PID of aerospace composite structures [30, 31]. Fig. 1.1 shows schematically how each research work contributes to OptiMACS [2].

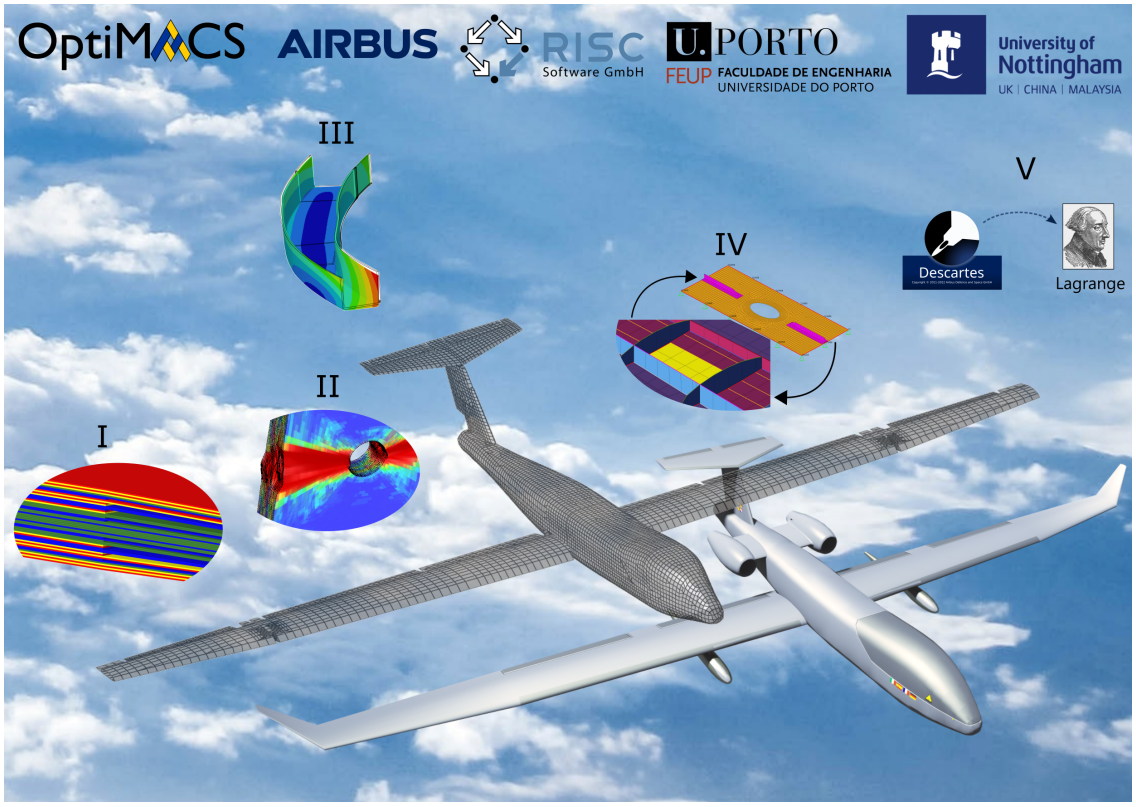


Figure 1.1: Contribution of each research topic explored in the OptiMACS project illustrated on OptiMALE [1], a Medium Altitude Long Endurance aircraft used as an academic demonstrator. In particular, these topics are: I) stacking sequence optimization; II) failure criteria and damage models; III) prediction of PID; IV) global-local optimization; V) integration of software tools [2].

## 1.2 Composite materials in the aviation industry

Composite materials are extensively used in various engineering applications, like cars, aircrafts, sport goods, wind turbines etc. The aerospace industry was one of the first industries to adopt and develop novel composite materials with the initial aim to design and optimize structures which are subjected to high loads during operation. This is due to the fact that composite materials offer better stiffness to weight and strength to weight properties compare to the conventional metallic alloys. Furthermore, they offer a greater design freedom, due mainly to their anisotropic characteristics.

Notable applications of composite materials in the modern aerospace industry, is the Airbus *A*350 XWB and its main competitor the Boeing 787 Dreamliner (Fig. 1.2). The Airbus *A*350 XWB is built of 52% weight ratio of composite materials including wing spars and fuselage components, while the Boeing 787 Dreamliner, is built out of 50% of composite materials. The Airbus *A*380 was one of the first commercial airliners to have a central wing-box made of Carbon Fibre Reinforced Plastics (CFRP).

The application of composite materials in the aerospace industry is expected to grow mainly driven by the need to reduce $CO_2$ emissions. The European green deal, the aim of which is to achieve climate neutrality, sets out the need to reduce transport emissions by 90% by 2050, compared to 1990s' levels. Aviation is considered by the European Union one of the fastest-growing sources of Greenhouse Gas (GHG) emissions and is the second biggest source of transport GHG emissions after road transport. In 2017, the direct emissions from aviation accounted for about 3.8% of the EU's total GHG and more than 2% of global emissions. Before the COVID-19 crisis, the International Civil Aviation Organization (ICAO) forecasted that by 2050 international aviation emissions could triple compared with 2015. Therefore, to achieve the targets set, the aviation sector will have to contribute to the reduction of GHG emissions [32].

An effective way to reduce the $CO_2$ emissions of an aircraft is to reduce its manufacturer's empty weight (the weight of the aircraft "as built") and this could be done by the extensive application of lightweight materials including composite materials. Furthermore, the use of recycled fibres for the manufacturing of composite structures can contribute to the reduction of the $CO_2$ emissions of the sector, but this remains a challenge as the recycled part has to meet the same specifications as the part made from virgin fibres.

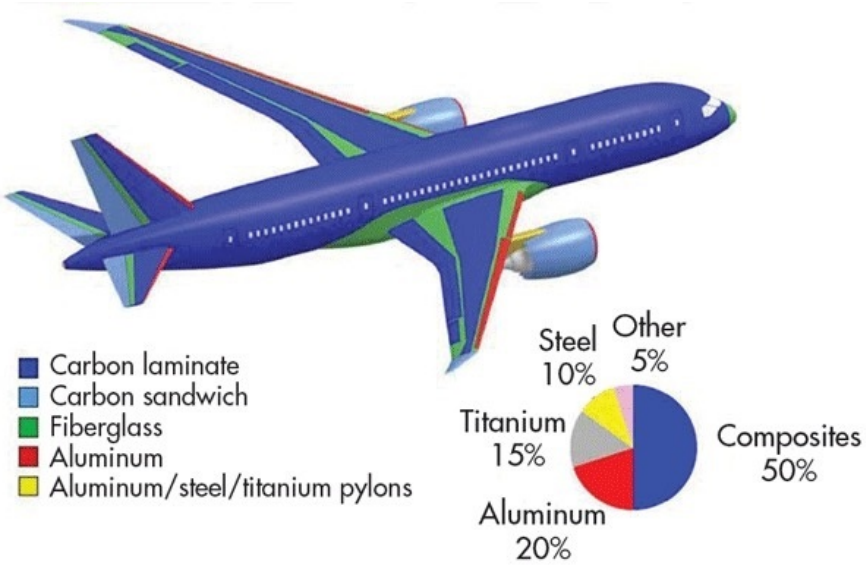


Figure 1.2: Usage of various materials in the Boeing 787 by location [3].

## 1.3 Materials

Composite materials consist of a reinforcement and a matrix. In aerospace structural applications, the reinforcements used are mainly carbon, glass or aramid fibres. The matrix is a polymer material around the fibres and for aircraft construction thermoset and thermoplastic matrices are mainly employed. The following sections describe in more detail the different types of fibre and matrix materials used in aerospace.

### 1.3.1 Fibres

Carbon fibres (Fig. 1.3) are used extensively in composite structures in the aerospace industry. They have good stiffness to weight and strength to weight properties and outstanding fatigue properties over aluminium. These fibres generally have high tensile strength and stiffness, have low moisture uptake, no corrosion problems (except $HNO_3$) and a wide operational temperature range (up to $400°C$) (Fig. 1.4). Moreover, they have negative thermal elongation in fibre direction ($0.7 \times 10^{-6}\ K^{-1}$). On the other hand, they have low ultimate strain, low shear strength and galvanic corrosion may exist when the fibres are directly in contact with aluminium [33].

Carbon fibres are produced by thermal dismantling of organic fibres. The material used to produce the carbon fibres is Polyacrylonitrile (PAN) or pitch. The majority of fibres are PAN based, a man-made fibre formerly known as Rayon. The carbon fibre consists of highly orientated graphite crystals where their 2 C-atoms are having a two dimensional covalent bonding. The adjustment of the crystals inside the fibre

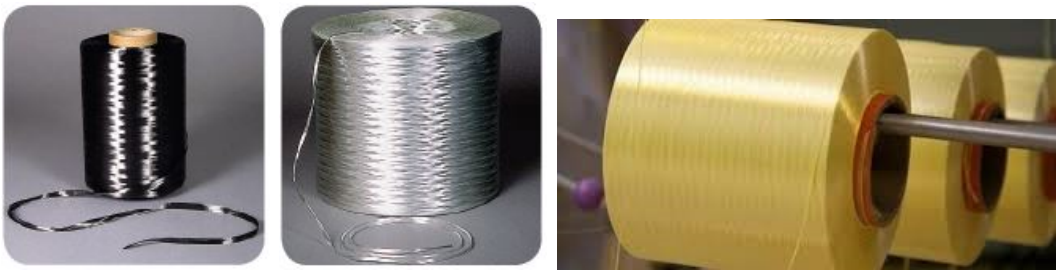

Figure 1.3: From left to right: Carbon, glass and KEVLAR fibre [4].

is defining the final properties of the fibres. The structure of the carbon fibre is similar to a $2D$ diamond, thus giving excellent properties in fibre direction but weak performance transverse to it. As a result the fibre itself is anisotropic. This explains why carbon fibres are sensitive in bending and shear (pure fibre) and surface protection is needed if the fiber is processed (weaving, knitting etc).

During the manufacture of carbon fibres a trade off occurs between strength and modulus (increased stiffness). This is dependent on the degree of alignment of the graphite crystals within the structure. Carbon fibers are produced in rovings of $1k$, $3k$, $6k$, $12k$, and $24k$ filaments each $5 - 7\mu m$.

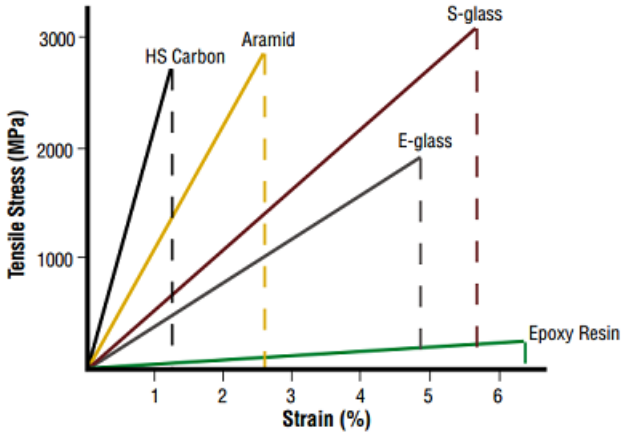


Figure 1.4: Tensile stress-strain plot of various fibres and epoxy resin [4].

Glass fibres are usually used in aerospace industry as an insulator between aluminium and carbon fibres to prevent galvanic corrosion of the aluminium part, in aicraft body panels and interiors. Glass is an inorganic melting product that was cooled down to solid without crystallisation. Glass fibres are drawn from melted glass and have a density of about $2.6\, g/cm^3$ (Fig. 1.3). The advantage of glass fibres is their high tensile strength (Fig. 1.4). However, glass fibres have low E-Modulus in the range of aluminium and high temperatures lead to moisture absorption and to strength and stiffness reduction. Glass fibres are extensively used instead of carbon fibres to manufacture wind and tidal turbine blades as well as hulls and decks of

large marine vessels to reduce cost.

Aromatic polyamides are called aramid. Aramid has good properties in tensile, good fatigue properties but poor properties in compression and transverse direction (Fig. 1.4). The manufacturing process of aramid fibres and the slow production rate are the main reason for their increased price [33]. Aramid fibres are used in engine containment rings, engine nacelles, filament-wound pressure bottles to mitigate the effects of a catastrophic failure of the part or subsystem they are applied to the rest of the aircraft. Another application of aramid fibres is in aircraft tires, where they provide enhanced toughness and thermal stability.

Two well-known product names of aramid fibres are KEVLAR (DuPont) and TWARON (Akzo) (Fig. 1.3). They have higher strength and stiffness than glass fibres, better ultimate tensile strain and energy absorption than carbon fibres and very good tensile characteristics. However, there is about 25% reduction in stiffness and 25%-40% in strength at $200°C$. They are very hygroscopic which leads to ageing, cracks, blistering and loss of material characteristics. Their thermal elongation is negative and they are hard to machine. Furthermore, they have low compression strength. Finally, aramid fibres as well as carbon and glass fibres, suffer from significant degradation of their properties when exposed to Ultraviolet (UV) radiation.

### 1.3.2 Fibre Forms

After the fibres have been manufactured, the "sizing" of the fibers follows. "Sizing" is a thin, homogeneous coating applied to the surface of fibers during the manufacturing process to protect the filaments during handling, processing, and also during subsequent compounding and composite processing. On the fiber surface, the sizing plays an important role in determining the properties of the final composite, such as improved adhesion between the fiber and the matrix, mechanical properties, chemical or water resistance, and thermal stability. Moreover, "sizing" ensures good cohesion between fibres, fibre protection against abrasion, suppression of the electric charges for glass and good fibre absorptivity by resin [33].

Then the fibres are assembled and supplied in two forms the UD tape or roving, which is composed of 100% of 0° oriented fibres, and the fabric with different kinds of weaving.

The fabric is defined by its warp which incorporates the 0° oriented fibres and the weft or fill which incorporates the $90^o$ oriented fibres. Balanced fabric is called the

fabric which is composed of 50% of fibres oriented with 0° and 50% of fibres oriented with $90^o$.

The weaving of the fabrics used in aerospace applications are mainly the plain weave or canvas (1 roving in warp, 1 roving in weft), the twill (2 roving in warp, 2 roving in weft), the 5 harness Satin (5 roving in warp, 1 roving in weft) and 8 harness Satin (8 roving in warp, 1 roving in weft) weaving (Fig. 1.5). The manufacturing is done in a modern loom based on the old principle of warp and weft. Thus, the fibre yarns in warp or longitudinal direction are led along the loom where they will be lifted or pushed down. In the gap between the warp yarns the weft yarns are introduced one by one.

Woven fabrics are easy to drape, in other words, to form over a complex surface. This allows the lay up of more complex parts, but fibre reorientation to the original stress requirements can occur. The drapability of the fabric is mainly related to the kind of weaving that was chosen for the fabric. Plain woven fabrics are generally the least pliable. Plain weave is better suited for flat applications where drape and conform-ability are not required. Satin and twill weaves have better drapability than the plain weave and can more easily conform to curved surfaces. The twill weave maintains more fabric stability than a harness satin weave and is recommended for use on parts that have compound curves.

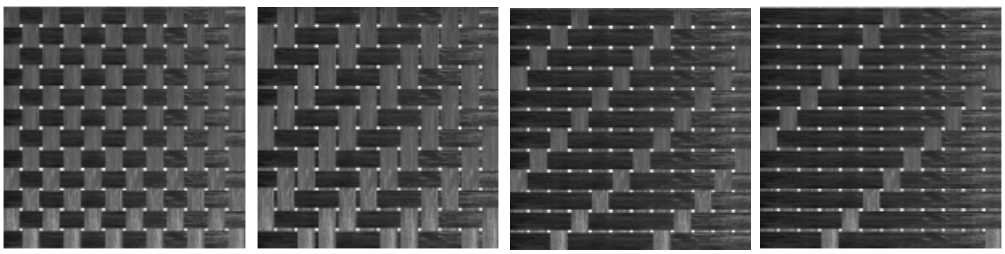

Figure 1.5: From left to right: Plain, Twill $2 \times 2$, 5-Harness and 8-Harness Satin Weave [5]

Another type of fabric is the Non Crimp Fabric (NCF) (Fig. 1.6). This normally consists of between two to nine UD plies knitted together to form a textile. So for two plies these are termed 'bi-axial', three 'tri-axial' and four 'quad-axial'. The UD plies after they have been stitched together are commonly known as a 'NCF blanket'.

NCF allows to modify a number of its features to optimize the design of the part. It is possible to have multiple plies within one stack, multiple orientations within one stack, multiple ply thickness and adapted stitching for specific drape behaviour of the NCF fabric. Moreover, binder powder material can be applied to NCF. This is added to the fabric surface by the material supplier and make the fibres stick together

when the fabric is heated. When the fabric returns back to room temperature the preform is stabilized.

NCF is used to manufacture rear pressure bulk heads and Vertical Tail Plane (VTP) of aircraft and their application is usually preferred for mass production parts as reduces the time and costs needed to create the preform compared to the use of equivalent number of UD plies.

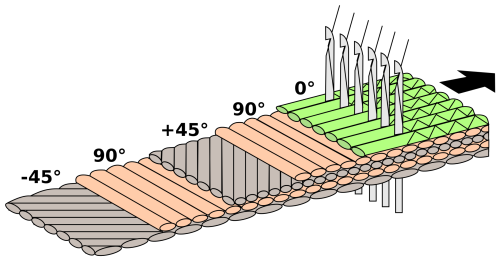


Figure 1.6: Non Crimp Fabric (NCF) [6]

### 1.3.3 Matrices

Thermoset materials have $3D$ molecular structure with strong covalent bonds. The application of temperature will cause the reticulation of the $3D$ network and create the polymer structure (polymerisation). Thermoset transformations are chemical and irreversible. Single component thermosets are non polymerised material and are considered unstable at room temperature ($23°C$). Therefore, storage at $-18°C$ for the unpolymerised state is required. The storage life is about 1 month at room temperature and 12 months at $-18°C$.

Single component thermosets are easy to implement, shape and wrap them at room temperature. In order for the polymerisation to occur the material is subjected to a curing cycle, usually in an oven, autoclave, or heated tool. Autoclaves are forced circulation type ovens with the capability to apply pressure on the parts during the curing cycle. For a typical aerospace grade, single component epoxy resin, the polymerisation occurs at $180°C$ for approximately 90 $min$ with the application of a 7 $bar$ pressure in the autoclave for a monolithic structure.

To increase storage life and reduce manufacturing costs two components resin systems are used, where the two components are mixed together in a specified by the material manufacturer ratio before manufacturing the part. Then, the part is usually cured at room temperature or in an oven. After polymerisation thermosets are impossible to reform.

Types of thermosets are epoxies, bismalemides, phenolics, unsaturated polyester and cyanate esters. Epoxies are the most widely used matrices in the aerospace industry, for manufacturing primary aero-structures due to their best mechanical properties. Bismalemides have good structural properties and intermediate temperature resistance. Phenolics are mainly used in secondary structures (cabin interiors), while unsaturated polyester and cyanate esters are low cost thermosets matrices used mainly in industrial applications.

The use of thermoplastics can offer great reduction in manufacturing time compared to thermoset materials for manufacturing relatively small parts with the thermo stamp forming process. As a result, there is an ongoing effort by the suppliers and Original Equipment Manufacturers (OEMs) to reduce the cost of the materials and substitute thermosets parts with thermoplastic ones. Thermoplastics are weldable and they are easy to recycle by grinding the material and forming a new part with short fibres. However, compared to thermosets thermoplastics require high process temperatures, high tooling and process cost and high material costs for high performance parts.

The most commonly used types of thermoplastics in aerospace are Polyetheretherketone (PEEK), Polyetherketoneketone (PEKK), Polyphenylene sulphide (PPS) and Polyether imide (PEI). Semi-crystalline thermoplastics like PEEK, PEKK and PPS are the only ones which give sufficient chemical stability against aggressive fluids like skydrol (fire-resistant aviation hydraulic fluid), as well as they guarantee temperature resistance. Amorphous thermoplastics like PEI are used for interior applications (in addition to PPS and PEEK) because of their better properties to fulfil fire, smoke, and toxicity requirements.

Thermoplastics are polymerised materials and are regarded as stable at room temperature. Therefore, they do not require particular storage conditions and their storage life is about 24 months at room temperature. Thermoplastics transformations are mechanical and reversible. It is impossible to implement, shape and wrap them at room temperature and additional heating is required to melt the material for that purpose. For PPS and PEI the melting temperature is about $300°C$ whereas for PEEK it is around $400°C$.

## 1.4 Manufacturing Processes

The dry reinforcement (fabric, NCF, braid, rovings, etc.) can either be used with Liquid Composite Moulding (LCM) manufacturing processes or be pre-impregnated with a thermoset or a thermoplastic matrix. The advantages of prepreg over the LCM technologies are constant quality of the parts due to pre-impregnated material, lower void content and increased fibre volume fraction. The thermoset prepreg manufacturing processes include HLU, ATL and AFP while for thermoplastic, thermo stamp forming.

### 1.4.1 Hand Lay-up (HLU)

In the HLU manufacturing process the whole laminate kit or the individual plies are placed manually on the surface of the tool (Fig. 1.7).

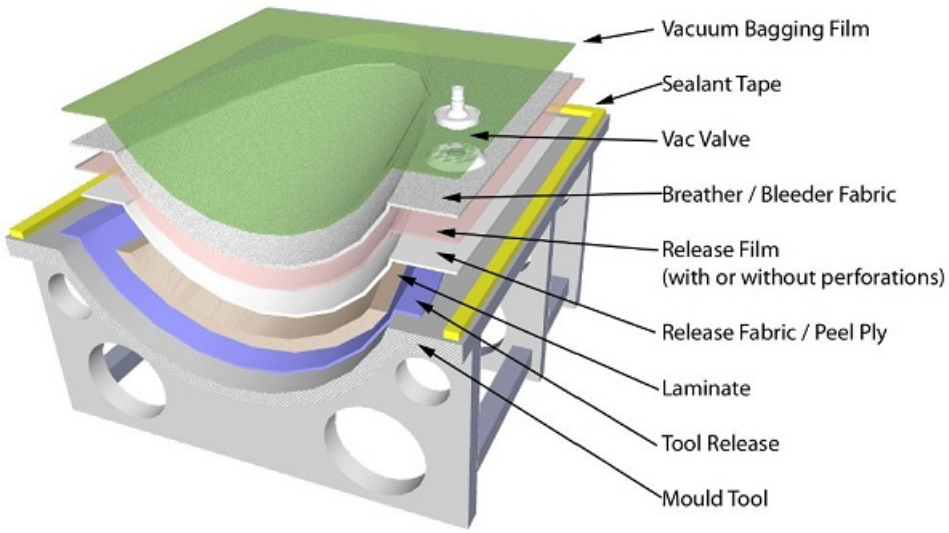


Figure 1.7: Consumables used in the Hand Lay-up (HLU) process [7].

The peel ply takes the excess resin during the curing of the laminate, the bagging film seals up the lay up, the breather fabric is used to facilitate the application of the vacuum, and the PS tapes stick with the application of pressure and are used to ensure the correct position of the laminate kit inside the tool during the application of pressure. The release film enables an easy removal of the additional materials after curing. Finally, the release agent facilitates the separation of the structure from the tool after the curing. The HLU manufacturing process is to used to manufacture curved panel components of nacelles and thrust reversers.

### 1.4.2 Automated Tape Laying (ATL)

ATL resembles the manual deposition of UD tape in the HLU process but can perform the task at higher deposition rates with greater process control. The ATL machine consists of a big portal/bridge and the tape layer head (Fig. 1.8). The head is fixed at the clamping plate of the bridge, which can be moved in two axes, sideward and longitudinal respectively. The linear fixation enables the head to go up and down as well as to turn around its axis. The prepreg is stored in the supply reel and is led via the uncoil reel to the cutter which will contour the prepreg. The material is then led to the application roll and fixed on the tooling [34].

Figure 1.8: Automated Tape Laying (ATL) on an Airbus $A350$ upper shell fuselage skin section at the premises of Premium AEROTEC GmbH [8].

ATL is used for manufacturing wing skin and composite body panels. For tape-laying along curved paths on double curved surfaces, steering or draping of tapes has to be performed to avoid gaps and overlaps on the final part and to ensure homogeneous properties of the part. Curving tape without tape shearing or draping could lead to wrinkling [35].

### 1.4.3 Automated Fibre Placement (AFP)

The AFP is a combination of ATL and winding (Fig. 1.9). It is used with thermoset prepregs for manufacturing double curvature panels with intergrated reinforcements. Nowadays, it is employed to produce composite structures for $A350$ and $B787$ aircraft [34] (Fig. 1.9).

AFP deposits bundles of impregnated carbon fibre, called slit UD tape, on complex tools or mandrels. A common tape width is approximately 12.7 $mm$ and the

machine typically has 12 to 32 tapes, wrapped up on spools, which can be placed simultaneously on a course. The slit tapes are placed in courses on a tool surface with a compaction roller and a heater on the AFP head. The head sits on a robotic arm that enables fast and accurate positioning of the head along the course. While the deposition rates of the AFP are lower compared to the ATL machines, more complex geometries can be manufactured with this process.

The fiber placement machines have a so-called Minimum Cut Length (MCL), which is the minimum length of a course a machine can put down on the tool. Typically the MCL is smaller than 100 mm. In order not to make a design specific for one type of machine, the MCL is kept as generous as possible (typically MCL = $100mm$) in the design process. Moreover, in order to be able to lay down 45° orientations the so called ears have to be created on the edge of a panel, which then have to be removed. These ears allow the fibre placement machine to lay down courses on the edge of the part by allowing courses lengths equal to MCL and the excess material can be machined away when finishing the part. In case of local reinforcements, ears can not be used because they can not be removed from the part. Therefore, local reinforcements should respect the MCL of the machine. Further manufacturing constraints of the AFP manufacturing process include the maximum curvature of the part on which the machine can lay down fibers and the maximum slope where slits can be laid down.

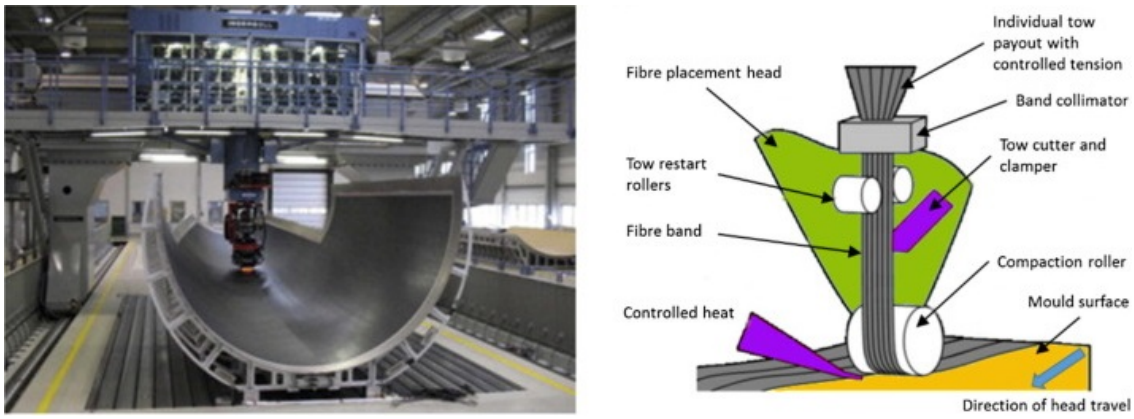


Figure 1.9: Automated Fibre Placement (AFP) of a fuselage section [9].

### 1.4.4 Thermo Stamp Forming

The idea of the thermoplastic prepreg is to buy the organo sheets and then form them using the thermo stamp forming process. This manufacturing process can be compared to normal stamp forming of sheet metal material. The difference is that for thermoplastics the organo sheets have to be heated up to $300°C$-$400°C$ in $1-5$ min before stamping. After being heated the sheets are transported to the tool,

during which a small drop of temperature is observed ($10°C$), where the stamping takes place. The part is demoulded at about $150°C$ and it cools down to room temperature.

The thermo stamping process imposes a few challenges to the designer of the thermoplastic part. Residual stresses are induced in the structure due to inhomogeneous temperature profile across the part during heating and cool down, interlaminar sliding of the organo sheets during the forming process, etc. The residual stresses lead to shape distortion of the part. Moreover, the control of the fibre fractures caused by local excess of strength values during forming remains a challenge. Wrinkles may also develop in areas of high geometrical variation (e.g sharp corners).

In aerospace, the Matched-Metal-Moulding process (Fig. 1.10) is mostly used for mass production. Parts manufactured by the thermo stamp forming include aileron ribs, engine pylon panels, leading edge of wing structures etc.

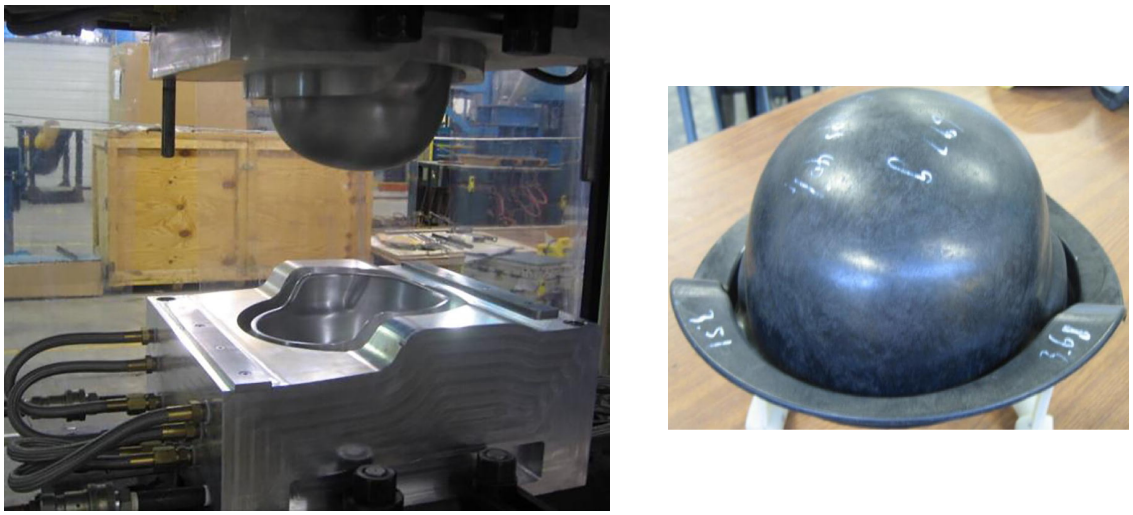

Figure 1.10: Thermoplastic helmet manufactured with thermo stamp forming process [10].

### 1.4.5 Resin Transfer Moulding (RTM)

In the RTM process resin is injected into a fibrous reinforcement inside a tool (Fig. 1.11). The advantages of the RTM process are high part quality and reproducibility, exact fibre volume fraction, low material costs and part costs for serial production (up to 50.000/year). Furthermore, complex geometries can be manufactured with RTM. However, the process requires many manual steps and there is high cost related to tool manufacturing and heating to perform the curing cycle. RTM is used to produce parts like spars, hinge brackets, spar fittings, blades, hubs, spinners etc.

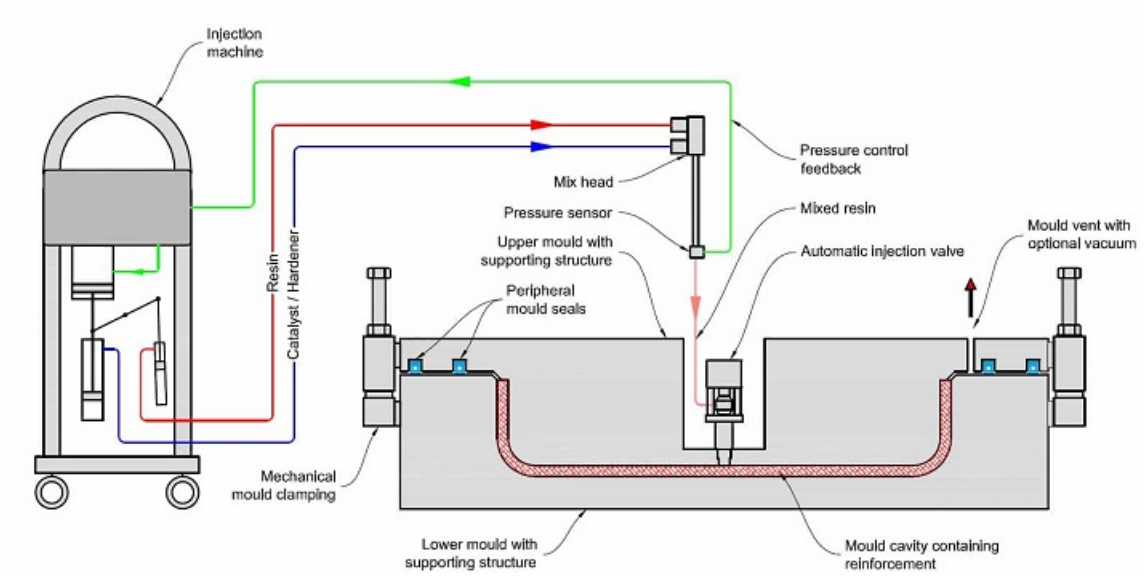


Figure 1.11: Resin Transfer Moulding (RTM) manufacturing process [11].

A commonly used liquid resin system for RTM applications in the aerospace is the $RTM6$ resin by HEXCEL. In the RTM process with $RTM6$ resin, the preform is usually prepared in a separate tool under vacuum at $60°C$ to $80°C$ in order for the binder material to be activated. Then the preform is transferred in the RTM tool where it is heated up to $150°C$. The resin is injected at $80°C$ at $< 7bar$. There are three types of resin injection in the tool, parallel injection, central injection and edge injection. In the central injection the resin is injected at the centre and it flows towards the edges of the tool. The opposite occurs at the edge injection where the resin is injected at the edges of the tool. In the parallel injection the resin flows in a parallel direction to the reinforcement [36]. After the infusion of the preform the assembly is heated at $180°C$ where the part is cured for 1.5 hours. Then the part cools down and is demoulded.

### 1.4.6 Vacuum Assisted Resin Transfer Moulding (VARTM)

In the VARTM process, the resin is infused into the reinforcement by connecting the tool with a resin tank and a vacuum pump (Fig. 1.12). The application of vacuum results in the transfer of the resin from the resin tank into the reinforcement. The infusion of the reinforcement is achieved by the flow of the resin inside the tool only due to a pressure gradient created by the vacuum pump. The tubes which are used to transfer the resin from the resin tank to the tool are called runners. A catch pot is used to collect the excess resin during the infusion.

The VARTM process is a single side tooling manufacturing process (Fig. 1.12). The

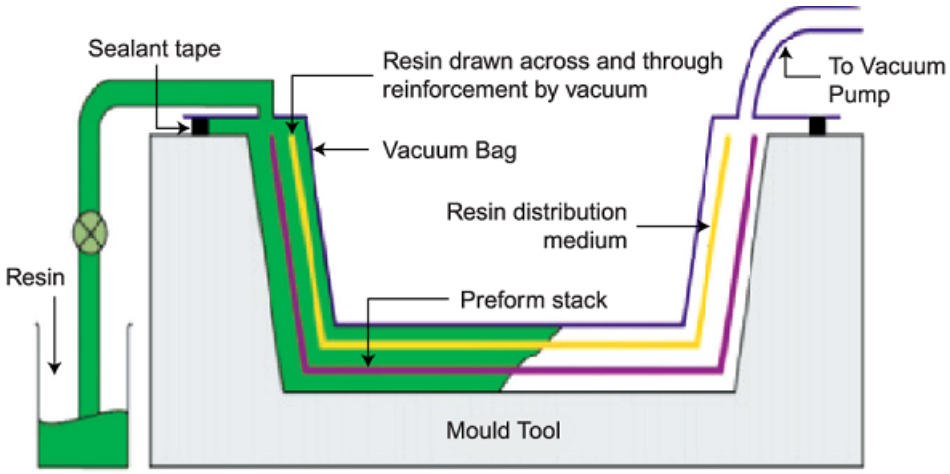


Figure 1.12: Diagram of the Vacuum Assisted Resin Transfer Moulding (VARTM) process [4].

second side is a flexible membrane which seals off the laminate by the application of vacuum. In this manufacturing process, the part is cured either at room temperature or inside the oven. The manufacturing costs associated with the VARTM process are lower compared to the prepreg technologies or RTM. VARTM is used to produce parts like flaptracks, cargo door, cross beams, ribs, frames etc [36].

### 1.4.7 Resin Film Infusion (RFI)

In the RFI process, a resin film is placed on the bottom of the reinforced material on a single sided tooling (Fig. 1.13). An autoclave is needed to initiate and maintain the through-thickness infusion of the reinforcement by the resin. During the curing cycle from the application of pressure from the autoclave, laminate displacement may occur [36].

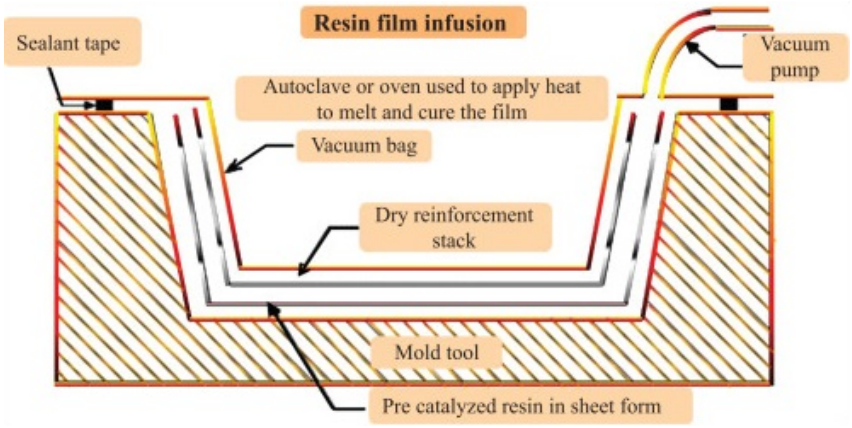


Figure 1.13: Resin Film Infusion (RFI) principle [12].

In the RFI process, only vertical infusion is possible. A commonly used resin film for RFI applications in aerospace is the $977-2$ resin film by Cytec. The manufacturing

costs in the RFI process are lower compared to the prepreg technologies or RTM. RFI is used to produce parts like the fuselage rear pressure bulkhead of Airbus $A380$ [37].

### 1.4.8 Pultrusion

Pultrusion is a continuous manufacturing process (Fig. 1.14). In a typical pultrusion set up the dispenser contains several rolls of either UD or fabric. The preform will be automatically assembled and then cured in a pressing die. Seventy percent of the curing occurs in the pressing die with the application of temperature and pressure. A post curing oven may also exist which finalizes the curing. The movement of the whole process is done by the pulling device at the end of the machine. Finally, the cutting device cuts the profiles in the desired length. Pultrusion was used for manufacturing VTP stringers, stiffeners and the upper deck cross beam of $A380$. Fig. 1.15 shows the distortion of a pultruded composite section as simulated and manufactured [13].

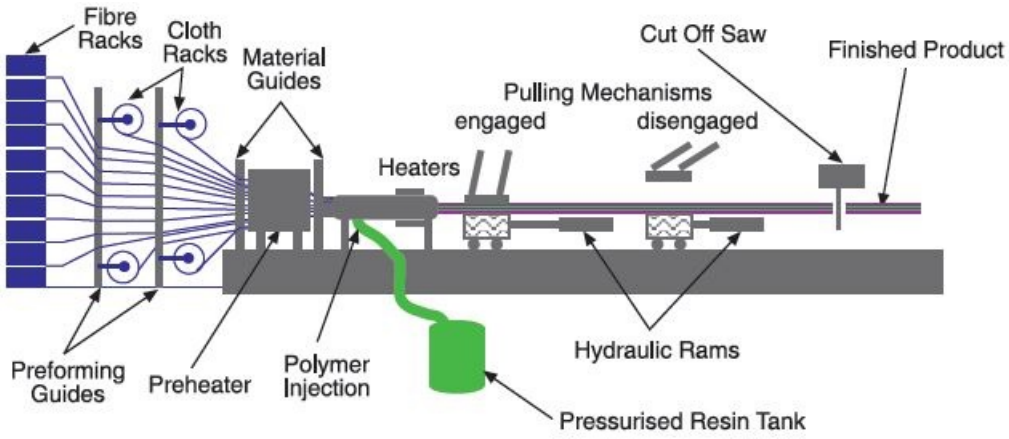


Figure 1.14: Pultrusion manufacturing process [4].

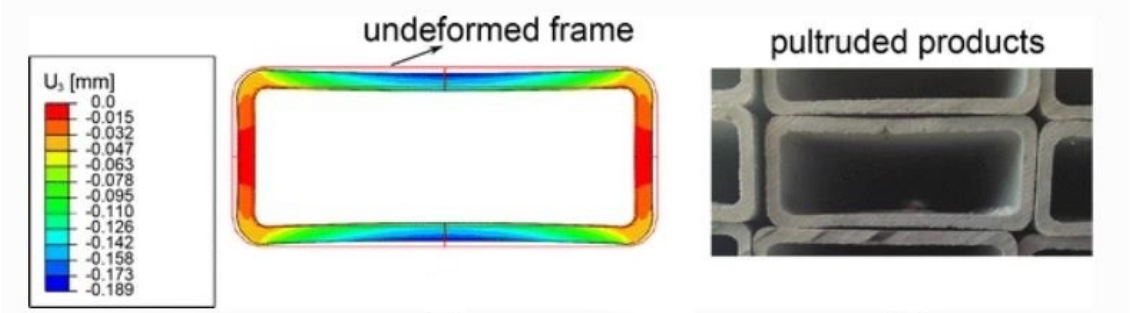


Figure 1.15: Distortion of a pultruded composite section. Predicted distortion (left, scaling factor of 5) and the manufactured product (right) [13].

## 1.5 Manufacturing defects

A number of defects arise in the manufacturing of composites. Some of the defects are process specific (e.g specific to AFP, ATL etc.) but the majority of them can be encountered in any composite structure.

In the AFP process, tow gaps and overlaps are present due to fiber steering and layup over complex surfaces (Fig. 1.16) [38]. These are resin rich areas and sites for failure initiation and wrinkles formation. Wrinkles are also caused due to tow placement at small steering radii. Tow twist can occur when increasing or decreasing the local thickness of the part. Fibre bridging is caused by too much tow tension and insufficient tack adhesion and is responsible for resin rich areas and delamination (Fig. 1.16) [38–40].

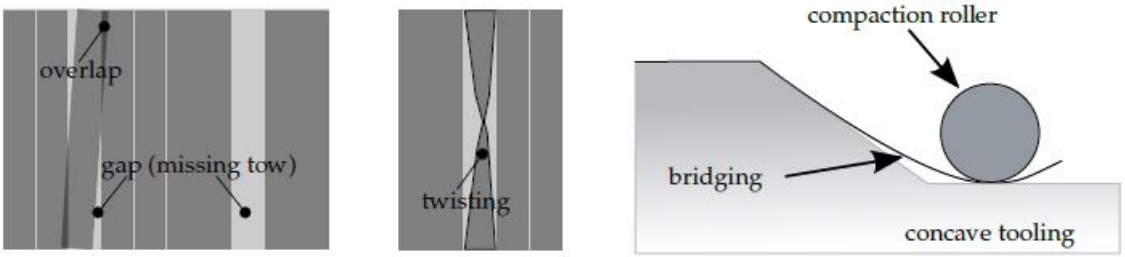


Figure 1.16: Tow gaps and overlaps, tow twist and fibre bridging encountered in the AFP process [14].

Fibre reorientation is a common defect present in many manufacturing processes (HLU,RTM,VARTM etc.) at the assembly of the preform. Usually, a laser projection system is used to ensure the correct positioning of the plies in the laminate however, deviations in fiber alignment are present due to reinforcement variability or inaccurate cutting of the plies. Also, preform handling operations might cause interlaminar slippage.

Fibre bridging can occur in areas where the friction between the plies prevents the preform to conform to the tool geometry. The applied pressure in these areas is not able to overcome the inter lamina friction. This usually happens in a small radius without the use of an autoclave. The space between the plies is filled with excess resin resulting in corner thickening and in non-uniform fiber volume fraction in the through thickness direction. As a result, the CTE and chemical shrinkage of the area is higher compared to other areas of the structure [13].

In LCM processes, non-uniform resin flow and compaction can cause variation in the thickness of the part and dry spots. Matrix cracks and delamination can occur due to high residual stresses induced in the structure from the manufacturing process

and the design of the structure (e.g. unsymmetric and or unbalanced laminates).

Another defect usually present in composites manufacturing is voids. Fig. 1.17 depicts the porosity distribution (% area) in two cross sections of a cylindrical composite specimen. The area of the voids is shown with white colour and was calculated after manufacturing the part, scanning the cross sections and using image processing filters to identify and measure the concentration of voids [15]. Voids are the result of either entrapped air during the manufacturing process or volatiles emitted from the resin during the curing due to the dissolved moisture in the resin. Furthermore, in the raw prepreg material there is an initial population of air bubbles due to deficient fiber impregnation. A high void content in CFRP structures causes a reduction in the mechanical properties of the part as well as fiber damage due to mutual abrasion of fibers and stress concentrations which trigger delamination and matrix cracks. Moreover, voids facilitate moisture absorption, which leads to the degradation of the fibre matrix interface [15].

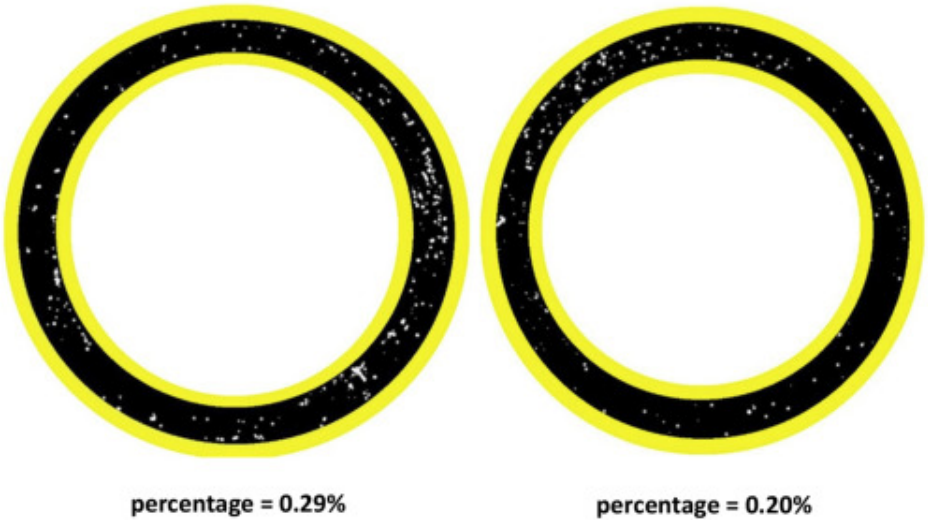


Figure 1.17: Porosity distribution (% area) in two cross sections of a cylindrical composite specimen [15].

The deviation of the structure's shape from the nominal one is referred to as Process Induced Distortion (PID). There are many factors contributing to PID such as the laminate design, resin chemical contraction, tool-part interaction, mismatch between the CTE of fibre and matrix, process conditions etc. This manufacturing defect is especially important during the assembly phase of the structure as parts with excessive distortions are difficult to assemble, requiring specific compensation procedures.

While it is possible to reduce the number and extent of the defects present in composite structures manufacturing through the appropriate design of the structure

and manufacturing process, it is impossible to eliminate them completely. This is due to the inherent anisotropic behaviour of composite structures, material variability and material property gradients imposed by the manufacturing process. Here, manufacturing simulation plays an important role to reduce manufacturing costs by predicting the manufacturing defects that will be present in the structure and enables the use of countermeasures or amendments to the manufacturing process or tools.

To mitigate the risk that the defects impose on the part a number of manufacturing quality criteria are set to evaluate whether the composite is qualified to enter into service. The manufacturing quality criteria used depend on the structure. In case it is proven, usually with the use of Non Destructive Testing (NDT) (ultrasound, CT scans, etc.), that the structure does not meet these manufacturing quality criteria, the manufacturing process or its design are reconsidered. The job of the manufacturing engineer is among others, not only to meet the manufacturing quality criteria of the structure but also reduce the manufacturing times and costs by proper selection of manufacturing process.

## 1.6 Challenges in the design of tools for composites

As the number of composite parts manufactured in the future is expected to rise, the manufacturing industry strives to reduce lead time, costs and increase product quality. Central to this effort is the reduction of the manufacturing defects as parts not meeting the high (compared to other industries e.g. automotive) aerospace specifications (e.g. maximum void content, tolerances etc.) are scrapped increasing lead time and costs.

PIDs are present in composites manufacturing irrespective of the process used (AFP,ATL,RTM etc.), matrix type (thermoset, thermoplastic) or reinforcement type (prepreg, fiber form etc.). The aerospace industry is interested in keeping the PID of the manufactured parts within a predefined range. If the structure is out of the tolerance range the tool is modified and in some cases completely redesigned (geometry, materials) to produce the desired geometry. In rare occasions, due to the associated costs, the design (geometry, materials or lay up strategy) of the final product has to be reconsidered in order to reduce PID after manufacturing.

To minimise PID of composite parts, OEMs employ the tool geometry compensation approach [41]. In this compensation approach, the deformation of the part is taken into account at the design phase of the tool, where the tool shape is different from

the nominal shape of the part. After manufacturing the part is deformed towards its nominal shape. As a starting point for the design of new tools, manufacturing experience, the result of analytical equations or PID simulations are used.

However, in complex aerospace parts, it is often the case that the initial tool manufactured is not able to produce a part within its tolerance range. This might be due to material variability (properties of the material supplied are not the same due to production disturbances), manufacturing process uncertainties (tool geometrical nonlinearities, inhomogeneous temperature field in the oven etc.) or inaccurate estimation of tool geometry (modelling assumptions/simplifications). In this case, a trial and error process follows where the tool is modified until the desired geometry can be manufactured.

A goal in manufacturing industry is to achieve a Right First Time (RFT) approach in the design and production of tools for composites. This principle indicates that a single tool is simulated, designed, manufactured and certified to produce the part of the required quality, without further modification of the tool needed afterwards. Here, simulation plays a key role, as without an accurate prediction of PID it is impossible to design a tool able to produce the right part without any manufacturing iterations.

Furthermore, the reduction of the manufacturing costs is also pursued through the use of cheaper tool materials, like steel or aluminium, compared to the expensive INVAR alloy which used due to its low CTE for the construction of tools. However, the use of alternatives to INVAR alloys for the construction of tools results in higher stresses transmitted from the tool to the part during manufacturing because of the big difference in the CTE of the tool material and the composite structure. As a result, the PIDs of a part manufactured out of steel or aluminium tool are greater than those of the part manufactured out of INVAR tool making the achievement of a Right First Time (RFT) approach in tool manufacturing a challenging task. In this case also, simulation plays a key role to accurately predict the transmitted from the tool stresses and the corresponding PID of the part.

From the industrial perspective, the scope of this thesis is to contribute to achieving a RFT approach in the design of new tools for composite structures. This is accomplished by experimental investigation and study of the factors contributing to PID of composites, software development for the prediction of PID and software validation. Furthermore, effort is made for the simulation framework to be efficiently applicable to large scale structures, yet accurate. The automation of the design process of new tools for composites is also considered.

## 1.7 Research questions

The research questions that motivated this work are the followings:

1. Can the factors contributing to PID of composite structures made from the EPIKOTE$^{TM}$ System 600 and IMS65 fibres be evaluated?
2. Can an efficient simulation framework be developed, able to take into account the driving factors causing PID of complex aerospace composite structures?
3. Can the proposed simulation framework be experimentally validated?
4. Can the applicability of the proposed solution be demonstrated on real parts?
5. Can the "mirroring" step in the design process of new tools for aerospace composite structures be automated?

## 1.8 Structure of Thesis

The thesis unfolds as follows:

- In Chapter 2 the methods used to compensate PID of composites in industry are introduced. A literature review of the factors contributing to PID of composites is presented. Furthermore, the methods proposed to predict PID are also discussed. The governing equations used by ABAQUS to solve the stress/displacement and the heat transfer problem are outlined.
- In Chapter 3 the experimental investigation performed is described. This includes a description of the tools, materials, curing cycle and manufacturing process used. Defects encountered in the manufacturing of the specimens and tools are reported. Moreover, the process used to measure the distortion of the parts is presented. The experimental findings are also presented and the uncertainties/errors affecting the results are elaborated.
- In Chapter 4 the simulation framework developed to predict PID of composites is demonstrated. The thermo-chemical and chemo-mechanical modules are presented in detail along with the material, micromechanics and constitutive equations used.
- In Chapter 5 the simulation framework is applied to simulate the experiment. A comparison between experimental measurements, analytical and simulation results is made and the impact of the modeling assumptions on the simulation results is elaborated.
- In Chapter 6 the simulation framework established is used to predict PID of a composite aerospace test frame. The scripts developed to automate the "mirroring" step in design process of new tools are discussed.

- Finally, in Chapter 7 the main conclusions of this work are outlined and points of future work are raised.

Chapter

# 2

# State of the art

## 2.1 Definition of Process Induced Distortions (PIDs)

Process Induced Distortions (PIDs) are the combined effect of spring-in and warpage, which are the two deformation mechanisms that coexist in complex composite structures [42]. Spring-in is defined as the reduction of the angle of a part from a nominal value, while warpage is defined as the change of a part curvature after manufacturing (Fig. 2.1). Fig. 2.2 depicts a composite spar which has suffered from spring-in and warpage of UD plates manufactured from an aluminum tool.

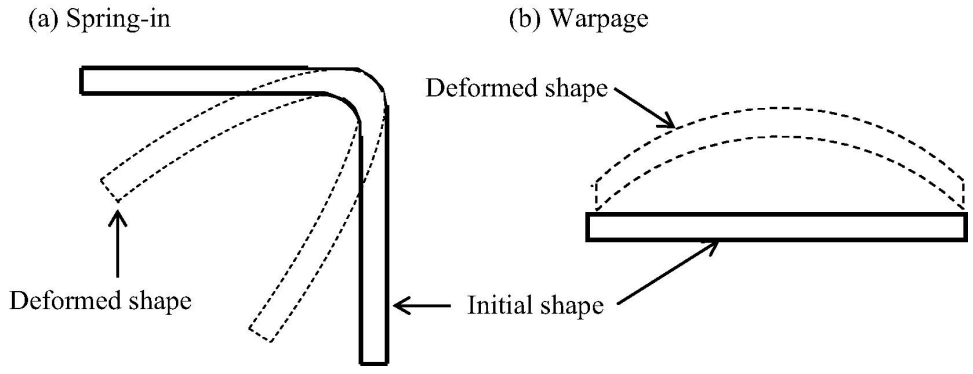


Figure 2.1: Shape distortions definition: (a) Spring-in (b) Warpage [16].

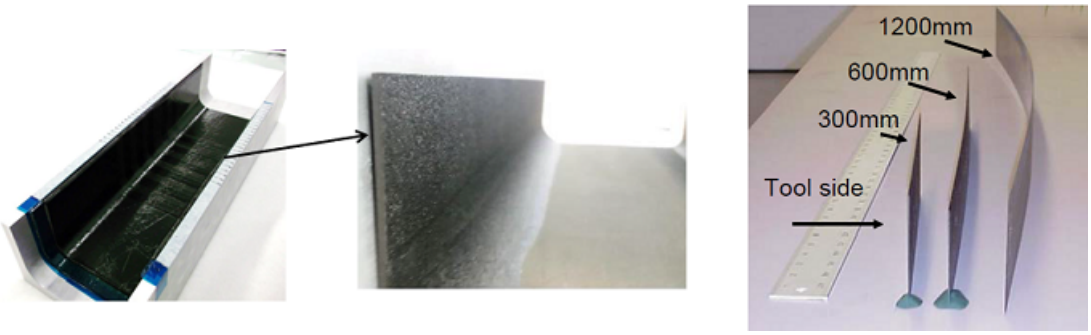


Figure 2.2: Spring-in of a composite spar section [17] and warpage of thin UD plates manufactured from an aluminium tool [18].

## 2.2 Methods to address PID of composite structures

To address PID, three approaches are used, namely the design, assembly and tool geometry compensation approach (Fig. 2.3) [19]. In the design compensation approach, the part is set to its nominal position with the use of another part, specifically built to serve this function. This approach increases assembly weight, manufacturing time and costs, as the total number of parts to be manufactured and assembled increases.

In the assembly compensation approach, there are designed gaps in the assembly, the purpose of which are to be filled by shims. The exact PIDs of the composite constituents of the assembly are usually not known, but measured after manufacturing. Based on the measurements hard or compliant shims are manufactured. This compensation approach also suffers from the disadvantages of the design compensation approach, since extra parts are needed to be manufactured.

In the tool geometry compensation approach, the shape of the tool is different from the shape of the final product. The PIDs of the composite structure are estimated either through experience, calculations or simulations and this knowledge is used to design the tool. The final structure is expected to obtain its nominal shape or lie inside the predefined tolerance range after demolding the composite structure.

Fig. 2.4 depicts the typical design process of new tools for composites with the use of simulation. In the first step, the PIDs of the nominal geometry are simulated by employing a material model. The next step in the tool design process is to reverse the distortion field to the opposite direction. This is usually referred as the "mirroring" step and its purpose is to produce an updated tool geometry.

At the "mirroring" step usually, the assumption of linear tool compensation is made. In other words, a geometry that is subjected to a certain level of PID will experience

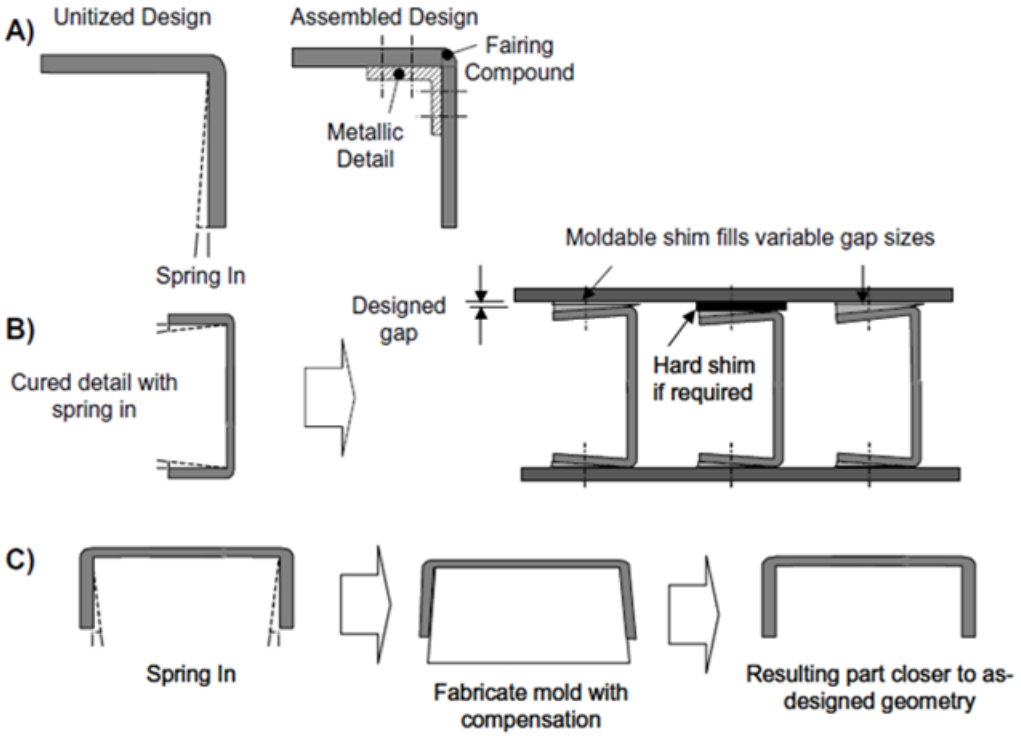


Figure 2.3: The approaches used to address PID. A) Design compensation, B) Assembly compensation, C) Tool geometry compensation [19].

the same level of PID if it is slightly modified. Kappel found out that this is not strictly valid and the tool compensation is a non-linear process [20].

The linear tool compensation approach overcompensates the distortion, producing a part with a greater angle than the nominal one. In other words, a part manufactured with a linear compensated tool will distort less than a part manufactured from the

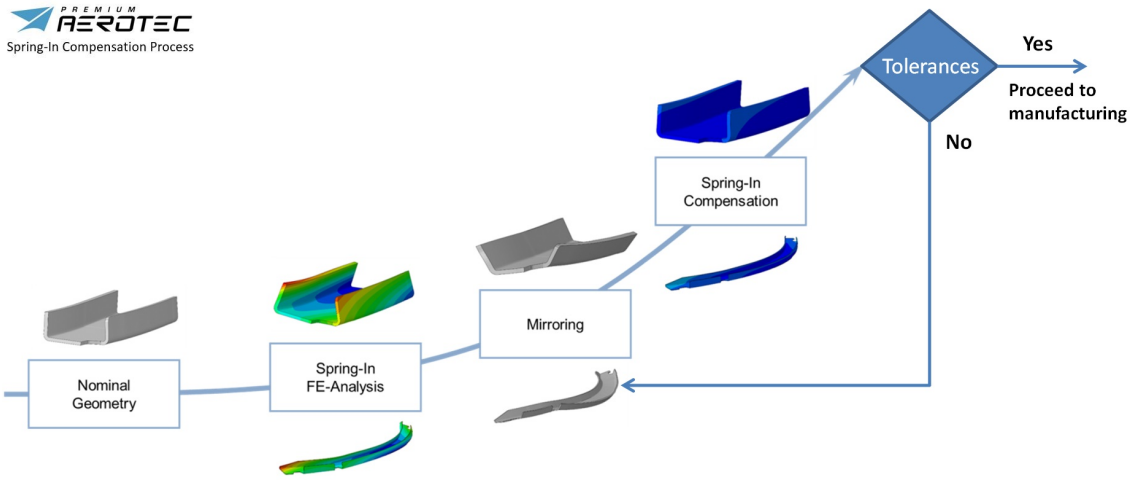


Figure 2.4: Typical design process of new tools with the use of the tool geometry compensation approach as performed by Premium AEROTEC GmbH.

nominal tool geometry as shown in Fig. 2.5. The difference between the linear compensation and the actual distortion of the part from the compensated geometry increases with the magnitude of the spring-in angle. However, this difference for the spring-in angles usually encountered in composite structures ($1° - 2°$) is considered small (1.7% for a 1.5° spring-in angle).

After the "mirroring" step the updated tool geometry is evaluated, in a subsequent step with the use of another PID analysis, with respect to its ability to produce a part within the tolerance range set for the structure. In case this condition is met the updated tool geometry is considered suitable for manufacturing and it is sent either to the manufacturing department or to suppliers specialized in tool manufacturing. In case the second PID analysis predicts that the part will be out of, or close to, its tolerance range another "mirroring" step and PID analysis occurs until a suitable tool geometry is found, as shown in Fig. 2.4.

The tool geometry compensation approach has the advantage that it does not require the use of extra parts which could add weight to the structure and minimises the assembly time and relevant costs. That is because the forces required to assemble the part at its nominal position would reduce as the PIDs of the part are reduced. Thus, the assembly tools, which in the case of the aerospace industry are specifically designed for a certain assembly operation, would be lighter, easier to build and operate. Moreover, minimum part PIDs imply reduced stresses applied to the structure at the assembly phase, which increases the load bearing capacity of the structure and fatigue life while simultaneously reducing the possibility of matrix cracks or delamination during service.

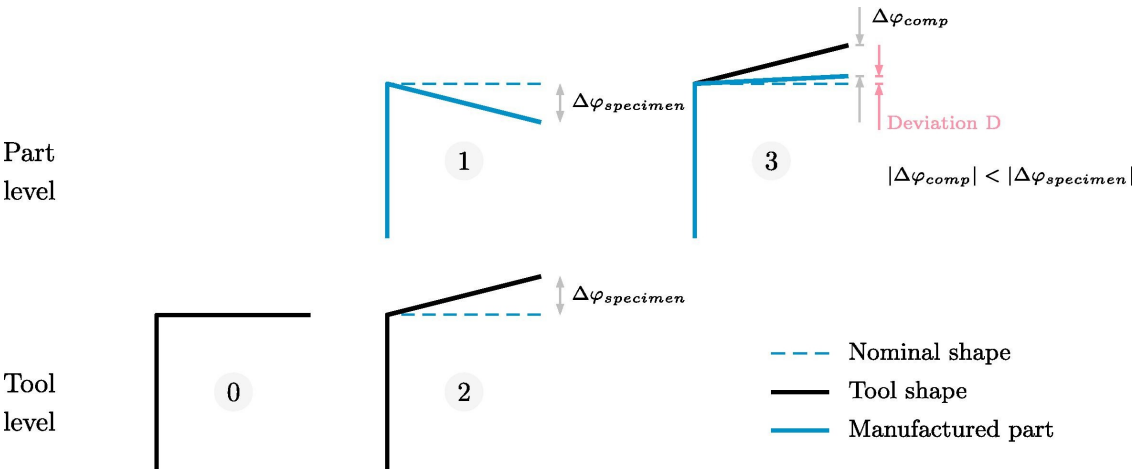


Figure 2.5: The tool compensation is a non-linear process. Step 0: Tool nominal geometry, Step 1: Distortion of a specimen manufactured from the nominal tool, Step 2: Linear tool compensation, Step 3: Deviation of the nominal to the actual compensated geometry [20].

## 2.3 Factors contributing to PID

To achieve a Right First Time (RFT) approach in the design process of new tools the designer should have an extensive knowledge of the factors contributing to the PID of the part under investigation.

The variety of factors that contribute to PID of composite structures and their relative significance has been studied by various researchers analytically [43, 44], experimentally [45–50] and numerically [51–55].

Albert *et al.* were the first to separate the factors that affect PID into two categories namely intrinsic and extrinsic [42]. The intrinsic factors arise from inside the structure and are defined as those related to part design i.e. part geometry, material properties and fibre/matrix interaction. The extrinsic factors are those related to tooling or processing and arise from the environmental conditions in which the structure is operating or from the manufacturing process (curing cycle, tool part interaction etc.).

An experimental investigation was also carried out by the researchers to understand the effect of design and process parameters on spring-in and warpage of C- and L-shaped composite specimens. Five design parameters (part shape, layup, flange length, part thickness and part angle) and three process parameters (tool material, tool surface and cure cycle) were considered [42]. They concluded that both design and process parameters can have a significant effect on spring-in and warpage and that there are multiple interactions between them. They also found that using aluminium tooling always results in higher spring-in compared to using steel tooling, a statement also confirmed by Kappel [56]. Kappel attributed this finding to the difference between the CTE of the tool and the composite structure when the latter is pressed to the tool due to the autoclave pressure along with geometrical locking if present. In his research on tool-part interaction on C- and L-profile specimens, Kappel concluded that a higher tool CTE leads to increased web warpage and web warpage occurs even though thermally compatible INVAR tooling is used [56]. INVAR, also known generically as FeNi36, is a nickel–iron alloy mainly used because of its low CTE which is comparable with the CTE of the composite structures. Zeng *et al.* suggest that the shape of the part has significant influence on the warpage, as its change during the curing cycle is one of the two components of the tool-part interaction with the other being the induced stress caused by constrained deformation of the part and the tool [57].

To reduce the stress transfer from the tool to the part, carbon epoxy and carbon foam

tools are proposed to be used [58]. Furthermore, the use of Carbon Nanofibers (CNFs) has been proposed to further reduce to residual stresses caused by the mismatch of resin and fiber strains during the cure [59–61].

Stefaniak *et al.* [62] investigated tool-part interaction of flat laminates and affirm that warpage of symmetric and initially flat laminates is mainly driven by tool-part interaction as a non-uniform stress field is developed, in the through-thickness direction as the resin cures. Tool surface roughness was observed to influence the magnitude of the deformations significantly as larger deflections were measured for higher tool roughness values when no release film is used. However, the use of release film on top of the tooling is able to transfer noticeable amounts of shear stress and affect the deformations. This is in agreement with the research of Liangliang *et al.* [63] and Twigg *et al.* [64] that the use of a Polytetrafluoroethylene (PTFE) release film or release agent cannot eliminate the effect of the tool-part interaction. The magnitude of the effect of the release film on the warpage of the part depends on the resin system used and on the coarseness of the tool surface.

An experimental method to study frictional behaviour during composites manufacturing was proposed by Ersoy *et al.* [65]. The researchers also studied the development of spring-in angle during cure of AS4/8552 thermosetting composite C-shaped specimens by using a cure quench technique [66]. They concluded that the thermoelastic component of spring-in, which refers to the shape change due to the mismatch of CTE in the in-plane and through-the-thickness directions, accounts for 50% of the final spring-in of fully cured components, while the non-thermoelastic component of the spring-in, which is predominantly due to cure shrinkage, accounts for the rest. Garstka *et al.* studied the relative contributions of cure shrinkage, thermal expansion and consolidation to the through-thickness strain during processing of AS4/8552 composites and developed an empirical relationship between the chemical shrinkage and the degree of cure [67].

In their effort to improve the accuracy of predictions of PID after cool down of carbon-fibre-epoxy composite frames, Kappel *et al.* studied the CTE of orthotropic laminates [68]. They found that measured CTE deviates from theoretical values, derived from unidirectional ply data using the Classical Lamination Theory (CLT) theory, when the degree of laminate orthotropy, which is quantified by the in-plane Young's moduli ratio $E_x/E_y$, increases. They consider the observed effect as critical, as inhomogeneous CTE leads to PID of curved composite structures. Incorrect CTE calculation leads to erroneous shape predictions, inaccurate tool compensation and ultimately to assembly problems.

PID of T-stiffeners and sandwich structures have also been investigated with the intention of increasing dimensional control of aerospace structures [69]. By investigating PID of sandwich structures it was found that by increasing core thickness and flexural rigidity the spring-in behaviour declines, due to the increased bending stiffness of the structure [70, 71]. Furthermore, Mahadik *et al.* found that the thermal expansion and Poisson's ratio of the core were the major contributors to spring-in [72]. Dhaheri *et al.* concluded that PID of curved sandwich structures is less than their laminated counterparts [73].

Svanberg separated the factors that contribute to PID into four main categories according to their relative significance (Fig. 2.6) [21]. Svanberg concluded that the difference in the CTE between the matrix and the fibres, the CSC of the resin, the laminate lay-up as well as the CTE of the tool have a large effect on the induced residual stresses in the part [21]. The void content and the fibre content gradients of the composite have moderate effect. Instead, cure time and tool thermal conductivity are reported to have little or no effect at all on shape distortions. Consequently, the factors related to resin or laminate properties are reported to have a large effect on the PID of the part. Process conditions that cause strain on the part are equally important, while manufacturing imperfections have a medium effect on the PID of the part.

To sum up the factors contributing to PID, the tool-part interaction, the design and properties of the laminate (effective CTE, stacking sequence, thickness, shape) are important contributors to the distortion of the part. Resin properties (CTE, CSC) and their difference to the respective fiber properties are key for an accurate prediction of PID. Finally, manufacturing imperfections (void content, fibre content gradients etc.) and curing cycle have only a modest effect.

## 2.4 Prediction of PID of composite structures

To predict PID of composites, analytical [74–76], semi analytical [77] and numerical approaches have been proposed [78–80].

### 2.4.1 Analytical models

The analytical models are usually used to get a first estimation of the spring-in angle of the structure and for benchmarking new material models [81, 82]. These type of models offer fast calculation times compared to other types of PID prediction methods.

| Factors | Effect[1] |
|---|---|
| Thermal expansion | Large |
| Cure shrinkage | Large |
| Laminate lay-up | Large |
| Cure temperature | Large |
| Mould thermal expansion | Large |
| Void content | Medium |
| Thermal gradients | Medium |
| Fibre content gradients | Medium |
| Cool-down rate | Medium |
| Cure time | Small |
| Fibre content | Small |
| Mould material surface | Small |
| Mould corner radius | No[2] |
| Mould thermal conductivity | No[3] |

1. The effect of the factors is classified in Large, Medium, Small and No effect on shape distortions.
2. May be important if this leads to a local thickness and fibre content variation.
3. The mould thermal conductivity is important if it is low. This may lead to unexpected temperature variations at the mould surface.

Figure 2.6: Segmentation of factors contributing to PID according to Svanberg [21].

Radford *et al.* proposed a simple analytical formula (Eq. (2.1)) for the calculation of spring-in angle of angled sections by taking into account the CTE of the structure [83]. The method assumes that the in-plane properties of the laminate are quasi-isotropic and that the through-thickness properties are uniform throughout the laminate. Eq. (2.1) has been used as a basis for the development of more complex analytical formulas offering better correlation with the experimental data [84–86].

$$\Delta\theta = \theta \left[ \frac{(CTE_L - CTE_T)\Delta T}{1 + CTE_T \Delta T} \right] \tag{2.1}$$

where $\theta$ is the included angle of the structure, $\Delta\theta$ is the change in included angle, $\Delta T$ is the change in temperature, $CTE_L$ and $CTE_T$ are the in-plane and through-thickness CTE, respectively.

In contrast, semi-analytical approaches can take into account the effect of some of these factors (e.g. thickness of the structure) that pure analytical models (e.g. Eq. (2.1)) cannot, but they require values measured by experiments as input data [87].

### 2.4.2 A complete numerical approach to simulate PID

Theoretically, a complete numerical process to simulate PID contains a fiber compaction simulation in order to ensure that no (or minimum) fiber wrinkling, bridging and fiber reorientation exist on the preform. Then, the permeability of the composite should be experimentally measured or modelled along with the viscosity of the resin during the curing cycle. Subsequently, a resin flow simulation is employed to calculate the distribution of fiber volume fraction in the part.

To this scope, Hubert *et al.* studied flow and compaction modelling on angled composite laminates [88]. Lightfoot *et al.* [89] studied the mechanisms responsible for fiber wrinkling and fiber misalignment of unidirectional plies during layup of prepreg in the tool while Potter *et al.* [90] directly measured fiber misalignment in as-delivered prepregs and observed that the material had fiber waviness. Furthermore, Lamers studied and modelled PID of composite structures due to processing induced fiber reorientation [91].

Then, a sequentially coupled or fully coupled thermal-chemical-analysis will enable the calculation of temperature and degree of cure distribution in the part. The mapping of these fields to the mechanical analysis and the use of a material constitutive equation results in the calculation of the residual stresses and the respective PID of the part [92–94].

However, a complete simulation process, as presented above, for the prediction of PID is rarely employed in the industry for every part as it would require extensive material characterization, expertise and processing power. Usually, assumptions are made like a uniform fiber volume fraction and temperature field in the part omitting much of the multi-physis complexity.

### 2.4.3 Material models

Material models simulate material behaviour under loading. These models correlate the strain experienced by the material with its stress state. This is achieved with the use of a constitutive equation which is characteristic for each model. Depending on the application the constitutive equation can range from a simple linear analytical equation to a complex mathematical expression which can be solved only numerically. Each model is designed to simulate a certain type of material behaviour. There are elastic, viscoelastic, plastic, viscoplastic, hyperelastic material models just to name a few.

The material models used for the simulation of PID in thermoset composites

manufacturing can be separated into three categories. These are the elastic, the modified elastic and the viscoelastic material models. The main reasons why elastic and modified elastic models are employed in the simulation of PID of composites, even if composite materials behave as viscoelastic materials during manufacturing, are to significantly reduce the material characterization effort, the model complexity and the computational time.

#### 2.4.3.1 Linear elastic model

The elastic material models focus on the development of the PID during the cool down phase of the curing cycle when the structure has attained its final degree of cure, assuming thermo elastic material behaviour at this stage. The residual stresses in the part arise due to the anisotropic thermal contraction [18]. The elastic models make use of the Hooke's law constitutive equation and require the smallest number of resin material properties to run. These are the CTE, the Young's modulus and Poisson constant of the unrelaxed (fully cured) resin state.

However, elastic models omit the effects of chemical shrinkage, the development of residual stress before cool-down and stress relaxation during the cure [95]. Ding *et al.* concluded in their research that purely elastic models can provide a good prediction of residual stress only for thin laminates because of the complex temperature field gradients in thick laminates which result in inhomogeneous through-thickness degree of cure evolution [96, 97]. To account for some of these deficiencies Bogetti *et al.* studied residual stresses and deformation of thick composite laminates and proposed a model able to take into account the chemical shrinkage of the resin during cure [98].

#### 2.4.3.2 Modified elastic models

The modified elastic models separate the curing history into a number of segments to which they assign an elastic modulus for calculating the residual stresses and distortion of the structure. The CHILE model divides the curing history into three states: a viscous state, the state where the modulus quickly builds, and the fully cured state where no further chemical reaction takes place [99]. The CHILE model has been used by several researchers [100–102] as well as used to benchmark the development of other material models [103–107]. However, it is still an instantaneously elastic model and cannot predict the stress relaxation during curing or post curing, as it is not a time dependent model [95, 97, 108].

Computational research on PID of L-shaped variable-stiffness composite structures

with the use of the CHILE model has been performed by Zhang *et al.* where the influence of corner radius, laminate thickness and flange length on spring-in was investigated. In this work it was found that spring-in is reduced as the specimen thickness is increased [109]. As the CHILE model is dependent on the degree of cure, it can take into account degree of cure gradients in the through-thickness direction of the part caused by temperature gradients. Therefore, it is better suited for the simulation of thick parts compared to purely elastic models which cannot capture this effect [96, 97].

#### 2.4.3.3 Viscoelastic models

Thermoset composite materials behave as viscoelastic materials. A viscoelastic material has an elastic component and a viscous component. The viscous component is responsible for the time dependence of the material properties. While purely elastic materials do not dissipate energy when a load is applied and removed, a viscoelastic substance does. Therefore, hysteresis is observed in the stress–strain curve, with the area between the loading and unloading cycle being equal to the energy lost.

The viscoelastic behaviour of composite materials originates from the polymeric nature of the resin. The fibres of the composite can be regarded as elastic materials and their properties do not change significantly during manufacturing. On the other hand, the resin changes its material state during manufacturing as it transforms from a viscous state to a viscoelastic state and finally to a glassy state which can be modelled as elastic or viscoelastic with large relaxation times.

Moreover, viscoelastic materials exhibit some phase-lag in strain when stress is applied. Purely elastic materials have stress and strain in phase, so that the response of one caused by the other is immediate. In purely viscous materials, the strain lags stress by a 90° phase. The amount of phase-lag in strain when stress is applied in viscoelastic materials is used to determine the loss modulus which represents the viscous portion of the material and the energy dissipated as heat.

In order to incorporate all the time dependent factors that affect shape distortion, such as heating and cooling rates, stress relaxation and cure time, viscoelastic material models are needed. Benavente *et al.* with the use of a viscoelastic material model predicted significant geometrical distortions at temperatures below the glass transition temperature which were not possible to predict with the use of elastic or CHILE model [92]. Zobeiry *et al.*, concluded that the CHILE model cannot successfully predict residual stresses and its effects on mechanical

performance of composites for cure cycles that the material experiences softening and devitrification, such as post curing cycles or complex curing cycles with intermediate holds. Therefore, in those cases viscoelastic material models are proposed to be implemented [108]. Furthermore, according to Zhang *et al.* an accurate simulation of the cure-induced residual stress should include the least two states of the entire cure process (relaxed state, a viscoelastic state and an elastic state), and consider the stress relaxation, thermal deformation and chemical shrinkage of the composite [95].

Zocher *et al.* presented a novel finite element scheme for linear anisotropic viscoelasticity [110]. The authors introduced a smart integration point constitutive update algorithm whereby the stress increment is separated into a part which is linear in the strain increment, and a non-linear contribution which can be computed from stored results in the previous increment. However, the authors make the assumption of a single reduced time for all directions which may be physically unrealistic for materials, such as fibre-reinforced composites.

To account for this deficiency, Poon *et al.* proposed a constitutive update scheme very similar in spirit to Zocher *et al.* able to obviate the need for non-physical assumptions with the proper choice of state variables [111]. The model takes as its input the converged values of stress, strain and state variables (named as "fictitious creep stresses") at time $n$ and the estimated strain at time $n+1$ and updates the stress tensor, state variables and the Consistent Tangent Operator (CTO), which is used in a Newton type iterative scheme. In a later publication the researchers extended their linear viscoelastic model to simulate solids exhibiting non-linearity of the Schapery type [112, 113]. This model is more appropriate for simulating cases where large deformations are expected and cases where the material changes its properties under deformation.

Ding *et al.* developed a $3D$ viscoelastic material model to simulate thermo-rheologically simple materials and extended their model to simulate also thermo-rheologically complex materials [96, 97]. Eom *et al.* have proposed a phenomenological model for the calculation of the relaxation modulus of a thermosetting system of the complete range of cure [114]. O' Brien *et al.* experimentally investigated the cure dependent relaxation modulus of an epoxy system over the entire range of cure extent and used the acquired data to develop a practical model for predicting the cure dependence of the relaxation modulus throughout cure under varying processing conditions [115]. However, both approaches require extensive material characterization over the entire cure range. While many viscoelastic material models have been proposed for the

prediction of PID of composites their adoption for the prediction of PID of large industrial parts is still limited.

The drawbacks of implementing viscoelastic material models are that they require extensive material characterization, have complex model formulations and require significantly longer calculation times and memory compared to elastic and modified elastic models, because of small time steps required and the state variables that need to be calculated and stored in memory at every time increment.

### 2.4.4 Boundary Conditions used to simulate PID

Boundary Conditions (BCs) play a key role in the accuracy of the simulation as they model the interaction of the system with the surrounding environment. In PID simulations the mechanical BCs model the interaction of the composite structure with the tool, which is usually referred to as tool-part interaction. In the heat transfer analysis, the thermal BCs model the heat transfer to the structure during the curing cycle.

#### 2.4.4.1 Mechanical BC

The mechanical BCs experienced by the composite during the curing cycle are complex. The Coefficient of Friction (CoF) between the part and the tool depends on the roughness of the tool surface and whether a release film or release agent has been applied on the tool surface. The fabric architecture (UD, NCF etc.) affects the contact behaviour of the part with the tool as shown by Avgoulas *et al.* [116]. Furthermore, the mechanical BCs depend on the shape of the structure and whether geometrical locking occurs between the part the tool. In the case of geometrical locking, the composite is forced to follow the expansional behaviour of the tool during the curing cycle, which is mainly driven by the tool CTE.

Moreover, the difference between the thermal strains of the tool and the composite structure's total strains (thermal plus chemical strains) determine the amount of shear stress transmitted from the tool to the composite in the presence of autoclave pressure. In case the shear stresses exceed the static shear friction limit, sliding occurs between the part and the tool during the curing cycle in the absence of geometrical locking. This type of tool-part interaction can be modelled with the use of friction models to simulate the shear stress transmitted from the tool to the composite structure. However, experimental investigations have to be conducted to determine the CoF at each phase of the curing history. The CoF during the curing process is not constant but depends on the state of material during the curing cycle

[57]. To accurately model the evolution of the CoF during the cure, an experimental investigation such as those presented in [64, 65, 117, 118] should be performed prior to the tool-part interaction modelling to determine the shear stress limit after which sliding occurs. Based on the experiment, an analytical formula is determined, which describes the evolution of CoF of the material system as a function of temperature or degree of cure of the curing cycle. This is a time consuming and costly process and usually this approach is not followed. Consequently, the definition of the mechanical BCs in PID simulations depends on the structure studied, the materials and the tool used and can be regarded as case specific.

For the above reasons, in most cases simple BCs are used to simulate PID of large scale structures. The most common mechanical BC used in the simulation of PID in thermoset composites manufacturing is the "fixed" or fully constrained nodes BC. In this case all nodes of the FE mesh of the model are not permitted to translate or rotate during cure (the Degrees of Freedom (DoF) of all nodes are set to zero). The demoulding of the structure is then simulated with the release of all the DoFs of the nodes except three. This is done to suppress rigid body motion and ensure numerical stability and convergence of the simulation.

Another type of mechanical BC is the "freestanding" BC. This BC assumes that there no significant tool-part interaction between the part and the tool and the composite is free to expand and contract without any restriction imposed from the tool. In this type of BC the DoFs of only three nodes are set to zero to suppress rigid body motion.

Svanberg examined the effect of "freestanding", fully constrained and contact BCs on the results of PID simulations. By comparing experimental measurements with simulation results the researcher found that contact during in-mould cure gave closest agreement to the experimental data and the prediction is between the bounds set by the "freestanding" and fully constrained BCs [21]. "Freestanding" and fixed BCs were also studied by Nielsen as two extreme cases between which the experimentally measured PID lie [119]. It was found that the use of the fixed BCs gives the closest result to the experimentally measured PIDs.

#### 2.4.4.2 Thermal BC

Thermal BCs on the composite structure are also difficult to determine accurately. Forced convection is the major mechanism of heat transfer between the tool and its surrounding fluid (air in the case of an oven, nitrogen in the case of an autoclave). The heat transfer coefficient $h$ in the oven is a complex function of oven free stream

temperature, pressure and fluid velocity, turbulence of the fluid, tool geometry, positioning and orientation of the assembly in the oven [57, 99]. To determine the heat transfer coefficient $h$ in the oven Computational Fluid Dynamics (CFD) simulation, empirical models or measurements are typically performed [57]. In industrial cases, the fluid flow around the tools inside an autoclave is rarely uniform. As a result the temperature field applied on the tool and subsequently to the composite structure is non-uniform during the cure.

Furthermore, the bagging set-up and materials affect the heat transfer as in some cases they can act as a thermal barrier. Therefore, in the case of one sided tools heat transfer to the part is not the same from each side. In addition, temperature gradients are present in the composite structure because of the anisotropic thermal conductivity of the composite materials and due to the property gradients which could be present because of the manufacturing configuration (e.g use of peel-ply cloth etc.).

For these reasons, in the industrial context, simplified thermal BCs are typically used. Usually, uniform temperature field is assumed in each time step of the curing history. In the simplest case, this temperature field is derived from the fluid temperature inside the oven. To increase the simulation accuracy the temperature field is obtained from thermocouples on the surface of the tool or between the part and the tool.

## 2.5 Material modeling in ABAQUS Software

In this research, the widely used commercial Finite Element solver ABAQUS was used to predict PID of composite structures. ABAQUS offers the ability to develop material models with the use of user material subroutines which interact with the solver. The UMAT and UMATHT subroutines of ABAQUS were used for the static structural and heat transfer analysis respectively.

### 2.5.1 UMAT interaction with the solver

The material models in the static structural analysis were implemented in ABAQUS with the use of UMAT subroutine. The role of this subroutine is to update the stress tensor and CTO of the material integration point that it is called at every time increment of the curing history. Fig. 2.7 depicts how UMAT interacts with the ABAQUS solver.

After the calculation of the updated stress tensor ($\boldsymbol{\sigma}^{n+1}$), state variables and the contribution of the integration point to the Jacobian matrix, ABAQUS checks if

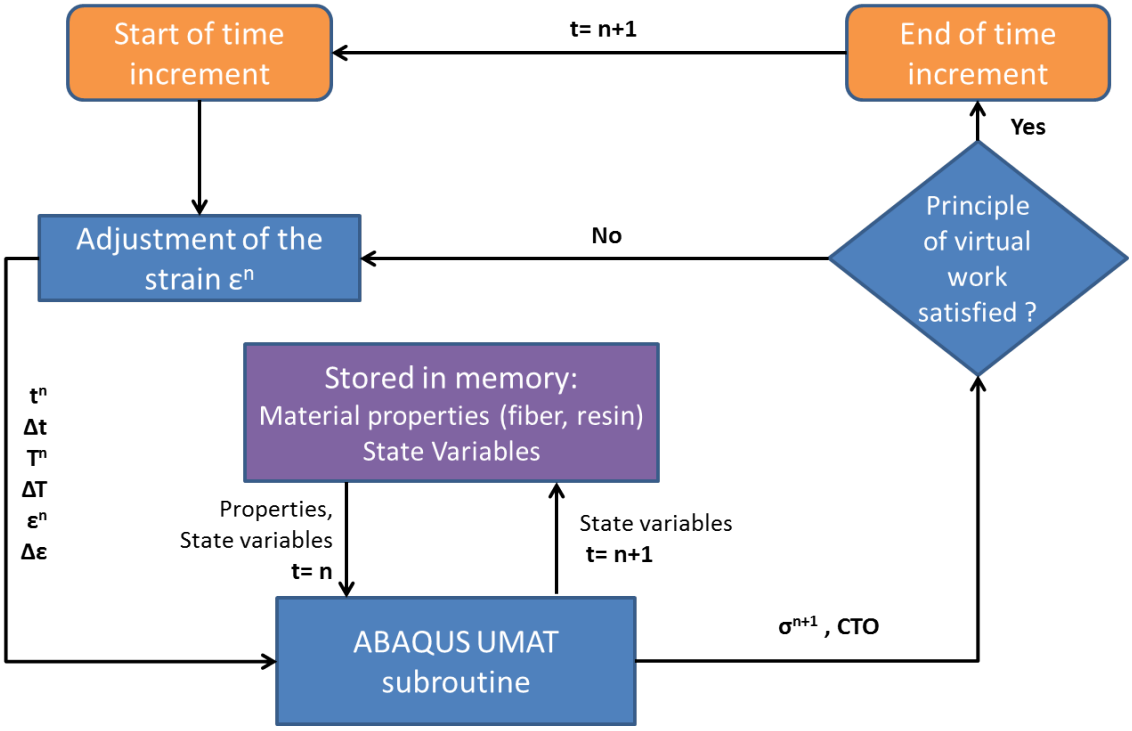


Figure 2.7: UMAT solution process.

the principle of virtual work is satisfied. In case this is true it proceeds with the calculation of the next integration point of the next or the same time increment in the case not all integration points of the current time increment have been calculated. In case the principle of virtual work is not met, ABAQUS adjusts the strain increments of the integration point and the UMAT calculations are repeated until the virtual work condition is met.

### 2.5.2 Type of element used in the stress/displacement problem

The three dimensional first order solid element *C3D8I* is used to discretize the geometry of the composite structure (Fig. 2.8). These elements are enhanced by incompatible modes to improve their bending behaviour [22].

The positions of the integration points in the layer closest to *face 1* are shown in Fig. 2.9.

Composite solid elements make use of multiple layers. In the thickness direction of the lamina, the integration points are referred to as section points. The location of the section points in the plane of the lamina coincides with the location of the integration points. The position and numbering of section points that are associated with an arbitrary integration point in a composite solid element are illustrated in Fig. 2.10.

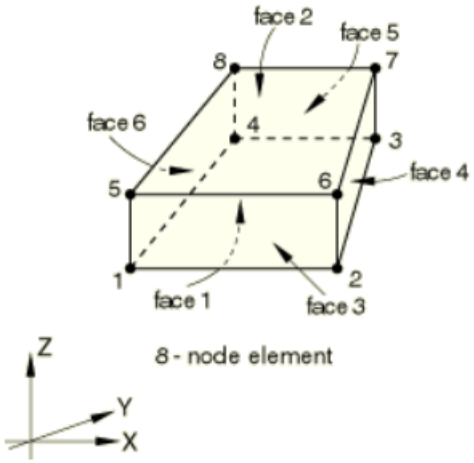


Figure 2.8: Three dimensional solid element [22].

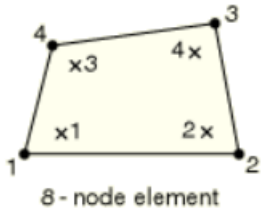


Figure 2.9: Integration points of an 8 node element in the layer closest to *face 1* [22].

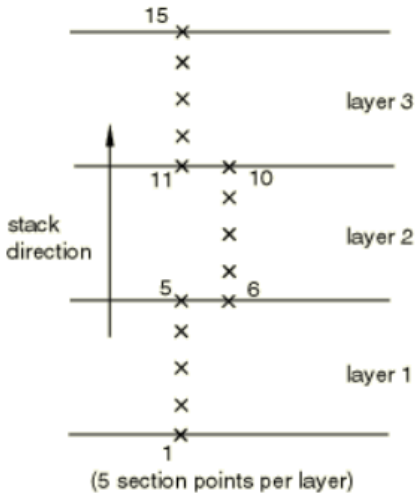


Figure 2.10: Section points of a 3 layered composite solid element [22].

The element matrices are obtained by numerical integration. Gauss quadrature is used in the plane of the lamina, and Simpson's rule is used in the stacking direction by ABAQUS. In the present research three section points were used in the thickness direction for each lamina.

### 2.5.3 Governing equations of the heat transfer analysis

The basic energy balance is the governing equation used by ABAQUS in heat transfer analysis [22].

$$\int_V \rho \dot{U} dV = \int_S \mathbf{q} dS + \int_V \mathbf{z} dV \tag{2.2}$$

where :

- $V$ : The volume occupied the body
- $S$ : The surface bounding volume $V$
- $\rho$ : Density of the material
- $\dot{U}$ : Material time rate of the internal energy
- $\mathbf{q}$ : Heat flux per unit area of the body, flowing into the body
- $\mathbf{z}$ : Heat supplied externally into the body per unit volume.

In Eq.(2.2) it is assumed that the internal energy of the system $U$ is function of temperature only $U(T)$ and the $\mathbf{q}$ and $\mathbf{z}$ are not related to the strains or displacements of the body. The specific heat capacity $c = \frac{dU}{dT}$ is usually used instead of $\dot{U}$ in Eq.(2.2) and the Fourier law Eq.(2.3) is employed to calculate the heat fluxes flowing into the body.

$$\mathbf{q} = -\mathbf{k} \cdot \frac{\partial T}{\partial \mathbf{x}} \tag{2.3}$$

where $\mathbf{k}$ is the conductivity tensor and $\mathbf{x}$ is the position. Finally, Eq.(2.2) is approximated with finite elements and the temperature is interpolated between the calculated nodal temperatures.

### 2.5.4 UMATHT interaction with the solver

The role of the UMATHT subroutine is to update the internal energy $U$, the heat flux vector $\mathbf{q}$, and their partial derivatives with respect to temperature and to spatial gradients of temperature, of the material integration point that it is called at every time increment of the curing history. Fig. 2.11 depicts how UMATHT interacts with the ABAQUS solver.

After the calculation of the updated variables and their partial derivatives, ABAQUS checks if the energy balance (Eq.(2.2)) is satisfied. In case this is true it proceeds with the calculation of the next integration point of the next or the same time

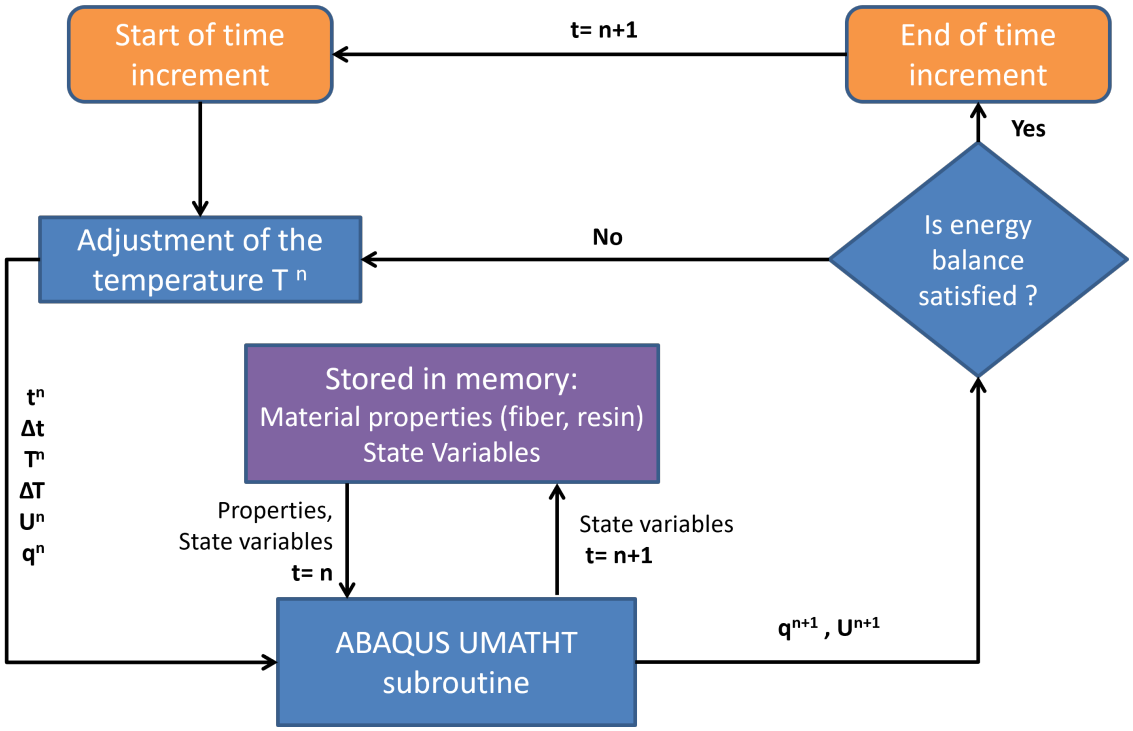


Figure 2.11: UMATHT solution process.

increment in the case not all integration points of the current time increment have been calculated. In case the energy balance is not met, ABAQUS adjusts the temperature of the integration point and the UMATHT calculations are repeated until this condition is met.

## 2.6 Novelty of the research

In spite of the amount of work performed in this field so far, an accurate estimation of PID in complex geometries remains an open research topic [120, 121]. This is mainly due to the great number of factors that contribute to PID, their interdependence and the variability of process conditions and material properties.

A goal of this research is to experimentally investigate the influence of stacking sequence, specimen thickness, tooling material and curing cycle on the spring-in angle of L-shape composite structures. The aim is to identify the driving factors affecting PID and to enrich the literature in this field by studying these parameters on the EPIKOTE$^{TM}$ System 600 resin system with UD and biaxial NCF consisting of IMS65 fibres. To the best knowledge of the author, such an extensive experimental investigation on PID for this material system does not exist in the literature and is presented here for the first time.

The motivation to study alternatives to INVAR tooling materials is to reduce

manufacturing costs by replacing the INVAR alloy with cheaper tooling materials where possible. Steel tools are already used to produce secondary structures in the aerospace industry but for the majority of the primary structures INVAR tooling is used. By evaluating the effect of tool-part interaction in this material system, the author wishes to facilitate the wider adoption of INVAR alternatives.

Another goal of this research is to develop a simulation framework suitable for the simulation of PID of large aerospace composite frames. Since stress relaxation is reported by various researchers as an important factor to be considered to accurately predict shape distortions of the studied part after demoulding [13, 122], the linear viscoelastic material model proposed by Poon *et al.* [111] was chosen to be evaluated. This was done due to its simple mathematical formulation compared to the material models proposed by Ding *et al.* [96, 97] and due to the convenient numerical implementation with the use of a commercial implicit finite element solver.

The combination of the time-cure-temperature superposition principle originally presented by Simon *et al.* [123] with the linear viscoelastic material model proposed by Poon *et al.* [111] is presented here for the first time. A novel feature in this research is the application of time-cure-temperature superposition principle with the use of the WLF model for both the temperature and degree of cure shift, instead of the use of the Arrhenius equation employed by Simon *et al.*, as the agreement of the material tested with the WLF formulation was very good.

As a reference for comparing the results of the visoelastic material model a modified CHILE material model is used which is often employed in the industry due to its simplicity and fast calculation times. Both material models were coupled with a cure kinetics model, functions to calculate instantaneous fibre volume fraction and Poisson's coefficient of the composite material and use the same micromechanics model to calculate lamina properties.

The proposed simulation framework focuses on the material modelling from the gelation point of the structure (after the fabric compaction and resin infusion process have been completed) to consolidation and demolding by deliberately omitting much of the multi-physics complexity prior to that point. However, the extension of the proposed simulation frameworks to capture this increased complexity would not require changes to the proposed modelling approach but only the addition of the relevant functionalities.

This chemo-mechanical simulation framework for PID prediction is extended to a thermo-chemo-mechanical one, with the addition of a heat transfer analysis prior

to the mechanical analysis for the material system under investigation. With the motivation to further increase the accuracy of the simulation framework, tool-part interaction is also included in the simulation by employing a constant and cure dependent coefficient of friction.

This extended simulation framework is applied to predict the spring-in angle of the composite L-shape specimens manufactured in the experiment. A comparison between simulation results using the modified CHILE and viscoelastic material models, an analytical equation and the experimentally measured spring-in angle of the specimens is presented. The aim is to identify a combination of the material model and boundary conditions which more efficiently predicts the shape of the manufactured part in terms of accuracy and modelling effort.

While the majority of the numerical and experimental investigations on PID found in the literature focus on flat, C- and L-shaped composite specimens, in this research a complex composite frame from the door surround structure of $A350$ aircraft was also studied. A comparison between the simulation results of the material models tested against $3D$ measurement data of the manufactured frame is presented here for the first time and the deformation modes that act on the frame are discussed.

This research aims to contribute to the maturity and adoption of higher fidelity PID simulation frameworks by OEMs and suppliers in the manufacturing process of aerospace composite structures.

Chapter

# 3

# Experimental Investigation

## 3.1 Manufacturing of specimens

The L-shape composite structures that were studied in this research are depicted in Fig. 3.1. The nominal included angle between the flanges of the specimens is 90°, the corner radius is 15 $mm$, the length of each flange is 100 $mm$ and the width of the specimens is 50 $mm$ (Fig. 3.2).

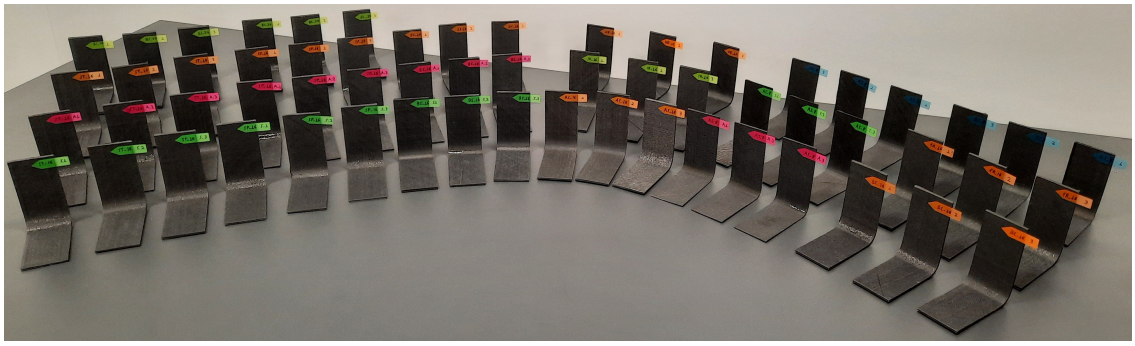

Figure 3.1: The L-shape composite specimens manufactured.

The composite specimens were manufactured using the EPIKOTE$^{TM}$ resin system 600 supplied by Hexion [124]. A UD and a biaxial (+45°/−45°) NCF, manufactured by Teijin Carbon, were used for creating preforms. The areal weight of UD and biaxial NCF was 194 $g/m^2$ and 407 $g/m^2$, respectively, including toughening veil (5

$g/m^2$) and powder binder (7 $g/m^2$). Both of the reinforcements consisted of IMS65 fibres, an indeterminate modulus fibre supplied by Toho Tenax.

The stacking sequences of the specimens manufactured are given in Table 3.1 along with their abbreviation. Underscores in the stacking sequence denote the use of NCF. Bending Stiff (BS) and Bending Flexible (BF) laminates were chosen to be manufactured in addition to representative Skin (SK), Frame (FR), Stiffener (ST) and Spar (SP) laminates to examine the effect of laminate bending stiffness on spring-in angle. Antisymmetric (AS) and heavily Unbalanced (UB) laminates were also manufactured to examine PID for these extreme cases. To increase the difference of the bending stiffness of the specimens, 8, 16 and 24 plies specimens were manufactured (Fig. 3.2). The subscripts of the laminate notations refer to the equivalent total number of plies of each design (e.g. $BS_8$ is composed of 8 UD plies.).

Table 3.1: The stacking sequences of the specimens manufactured.

| Laminate | Stacking sequence | 0 (%) | ±45 (%) | 90 (%) |
|---|---|---|---|---|
| $AS_8$ | $[\underline{45/-45}]_4$ | 0 | 100 | 0 |
| $BS_8$ | $[\underline{0/90}, \underline{45/-45}]_s$ | 25 | 50 | 25 |
| $BF_8$ | $[\underline{45/-45}, \underline{90/0}]_s$ | 25 | 50 | 25 |
| $BS_{16}$ | $[\underline{0/90}_2, \underline{45/-45}_2]_s$ | 25 | 50 | 25 |
| $BF_{16}$ | $[\underline{45/-45}_2, \underline{90/0}_2]_s$ | 25 | 50 | 25 |
| $SK_{16}$ | $[\underline{45/-45}_2, \underline{0/90}, 0_2]_s$ | 38 | 50 | 13 |
| $FR_{16}$ | $[\underline{45/-45}, 0, \underline{45/-45}, \underline{0/90}, 45]_s$ | 25 | 63 | 13 |
| $ST_{16}$ | $[\underline{45/-45}, \underline{0/90}, 0_4]_s$ | 63 | 25 | 13 |
| $SP_{16}$ | $[\underline{45/-45}_3, \underline{90/0}]_s$ | 13 | 75 | 13 |
| $AS_{16}$ | $[\underline{0/90}_2, \underline{45/-45}_4, \underline{0/90}_2]$ | 25 | 50 | 25 |
| $UB_{16}$ | $[\underline{0/90}_2, 45_4]_s$ | 25 | 50 | 25 |
| $BS_{24}$ | $[\underline{0/90}_3, \underline{45/-45}_3]_s$ | 25 | 50 | 25 |
| $BF_{24}$ | $[\underline{45/-45}_3, \underline{90/0}_3]_s$ | 25 | 50 | 25 |

To manufacture the preforms, rectangular plies with a length of 220 *mm* and width 70 *mm* were stamped in a press from the fabric rolls with the use of a custom die. Then the stacking sequence of the laminate designs was created and the preforms were stored in bags (Fig. 3.3) before manufacturing the parts.

In order to investigate the effect of the CTE of the tool material on the PID of the specimens, three tools were manufactured from INVAR, steel and aluminium alloy as depicted in Fig. 3.4. To manufacture the tools, 6 *mm* thick plates were laser cut, bent and welded to their nominal dimensions. The properties of the tooling

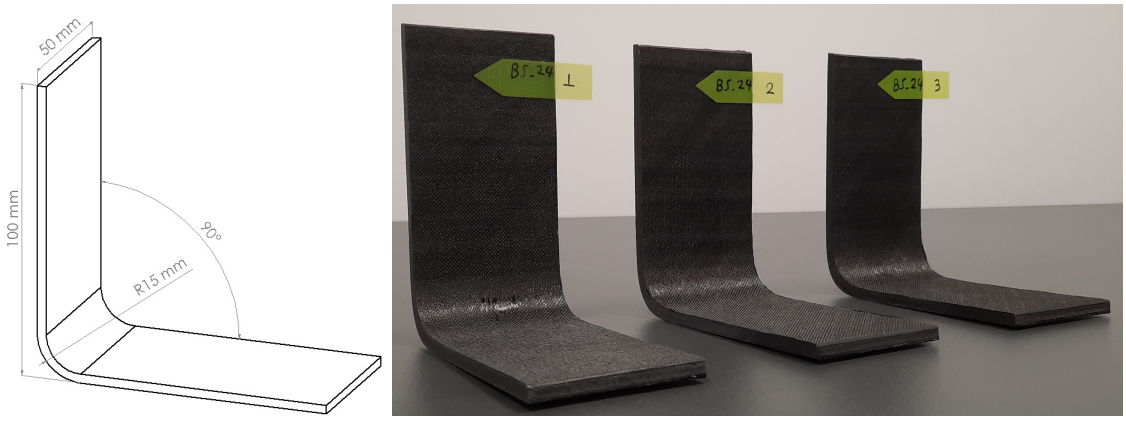


Figure 3.2: Left: Dimensions of the L-shape specimens, Right: The specimens of the Bending Stiff 24 plies ($BS_{24}$) laminate group studied.

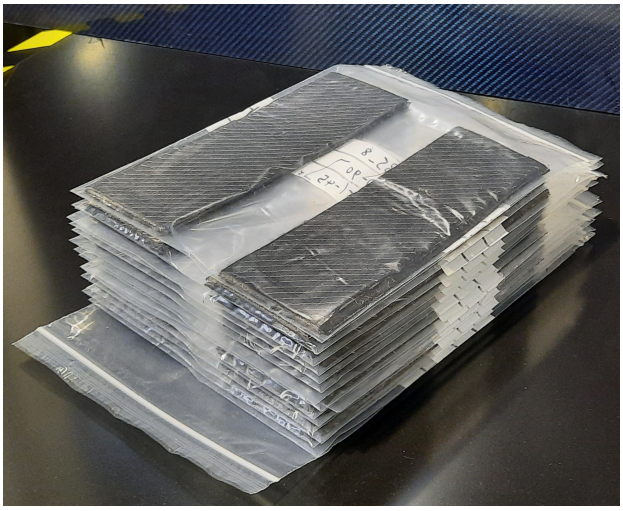

Figure 3.3: Preforms stored in bags before infusion.

materials are presented in Table 3.2 and the dimensions of the manufactured tools in Fig. 3.5.

Table 3.2: Material properties of the tools manufactured.

| Physical Property | INVAR | Steel | Aluminium |
|---|---|---|---|
| CTE ($K^{-1}$) | 6 E-07 | 1.2 E-05 | 2.34 E-05 |
| E-Modulus (GPa) | 140 | 207 | 70 |
| Poisson coef. | 0.29 | 0.30 | 0.35 |

Three specimens of each laminate design presented in Table 3.1 were manufactured using the INVAR tool. Also, three specimens of the $BS_{16}$, $SP_{16}$, $ST_{16}$ and $AS_8$ laminate designs were manufactured using each of the aluminium and steel tools. The specimens of the laminate designs manufactured from all available tools are shown in Fig. 3.6.

VARTM was used to manufacture the specimens. The infusion set-up consists

Figure 3.4: The three tools used to manufacture the specimens (From top to bottom: Steel, Aluminium and INVAR).

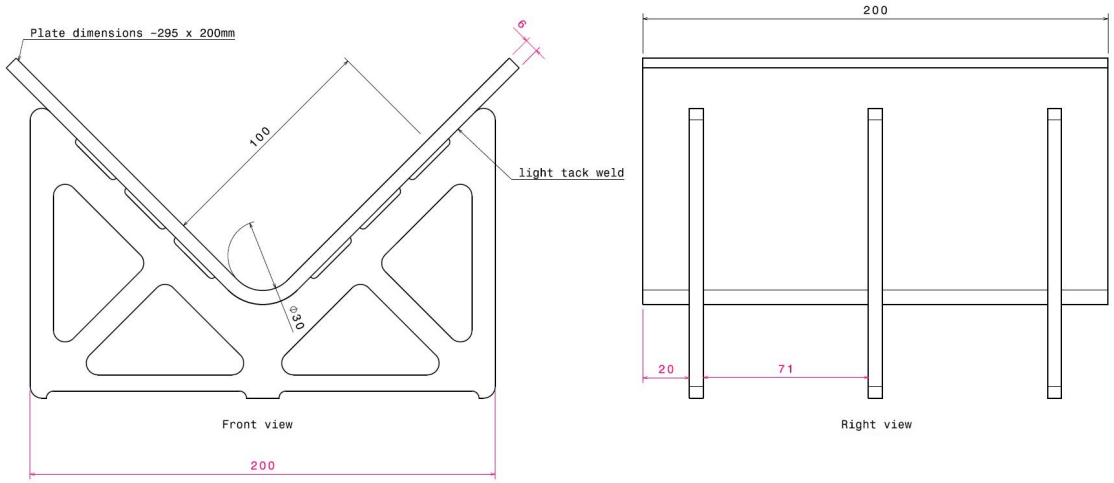


Figure 3.5: Drawing of the manufactured tools.

of a vacuum pump, high temperature lines (blue silicon tubes), a resin catch-pot equipped with a vacuum gauge to gather the excess of resin during infusion, K-type thermocouples and a four channel data recorder connected to the thermocouples to monitor and store temperatures (Fig. 3.7).

Four thermocouples were used for monitoring the temperature of each tool. Two were placed on the underside of the tool at each flange near the tool corner (Fig. 3.8). One thermocouple was placed in the bag and another one on top of the vacuum bag at the L-shape corner (Fig. 3.9) to measure the air temperature at this location. The sampling rate used was 12 measurements per minute (1 measurement per 5 sec).

Prior to resin infusion, the assembly was preheated to $120°C$ in a hot air oven. The

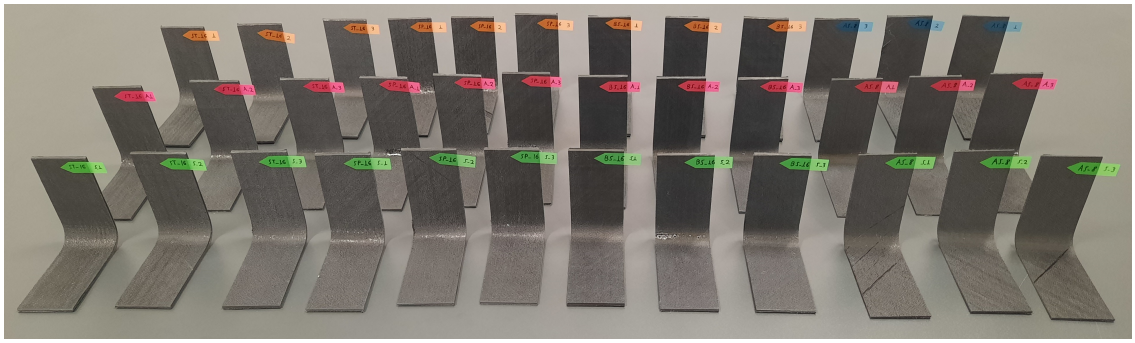

Figure 3.6: Specimens of the laminate designs manufactured from all available tools. From front to back: Parts manufactured from the steel, aluminum and INVAR tool respectively.

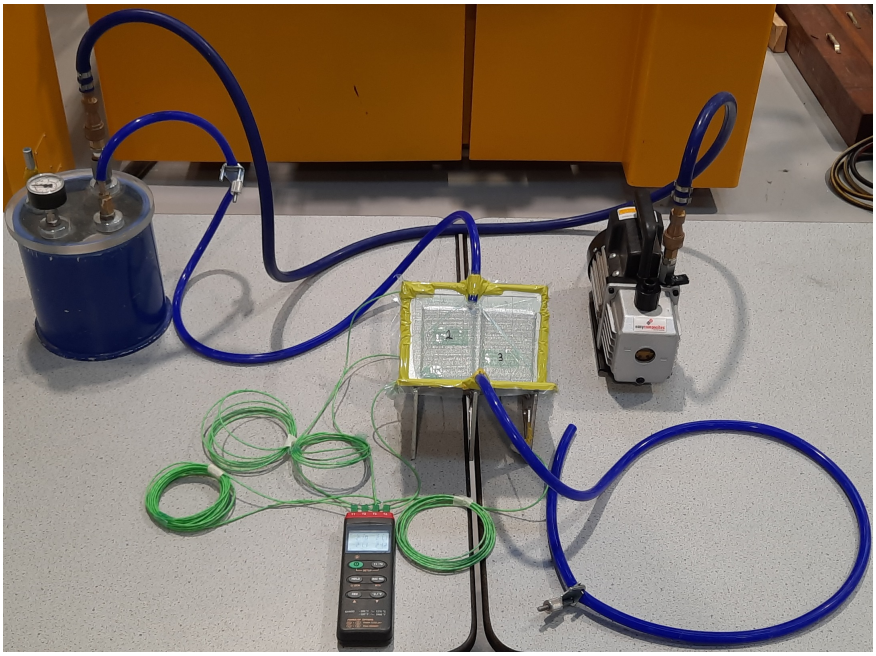

Figure 3.7: Two specimens side by side under vacuum, prior to the resin infusion process. The infusion takes place through the inlet tube (right) connected to the tool and the outlet tube connected to the catch-pot (left). The vacuum pump connected to the catch-pot provides the necessary pressure difference to the atmospheric pressure, which is necessary for the infusion to commence.

resin was preheated in a separate oven to $80°C$ in order to achieve the manufacturer's recommended resin viscosity of approximately 280 $mPa \times s$ [124]. When the assembly in the oven reaches $120°C$, the resin infusion starts, and the resin's viscosity drops while its temperature increases as it enters the preform.

The ovens used in the experiment are forced air circulation ovens both for curing the specimens and for preheating the resin. Fig. 3.10 shows the arrangement of the equipment before and during the curing cycle. Usually two specimens were placed side by side on a tool as shown in Fig. 3.7 and where possible, placed in the oven

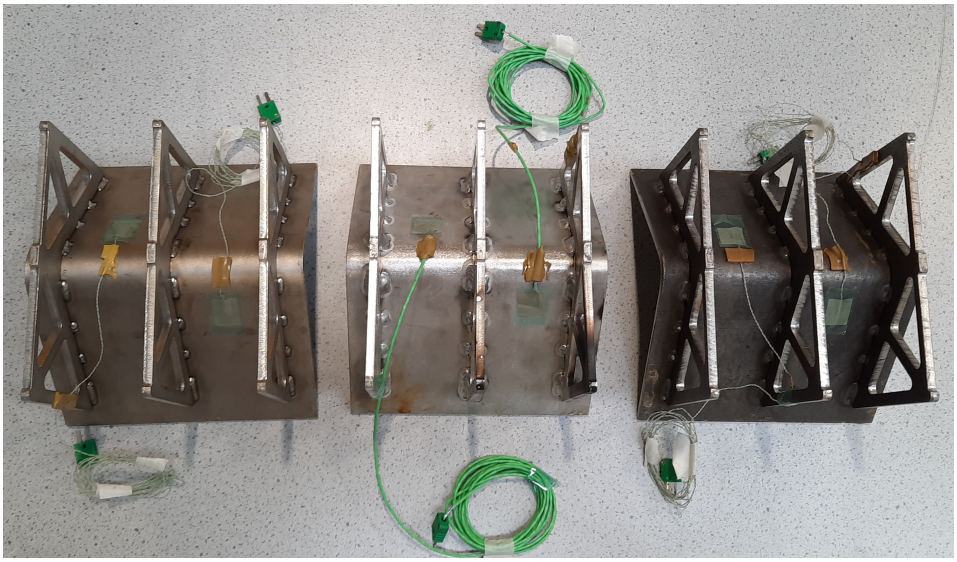

Figure 3.8: Thermocouples setup: Two thermocouples were placed on the underside of the tool near the corner.

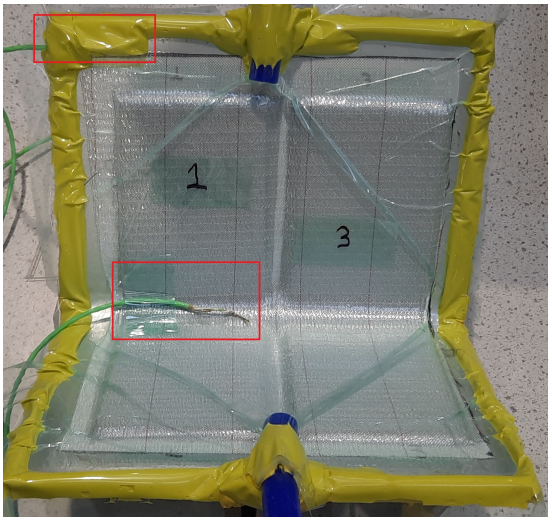


Figure 3.9: Thermocouples setup: One thermocouple was placed in the bag under the sealant tape (top left) and another one was placed on top of the vacuum bag at the L-shape corner to measure air temperature at this location.

with other tools that were to be subjected to the same curing cycle. One peel ply fabric layer was used per molding on top of which the resin flow mesh was placed. The peel ply fabric layer and the resin flow mesh had the same dimensions per bagging set-up. Furthermore, the location of the resin injection and outlet hose was approximately the same for every molding. The infusion of the preform took place from the high temperature lines entering the oven at the bottom of it as shown in Fig. 3.10.

All laminate designs shown in Table 3.1 were manufactured using the MRCC [124]. The MRCC consists of a two hour dwell at $180°C$. In order to evaluate the effect of


Figure 3.10: Arrangement of the equipment before (left) and during (right) the curing cycle. The oven used to preheat the resin is the small one next to the oven used to manufacture the specimens.

the curing cycle on PID of the parts, the $BS_8$, $BF_8$ and $AS_8$ laminate designs were also manufactured by another curing cycle denoted hereafter as the "Fast" curing cycle. This curing cycle differs from the MRCC as the two hours of 180°$C$ dwell was substituted by a 15 *min* 195°$C$ dwell. The 195°$C$ dwell was chosen in order for the two curing cycles to have the greatest difference possible in the curing temperatures, yet retain a small safety margin of 5°$C$ to the maximum operating temperature of the consumables (200°$C$). The "Fast" curing cycle was designed to produce approximately the same final degree of cure as the MRCC (Fig. 5.1). This was done by running 0$D$ simulations of the cure kinetics Eq.(4.1), where the 15 *min* dwell was found enough for the two curing cycles to produce parts with approximately the same degree of cure. Fig. 3.11 depicts the specimens manufactured by the "Fast" curing cycle.

Fig. 3.12 shows the temperatures recorded from the thermocouple placed in the vacuum bag (Fig. 3.9) for the two curing cycles investigated. The blue curve shows the MRCC recorded at the manufacturing of the $AS_8$ specimen 3, while the green curve shows the temperature profile of the "Fast" curing cycle recorded at the manufacturing of a specimen having the same stacking sequence. Both specimens were manufactured with the INVAR tool.

As shown in the case of the MRCC during the infusion, a slight drop of the assembly temperature is recorded by the thermocouple because the resin is cooler than the tool and preform. After the infusion is finished the assembly temperature again reaches 120°$C$ and a heat-up phase follows to the curing temperature. When the curing process is over, the oven is switched off and the assembly is left in the oven to cool down to room temperature.

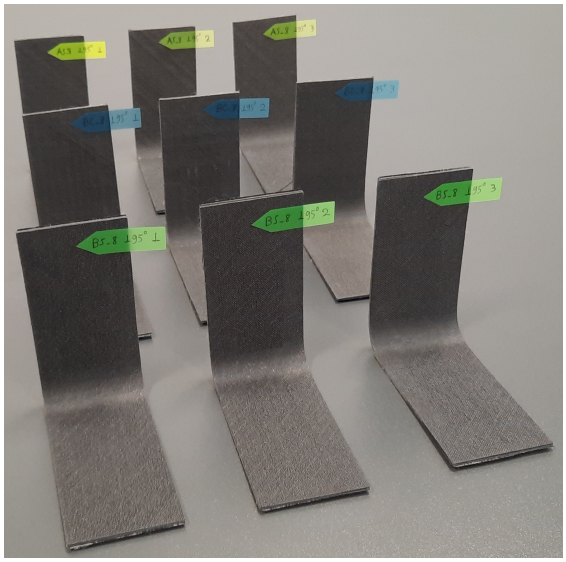

Figure 3.11: The specimens manufactured with the "Fast" curing cycle (15 *min* dwell at 195°*C*).

The heating and cool down rates of the cycles depend on the loading of the oven (number of tools in the oven), the material of the tool and the ventilation set-up of the oven (low, medium, high). However, effort was made to keep these rates below 2.5°*C*/*min* (by manually adjusting the oven operating parameters such as ventilation level) to avoid the development of significant temperature gradients through the thickness of the parts. Fig. 3.13 shows the INVAR tool in the oven before and after the infusion.

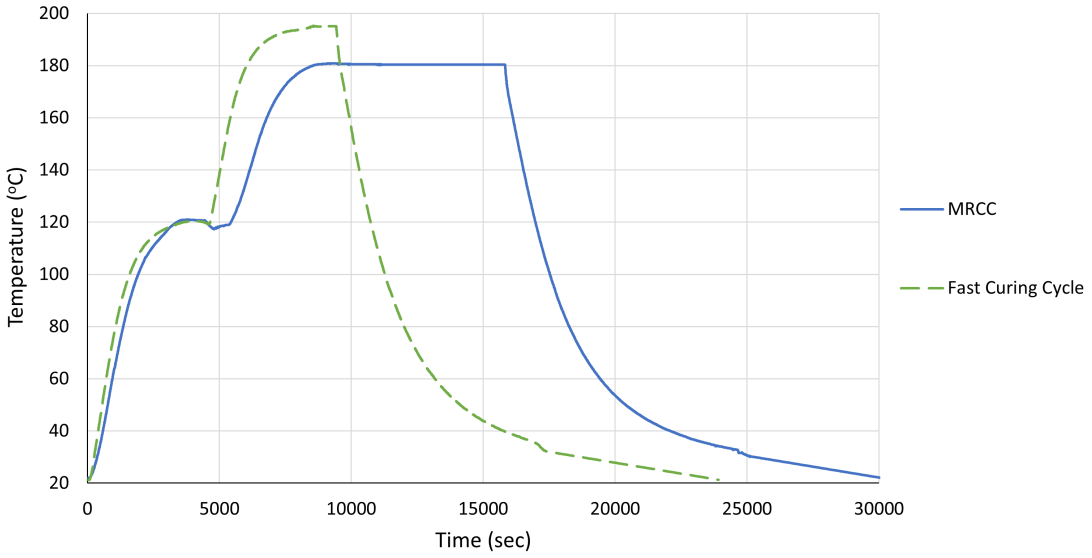


Figure 3.12: The two curing cycles investigated: According to the MRCC (blue curve) the part cures for 2 hours at 180°*C*. The "Fast" curing cycle investigated (green curve) consists of 15 min dwell at 195°*C*. The temperature data of the curing cycles was obtained from the thermocouple placed in the vacuum bag.

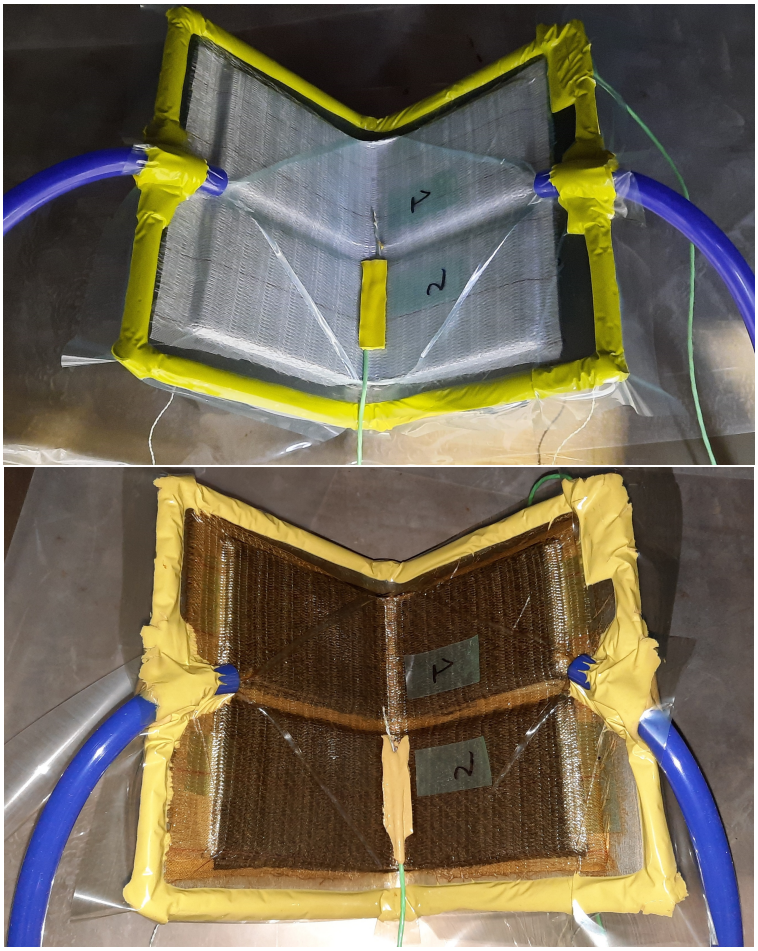

Figure 3.13: The INVAR tool in the oven before (top) and after (bottom) the infusion.

## 3.2 Manufacturing defects encountered

After the curing process was finished the specimens were demoulded and visually inspected for manufacturing defects. These include fibre bridging, dry spots, pinholes, fibre pull out, preform misalignment and corner thickening. According to the extent of the defects encountered the experiment was either repeated or it was assumed that they affect insignificantly the PID of the specimen.

The type of defect present in each specimen is presented in Tables 3.3-3.5. Thickening in Tables 3.3-3.5 refers to both flange and corner thickening. Fig. 3.14 shows fibre bridging which occurred at the manufacturing of the $ST_{16}$ specimen 3 with the use of the aluminum tool. As shown in Table 3.3 all specimens of the $UB_{16}$ group suffer from bridging. This is mainly due to the manufacturing of the stacking sequence of the parts which has many consecutive 45° plies. Each 45° ply was manufactured by two patches by splitting the UD roll as its width did not allow to cut a single patch from it. The two patches met near the corner of the specimen to form the ply and this is believed to cause the bridging of those parts. Fig. 3.15 shows a dry area in the corner of the $BS_{16}$ specimen 2. Pinholes present at the tool side of the $AS_{16}$ specimen 2 are shown in Fig. 3.16. At the demoulding step of the specimens, the removal of the consumables from the part by pulling the peel ply may result in fibre pull out from the specimen surface as shown in Fig. 3.17.

Specimens that passed the visual inspection were then machined to their nominal dimensions by cutting approximately 10 *mm* from each side with the use of a diamond wheel saw. After machining, the thickness of the corner and flanges of the manufactured specimens was measured with a digital vernier caliper of 0.01 *mm* resolution. The thickness of each flange was measured at 9 locations across the flange (18 locations for each specimen). The thickness of the specimen corner was measured at the edges of the part (2 locations). The average value of the measurements along with the standard deviation of each laminate design is presented in Table 3.6. The nominal thickness of the 8, 16 and 24 ply specimens is 1.47 *mm*, 2.94 *mm*, and 4.42 *mm*, respectively, resulting from the nominal thickness of the UD and biaxial NCF which is 0.184 *mm* and 0.368 *mm* respectively.

As shown in Tables 3.3-3.6 flange and corner thickening (compared to the nominal laminate thickness) is observed for all the parts manufactured. The average thickness of the flanges of the specimens is approximately +0.14 *mm*, +0.13 *mm* and +0.17 *mm* greater than the nominal value, for the 8, 16 and 24 ply specimens respectively. This might be due to material variability as well as not perfect fibre compaction. Moreover, the thickness of the corner is $24 - 52\%$ greater than the average thickness

Table 3.3: Type of defect present in the specimens manufactured from the INVAR tool and MRCC.

| Laminate | | Thickening | Pinholes | Dry Spots | Fibre pull-out | Fibre bridging |
|---|---|---|---|---|---|---|
| $BS_8$ | Spec.1 | X | | | X | |
| | Spec.2 | X | | | | |
| | Spec.3 | X | | | | |
| $BF_8$ | Spec.1 | X | | | | |
| | Spec.2 | X | | | | |
| | Spec.3 | X | | | | |
| $AS_8$ | Spec.1 | X | X | | | |
| | Spec.2 | X | X | | | |
| | Spec.3 | X | X | | | |
| $BS_{16}$ | Spec.1 | X | X | | | |
| | Spec.2 | X | X | | | |
| | Spec.3 | X | X | | | |
| $BF_{16}$ | Spec.1 | X | X | | | |
| | Spec.2 | X | X | | X | |
| | Spec.3 | X | X | | | |
| $SK_{16}$ | Spec.1 | X | X | | | |
| | Spec.2 | X | X | | X | |
| | Spec.3 | X | X | | | |
| $FR_{16}$ | Spec.1 | X | X | | X | |
| | Spec.2 | X | X | | | |
| | Spec.3 | X | X | | | |
| $ST_{16}$ | Spec.1 | X | X | | | |
| | Spec.2 | X | X | | | |
| | Spec.3 | X | X | | | |
| $SP_{16}$ | Spec.1 | X | X | | | |
| | Spec.2 | X | X | | X | |
| | Spec.3 | X | X | X | | |
| $AS_{16}$ | Spec.1 | X | X | | | |
| | Spec.2 | X | X | | | |
| | Spec.3 | X | X | | | |
| $UB_{16}$ | Spec.1 | X | X | | X | X |
| | Spec.2 | X | X | | | X |
| | Spec.3 | X | X | X | X | X |
| $BS_{24}$ | Spec.1 | X | X | X | | |
| | Spec.2 | X | X | X | | |
| | Spec.3 | X | X | X | | |
| $BF_{24}$ | Spec.1 | X | X | | | |
| | Spec.2 | X | X | | | |
| | Spec.3 | X | X | | | |

Table 3.4: Type of defect present in the specimens manufactured from the INVAR tool and the "Fast" curing cycle.

| Laminate | | Thickening | Pinholes | Dry Spots | Fibre pull-out | Fibre bridging |
|---|---|---|---|---|---|---|
| $BS_8$ | Spec.1 | X | X | | | |
| | Spec.2 | X | X | | | |
| | Spec.3 | X | X | | | |
| $BF_8$ | Spec.1 | X | X | | | |
| | Spec.2 | X | X | | | |
| | Spec.3 | X | X | | | |
| $AS_8$ | Spec.1 | X | X | | | |
| | Spec.2 | X | X | | | |
| | Spec.3 | X | | | X | |

Table 3.5: Type of defect present in the specimens manufactured from the steel and aluminium tools and MRCC.

| Laminate | | | Thickening | Pinholes | Dry Spots | Fibre pull-out | Fibre bridging |
|---|---|---|---|---|---|---|---|
| $BS_{16}$ | Steel | Spec.1 | X | | | | |
| | | Spec.2 | X | | X | | |
| | | Spec.3 | X | X | | | |
| | Alum. | Spec.1 | X | X | | | |
| | | Spec.2 | X | X | | | |
| | | Spec.3 | X | X | | | |
| $ST_{16}$ | Steel | Spec.1 | X | X | | | |
| | | Spec.2 | X | X | | | |
| | | Spec.3 | X | X | | | |
| | Alum. | Spec.1 | X | | | | |
| | | Spec.2 | X | X | | | |
| | | Spec.3 | X | | | | X |
| $SP_{16}$ | Steel | Spec.1 | X | X | | | |
| | | Spec.2 | X | X | | X | |
| | | Spec.3 | X | X | | | |
| | Alum. | Spec.1 | X | X | X | | |
| | | Spec.2 | X | X | | | |
| | | Spec.3 | X | X | | | |
| $AS_8$ | Steel | Spec.1 | X | | | X | |
| | | Spec.2 | X | | | | |
| | | Spec.3 | X | | | X | |
| | Alum. | Spec.1 | X | | | X | |
| | | Spec.2 | X | | | | |
| | | Spec.3 | X | X | X | | |

Table 3.6: Thickness of the specimens manufactured and increase (%) of the corner to wall thickness.

| Laminate | $t_{wall}(mm)$ | $t_{corner}(mm)$ | Increase(%) |
|---|---|---|---|
| $AS_8$ | 1.62±0.05 | 2.06±0.31 | 27.16 |
| $BS_8$ | 1.62±0.06 | 2.32±0.21 | 43.21 |
| $BF_8$ | 1.60±0.05 | 1.97±0.12 | 23.13 |
| $BS_{16}$ | 3.08±0.08 | 4.54±0.59 | 47.40 |
| $BF_{16}$ | 3.07±0.09 | 3.77±0.19 | 22.80 |
| $SK_{16}$ | 3.04±0.07 | 4.15±0.13 | 36.51 |
| $FR_{16}$ | 3.09±0.08 | 4.20±0.18 | 35.92 |
| $ST_{16}$ | 3.04±0.08 | 4.59±0.53 | 50.99 |
| $SP_{16}$ | 3.06±0.08 | 3.79±0.39 | 23.86 |
| $AS_{16}$ | 3.12±0.11 | 4.32±0.23 | 38.46 |
| $UB_{16}$ | 3.05±0.08 | 4.64±0.32 | 52.13 |
| $BS_{24}$ | 4.62±0.09 | 6.13±0.25 | 32.68 |
| $BF_{24}$ | 4.56±0.10 | 5.67±0.08 | 24.34 |

of the flanges of the specimens. However, its effect on the induced distortion of the part is thought to be small [21]. Fig. 3.18 shows corner thickening of the $BF_{16}$ specimen group.

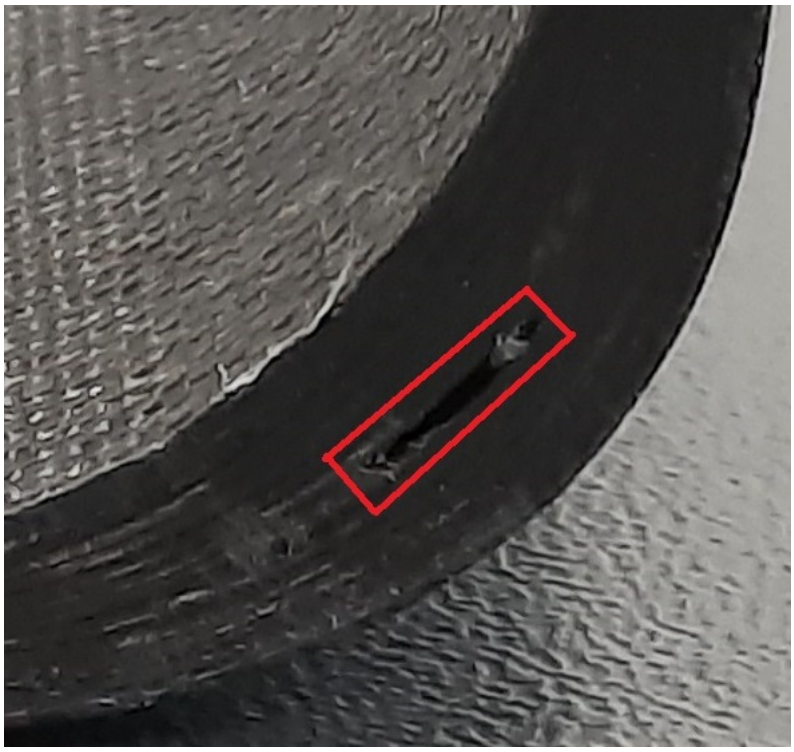

Figure 3.14: Fibre bridging of the $ST_{16}$ specimen 3 manufactured from the aluminum tool.

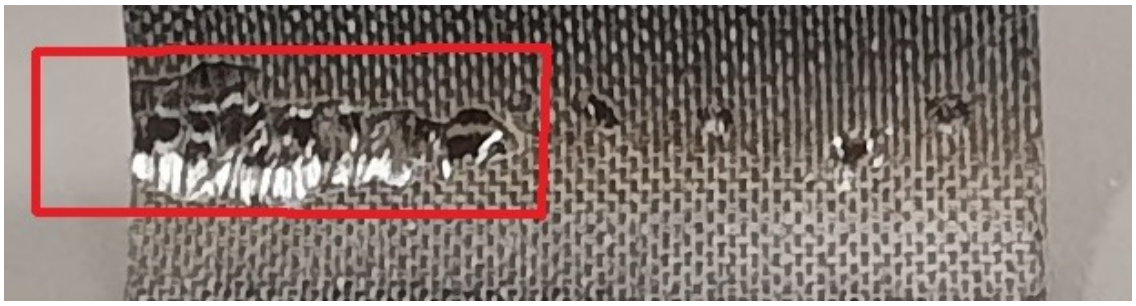

Figure 3.15: Dry spots in the corner of the $BS_{16}$ specimen 2 manufactured by the steel tool.

Figure 3.16: Pinholes at the tool side of the $AS_{16}$ specimen 2.

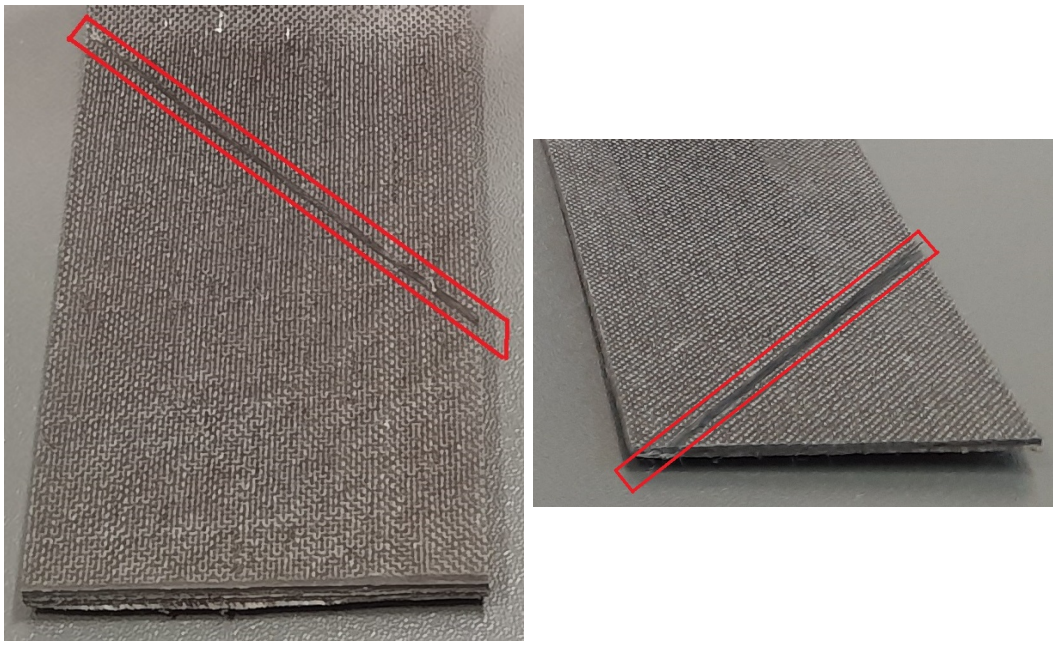

Figure 3.17: Fibre pull out from the specimen surface at the removal of the consumables (left: $SK_{16}$ specimen 2 manufactured with the MRCC, right: $AS_8$ specimen 3 manufactured with the "Fast" curing cycle.)

Figure 3.18: Corner thickening of the $BF_{16}$ specimen group.

### 3.2.1 Defects resulting in the repetition of the experiment

The requirement to perform the infusion at high temperature ($80°C$ & $120°C$ resin and assembly temperature respectively) in order to reduce its viscosity and enable the infusion imposes a few challenges at the manufacturing of the parts. To begin with, the mould release agent must not have been applied at the area where the sealant tape is placed. In case the mould release agent has been applied to this area it should be carefully removed with the use of acetone before the bagging process. The result of the application of the mould release agent to the area where the sealant tape is placed is only evident at high temperatures, where the sealant tape cannot keep its tacky properties and the vacuum is lost while the assembly is in the oven. Moreover, at $120°C$ the consumables and especially the sealant tape softens. This may result in the sucking of the sealant tape in the outlet hose due to the vacuum if the tape has been placed in close proximity with the hose end. In such occasion the infusion is very slow or it cannot even commence. Those cases appeared at the first manufacturing runs and the manufacturing run had to be repeated.

At one of the first manufacturing runs, the mould release agent was not properly removed from the sealant tape area. At the infusion phase a drop in the vacuum level was observed in the vacuum gauge indicating a leak. It was decided to open the oven door to identify the leak in the hope to seal it locally with the application of some more sealant tape and a clamp. The leak was easy to identify from the air bubbles entering the tool and a small quantity or resin around the leak. Paper was used to absorb the excess of resin but was forgotten under the tool. The leak was isolated, the vacuum level was acceptable, the infusion was completed, the oven

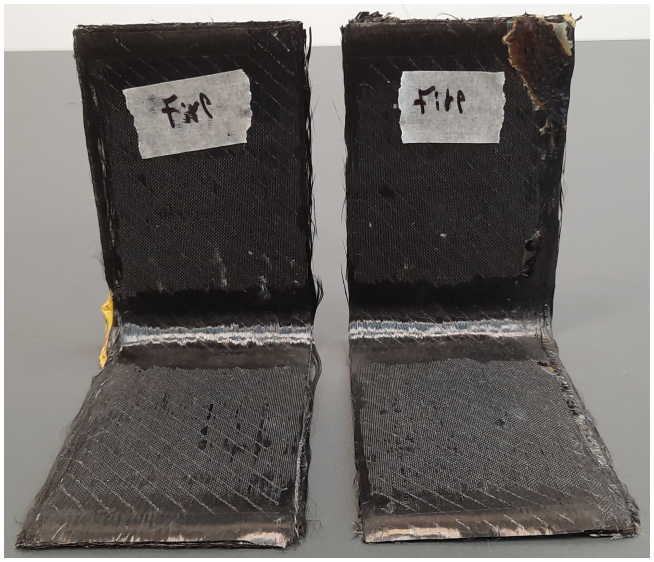

Figure 3.19: Consumables impregnated with resin were left under the tool during the curing cycle. At the curing temperature of 180°$C$ self-ignition of the flammable material occurred and the fire spread out to the specimens before the fire was put out (no apparatus or person was harmed).

door was closed and the curing cycle was decided to resume. Around the curing temperature though, fire initiated from the paper left in the oven, the result of which at the specimens is shown in Fig. 3.19.

Fig. 3.20 shows the result of one of the first manufacturing runs where a pressure sensitive tape was not used to fix the preform in the tool. As a consequence at the application of the vacuum and during the infusion preform misalignment occurred. In the subsequent manufacturing runs a pressure sensitive tape was used at the top of each flange to fix the preform.

Fig. 3.21 shows the result of vacuum bag burst during the "Fast" curing cycle. The manufacturing of these specimens proved to be a challenging task because the curing temperature of 195°$C$ is close to the maximum operating temperature (200°$C$) of the consumables used (vacuum bag, sealant tape, resin flow mesh etc.). As a result on some occasions the vacuum bag burst above 190°$C$. In this case, large areas of the specimens were not fully impregnated with resin as shown in Fig. 3.21 because the resin was still in a semi-liquid state at that point in the curing cycle.

To mitigate the risk of bag bursting during the curing cycle the bagging process required extra time to ensure that no sharp edges exist (e.g. in the area where the hoses are placed in the bag) or they are properly covered with sealant tape to avoid stress concentration in the bag that leads to the burst. Furthermore, it was observed that the tool should not be placed in the downstream of the hot air entering the

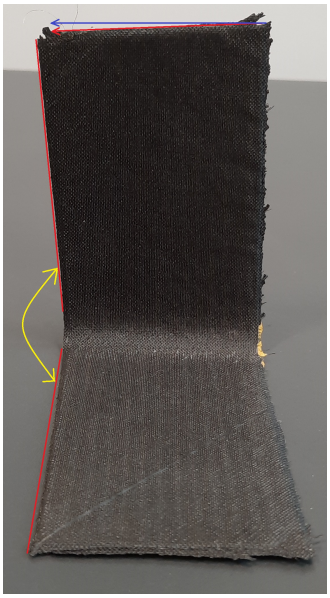

Figure 3.20: Not using pressure sensitive tape to fix the preform in place resulted in preform misalignment during the application of vacuum and infusion. Blue line depicts the straight line that the preform should follow, red lines depict the boundaries of the preform as manufactured. The two red lines shown by yellow arrow should be co-linear however due to preform misalignment they form an angle.

oven as this may lead to the increase of the bag temperature locally. Moreover, the temperature gradients before reaching the curing temperature should be kept as low as possible to avoid inhomogeneous thermal stress in the bag. As a result, the ventilation of the oven was set at its maximum capacity. A simple solution to mitigate the risk of bag bursting with the use of this curing cycle would be to use consumables capable of withstanding higher temperatures. However, this solution would increase the cost of the experiment and was not chosen.

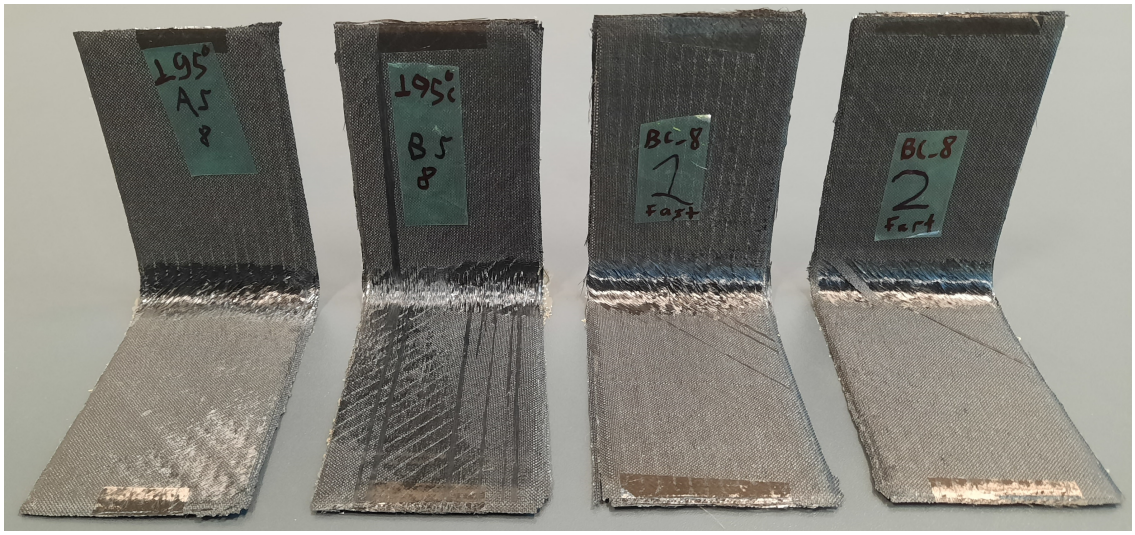


Figure 3.21: Bag burst at the manufacturing of specimens with the "Fast" curing cycle. This resulted in large areas of the specimens not fully impregnated with resin.

## 3.3 Measurement of specimens and tools

The geometry of the specimens and tools was measured both with the use of a CMM and a $3D$ scanner. The CMM is a tactile (contact) measurement method which is known for the accuracy and traceability of the measurements. The $3D$ scanner is an optical measuring method capable of measuring large scale structures while offering high measuring speeds. The motivation to measure the same geometry with two measurement methods was to identify any significant differences in the measurement results.

The CMM system used is the Mitutoyo Crysta Apex S7106 (Fig. 3.22). It is a high accuracy, high speed moving bridge type CMM. However, compared to a $3D$ scanner it has a limited data acquisition speed and data density and is considered unsuitable for measuring the geometry of compliant materials [23].


Figure 3.22: The CMM used to measure PID of the specimens [23].

To measure the specimens in the CMM, the parts were mounted in the machine as shown in Fig. 3.23. Then, the outer surfaces of the flanges were approximated with the use of $10 \times 10$ points for each surface, equally spaced across the area of the flange (Fig. 3.23). Accordingly, each tool surface was approximated with a maximum of $19 \times 10$ points. The measurement of the specimens and tools in the CMM was performed by the technicians of the manufacturing metrology team of the University of Nottingham.

The measured points on a flange surface were used to fit a plane, by employing a

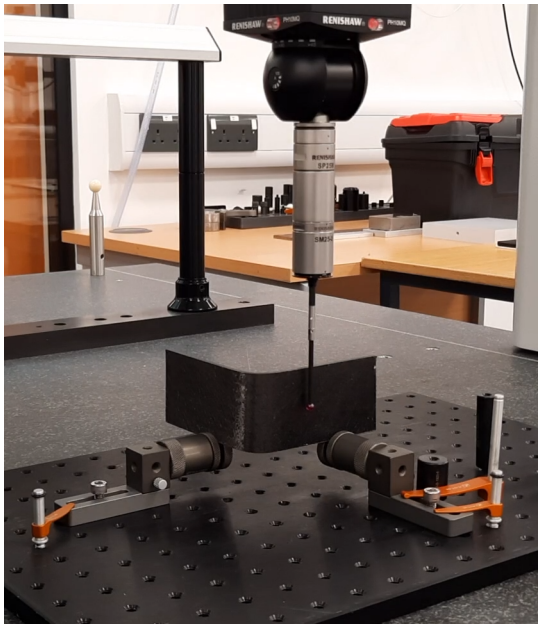

Figure 3.23: Measurement of PID of the $BF_{16}$ specimen 1 in the CMM.

Gaussian best fit algorithm, that represents the actual flange surface. Finally, the included angle of the specimen was determined as the angle between the normal vectors of the two fitted planes as shown in Fig. 3.24. The plane fitting and measurement of the angles of the specimens was done with the use of the respective functions provided in GOM Inspect suite [125].

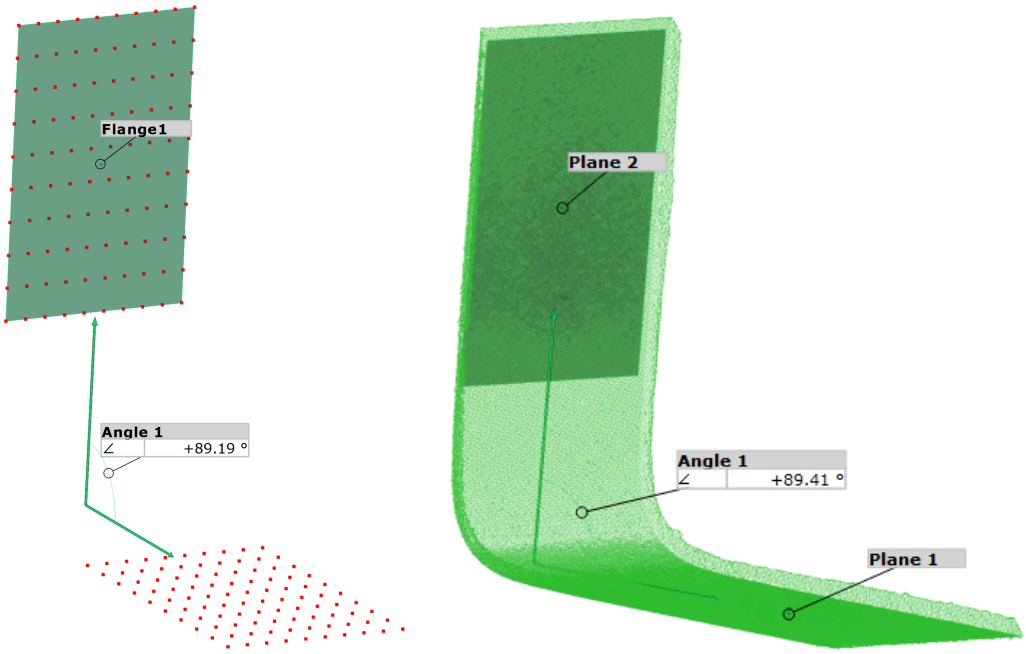


Figure 3.24: Fitting of planes to the acquired data and measurement of enclosed angle. Left: CMM data of the $BF_{16}$ specimen 1. Right: $3D$ scanner data consisting of 226769 points of the $SP_{16}$ specimen 1 manufactured from the INVAR tool.

The Creaform $3D$ HandySCAN was used to scan the specimens and tools (Fig. 3.25). The accuracy of this $3D$ scanner is 0.2 $mm$. As the scanning process is a contact-less measurement method it is better suited to measure parts of low stiffness like the specimens of the $BF_8$ laminate group. That is because the measurement error that the fixture of the CMM may induce to the measurement of these parts is avoided.

To measure the item of interest, a number of targets in the form of circular stickers were placed around the part to facilitate the measurement as shown in Fig. 3.25. After the scanning is completed the database of the cloud of points acquired needs to be cleaned by removing the points belonging to the background of the item and the points of the scanned targets. Afterwards, the same post-processing procedure as described above is used to calculate the angles of the specimens (Fig. 3.24).

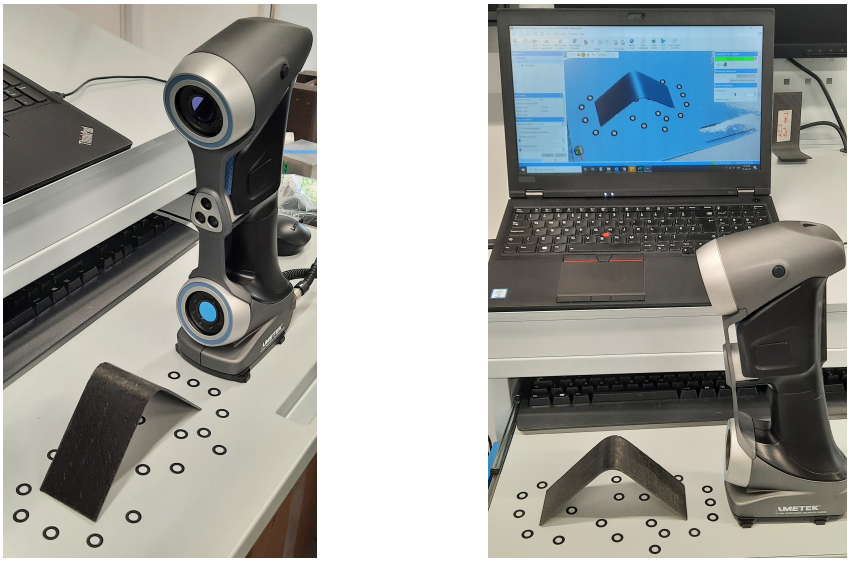

Figure 3.25: Measurement of PID of the $BS_8$ specimen 2 with the Creaform $3D$ HandySCAN.

The included angles of the tools manufactured, as measured with the CMM and $3D$ scanner are presented in Table 3.7. The standard deviation $\sigma$ and the maximum absolute deviation of the points from the plane are used as metrics to evaluate the quality of the plane fit. Lower values of $\sigma$ indicate that the points lie close to the resulting plane. As shown in Table 3.7 the $\sigma$ and the maximum absolute deviation ($\max|d_i|$) of the points from the fitting plane of the $3D$ scanner are usually greater than the corresponding values of the CMM measurement. This is believed to be due to the large number of point acquired from the $3D$ scanner and the accuracy of the measurement.

In an effort to assess the dimensional quality of the tools, each tool was split in half and planes were fitted at the resulting surfaces as shown in Fig. 3.26. Consequently,

Table 3.7: Tool enclosed angle.

| Tool material | | | INVAR | Steel | Aluminium |
|---|---|---|---|---|---|
| CMM | Angle(°) | | 90.24 | 89.68 | 89.37 |
| | Plane 1 | $\sigma$ (mm) | 0.065 | 0.062 | 0.093 |
| | | max $\lvert d_i \rvert$(mm) | 0.189 | 0.277 | 0.250 |
| | Plane 2 | $\sigma$ (mm) | 0.108 | 0.092 | 0.046 |
| | | max $\lvert d_i \rvert$(mm) | 0.291 | 0.360 | 0.140 |
| $3D$ scanner | Angle(°) | | 90.18 | 89.79 | 89.49 |
| | Plane 1 | $\sigma$ (mm) | 0.094 | 0.094 | 0.105 |
| | | max $\lvert d_i \rvert$(mm) | 0.373 | 0.444 | 0.438 |
| | Plane 2 | $\sigma$ (mm) | 0.074 | 0.087 | 0.046 |
| | | max $\lvert d_i \rvert$(mm) | 0.271 | 0.456 | 0.178 |

the tool is now described by two enclosed angles, a left and right one. This was done to spot any differences in the enclosed angles of the two sides. This difference is inherited by the specimens due to their positioning on the tool at the manufacturing of two specimens side by side under the same manufacturing conditions as shown in Figs. 3.7,3.13.

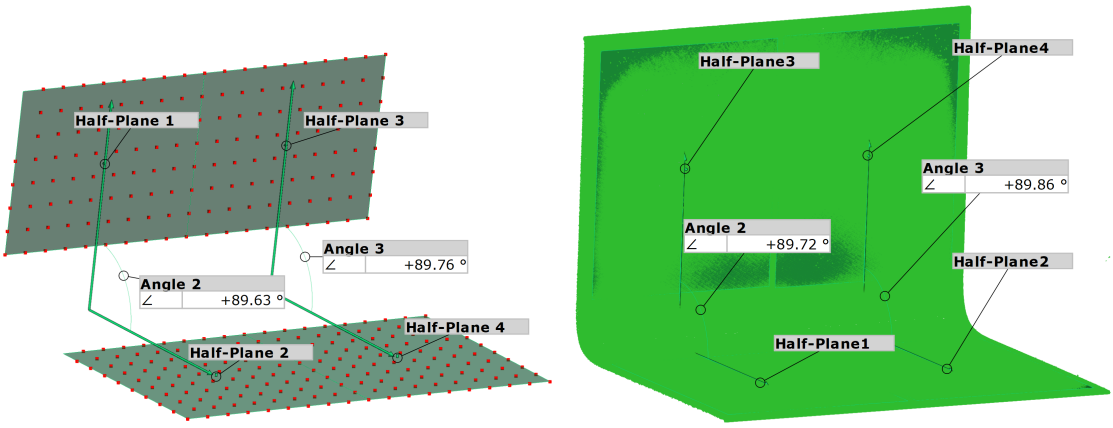


Figure 3.26: Splitting the steel tool surface in half to characterize it by two angles. Left: CMM, right: $3D$ scanner

Table 3.8: Difference between the enclosed angles of the tools when they are split in half and each half is measured independently.

| Tool material | | $\text{Half}_1$(°) | $\text{Half}_2$(°) | Difference(°) |
|---|---|---|---|---|
| CMM | INVAR | 90.24 | 90.23 | 0.01 |
| | Steel | 89.63 | 89.76 | 0.13 |
| | Aluminium | 89.30 | 89.44 | 0.14 |
| $3D$ scanner | INVAR | 90.23 | 90.16 | 0.07 |
| | Steel | 89.72 | 89.86 | 0.14 |
| | Aluminium | 89.40 | 89.50 | 0.10 |

It was found that the steel and aluminium tools did not have the same enclosed angle along their length. As shown in Table 3.8 a difference in the enclosed angles

of 0.13° and 0.14° in the case of the CMM measurement was found for the steel and aluminium tools respectively. In other words, if a part was manufactured on the right hand side of the aluminium tool would have a difference of 0.14° compared to the same part manufactured on the left side under the same conditions assuming linear tool compensation. The difference in the enclosed angles of the INVAR tool proved to be insignificant.

To measure the corner radius of the tools, three tangent circles were fitted in their corner as shown in Fig. 3.27. The cloud of points acquired by the $3D$ scanner was used for this purpose as the geometry of the corner was not measured by the CMM. Two circles were fitted near the edges of the tools and another one in the middle of the tool. The radii of the tools as measured at these three locations are presented in Table 3.9. As shown the INVAR and steel tool corner radius is close to the nominal value (15 mm). On the other hand, the radius of the aluminium tool was measured smaller compared to the nominal value.

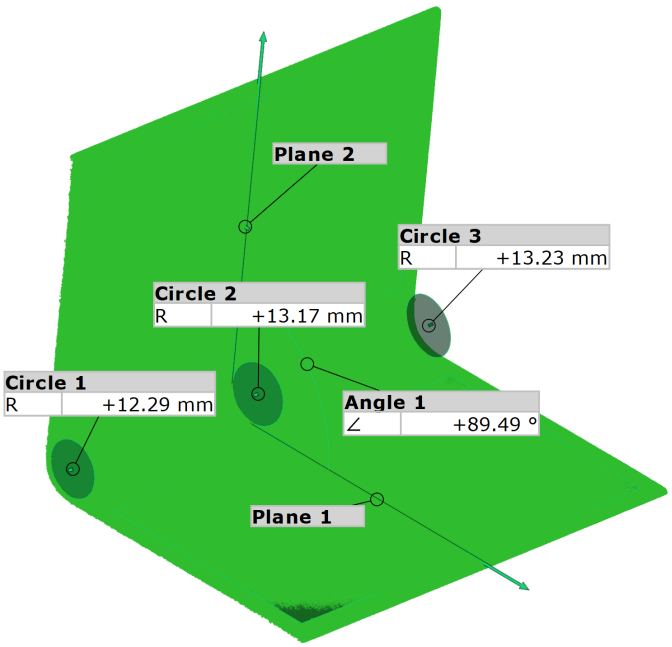


Figure 3.27: Corner radius of the aluminium tool measured near the edges and middle of the tool ($3D$ scanner point cloud).

Table 3.9: Corner radius near the edges and middle of the tools (Fig. 3.27).

| Tool material | $R_1$ (mm) | $R_2$ (mm) | $R_3$ (mm) |
|---|---|---|---|
| INVAR | 14.84 | 15.65 | 16.58 |
| Steel | 14.73 | 14.62 | 15.37 |
| Aluminium | 12.29 | 13.17 | 13.23 |

To derive the spring-in angle of the specimens according to each measurement method from the tool angle (Table 3.7) the calculated enclosed angle of the specimen

(Fig. 3.24) is subtracted. Tables 3.10-3.13 present the resulting spring-in angle of the specimens for each measuring method used, along with the average spring-in angle $\overline{\gamma}(^\circ)$, the standard deviation $s(^\circ)$ and the confidence interval $CI(^\circ)$ at 85% confidence level of each group.

Table 3.10: Measured spring-in angle (degrees) of the 8 plies specimens manufactured with the MRCC and "Fast" curing cycle. The parts were manufactured from the INVAR tool.

| Laminate | | $BS_8$ | | $BF_8$ | | $AS_8$ | |
|---|---|---|---|---|---|---|---|
| Curing cycle | | MRCC | "Fast" | MRCC | "Fast" | MRCC | "Fast" |
| CMM | Spec.1 | 1.64 | 1.36 | 0.37 | 0.72 | 1.21 | 1.41 |
| | Spec.2 | 1.61 | 1.23 | 1.64 | 0.95 | 1.73 | 0.13 |
| | Spec.3 | 1.49 | 1.33 | 1.08 | 1.01 | 1.64 | 0.45 |
| | $\overline{\gamma}(^\circ)$ | 1.58 | 1.31 | 1.03 | 0.89 | 1.53 | 0.66 |
| | $s(^\circ)$ | 0.08 | 0.07 | 0.64 | 0.15 | 0.28 | 0.67 |
| | $CI(^\circ)$ | 0.11 | 0.10 | 0.89 | 0.21 | 0.39 | 0.93 |
| $3D$ scanner | Spec.1 | 1.59 | 1.24 | 0.34 | 0.48 | 0.58 | 0.62 |
| | Spec.2 | 1.22 | 1.28 | 1.00 | 0.62 | 0.27 | 0.60 |
| | Spec.3 | 1.24 | 1.28 | 0.55 | 0.81 | 0.51 | 0.39 |
| | $\overline{\gamma}(^\circ)$ | 1.35 | 1.27 | 0.63 | 0.64 | 0.45 | 0.54 |
| | $s(^\circ)$ | 0.21 | 0.02 | 0.34 | 0.17 | 0.16 | 0.13 |
| | $CI(^\circ)$ | 0.29 | 0.03 | 0.47 | 0.24 | 0.22 | 0.18 |

Table 3.11: Measured spring-in angle (degrees) of the 16 ply specimens manufactured with the MRCC and INVAR tool.

| Laminate | | $BS_{16}$ | $BF_{16}$ | $SK_{16}$ | $FR_{16}$ | $ST_{16}$ | $SP_{16}$ | $AS_{16}$ | $UB_{16}$ |
|---|---|---|---|---|---|---|---|---|---|
| CMM | Spec.1 | 1.17 | 1.05 | 1.45 | 1.41 | 1.30 | 0.92 | 1.39 | 1.19 |
| | Spec.2 | 1.05 | 1.19 | 1.25 | 1.30 | 1.26 | 1.18 | 1.25 | 1.19 |
| | Spec.3 | 0.98 | 1.23 | 1.17 | 1.26 | 1.40 | 0.92 | 1.14 | 0.91 |
| | $\overline{\gamma}(^\circ)$ | 1.07 | 1.16 | 1.29 | 1.32 | 1.32 | 1.01 | 1.26 | 1.10 |
| | $s(^\circ)$ | 0.10 | 0.09 | 0.14 | 0.08 | 0.07 | 0.15 | 0.13 | 0.16 |
| | $CI(^\circ)$ | 0.14 | 0.12 | 0.19 | 0.11 | 0.10 | 0.21 | 0.18 | 0.22 |
| $3D$ scanner | Spec.1 | 0.90 | 0.63 | 1.01 | 1.15 | 0.95 | 0.77 | 1.25 | 1.09 |
| | Spec.2 | 0.91 | 0.79 | 0.91 | 1.23 | 0.96 | 0.71 | 1.29 | 1.07 |
| | Spec.3 | 0.88 | 0.92 | 0.97 | 0.97 | 1.16 | 0.80 | 1.05 | 0.79 |
| | $\overline{\gamma}(^\circ)$ | 0.90 | 0.78 | 0.96 | 1.12 | 1.02 | 0.76 | 1.20 | 0.98 |
| | $s(^\circ)$ | 0.02 | 0.15 | 0.05 | 0.13 | 0.12 | 0.05 | 0.13 | 0.17 |
| | $CI(^\circ)$ | 0.03 | 0.21 | 0.07 | 0.18 | 0.17 | 0.07 | 0.18 | 0.24 |

Table 3.12: Measured spring-in angle (degrees) of the specimens manufactured also with the steel and aluminium tools. The parts were manufactured with the MRCC.

| Laminate | | $BS_{16}$ | | $ST_{16}$ | | $SP_{16}$ | | $AS_8$ | |
|---|---|---|---|---|---|---|---|---|---|
| Tool | | Steel | Alum. | Steel | Alum. | Steel | Alum. | Steel | Alum. |
| CMM | Spec.1 | 1.56 | 1.52 | 1.52 | 1.47 | 1.05 | 1.37 | 0.34 | 1.01 |
| | Spec.2 | 1.46 | 1.64 | 1.70 | 1.67 | 1.25 | 1.16 | 0.98 | 1.22 |
| | Spec.3 | 1.50 | 1.62 | 1.58 | 1.94 | 1.36 | 1.27 | 1.17 | 0.22 |
| | $\overline{\gamma}(^\circ)$ | 1.51 | 1.59 | 1.60 | 1.69 | 1.22 | 1.27 | 0.83 | 0.82 |
| | $s(^\circ)$ | 0.05 | 0.06 | 0.09 | 0.24 | 0.16 | 0.11 | 0.43 | 0.53 |
| | $CI(^\circ)$ | 0.07 | 0.08 | 0.12 | 0.33 | 0.22 | 0.15 | 0.60 | 0.74 |
| $3D$ scanner | Spec.1 | 1.61 | 1.66 | 1.45 | 1.60 | 1.10 | 1.34 | 0.70 | 1.76 |
| | Spec.2 | 1.60 | 1.68 | 1.62 | 1.82 | 1.23 | 1.12 | 0.75 | 1.43 |
| | Spec.3 | 1.52 | 1.77 | 1.49 | 2.03 | 1.31 | 1.33 | 1.08 | 1.07 |
| | $\overline{\gamma}(^\circ)$ | 1.58 | 1.70 | 1.52 | 1.82 | 1.21 | 1.26 | 0.84 | 1.42 |
| | $s(^\circ)$ | 0.05 | 0.06 | 0.09 | 0.22 | 0.11 | 0.12 | 0.21 | 0.35 |
| | $CI(^\circ)$ | 0.07 | 0.08 | 0.12 | 0.31 | 0.15 | 0.17 | 0.29 | 0.49 |

Table 3.13: Measured spring-in angle (degrees) of the 24 plies specimens manufactured with the MRCC and INVAR tool.

| Laminate | | $BS_{24}$ | $BF_{24}$ |
|---|---|---|---|
| CMM | Spec.1 | 0.92 | 0.87 |
| | Spec.2 | 1.00 | 0.96 |
| | Spec.3 | 1.01 | 1.05 |
| | $\overline{\gamma}(^\circ)$ | 0.98 | 0.96 |
| | $s(^\circ)$ | 0.05 | 0.09 |
| | $CI(^\circ)$ | 0.07 | 0.12 |
| $3D$ scanner | Spec.1 | 0.75 | 0.76 |
| | Spec.2 | 0.88 | 0.82 |
| | Spec.3 | 0.93 | 0.88 |
| | $\overline{\gamma}(^\circ)$ | 0.85 | 0.82 |
| | $s(^\circ)$ | 0.09 | 0.06 |
| | $CI(^\circ)$ | 0.12 | 0.08 |

### 3.3.1 Comparison of measurements

Fig. 3.28-3.31 present a comparison between the average spring-in angles measured with the CMM and the $3D$ scanner for each case investigated. The error bars of the figures represent the confidence intervals at 85% confidence level. To assess whether the CMM and the $3D$ scanner measurements agree, a Student's t-test was conducted for each case investigated [126]. The null hypothesis ($H_\circ$) is that the two measurement methods produce the same result, in terms of average spring-in angle, whereas the alternative hypothesis ($H_1$) is that they don't. Therefore, to accept the null hypothesis the significance level ($\alpha_s$) is 5%. In case $H_\circ$ cannot be accepted a second t-test was conducted with the significance level ($\alpha_s$) equal to 1% to reject $H_\circ$.

For the test the standard deviation ($\sigma$) of the two populations are assumed to be unequal and unknown. Thus, the $t_s$ variable to test whether the population means are different is calculated using Eq.(3.1).

$$t_s = \frac{\overline{\gamma_1} - \overline{\gamma_2}}{\sqrt{\frac{s_1^2}{n_1} + \frac{s_2^2}{n_2}}} \tag{3.1}$$

The numbers of degrees of freedom $\nu_s$ of the test is calculated using Eq.(3.2).

$$\nu_s = \frac{\left(\frac{s_1^2}{n_1} + \frac{s_2^2}{n_2}\right)^2}{\frac{\left(\frac{s_1^2}{n_1}\right)^2}{n_1 - 1} + \frac{\left(\frac{s_2^2}{n_2}\right)^2}{n_2 - 1}} \tag{3.2}$$

where:

- $\overline{\gamma}$ : Average spring-in angle of the sample
- $s$ : Standard deviation of the sample
- $n$ : Sample size $n = 3$

Table 3.14 contains the results of the Student's t-test for each case investigated. For the majority of the cases the null hypothesis ($H_\circ$) is accepted meaning that the CMM and $3D$ scanner measurements agree. However, in four cases $H_\circ$ can neither be accepted nor be rejected, meaning that the result of the test is within the statistical uncertainty area.

In Table 3.15 a segmentation of the investigated cases according to the standard deviation of the spring-in angles for each measurement method is presented. The

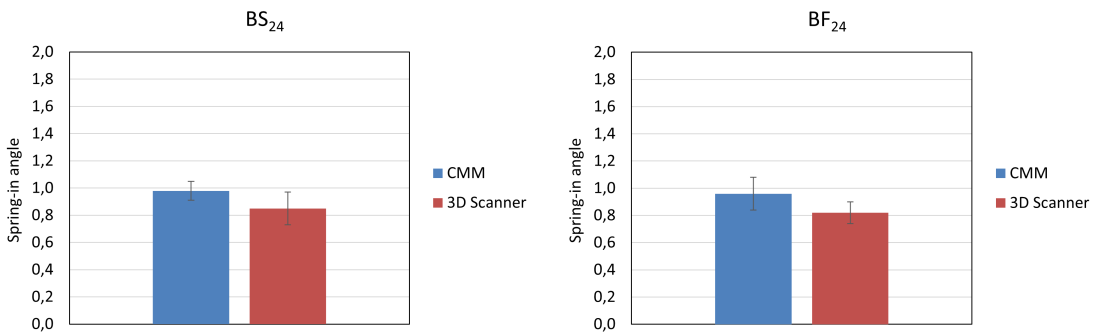


Figure 3.28: Comparison of the average spring-in angles measured (3$D$ scanner vs. CMM) for the 24 plies specimens manufactured with the MRCC and the INVAR tool.

Table 3.14: Result of the Student's t-test for each case investigated.

| Curing Cycle | Laminate | Tool | $\nu_s$ | $t_s$ | $H_\circ$ |
|---|---|---|---|---|---|
| MRCC | $BS_8$ | INVAR | 2.57 | 1.77 | Accepted |
| | $BF_8$ | INVAR | 3.05 | 0.96 | Accepted |
| | $AS_8$ | INVAR | 2.02 | 6.16 | Cannot be rejected |
| | | Steel | 2.59 | 1.46 | Accepted |
| | | Alum. | 2.81 | 0.52 | Accepted |
| | $BS_{16}$ | INVAR | 2.16 | 2.89 | Accepted |
| | | Steel | 4.00 | 1.71 | Accepted |
| | | Alum. | 4.00 | 2.25 | Accepted |
| | $BF_{16}$ | INVAR | 3.27 | 3.76 | Cannot be rejected |
| | $SK_{16}$ | INVAR | 2.50 | 3.84 | Cannot be rejected |
| | $FR_{16}$ | INVAR | 3.32 | 2.27 | Accepted |
| | $ST_{16}$ | INVAR | 3.22 | 3.74 | Cannot be rejected |
| | | Steel | 4.00 | 1.09 | Accepted |
| | | Alum. | 3.97 | 0.69 | Accepted |
| | $SP_{16}$ | INVAR | 2.44 | 2.74 | Accepted |
| | | Steel | 3.55 | 0.09 | Accepted |
| | | Alum. | 3.97 | 0.11 | Accepted |
| | $AS_{16}$ | INVAR | 4.00 | 0.57 | Accepted |
| | $UB_{16}$ | INVAR | 3.99 | 0.89 | Accepted |
| | $BS_{24}$ | INVAR | 3.13 | 2.19 | Accepted |
| | $BF_{24}$ | INVAR | 3.48 | 2.24 | Accepted |
| Fast | $BS_8$ | INVAR | 2.32 | 0.95 | Accepted |
| | $BF_8$ | INVAR | 3.94 | 1.91 | Accepted |
| | $AS_8$ | INVAR | 2.15 | 0.30 | Accepted |

standard deviation of the spring-in angle for the majority of the groups investigated is less than 0.2° for both measurement methods.

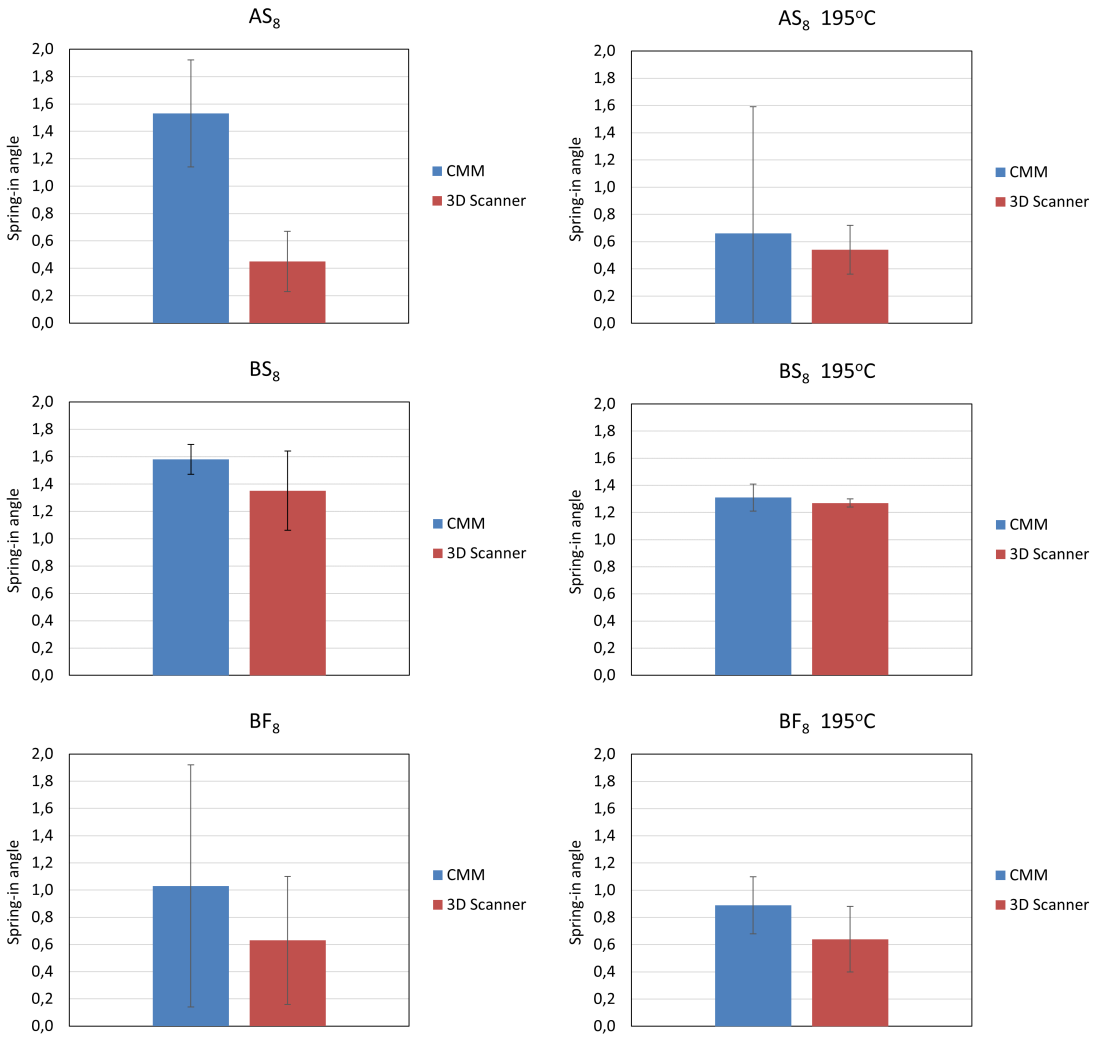


Figure 3.29: Comparison of the average spring-in angles measured ($3D$ scanner vs. CMM) for the 8 plies specimens manufactured with the MRCC and "Fast" curing cycle. The parts were manufactured from the INVAR tool.

Table 3.15: Segmentation of the investigated cases according to their standard deviation for each measurement method.

| Standard deviation | CMM | $3D$ scanner |
|---|---|---|
| $s > 0.3°$ | 4 | 2 |
| $0.2° < s \leq 0.3°$ | 2 | 3 |
| $0.1° < s \leq 0.2°$ | 8 | 10 |
| $s \leq 0.1°$ | 10 | 9 |

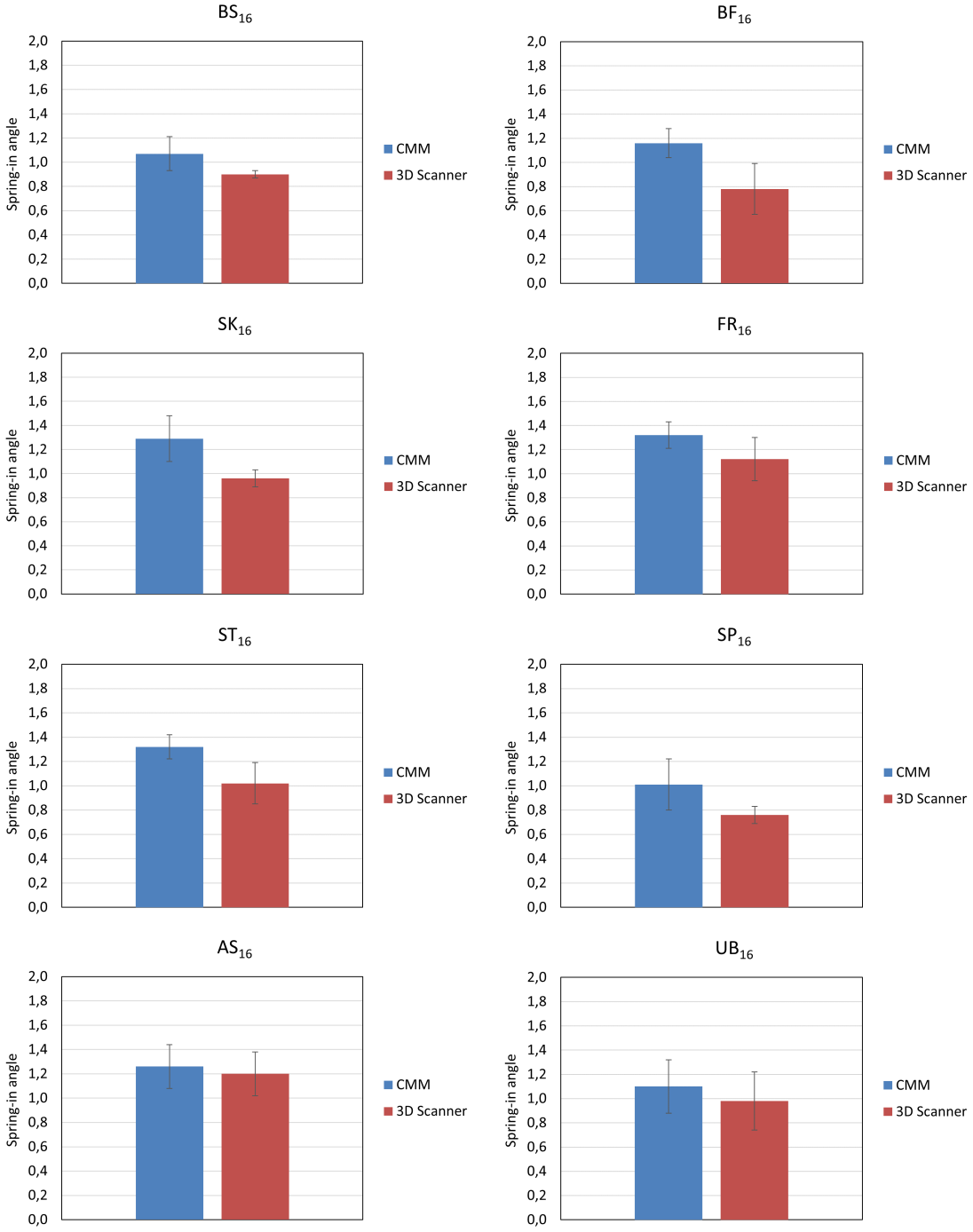


Figure 3.30: Comparison of the average spring-in angles measured ($3D$ scanner vs. CMM) for the 16 plies specimens manufactured with the MRCC and the INVAR tool.

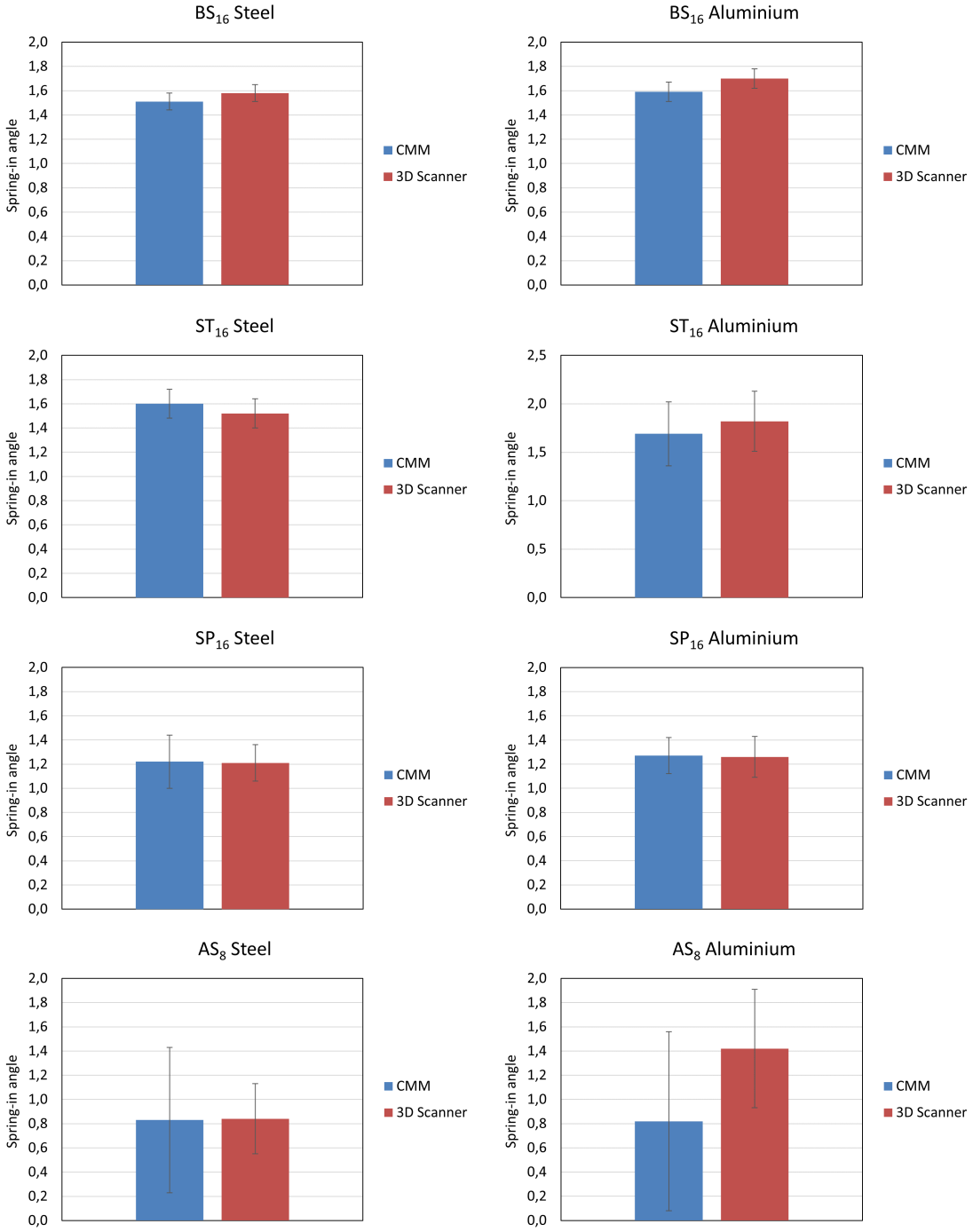


Figure 3.31: Comparison of the average spring-in angles measured ($3D$ scanner vs. CMM) for the specimens manufactured also with the steel and aluminium tools.

## 3.4 Experimental findings

### 3.4.1 Effect of the tool material

From the experiments, it was found that the material of the tool has a significant effect on the spring-in angle of the parts. The parts manufactured from the INVAR tool experience on average less deformation compared to the parts manufactured from the steel or aluminium tools. This phenomenon was also observed by [56]. The specimens manufactured from the aluminium tool have a higher average spring-in angle compared to the parts manufactured from the steel tool, both for the $3D$ scanner and CMM results (Table 3.12). However, the confidence intervals (at confidence level 85%) of the spring-in angle of the parts made from the steel and aluminium tool overlap. Consequently, a solid conclusion about which tool produces less distortion cannot be made with experiments alone, even though the CTE of the aluminium tool is significantly higher that the CTE of the steel tool (Table 3.2). It is postulated that the steel and aluminium tools produce similar spring-in angles for the $AS_8$, $BS_{16}$, $ST_{16}$ and the $SP_{16}$ laminate designs due the inhomogeneous deformation behaviour induced to the tools from the welding of the supporting substructure with the bent plate during the curing cycle. The material of the welding was not exactly the same as the alloy of the tools and the position of the weldings might induce some bending and twisting forces to the plate during the curing cycle. This effect also exist in the INVAR tool, however, it does not significantly affect the spring-in angle of the part due to the very low CTE of the INVAR tool (Table 3.2). This might be another reason why the INVAR alloy is the preferred choice by the industry to manufacture tools that produce parts of high dimensional accuracy.

### 3.4.2 Effect of the laminate design

The effect of the laminate design and thickness on the spring-in angle of the parts is investigated in relation to their bending stiffness $D_{11}$ as these factors are coupled. Direction 1 of the laminate corresponds to the longitudinal direction of the plies (Fig. 5.13). Fig. 3.32 depicts the spring-in angle of the laminates, measured with the CMM and manufactured with the INVAR tool and the MRCC, in relation to the bending stiffness $D_{11}$ derived from CLT [127]. As depicted in Fig. 3.32, the 24 plies laminates which have the highest $D_{11}$ value experience the least average spring-in (below 1°) compared to the 8 and 16 plies laminates. The average spring-in of the 16 plies laminates (the group of laminates depicted in the middle of Fig. 3.32) is in the range of 1° to 1.3° which is below the 8 plies group. As shown, at the $BF_8$ group there is a large scatter of measurement data possibly due to the error induced

in the measurement from the fixture of the parts to the CMM due to their very low bending stiffness. Because the confidence intervals (at confidence level 85%) of the laminates overlap in many cases (Tables 3.10,3.11,3.13) only the qualitative conclusion can be made that the spring-in angle on the parts reduces as the bending stiffness $D_{11}$ of the laminate increases, which is also observed by other researchers [49, 109]. Moreover, it is observed that as the bending stiffness $D_{11}$ increases, the standard deviation of the measured spring-in angles reduces, indicating that the laminate is less sensitive to manufacturing process or material variabilities.

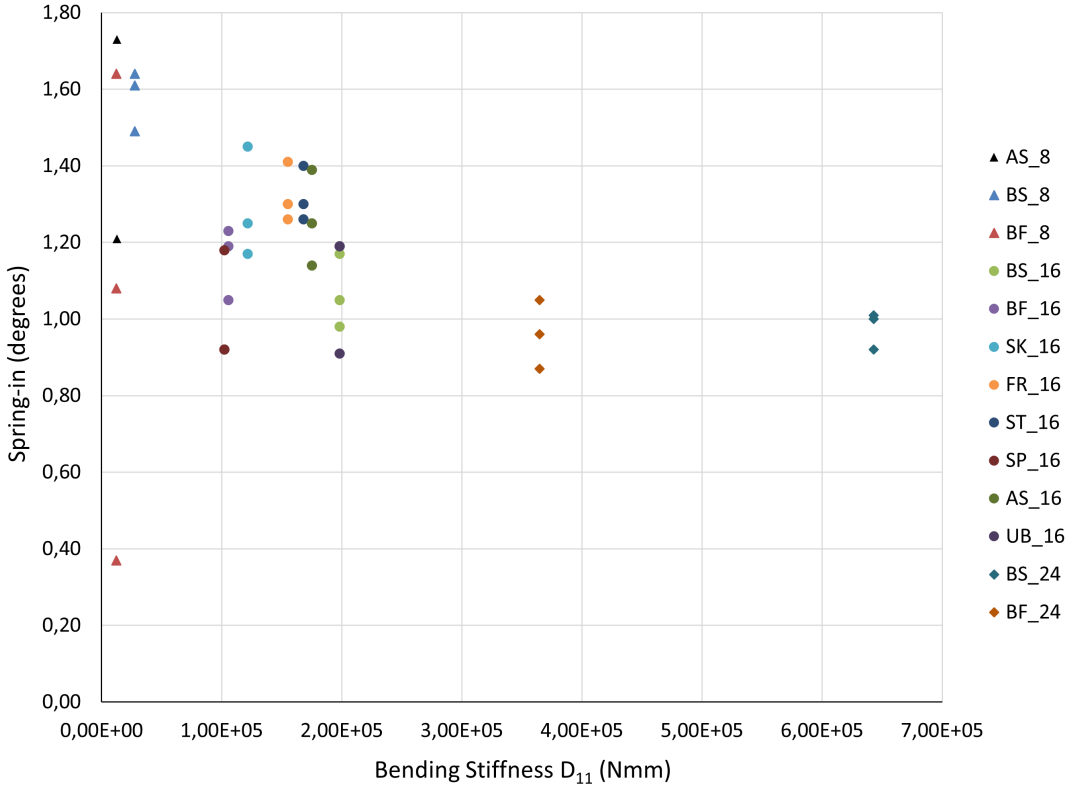


Figure 3.32: Spring-in angle of the parts (CMM data), manufactured with the INVAR tool and MRCC, in relation to their bending stiffness $D_{11}$.

Furthermore, as expected the AS and heavily UB laminates experience in addition to spring-in significant warpage or twist. Therefore, it is recommended to design symmetric and balanced laminates to avoid the coupling of the bending and twisting distortions of the laminate, unless this is required by the design of the part.

### 3.4.3 Effect of the curing cycle

The curing cycle proved to have a small effect on the spring-in angle of the parts for the laminate designs ($BS_8$,$BF_8$,$AS_8$) also manufactured with the "Fast" curing cycle. Due to the low bending stiffness of the specimens in this case (Fig. 3.32) the $3D$ scanner data was used to draw conclusions.

It was found that the $BS_8$ laminate design manufactured with the "Fast" curing cycle has a lower average spring-in value compared to the group manufactured with the MRCC (Table 3.10). However, when excluding specimen 1 of the $BS_8$ group manufactured with the MRCC, which has significantly higher spring-in value compared to specimen 2 and 3, as shown in Table 3.10 (the pull-out of some 0° fibers from the specimen surface might contribute to this as shown Table 3.3), the average spring-in value of the MRCC group is lower compared to the "Fast" curing cycle (1.23° vs. 1.27°) and the standard deviations ($s$) of the two groups do not overlap.

The average spring-in angle of the $BF_8$ and $AS_8$ laminate designs manufactured with the "Fast" curing cycle is higher compared to the respective spring-in angle of the specimens manufactured by the MRCC. However, the $BF_8$ group suffers from a large scatter of the measurement data, which is believed to be due to its low bending stiffness that makes it prone to the bending and shear forces of the machining operations. Therefore, a solid conclusion from the experimental data cannot be made about the influence of the curing cycle on the PID of the parts.

## 3.5 Experimental uncertainties

Regarding the experimental factors or uncertainties that affect the parts produced, the change of the tools enclosed angle along their length as described in Section 3.3 was investigated after manufacturing the specimens. Consequently, it is not possible to trace back the error induced to the specimens due to their positioning on the tool.

Moreover, even though the plies were cut in the press from the carbon fabric roll with the use of a custom made die, which ensured the accurate dimensions of the patches, the stacking sequence of the parts was manufactured manually on the tools without any laser projection method. This may lead to fibre reorientation during the handling and bagging operations which affect PID.

Also, the temperature profile depicted in Fig. 3.12 could not be replicated in every manufacturing run. The infusion and dwell times as well as heating and cool down rates differ at each case, depending on the position of the tool in the oven, the number of the tools in the oven and setting of the oven (speed of ventilation fan etc.). Nevertheless, it was attempted to keep heating and cool down rates below $2.5^oC/min$ and let the parts cure for a least 2 hours at MRCC. The difference between the temperature profiles that the tools experience under the same curing cycle is more evident when the aluminium tool is placed in the oven along with

the steel or INVAR tool as shown in Fig. 3.33. Due to its reduced thermal mass compared to the other tools, the parts from the aluminium tool reach the curing temperature sooner and are thus kept at the curing temperature longer until the two hour cycle is completed for the other slowest parts in the oven. This may lead to a higher final degree of cure at the end of the cycle compared to the parts made from steel or INVAR tools.

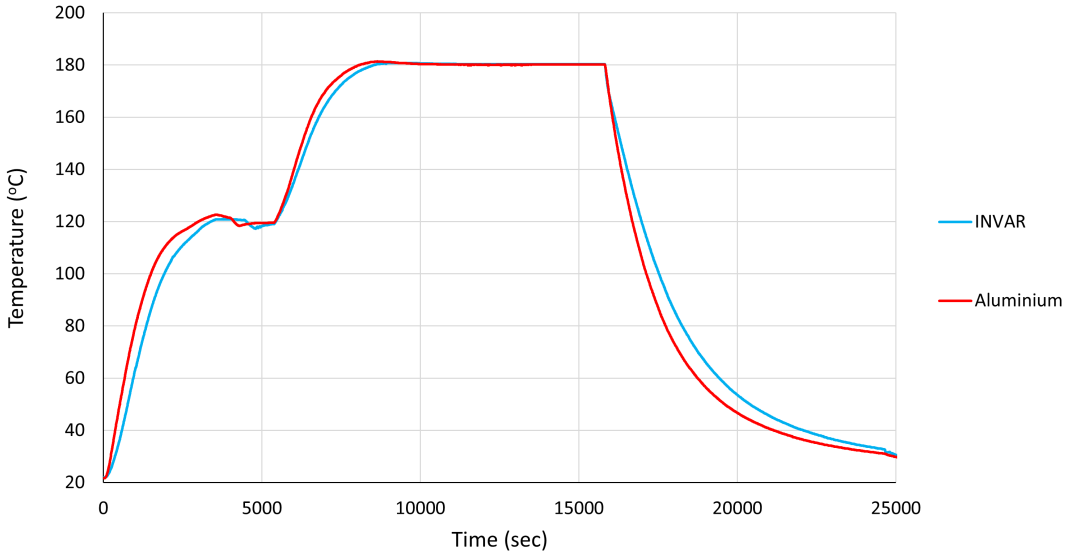


(a) Both tools were placed on the middle rack of the oven. The INVAR tool was placed closer to the oven door and the aluminium tool behind the INVAR tool at the center of the oven.

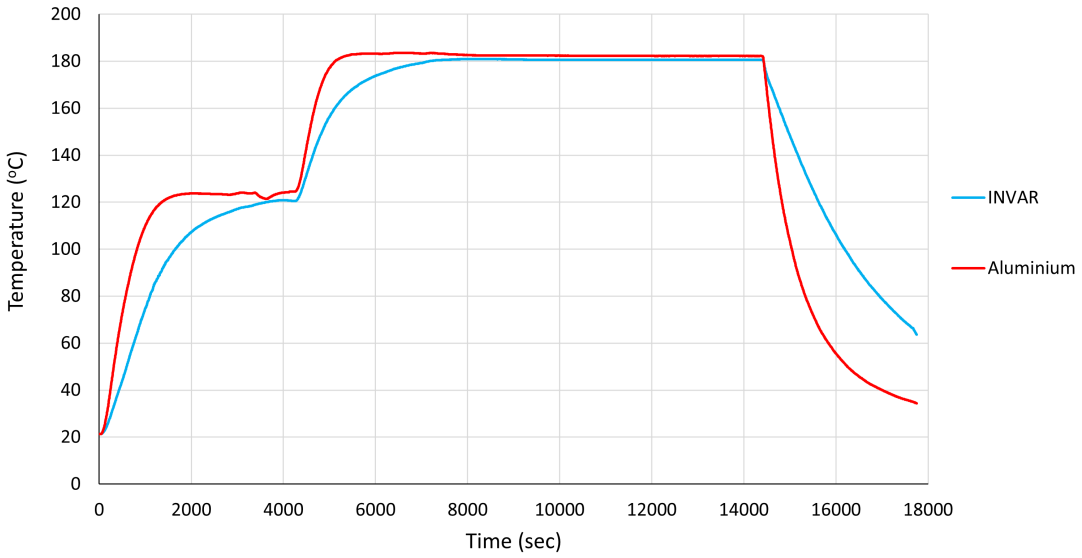


(b) The INVAR tool was placed on the middle rack and the aluminium tool on the lower rack in the middle of the oven.

Figure 3.33: Temperature lag of the INVAR compared to the aluminium tool subjected to the same curing cycle. In both cases the aluminium tool reaches the dwell temperature earlier.

Moreover, the trimming of the parts to their final dimensions contribute to the variability of the measured spring-in angles. Furthermore, the fixture of the parts to the CMM (Fig. 3.23) could potentially induce error to the measurement of their spring-in angle. These effects are more evident to the parts having low bending stiffness and contribute to the large confidence intervals presented in Figs. 3.29,3.31 for the 8 ply specimens. With the use of the $3D$ scanner the error induced to the measurement from the fixture of the part can be avoided, as it is a contact-less measurement method, where no fixture of the part is needed. Therefore, the $3D$ scanner is considered the most appropriate method to measure the geometry of specimens having low bending stiffness such as those of the $BF_8$ or $AS_8$ groups.

In addition to the above presented factors, the data reduction method used to calculate the spring-in angle of the parts (Gaussian best fit of planes to the CMM or $3D$ scanner data) is a potential source of error. This method is less efficient as the twist or warpage of the part increases as in the case of the $AS_8$ & $AS_{16}$ laminate because the standard deviation ($\sigma$) of the data to the plane increases as shown in Table A.1. In those cases it is recommended that more than one plane should be fitted to the surface to reduce the deviation. Consequently, those parts should be described by more than one spring-in angle along their length or an alternative contour plot of the point cloud deviation from CAD. Furthermore, as said before it was found that the standard deviation ($\sigma$) of the points from the fitting planes of the $3D$ scanner was usually greater compared to the CMM measurement (Table A.1).

Chapter

# 4

# Simulation Framework

## 4.1 Overview of material modelling

The material modelling effort focuses mainly on the evolution of the EPS600 matrix properties during cure, since fibre properties change insignificantly during the manufacturing process.

The properties of the IMS65 fibre were found in literature [128] or, where not explicitly defined by the supplier, were assumed to be equal to the properties of HEXCEL AS4, a common standard modulus fibre [99]. The fibre properties used in this research are presented in Table 4.1.

Table 4.1: Material properties of the IMS65 carbon fibre.

| Physical Property | Symbol | Value | Units | Source |
|---|---|---|---|---|
| CTE | $CTE_{11}$ | -1.00 E-07 | $[1/°C]$ | Composite Oracle [129] |
| | $CTE_{22}$ | 4.83 E-06 | $[1/°C]$ | AS4 fibre [99] |
| Modulus | $E_{11}$ | 290 | [GPa] | Toho Tenax [128] |
| | $E_{22}$ | 17.24 | [GPa] | AS4 fibre [99] |
| | $G_{12}$ | 27.60 | [GPa] | AS4 fibre [99] |
| | $G_{23}$ | 6.89 | [GPa] | AS4 fibre [99] |
| Poisson coef. | $\nu_{12}$ | 0.20 | - | AS4 fibre [99] |
| | $\nu_{23}$ | 0.25 | - | AS4 fibre [99] |
| Density | $\rho_f$ | 1780 | $[kg/m^3]$ | Toho Tenax [128] |

The chemo-mechanical and thermo-chemical modules presented hereafter can be used independently or can be coupled. Where a sequentially coupled thermo-chemo-mechanical analysis is needed, the thermal analysis runs first and the temperature field at every time step is mapped to the spring-in analysis as depicted in Fig. 4.1. This would be typically needed to calculate PID of thick parts where temperature gradients in the part are expected to cause significant property gradients affecting its distortion.

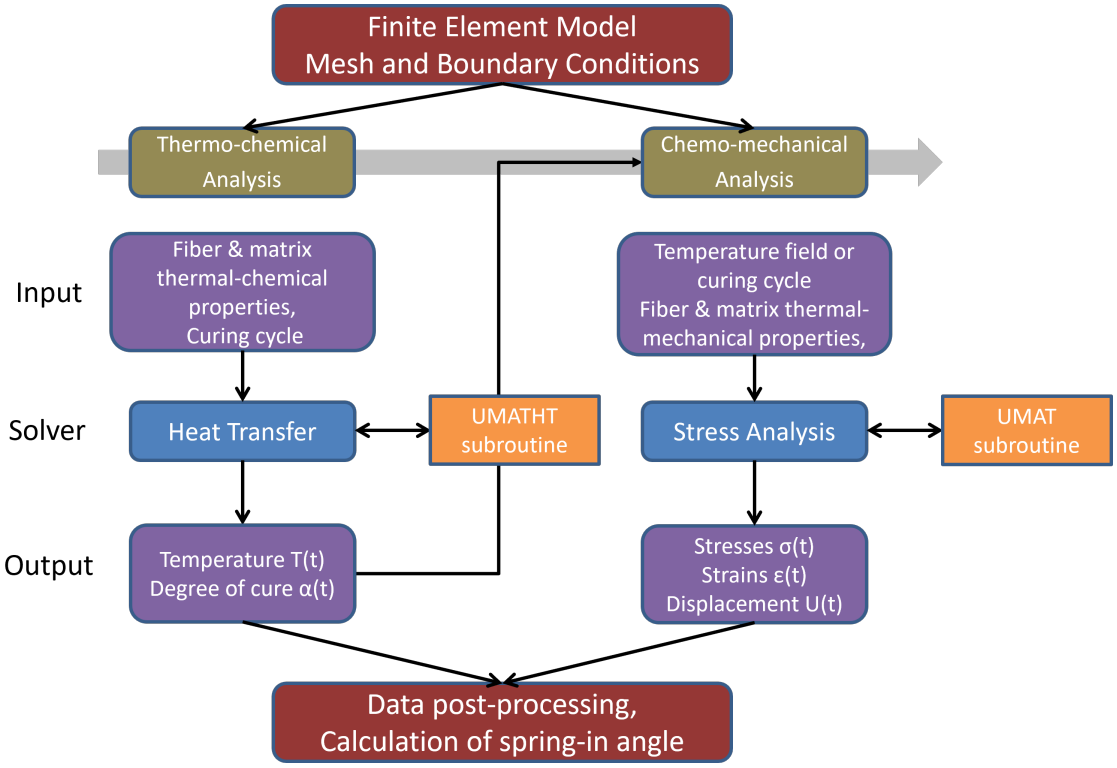


Figure 4.1: Interaction between the thermo-chemical and chemo-mechanical modules. Blue colour indicates variable calculation, purple access of memory, orange call of the subroutines developed and red use of pre and post processing software.

### 4.1.1 Thermo-chemical module

The scope of the thermo-chemical module developed is to calculate the temperature field in the part at every time step. First, the matrix conductivity ($k_m$) and specific heat capacity ($c_{p_m}$) are calculated as a function of temperature ($T$) and degree of cure ($\alpha$). The thermal properties of the fibre are calculated as a function of temperature only. The fibre volume fraction ($V_f$) is also calculated based on the matrix chemical contraction and thermal expansion as depicted in Fig. 4.2.

Then, the effective thermal properties of the lamina can be calculated with the use of the instantaneous thermal properties of the matrix and fibers, along with the

matrix exothermic heat reaction. Finally, this information is given as input to the thermal constitutive equation to calculate the temperature distribution of the time increment in the part as shown in Fig. 4.2.

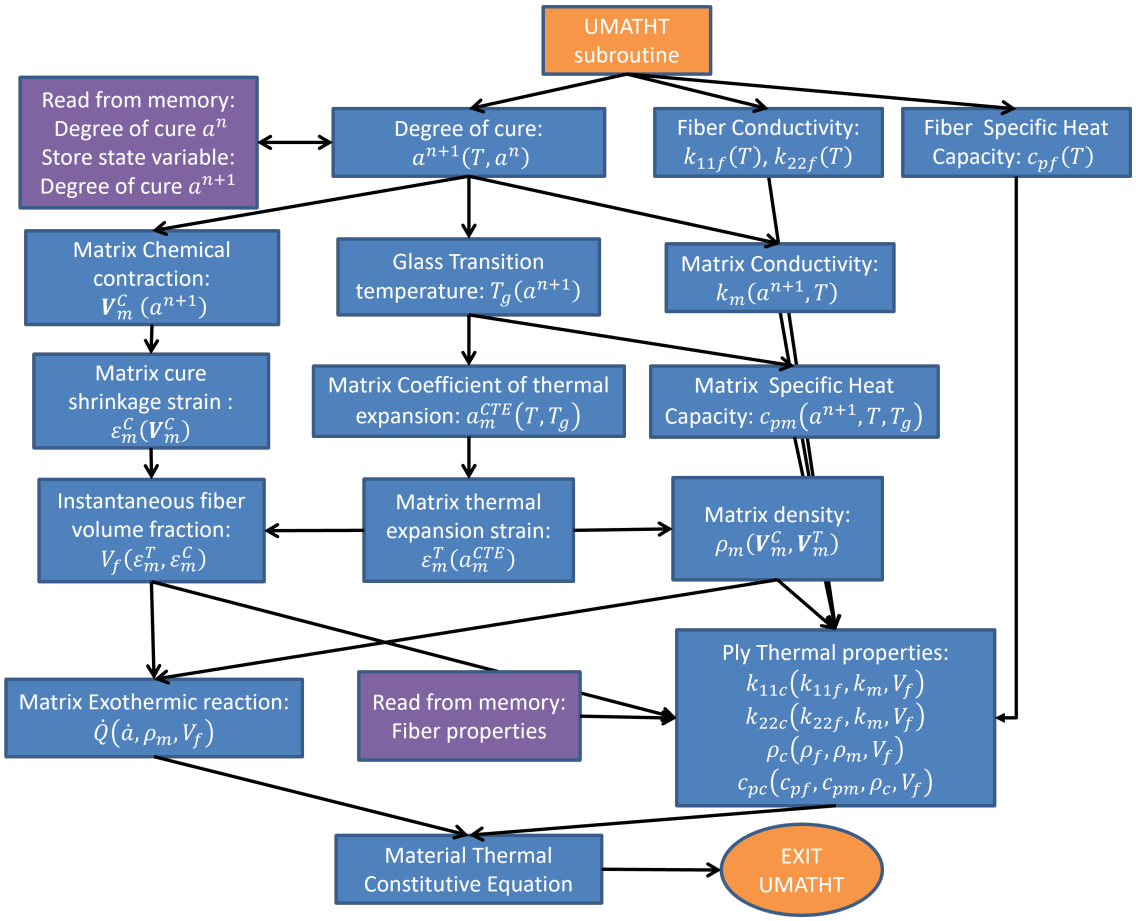


Figure 4.2: Thermo-chemical module.

### 4.1.2 Chemo-mechanical module

The chemo-mechanical module updates the stress tensor and CTO at the material integration points at every time increment of the curing history. As shown in Fig. 4.3, the matrix properties depend on the degree of cure and temperature of the time increment. The colour code adopted here is the same as previously. Blue colour indicates variable calculation, purple access of memory, orange start/finish of the calculation process. The calculation of the combined shift factor $a_{Tx}$ (green box) is employed only by the viscoelastic material model.

The first step in the calculation process is to calculate the degree of cure at the current time increment. Then, the matrix material properties such as the instantaneous glass transition temperature $T_g$, $E$ and $G$ moduli and Poisson coefficient $\nu_m$ can be calculated. The instantaneous thermal and chemical strains and fibre volume fraction

coefficient are calculated prior to the calculation of the effective material point's properties (homogenisation step). The homogenisation step refers to the use of a micromechanics model to calculate the effective modulus and expansion coefficients of the material point by assuming transversely isotropic material behaviour.

Following the homogenisation step, the stiffness matrices can be assembled along with the calculation of the strains at the material points. Finally, this information is supplied as input to the constitutive equation of the material model employed, in order to update the stress tensor and CTO of the time increment for the next iteration to proceed.

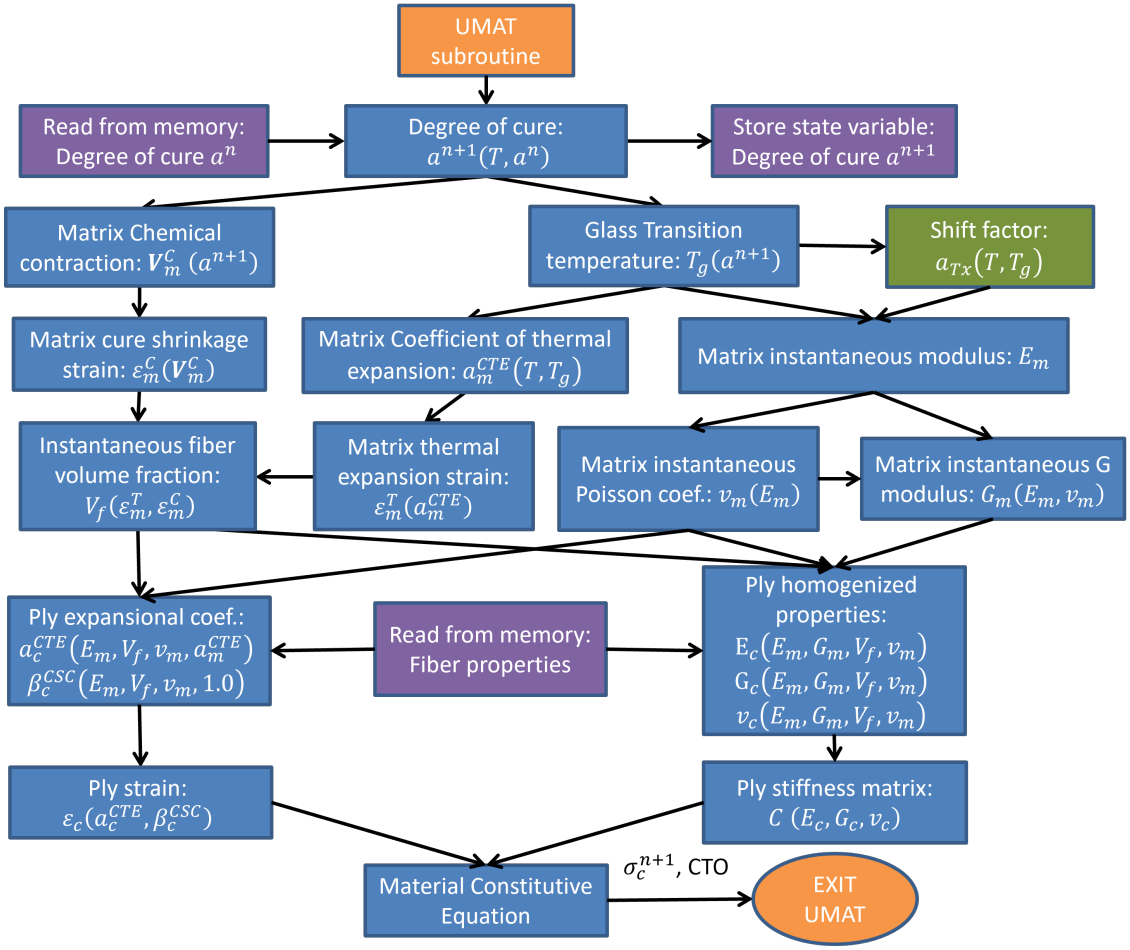


Figure 4.3: Chemo-mechanical module.

## 4.2 Instantaneous material properties

All material models, micromechanics and constitutive equations used by the thermo-chemical and chemo-mechanical module are presented thereafter.

### 4.2.1 Cure kinetic model

The cure kinetic model used to describe the evolution of the degree of cure rate ($\dot{\alpha}$) at each time step is presented in Eq.(4.1). This model is the result of the linear combination of two autocatalitic models as presented by Lee *et al.* [130] with one of them combined with a diffusion factor function as proposed by Cole *et al.* [131]. To calculate the degree of cure $\alpha$ from the curing rate $\dot{\alpha}$, Simpson's integration is used.

$$\dot{\alpha} = \frac{A_1 e^{\frac{-E_{1_a}}{RT}} \alpha^{m_1} (1-\alpha)^{n_1}}{1 + e^{D(\alpha - (\alpha_{c0} + \alpha_{cT} T))}} + A_2 e^{\frac{-E_{2_a}}{RT}} \alpha^{m_2} (1-\alpha)^{n_2} \tag{4.1}$$

where :

- $\dot{\alpha}$ : Degree of cure rate
- $T$ : Temperature $(K)$
- $R$ : Universal gas constant $R = 8.314 J\, K^{-1}\, mol^{-1}$
- $A_1, A_2$: Arrhenius constants
- $E_{1_a}, E_{2_a}$: Activation energies of the autocatalitic models
- $m_1, n_1, D, \alpha_{c0}, \alpha_{cT}, m_2, n_2$ : Material constants (Table 4.2)

The material characterization of the degree of cure was performed by Weiland on behalf of Premium AEROTEC GmbH [132]. Differential Scanning Calorimetry (DSC) was used to characterize the cure kinetics of the EPS600 resin system. The experimental investigations were carried out according to the ISO 11357 standard. Then, Eq.(4.1) was fitted to the experimental data with the use of least-square fit and the material constants of the equation were determined. The maximum deviation of Eq.(4.1) from the experimental data is 2%. Table 4.2 contains values of the material constants used in Eq.(4.1). Due to confidentially the exact values could not be presented but are within 20% range of the values presented.

Table 4.2: Material constants used in Eq.(4.1)

| $A_1$ | $E_{1_a}$ | $m_1$ | $n_1$ | $D$ | $\alpha_{c0}$ | $\alpha_{cT}$ | $A_2$ | $E_{2_a}$ | $m_2$ | $n_2$ |
|---|---|---|---|---|---|---|---|---|---|---|
| $s^{-1}$ | $J\, mol^{-1}$ | - | - | - | - | $^{\circ}C^{-1}$ | $s^{-1}$ | $J\, mol^{-1}$ | - | - |
| 21687 | 63984 | 2.365 | 1.902 | 52.69 | 0.15 | 0.00167 | 12122 | 54849 | 0.291 | 4.167 |

Fig. 4.4 shows the contribution of each term of Eq.(4.1) in the evolution of degree of cure. The second term of Eq.(4.1) ($A_2 e^{\frac{-E_{2_a}}{RT}} \alpha^{m_2} (1-\alpha)^{n_2}$) is responsible for the low values of degree of cure, approximately to $a = 0.10$, where the matrix is in a viscous state. As the matrix transforms from a viscous state to a viscoelastic state, the first autocatalitic model of Eq.(4.1) ($A_1 e^{\frac{-E_{1_a}}{RT}} \alpha^{m_1} (1-\alpha)^{n_1}$) is the major contributor to the degree of cure evolution. Finally, as the matrix passes from a rubbery to

a glassy state and vitrifies the diffusion factor (the denominator of the first term of Eq.(4.1)) is responsible for reducing the final degree of cure, as the reaction is controlled by diffusion rather than by chemical factors [131].

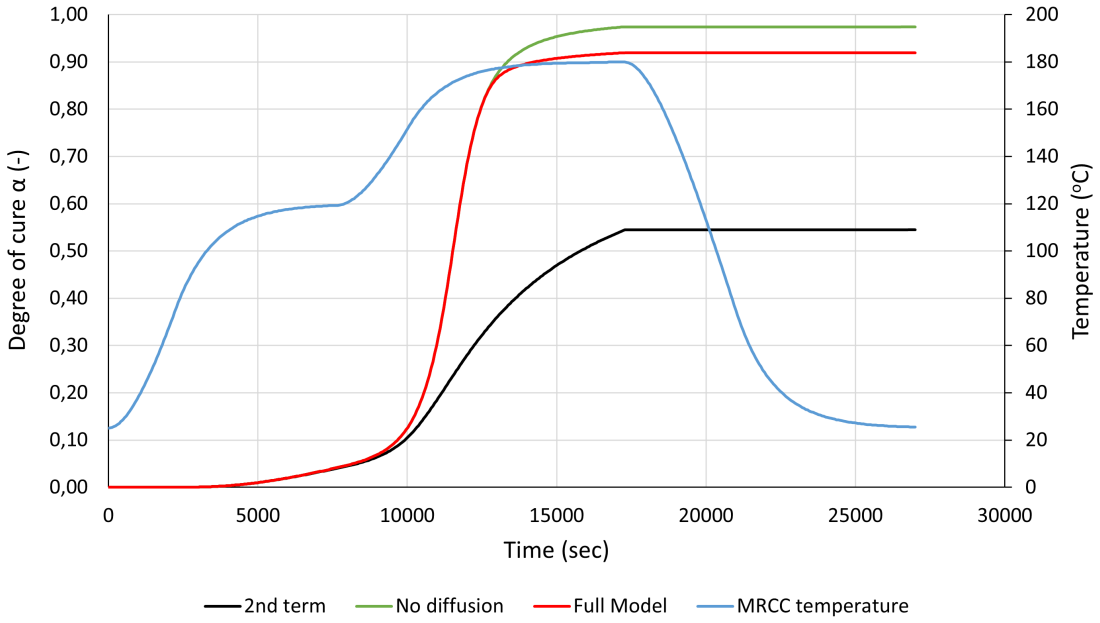


Figure 4.4: Contribution of each term of Eq.(4.1) in the evolution of degree of cure.

### 4.2.2 Glass Transition Temperature

The DiBenedetto Eq.(4.2) was used to calculate the glass transition temperature $T_g$ of the structure at each time step.

$$T_g = T_g^0 + \frac{\alpha\lambda(T_g^\infty - T_g^0)}{1 - (1-\lambda)\alpha} \tag{4.2}$$

where :

- $\lambda$ : DiBenedetto material constant
- $T_g^0$ : Glass transition temperature at $\alpha^0 = 0$
- $T_g^\infty$ : Glass transition temperature at $\alpha^\infty = 1$

The material characterization of the glass transition temperature was performed by Weiland on behalf of Premium AEROTEC GmbH [132]. DSC was used to measure the $T_g$ of five resin specimens and determine the DiBenedetto material constant $\lambda$ by least squares fit of Eq.(4.2) to the experimental results. The degree of cure of the manufactured specimens was $\alpha = 0$, $\alpha = 0.15$, $\alpha = 0.25$, $\alpha = 0.4$ and $\alpha = 1$. Table 4.3 contains values of the material constants used in Eq.(4.2). Due to confidentially

the exact values could not be presented but are within 20% range of the values presented.

Table 4.3: Material constants used in Eq.(4.2)

| $T_g^0$ | λ[119] | $T_g^\infty$ |
|---|---|---|
| $°C$ | - | $°C$ |
| -7.4 | 0.430 | 198 |

### 4.2.3 Matrix Coefficient of Thermal Expansion (CTE)

The CTE of the matrix depends on its state during the curing cycle. In the rubbery state, the CTE of the matrix was approximated as 2.5 times greater than the CTE in the glassy state according to the assumption made by Svanberg [21]. Eq.(4.3) was used to determine the CTE of the matrix according to its state [21]:

$$\boldsymbol{\alpha}_m^{CTE} = \begin{cases} \boldsymbol{\alpha}_{m_r}^{CTE} & T_{C_1} < T^* \\ C_2 + C_3 T^* + C_4 T^{*2} & T_{C_2} < T^* < T_{C_1} \\ \boldsymbol{\alpha}_{m_g}^{CTE} + \alpha_\alpha (T^* - T_{C_2}) & T^* < T_{C_2} \end{cases} \tag{4.3}$$

where $T^*$ is the temperature difference to the $T_g$ (Eq.(4.4))

$$T^* = T - T_g \tag{4.4}$$

The quantities $\boldsymbol{\alpha}_{m_r}^{CTE}$ and $\boldsymbol{\alpha}_{m_g}^{CTE}$ are the CTE of the matrix at the rubbery and glassy state respectively. $T_{C_1}, T_{C_2}, C_2, C_3, C_4, \alpha_\alpha$ used in Eq.(4.3) are material constants.

The material characterization of the matrix CTE was performed by Weiland on behalf of Premium AEROTEC GmbH [132]. The CTE of the matrix was measured with the use of DMA. Three specimens were manufactured from the same tool and measured from room temperature to $250°C$. To determine the material constants Eq.(4.3) was fitted to the experimental measurements. Table 4.4 contains values of the material constants used in Eq.(4.3). Due to confidentially the exact values could not be presented but are within 20% range of the values presented.

Table 4.4: Material constants used in Eq.(4.3)

| $T_{C_1}$ | $T_{C_2}$ | $\boldsymbol{\alpha}_{m_r}^{CTE}$ | $\boldsymbol{\alpha}_{m_g}^{CTE}$ | $C_2$ | $C_3$ | $C_4$ | $\alpha_\alpha$ |
|---|---|---|---|---|---|---|---|
| $°C$ | $°C$ | $°C^{-1}$ | $°C^{-1}$ | $°C^{-1}$ | $°C^{-2}$ | $°C^{-3}$ | $°C^{-1}$ |
| 5.2 | -18.7 | $1.29 \times 10^{-4}$ | $6.31 \times 10^{-5}$ | $1.16 \times 10^{-4}$ | $3.59 \times 10^{-6}$ | 0.15 | $5.60 \times 10^{-8}$ |

Fig. 4.5 shows representative behaviour of the matrix CTE with respect to $T^*$. As depicted the matrix CTE has its maximum value at the rubbery state (a constant value in the first branch of Eq.(4.3)). As the value of $T^*$ reduces, due to the increase of $T_g$ owning to the increase of the degree of cure of the matrix, the CTE reduces. A sharp decrease of the CTE is observed around the gel point of the matrix (second branch of Eq.(4.3)) which is followed by a linear decrease (third branch of Eq.(4.3)) until the end of the curing cycle. The CTE of the matrix along with $T^*$ and $T_g$ for the MRCC from gelation to cool down is depicted in Fig. 5.4.

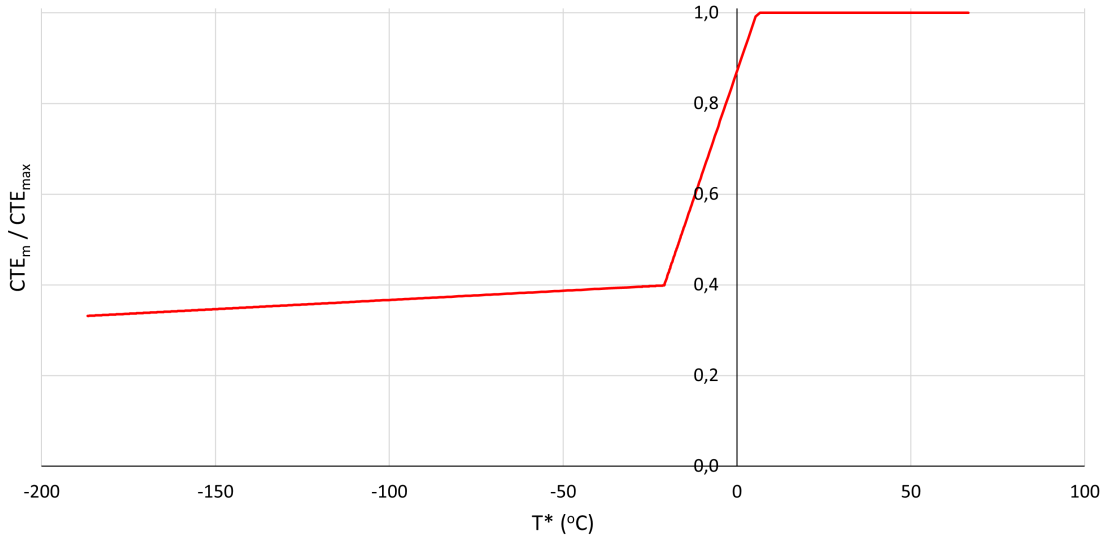


Figure 4.5: Matrix CTE evolution with respect to $T^*$.

### 4.2.4 Matrix volumetric chemical shrinkage

The chemical contraction model Eq.(4.5) proposed by Johnston [99] based on the work of Bogetti [98] was used to describe the chemical shrinkage of the matrix. The volumetric chemical shrinkage of the matrix before the gelation point was approximated as zero, as due to the limited cross-linking of the matrix before that point the contraction of the material is considered insignificant.

$$\boldsymbol{V}_m^C = \begin{cases} 0.0 & \alpha < \alpha_{c_1} \\ B\alpha_c + (\boldsymbol{V}_m^{C^\infty} - B)\alpha_c^2 & \alpha_{c_1} \leq \alpha < \alpha_{c_2} \\ \boldsymbol{V}_m^{C^\infty} & \alpha \geq \alpha_{c_2} \end{cases} \tag{4.5}$$

where :

$$\alpha_c = \frac{\alpha - \alpha_{c_1}}{\alpha_{c_2} - \alpha_{c_1}} \tag{4.6}$$

The quantities $B, \alpha_{c_1}, \alpha_{c_2}$ used in Eq.(4.5) are material constants and $\boldsymbol{V}_m^{C\infty}$ is the maximum volumetric chemical shrinkage of the matrix.

The material characterization of the chemical shrinkage of the matrix was performed by Weiland on behalf of Premium AEROTEC GmbH [132]. Four specimens were manufactured and measured with the use of a rheometer according to the American Society for Testing and Materials (ASTM) D4473 standard. Then, Eq.(4.5) was fitted to the experimental measurements. The volumetric chemical shrinkage of the matrix could be experimentally measured from the gel point. Table 4.5 contains values of the material constants used in Eq.(4.5),(4.6). Due to confidentially the exact values could not be presented but are within 20% range of the values presented.

Table 4.5: Material constants used in Eq.(4.5),(4.6)

| $\boldsymbol{V}_m^{C\infty}$ | $B$ | $\alpha_{c_1}$ | $\alpha_{c_2}$ |
|---|---|---|---|
| - | - | - | - |
| 0.0167 | 0.026 | 0.59 | 1.01 |

Fig. 4.6 shows $\boldsymbol{V}_m^C$ with respect to the degree of cure of the matrix. As shown the chemical shrinkage of the matrix takes place after gelation to $\alpha \approx 0.78$, where it reaches its maximum value and the chemical contraction of the part stops.

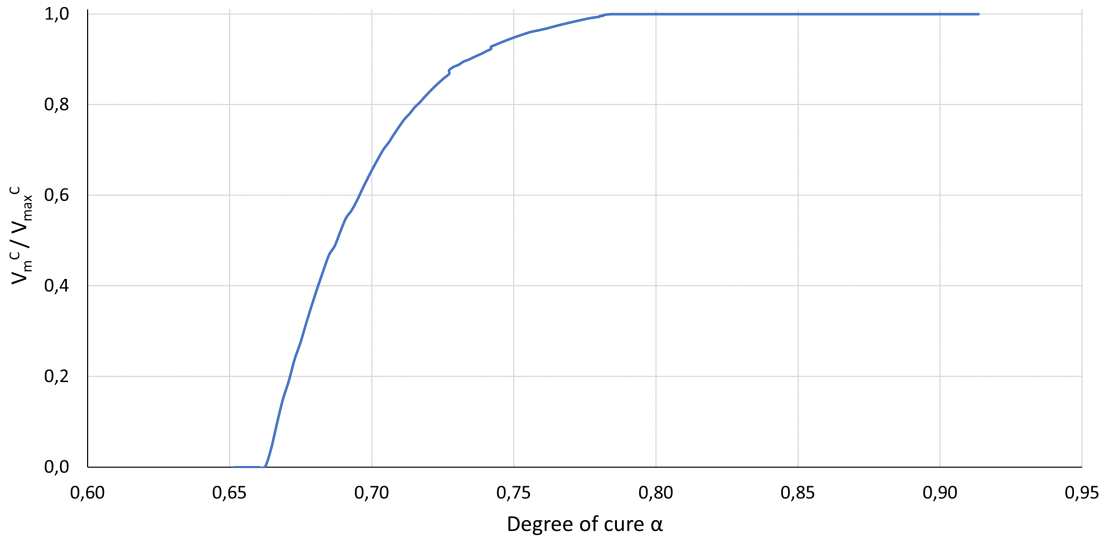


Figure 4.6: Matrix volumetric chemical shrinkage from gelation to the end of the curing cycle, where the part reaches its maximum degree of cure.

### 4.2.5 Matrix thermal and chemical strain

The matrix is modelled as an isotropic material having the same CTE in all its principal directions. Eq. (4.7) is used to calculate the matrix thermal linear expansional strain:

$$\boldsymbol{\varepsilon}_m^T = \boldsymbol{\alpha}_m^{CTE} \Delta T \tag{4.7}$$

where $\Delta T$ is the increment of temperature and $\boldsymbol{\alpha}_m^{CTE}$ is calculated according to Eq. (4.3).

Similarly to the calculation of thermal strains, uniform strain contraction for all principal strain components is assumed. To calculate the isotropic chemical shrinkage strain, Eq. (4.8) was used [98]:

$$\boldsymbol{\varepsilon}_m^C = (1 + \boldsymbol{V}_m^C)^{\frac{1}{3}} - 1.0 \tag{4.8}$$

where $\boldsymbol{V}_m^C$ is the instantaneous volumetric chemical shrinkage of the matrix (Eq. (4.5)).

### 4.2.6 Matrix Young's modulus

#### 4.2.6.1 Modified CHILE material model

The matrix instantaneous $E_m$ modulus is a function of temperature $T$ and degree of cure $\alpha$. A modified CHILE model (Eq. (4.9)) was used to describe the evolution of the matrix $E$ modulus during cure, based on the work of Johnston [99]. This model differs from the originally proposed CHILE model based on the fact that it separates the development of the resin modulus during the curing cycle into seven branches instead of three as discussed in Section 2.4.3.2.

$$E_m = \begin{cases} E_m^0 & \alpha < \alpha^{gel} \\ E_1 & T^* < T_1 \\ E_2 + (E_1 - E_2)\dfrac{(T^* - T_2)}{T_1 - T_2} & T_1 \leq T^* < T_2 \\ E_3 + (E_2 - E_3)\dfrac{(T^* - T_3)}{T_2 - T_3} & T_2 \leq T^* < T_3 \\ E_4 + (E_3 - E_4)\dfrac{(T^* - T_4)}{T_3 - T_4} & T_3 \leq T^* < T_4 \\ Ae^{-k_e T^*} & T_4 \leq T^* < T_5 \\ E_5 & T^* > T_5 \end{cases} \tag{4.9}$$

The quantities $E_1, E_2, E_3, E_4, E_5, A, k_e, T_1, T_2, T_3, T_4, T_5$ used in Eq.(4.9) are material constants and $E_m^0$ is the modulus of the matrix in the viscous state. $T^*$ can be

calculated according to Eq.(4.4).

The material characterization of the $E$ modulus was performed by Weiland on behalf of Premium AEROTEC GmbH [132]. To determine the material constants of Eq.(4.9, four UD specimens were manufactured and measured in three-point bending test in the DMA apparatus according to ASTM D5023-07 standard. The degree of cure of the tested specimens were 0.927 and the maximum difference of the $E$-modulus of the specimens measured at the glassy state was less than 3%. The gel point was $\alpha^{gel} = 0.66$. Table 4.6 contains values of the material constants used in Eq.(4.9). Due to confidentially the exact values could not be presented but are within 20% range of the values presented.

Table 4.6: Material constants used in Eq.(4.9)

| $E_1$ | $E_2$ | $E_3$ | $E_4$ | $E_5$ | $E_m^0$ | $A$ | $k_e$ | $T_1$ | $T_2$ | $T_3$ | $T_4$ | $T_5$ |
|---|---|---|---|---|---|---|---|---|---|---|---|---|
| $GPa$ | $GPa$ | $GPa$ | $MPa$ | $MPa$ | $kPa$ | $GPa$ | $°C^{-1}$ | $°C$ | $°C$ | $°C$ | $°C$ | $°C$ |
| 2.92 | 2.28 | 1.97 | 432 | 78.2 | 94 | 1.79 | 0.113 | -196 | -125 | -7.3 | 14 | 28 |

#### 4.2.6.2 Linear viscoelastic material model

To derive the viscoelastic material properties of the EPS600 matrix, DMA was performed by the Karlsruher Institut of Technology (KIT), Institut für Technische Mechanik on behalf of Premium AEROTEC GmbH [133]. The DMA test was performed at the temperature range of $-30°C$ to $250°C$ with a temperature step of $5°C$ at five discrete frequencies (0.5, 1.58, 5, 15.8 and 50 $Hz$) per temperature as shown in Fig. 4.8. The storage $E^{'}$ and loss modulus $E^{''}$ of each measurement was divided by the maximum measured value of each set, as due to confidentially the exact values could not be presented. The degree of cure of the specimens tested was $a_{ref} = 0.94$.

After obtaining the experimental data from the DMA test, master curves of the storage $E^{'}$ and loss modulus $E^{''}$ of the material need to be created. The role of a master curve is to describe the viscoelastic behaviour of the material beyond the range of frequencies covered by experimental measurements.

The creation of the master curves is based on the time-cure-temperature superposition principle proposed by Simon *et al.* [123]. According to this principle, the effect of temperature and degree of cure on the relaxation times are accounted for by applying the time-temperature superposition principle [114] and the time-cure superposition principle [134, 135].

The time-temperature superposition principle implies that the viscoelastic behaviour

at one temperature can be related to that at another temperature by a change in the time scale only [114]. In the case of thermo-rheologically simple materials, the curves of the instantaneous modulus as a function of time do not change shape as the temperature is changed but appear only to shift left or right. To construct the master curve from the available DMA data the reference temperature $T_{ref}$ was chosen to be equal to the glass transition temperature at the reference degree of cure $T_{ref} = T_g(a_{ref}) = 214.9°C$. Then the DMA data of the specimens having different temperatures than $T_{ref}$ are shifted horizontally along the frequency axis so that they superimpose with the DMA data of the $T_{ref}$ specimen in order to form a continuous curve as shown in Fig. 4.9.

For the time-temperature superposition, the empirical relation first established by Malcolm L. Williams, Robert F. Landel and John D. Ferry, also called, the WLF model Eq.(4.10) was used to calculate the temperature shift factor $a_T$ [136]:

$$log(a_T) = \frac{-C_{g_1}(T - T_{ref})}{C_{g_2} + (T - T_{ref})} \tag{4.10}$$

where :

- $a_T$ : Temperature shift factor
- $C_{g_1}, C_{g_2}$ : Material constants
- $T_{ref}$ : Reference temperature chosen to be equal to the glass transition temperature at the reference degree of cure $T_{ref} = T_g(a_{ref})$

The calculation of the $C_{g_1}, C_{g_2}$ is achieved by curve fitting to the available DMA data. The WLF equation proved to match the experimentally derived master curves very well. Consequently, the time-temperature superposition principle holds true with the studied matrix system (Fig. 4.10).

In correspondence to the temperature shift factor $a_T$, a degree of cure shift factor $a_x$, accounts for the degree of cure dependence of the relaxation times. For the time-cure superposition principle, it is assumed that the degree of cure shift factor $a_x$ has a similar form independent of degree of cure if the reference temperature is taken as $T_g$ [123, 134, 135]. Therefore, similarly to the time-temperature superposition principle the WLF formula is also applied here with $T_{ref} = T_g^{ref}$ according to Eq.(4.11) to calculate the degree of cure shift factor $a_x$:

$$log(a_x) = \frac{-C_{g_1}(T_g(a) - T_g^{ref})}{C_{g_2} + (T_g(a) - T_g^{ref})} \tag{4.11}$$

where :

- $a_x$ : Degree of cure shift factor
- $C_{g_1}, C_{g_2}$ : Material constants as calculated above
- $T_g^{ref}$ : Reference glass transition temperature chosen to be equal to the glass transition temperature at the reference degree of cure $T_g^{ref} = T_g(a_{ref})$

Fig. 4.7 shows the temperature shift factor $a_T$ and degree of cure shift factor $a_x$ as function of temperature and glass transition temperature according to Eq. 4.10 and 4.11 respectively. In both cases the reference temperature $T_{ref}$ was chosen to be equal to the glass transition temperature at the reference degree of cure $T_{ref} = T_g(a_{ref}) = 214.9°C$.

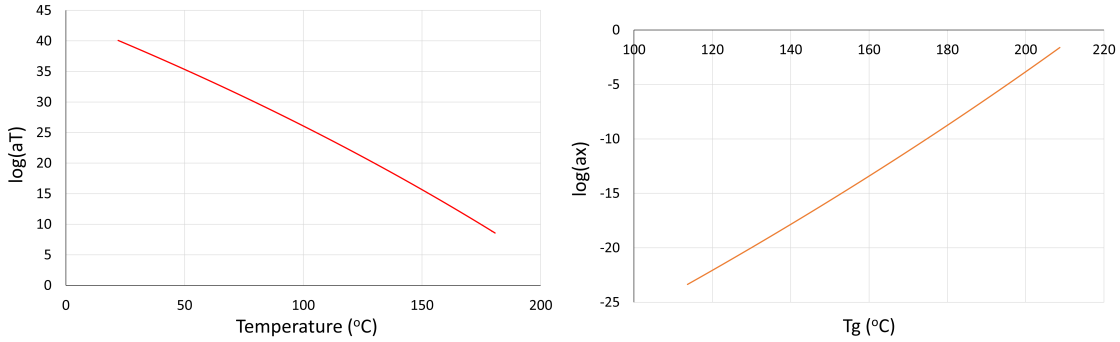


Figure 4.7: Temperature shift factor $a_T$ (left) and degree of cure shift factor $a_x$ (right) as function of $T$ and $T_g$. In both cases $T_{ref} = T_g(a_{ref}) = 214.9°C$.

The combined cure-temperature shift factor is calculated as the sum of the temperature shift factor and degree of cure shift factor (Eq.(4.12)):

$$log(a_{T_x}) = log(a_T) + log(a_x) \tag{4.12}$$

The result of shifting the experimental data is the creation of two master curves one for the storage modulus $E^{'}$ and one for the loss modulus $E^{''}$ of the matrix. Then, the Generalised Maxwell element model, which diagram is shown in Fig. 4.12, was chosen to be fitted to the master curves to describe the viscoelastic material behaviour of the matrix [24].

The Generalised Maxwell element model consists of many spring-dashpot (Maxwell) elements connected in parallel and a spring. The use of many Maxwell elements is done in order to take into account that the relaxation does not occur at a single time, but at a set of times. The purpose of the spring is to ensure that the stresses does not fully relax and the viscoelastic material retains a small storage modulus when strain is applied to the material.

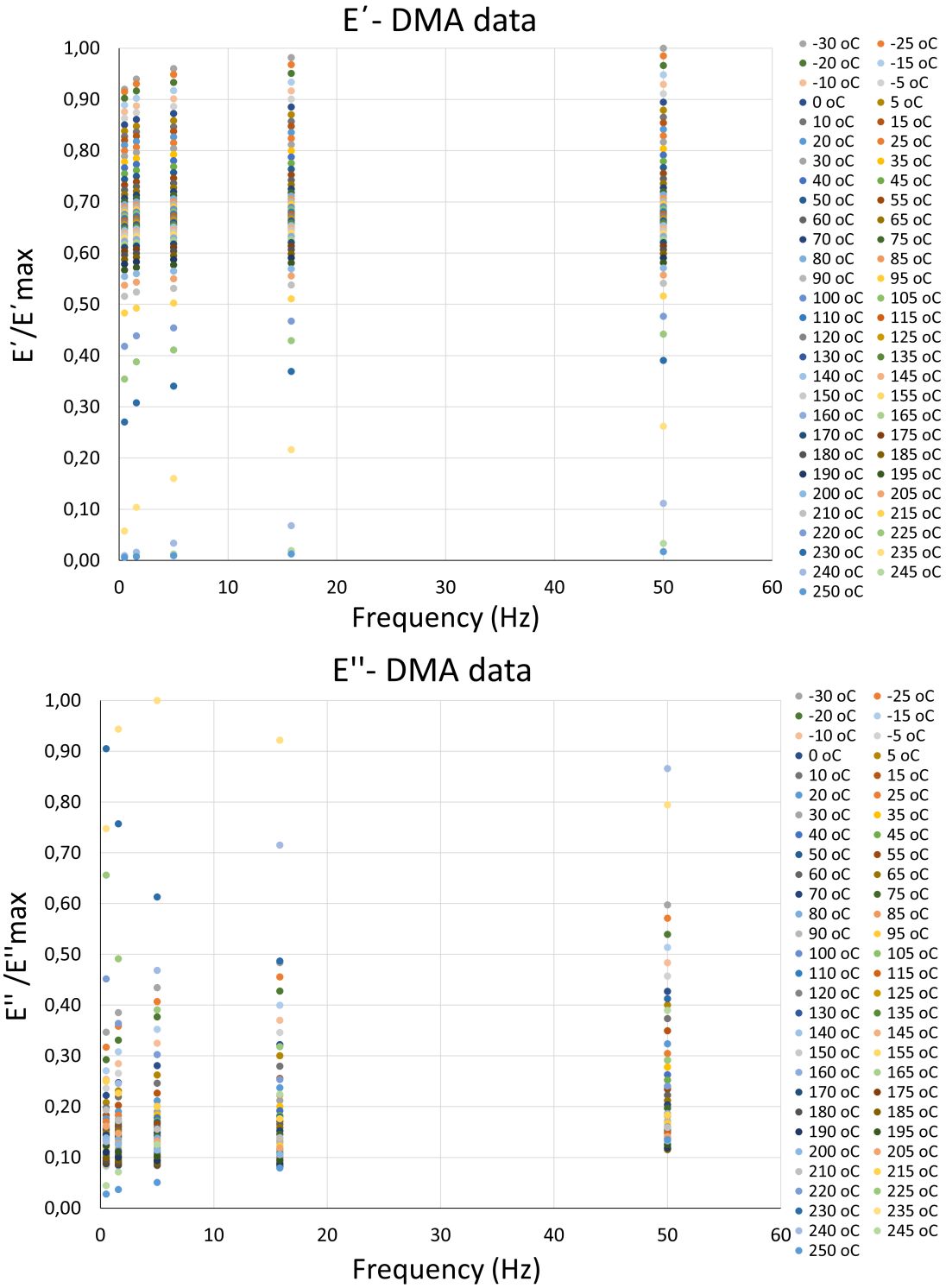


Figure 4.8: The data acquired from the DMA for the storage $E^{'}$ and loss $E^{''}$ modulus.

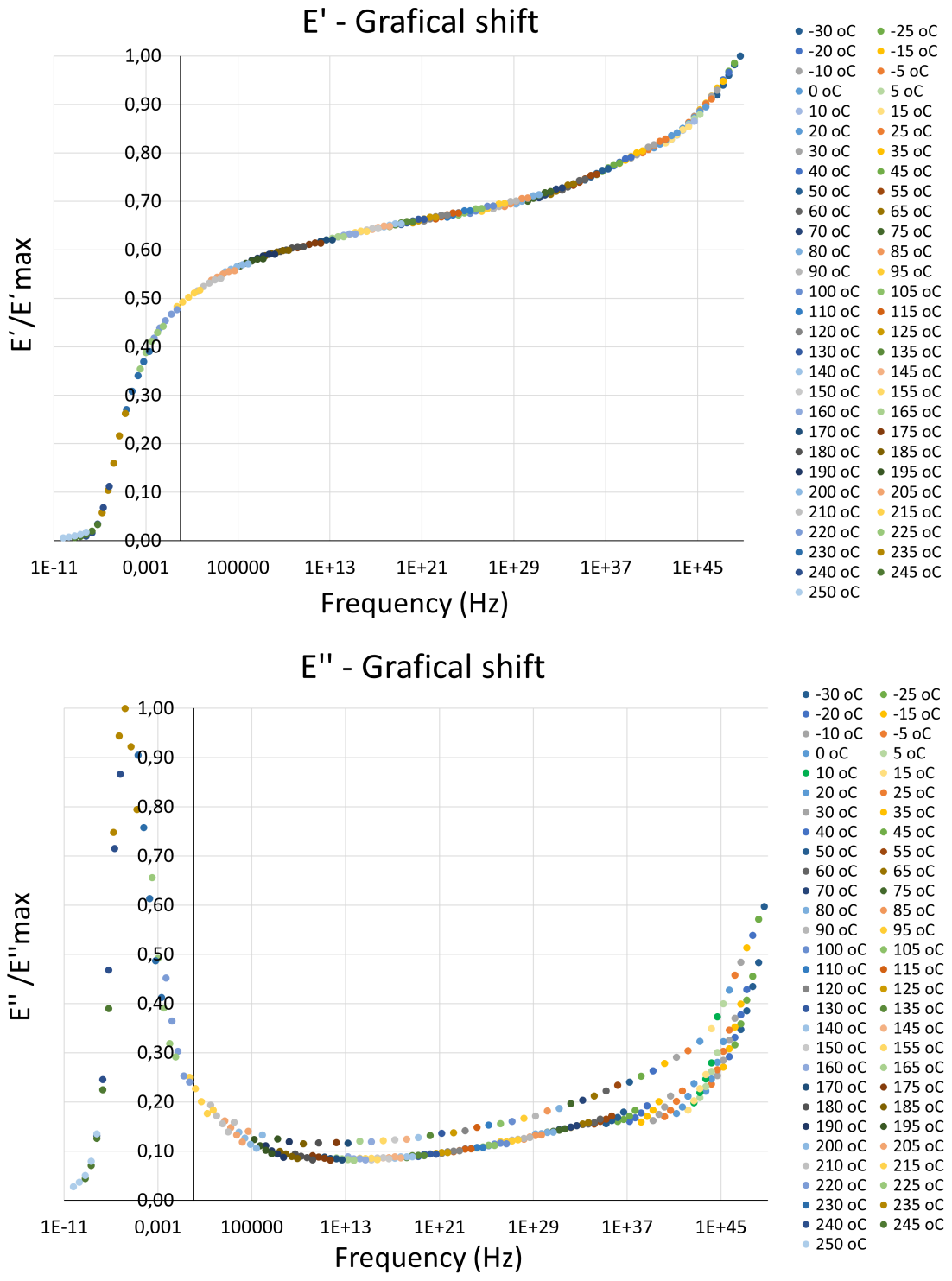


Figure 4.9: Graphical shift of the DMA data for the storage $E^{'}$ and loss $E^{''}$ modulus. The data acquired from the DMA (Fig. 4.8) were manually shifted in order to superimpose and form a continuous curve.

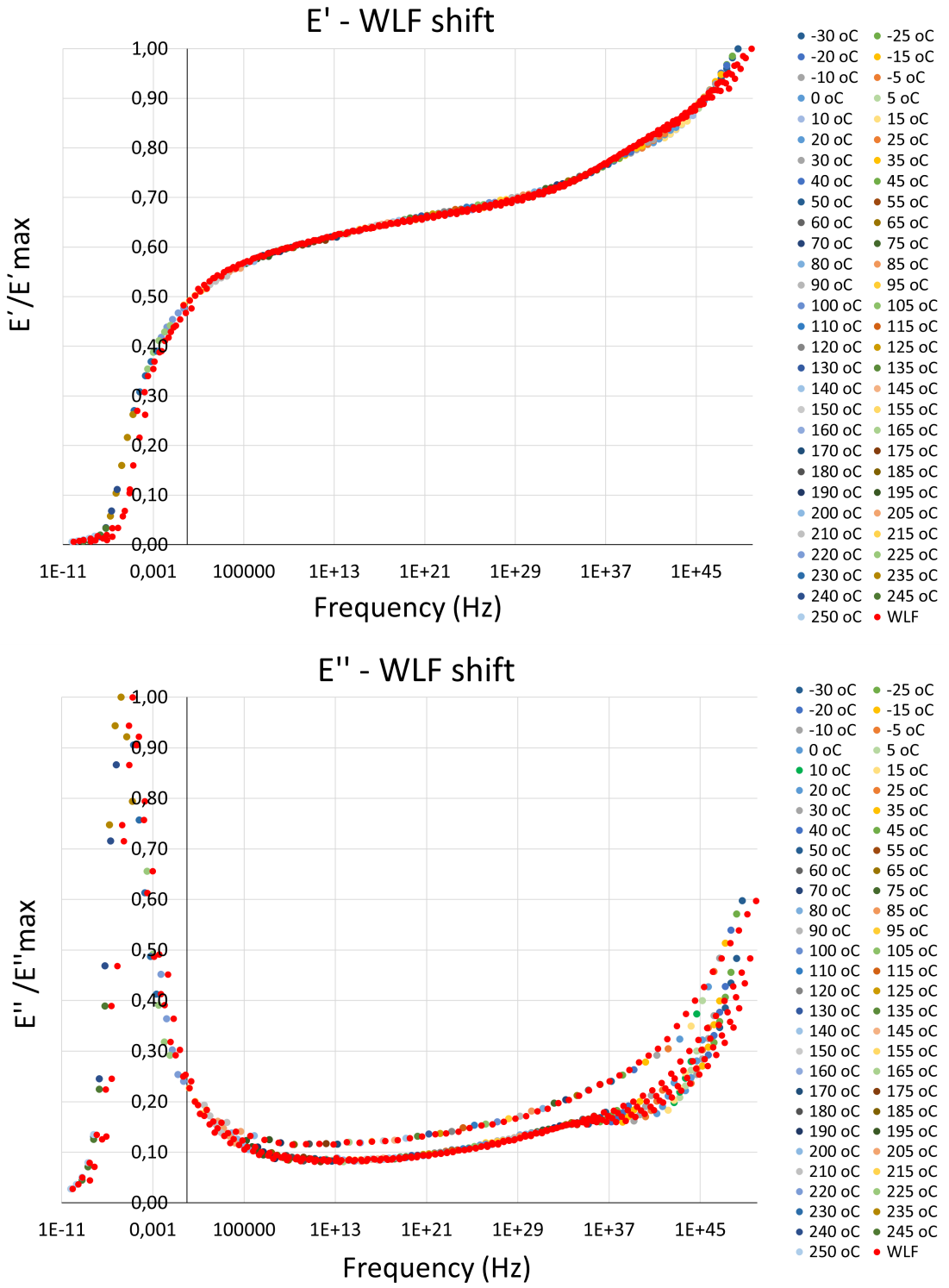


Figure 4.10: WLF shift of the DMA data of the storage $E^{'}$ and loss $E^{''}$ modulus. Eq.(4.10) was fitted to the curve of Fig. 4.9 and the constants of the equation were determined.

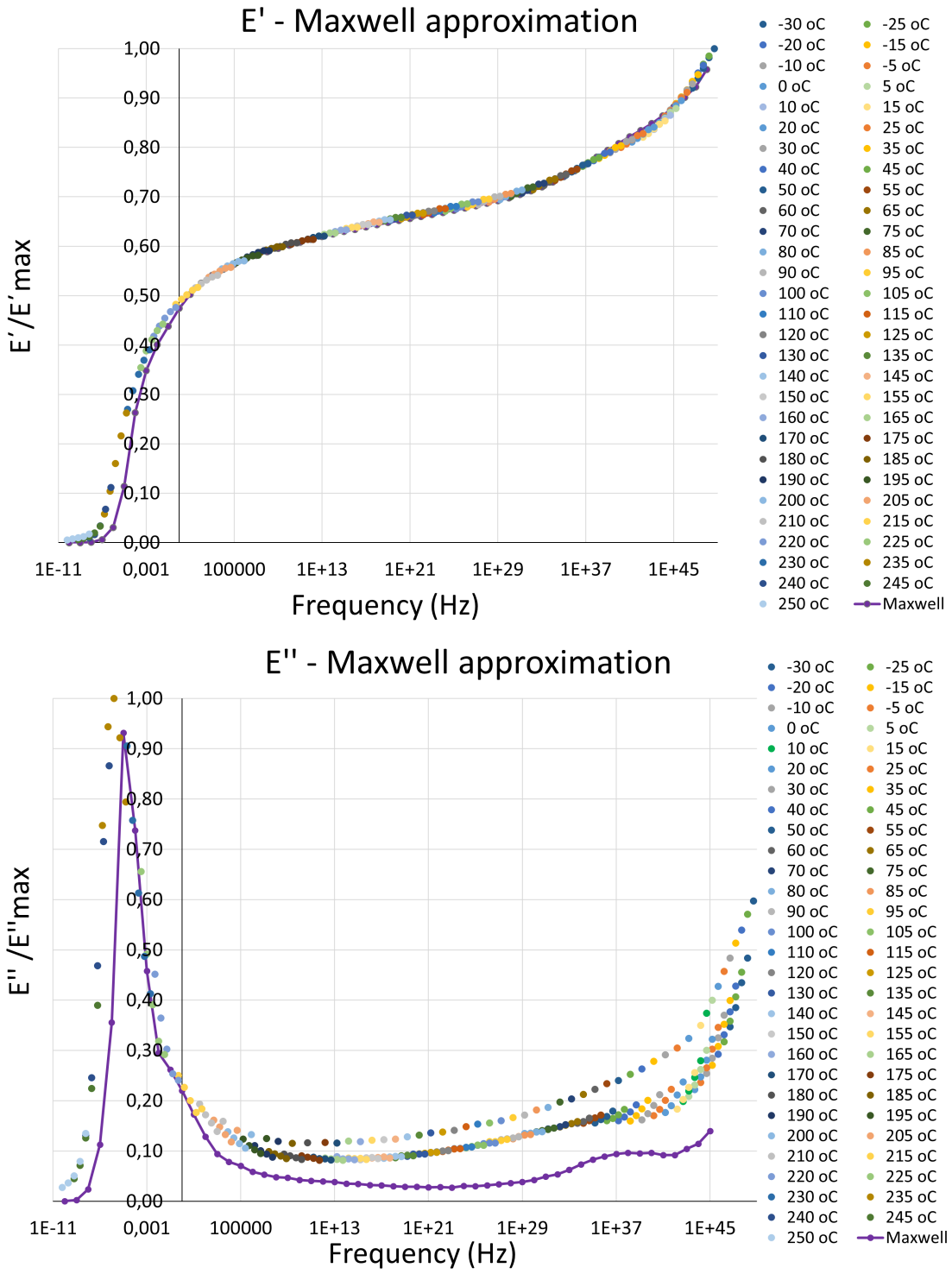


Figure 4.11: Maxwell approximation of the master curve of the storage $E^{'}$ and loss $E^{''}$ modulus. Eq.(4.13) was fitted to the WLF shifted curve of Fig. 4.10 and the relative stiffness $E_i$ of the Maxwell elements were determined.

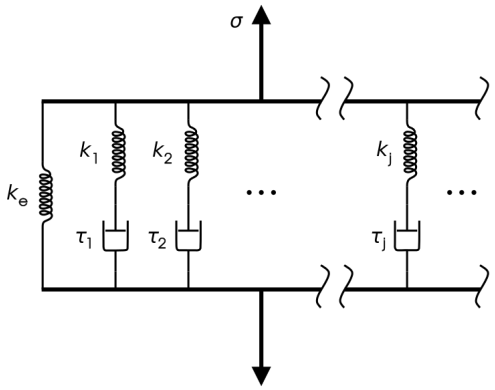


Figure 4.12: Generalised Maxwell element consisting of many spring-dashpot Maxwell elements [24].

The total number ($N$) of Maxwell elements which are needed by the Generalised Maxwell element model to accurately fit the experimental data depends on the range of frequencies studied. A common practice is to separate the frequency range to $N$ segments at every logarithmic decade and assign to each segment a Maxwell element (spring-dashpot) to model the viscoelastic behaviour. The storage modulus $E^{'}$ and the loss modulus $E^{''}$ of the material can be calculated using Eq.(4.13).

$$\begin{aligned} E^{'} &= \sum_{i=1}^{N} E_i \frac{(\omega\tau_i)^2}{1+(\omega\tau_i)^2} + E_r \\ E^{''} &= \sum_{i=1}^{N} E_i \frac{\omega\tau_i}{1+(\omega\tau_i)^2} \end{aligned} \tag{4.13}$$

where :

- $N$ : Total number of the Maxwell elements
- $E_i$ : The relative stiffness of the $i^{th}$ Maxwell element
- $\tau_i$ : Relaxation time of the $i^{th}$ Maxwell element
- $\omega$ : The frequency of oscillation
- $E^{'}, E^{''}$ : The experimental value of the storage and loss modulus respectively

For the calculation of the relative stiffness of the Maxwell elements $E_i$, the non linear fit functionality of the Maple software was used. The purpose of the fit is to identify the value of the relative stiffness of the Maxwell elements that minimize the least-squares error of the model with the experimental data [137]. The fitting of Eq.(4.13) was performed for the storage modulus $E^{'}$ responsible for the elastic behaviour of the material. Therefore, the deviation of the model from the loss modulus is greater than the storage modulus as shown in Fig. 4.11. However, since the loss modulus of the material is orders of magnitude smaller than the

storage modulus the fit was considered suitable for the purpose of this work. After determining the relaxation times $\tau_i$ and the relative stiffness of every Maxwell element $E_i$, the matrix relaxation tensile modulus can be calculated at every time step of the curing cycle using the Prony series as shown in Eq.(4.14) [24]:

$$E_m(t) = E_r + (E_g - E_r) \sum_{i=1}^{N} E_i \exp\left(\frac{-t}{a_{T_x}\tau_i}\right) \tag{4.14}$$

where :

- $E_m(t)$ : The matrix relaxation tensile modulus
- $E_r$ : The rubbery or equilibrium tensile modulus once the material is totally relaxed (Long term modulus)
- $E_g$ : The glassy or unrelaxed matrix modulus
- $E_i$ : The relative stiffness of the $i^{th}$ Maxwell element
- $\tau_i$ : Relaxation time of the $i^{th}$ Maxwell element
- $a_{T_x}$ : Degree of cure - temperature shift factor of the time step
- $t$ : Time

The rubbery modulus $E_r$ was set equal to the value of the loss modulus $E^{''}$ at the highest temperature ($250°C$) and frequency ($50Hz$) tested in the DMA analysis. This was one of the lowest values measured in the experiment and was considered representative of the rubbery material behaviour. On the other hand, at low temperatures the material shows glassy behaviour. As a result the glassy modulus $E_g$ is equal to the storage modulus $E^{'}$ at the lowest temperature ($-30°C$) and highest frequency ($50Hz$) tested in the DMA analysis.

### 4.2.7 Matrix Poisson's coefficient

The instantaneous Poisson's coefficient of the matrix is calculated from Eq. (4.15) [99]. Here it was assumed that the bulk modulus ($K$) of the resin is constant. The matrix Poisson's coefficient for the case of the MRCC from gelation to cool down is depicted in Fig. 6.11. As shown in the melt state the value of the Poisson's coefficient is approximately 0.5 reducing to 0.38 as the parts vitrifies.

$$\nu_m = \frac{1}{2}(1 - \frac{E_m(1 - 2\nu^{\infty})}{E_m^{\infty}}) \tag{4.15}$$

where :

- $\nu^{\infty}$ : The matrix Poisson's ratio at $\alpha^{\infty} = 1.0$
- $E_m^{\infty}$ : Matrix elastic modulus at $\alpha^{\infty}$
- $E_m$ : Matrix Young's modulus (Eq. (4.9) or (4.14)).

### 4.2.8 Matrix G modulus

Assuming isotropic material behaviour the matrix instantaneous shear modulus $G_m$ is calculated according to Eq. (4.16).

$$G_m = \frac{E_m}{2(1+\nu_m)} \tag{4.16}$$

where $\nu_m$ is the instantaneous Poisson's coefficient of the matrix (Eq. (4.15)). The matrix shear modulus for the case of the MRCC and "Fast" curing cycle from gelation to cool down is depicted in Fig. 5.7.

### 4.2.9 Matrix thermal conductivity

The matrix thermal conductivity, $k_m$ $(W/(m\,K))$, was approximated as a weighted sum of the fraction of the values of the liquid and fully cured state as given in Eq. (4.17). In the absence of specific material data of the matrix under investigation, the material constants of the EPON 862/EPIKURE 3300 epoxy system are used [78].

$$k_m = 0.148(1-\alpha) + k_m^{\infty}\alpha \tag{4.17}$$

where $k_m^{\infty}$ is the conductivity of the fully cured matrix defined as:

$$k_m^{\infty} = 6.097 * 10^{-4}T + 0.0236 \tag{4.18}$$

### 4.2.10 Matrix specific heat capacity

The specific heat capacity of the matrix $(J/(kg^{\circ}C))$ was approximated according to Eq. (4.19) and (4.20) [138]. This model takes into account the effect of the matrix transition from a rubbery to a glassy state on the specific heat capacity. Both material states are a function of temperature and degree of cure.

$$c_{p_m} = c_{p_r} + \frac{c_{p_g} - c_{p_r}}{1 + e^{k_{fac}(T^* - D_{TC})}} \tag{4.19}$$

$c_{p_g}$ and $c_{p_r}$ are linear combination the uncured and fully cured state of the material is given by Eq. (4.20).

$$\begin{aligned} c_{p_g} &= (1-\alpha)c_{p_{g^0}} + \alpha c_{p_{g^\infty}} \\ c_{p_{g^0}} &= s_{g^0}T + c_{g^0} \\ c_{p_{g^\infty}} &= s_{g^\infty}T + c_{g^\infty} \\ c_{p_r} &= (1-\alpha)c_{p_{r^0}} + \alpha c_{p_{r^\infty}} \\ c_{p_{r^0}} &= s_{r^0}T + c_{r^0} \\ c_{p_{r^\infty}} &= s_{r^\infty}T + c_{r^\infty} \end{aligned} \tag{4.20}$$

where $s_{r^0}, s_{r^\infty}, s_{g^0}, s_{g^\infty}, c_{r^0}, c_{r^\infty}, c_{g^0}, c_{g^\infty}, k_{fac}, D_{TC}$ are material constants, and $T^*$ can be calculated according to Eq. (4.4).

The material characterization of the matrix specific heat capacity was performed by Weiland on behalf of Premium AEROTEC GmbH [132]. Three specimens were manufactured and tested with the use of DSC according to International Organization for Standardization (ISO) 11357-4. Then, Eq. (4.19) was fitted to the measurements to determine the material constants. Table 4.7 contains values of the material constants used in Eq.(4.19),(4.20). Due to confidentially the exact values could not be presented but are within 20% range of the values presented.

Table 4.7: Material constants used in Eq.(4.19),(4.20)

| $s_{r^0}$ | $s_{r^\infty}$ | $s_{g^0}$ | $s_{g^\infty}$ | $c_{r^0}$ | $c_{r^\infty}$ | $c_{g^0}$ | $c_{g^\infty}$ | $k_{fac}$ | $D_{TC}$ |
|---|---|---|---|---|---|---|---|---|---|
| $\frac{J}{kg\,°C^2}$ | $\frac{J}{kg\,°C^2}$ | $\frac{J}{kg\,°C^2}$ | $\frac{J}{kg\,°C^2}$ | $\frac{J}{kg\,°C}$ | $\frac{J}{kg\,°C}$ | $\frac{J}{kg\,°C}$ | $\frac{J}{kg\,°C}$ | $\frac{1}{°C}$ | $°C$ |
| 7.2 | 2.2 | 9.0 | 8.0 | 1400 | 2000 | 850 | 680 | 0.42 | 2.10 |

Fig.4.13 shows the evolution of the specific heat capacity of the matrix with respect to temperature for different cure states. As depicted the $c_{p_m}$ transitions between the straight lines formed by the $c_{p_m}$ of the viscous ($\alpha = 0$) and fully cured ($\alpha = 1$) state. The vitrification/devitrification transition is modelled as an s-type curve which depends on $T^*$ (Eq. (4.4)) and its proximity to a value specific to the material ($D_{TC}$). The breadth of the transition is controlled by the shaping parameter $k_{fac}$ [138].

### 4.2.11 Fibre thermal conductivity

The thermal conductivity of the fibre ($W/(m\ K)$) (Eq.(4.21)) is a function of temperature and was assumed to be the same as that of AS4 fibre [99]. The

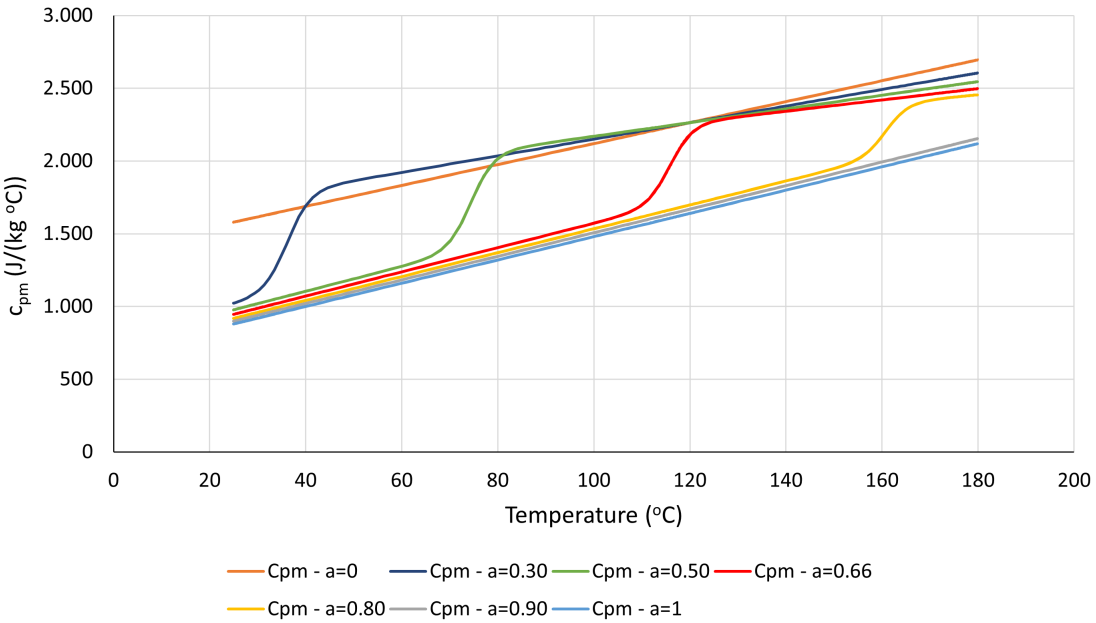


Figure 4.13: Evolution of $c_{p_m}$ with respect to temperature for different cure states.

conductivity of the fibre for the case of the MRCC from gelation to cool down is shown in Fig. 5.11.

$$\begin{aligned} k_{11_f} &= 7.69 + 1.56 * 10^{-2} T \\ k_{22_f} &= 2.4 + 5.07 * 10^{-3} T \end{aligned} \tag{4.21}$$

### 4.2.12 Fibre specific heat capacity

The specific heat capacity $(J/(kg°C))$ of the fibre is a function of temperature (Eq.(4.22)) and was assumed to be the same as that of AS4 fibre [99].

$$c_{p_f} = 750 + 2.05T \tag{4.22}$$

## 4.3 Micromechanics models

After the calculation of the instantaneous properties of the matrix and the fibre, the next step in the material modelling process is to calculate the effective lamina mechanical and thermal properties by employing micromechanics homogenisation models.

### 4.3.1 Lamina fibre volume fraction

The fibre volume fraction of the laminate is a function of the matrix's volumetric thermal expansion and chemical contraction. Therefore, the following calculation process is employed to calculate the lamina's instantaneous fibre volume fraction.

- Calculation of the matrix's specific volume at final product is given by Eq.(4.23):

$$V_m^\infty = 1.0 - V_{void}^\infty - V_f^\infty \tag{4.23}$$

  where :
  - $V_m^\infty$ : Specific volume of the matrix in the final product.
  - $V_{void}^\infty$ : Specific volume of the voids in the final product. Assumed constant during the cure $V_{void}^\infty = 0.02$, which is typical for a part manufactured with HLU out of autoclave [139].
  - $V_f^\infty$ : Fibre volume fraction of the final product. Assumed $V_f^\infty = 0.56$.
- Calculation of the matrix's specific volume change due to thermal strains Eq.(4.24) [98]:

$$V_m^T = \varepsilon_1^T + \varepsilon_2^T + \varepsilon_3^T + \varepsilon_1^T\varepsilon_2^T + \varepsilon_1^T\varepsilon_3^T + \varepsilon_2^T\varepsilon_3^T + \varepsilon_1^T\varepsilon_2^T\varepsilon_3^T \tag{4.24}$$

  $T$ in Eq.(4.24) refers to thermal strains of the matrix.
- Calculation of the matrix's specific volume at the start of the manufacturing process based on its value in the final product is given by Eq.(4.25):

$$V_m^0 = \frac{V_m^\infty}{1 - V_m^{C\infty} + V_m^{T\infty}} \tag{4.25}$$

  where:
  - $V_m^{C\infty}$ : Matrix specific volume maximum chemical contraction (Eq.(4.5)).
  - $V_m^{T\infty}$ : Matrix specific volume thermal expansion at the end of the curing cycle.
- Calculation of the instantaneous matrix specific volume is defined by Eq.(4.26):

$$V_m = V_m^0(1.0 + V_m^T - V_m^C) \tag{4.26}$$

  where $V_m^C$ is the matrix specific volume change due to chemical shrinkage (Eq.(4.5)).
- Calculation of the instantaneous fibre volume fraction is defined by Eq.(4.27):

$$V_f = 1.0 - V_{void}^\infty - V_m \tag{4.27}$$

### 4.3.2 Thermal micromechanics model

The matrix instantaneous density is calculated according to Eq.(4.28) based on the matrix's specific volume change due to thermal and chemical strains:

$$\rho_m = \frac{\rho_m^0}{1.0 + V_m^T - V_m^C} \tag{4.28}$$

where $\rho_m^0 = 1.15 g/cm^3$ is the matrix density at $25°C$ and $\alpha = 0$ [124]. $V_m^T$ and $V_m^C$ are the matrix specific volume change due to thermal and chemical strain respectively (Eq. (4.24) and (4.5)).

The density of the lamina is calculated using the rule of mixtures (Eq.(4.29)) [99]:

$$\rho_c = \rho_f V_f + \rho_m (1 - V_f) \tag{4.29}$$

where $V_f$ is the instantaneous fibre volume fraction (Eq.(4.27)).

The effective specific heat capacity of the lamina is calculated according to (Eq.(4.30)) [99]:

$$c_{p_c} = \frac{c_{p_f} \rho_f V_f + c_{p_m} \rho_m (1 - V_f)}{\rho_c} \tag{4.30}$$

The lamina longitudinal conductivity $k_{11_c}$ is determined using the rule of mixtures. The transverse conductivity $k_{22_c}$ is calculated according to the Extended Concentric Cylinder Assemblage (ECCA) model (Eq.(4.31)) [78]:

$$\begin{aligned} k_{11_c} &= k_{11_f} V_f + k_m (1 - V_f) \\ k_{22_c} &= \frac{(1 + V_f) k_{22_f} + (1 - V_f) k_m}{(1 - V_f) k_{22_f} + (1 + V_f) k_m} k_m \end{aligned} \tag{4.31}$$

### 4.3.3 Mechanical micromechanics model

To calculate the effective mechanical lamina properties, various micromechanics models have been proposed, such as the rule of mixtures, the representative volume elements (RVE) method etc. [140, 141]. Here, the model proposed by Bogetti was used to calculate the $E$, $G$ modulus and the Poisson's ratio $\nu$ of the lamina by assuming transversely isotropic material behaviour [98]. This is a self-consistent field model for UD continuous fiber reinforced composites, which provides a more realistic

approximation of the effective lamina properties than mechanics of materials models based on the uniform stress or strain assumption.

This model is used with elastic (Section 2.4.3.1) or modified elastic models (Section 2.4.3.2) to calculate the effective lamina properties. In this case, the unrelaxed, fully cured, resin modulus or instantaneous modulus is used to feed the homogenisation equations. The fibre properties are considered elastic and do not change during the curing cycle. However, in the modeling of composites as viscoelastic materials a more cumbersome approach exists. An elastic-viscoelastic analogy is used where the time dependent material properties (e.g matrix $E$ modulus Eq.(4.14)) are Laplace transformed into the frequency domain. Then, the effective mechanical properties of the composite are calculated using elastic micromechanics models in the Laplace domain and an inverse Laplace transformation is used, producing the solution in time domain of the effective material property of the composite. However, an exact solution may not always be found and approximations need to be made. In any case, this is a time consuming process involving many steps. Instead, here the effective properties of the composite material are modeled using the self-consistent model having as input the response of the matrix material (Eq.(4.14)) at every time increment as proposed by [119, 142]. Therefore, the time-dependent behaviour of the composite follows the Prony series representation of Eq.(4.14)).

In the self-consistent model used here, the variable $K$ in Eq.(4.32) is referred as isotropic plane strain bulk modulus :

$$K = \frac{E}{2(1-\nu-2\nu^2)} \tag{4.32}$$

The longitudinal Young's modulus of the lamina is defined by Eq.(4.33) :

$$E_{1c} = E_{1f}V_f + E_{1m}(1-V_f) + \frac{4(\nu_{12m}-\nu_{12f}^2)K_fK_mG_{23m}(1-V_f)V_f}{(K_f+G_{23m})K_m + (K_f-K_m)G_{23m}V_f} \tag{4.33}$$

The major Poisson's ratio is defined by Eq.(4.34):

$$\nu_{12c} = \nu_{13c} = \nu_{12f}V_f + \nu_{12m}(1-V_f) + \frac{(\nu_{12m}-\nu_{12f})(K_m-K_f)G_{23m}(1-V_f)V_f}{(K_f+G_{23m})K_m + (K_f-K_m)G_{23m}V_f} \tag{4.34}$$

The inplane shear modulus is defined by Eq.(4.35):

$$G_{12c} = G_{13c} = G_{12m}\frac{(G_{12f} + G_{12m}) + (G_{12f} - G_{12m})V_f}{(G_{12f} + G_{12m}) - (G_{12f} - G_{12m})V_f} \tag{4.35}$$

The transverse shear modulus is given by Eq.(4.36):

$$G_{23c} = \frac{G_{23m}[K_m(G_{23m} + G_{23f}) + 2G_{23f}G_{23m} + K_m(G_{23f} - G_{23m})V_f]}{K_m(G_{23m} + G_{23f}) + 2G_{23f}G_{23m} - (K_m + 2G_{23m})(G_{23f} - G_{23m})V_f} \tag{4.36}$$

The effective plane strain bulk modulus of the composite ply is given by Eq.(4.37):

$$K_c = \frac{(K_f + G_{23m})K_m + (K_f - K_m)G_{23m}V_f}{(K_f + G_{23m}) - (K_f - K_m)V_f} \tag{4.37}$$

The transverse Young's modulus is given by Eq.(4.38):

$$E_{2c} = E_{3c} = \frac{1}{\frac{1}{4K_c} + \frac{1}{4G_{23c}} + \frac{\nu_{12c}^2}{E_{1c}}} \tag{4.38}$$

The transverse Poisson's ratio is given by Eq.(4.39):

$$\nu_{23c} = \frac{2E_{1c}K_c - E_{1c}E_{2c} - 4\nu_{12c}^2K_cE_{2c}}{2E_{1c}K_c} \tag{4.39}$$

#### 4.3.3.1 Lamina expansional coefficients

The lamina expansional coefficients were also calculated according to the formulations proposed by Bogetti [98].

The longitudinal expansional strain of the ply is given by Eq.(4.40):

$$\varepsilon_{1c} = \frac{\varepsilon_{1f}E_{1f}V_f + \varepsilon_{1m}E_{1m}(1 - V_f)}{E_{1f}V_f + E_{1m}(1 - V_f)} \tag{4.40}$$

The transverse expansional strain of the ply is given by Eq.(4.41):

$$\varepsilon_{2c} = \varepsilon_{3c} = (\varepsilon_{2f} + \nu_{12f}\varepsilon_{1f})V_f + (\varepsilon_{2m} + \nu_{12m}\varepsilon_{1m})(1 - V_f) - (\nu_{12f}V_f + \nu_{12m}(1 - V_f))\varepsilon_{1c} \tag{4.41}$$

In order to calculate from Eq.(4.40) and Eq.(4.41) the CTE of the ply ($\alpha_c^{CTE}$), the expansional strains of the fiber and matrix ($\varepsilon_{1f}, \varepsilon_{1m}, \varepsilon_{2f}$ etc.) are substituted by the CTE coefficients of the materials in the relevant directions.

Regarding the calculation of the CSC of the ply ($\beta_c^{CSC}$), the expansional strains of the fiber ($\varepsilon_{1f}, \varepsilon_{2f}$) are set equal to zero as the fiber naturally does not chemically react. The expansional strains of the matrix ($\varepsilon_{1m}, \varepsilon_{2m}$) are set equal to one.

#### 4.3.3.2 Lamina strains

The strains in the lamina can be calculated with the use of the expansional coefficients of the lamina calculated by the micromechanics model.

The thermal strain of the ply is calculated with the use of Eq.(4.42):

$$\boldsymbol{\varepsilon}_c^T = \boldsymbol{\alpha}_c^{CTE} \Delta T \tag{4.42}$$

where $\boldsymbol{\alpha}_c^{CTE}$ is the coefficient of thermal expansion of the lamina.

The chemical strain of the ply is calculated with the use of Eq.(4.43):

$$\boldsymbol{\varepsilon}_c^C = \boldsymbol{\beta}_c^{CSC} \boldsymbol{\varepsilon}_m^C \tag{4.43}$$

where $\boldsymbol{\beta}_c^{CSC}$ is the chemical shrinkage coefficient of the lamina.

The sum of the thermal and chemical strain is defined as non-mechanical strain and can be calculated from Eq.(4.44). The chemical strain during the curing cycle is negative as the structure contracts while the thermal strain is positive during the heat-up phase and negative during cool down.

$$\boldsymbol{\varepsilon}_c^{NonMech} = \boldsymbol{\varepsilon}_c^T - \boldsymbol{\varepsilon}_c^C \tag{4.44}$$

By subtracting the non-mechanical strains from the total strains, the mechanical strains of the ply can be calculated Eq.(4.45).

$$\boldsymbol{\varepsilon}_c^{Mech} = \boldsymbol{\varepsilon}_c^{Total} - \boldsymbol{\varepsilon}_c^{NonMech} \tag{4.45}$$

where:

- $\Delta T$ : Increment of temperature
- $\boldsymbol{\varepsilon}_c^{Total}$ : Total strain at the end of the time increment.
- $\boldsymbol{\varepsilon}_m^C$ : Matrix chemical strain Eq. (4.8).

## 4.4 Stiffness matrix

For the calculation of the stiffness matrix, transversely isotropic material behaviour is assumed. Transversely isotropic materials are special orthotropic materials that have one axis of symmetry. Composite materials fall into this material category because the strength and stiffness of composite materials is greater in a direction parallel to the fibres than in the transverse direction, and the thickness direction usually has properties similar to the transverse direction.

The orthotropic stiffness matrix ($\boldsymbol{C}$) has the following definition (Eq.(4.46)):

$$\boldsymbol{C} = \begin{bmatrix} C_{11} & C_{12} & C_{13} & 0 & 0 & 0 \\ C_{12} & C_{11} & C_{13} & 0 & 0 & 0 \\ C_{13} & C_{13} & C_{33} & 0 & 0 & 0 \\ 0 & 0 & 0 & C_{44} & 0 & 0 \\ 0 & 0 & 0 & 0 & C_{55} & 0 \\ 0 & 0 & 0 & 0 & 0 & (C_{11} - C_{12})/2 \end{bmatrix} \tag{4.46}$$

where :

$$\begin{aligned} C_{11} &= E_1(1 - \nu_{23}\nu_{32})\Upsilon \\ C_{22} &= E_2(1 - \nu_{13}\nu_{31})\Upsilon \\ C_{33} &= E_3(1 - \nu_{12}\nu_{21})\Upsilon \\ C_{12} &= E_1(\nu_{21} + \nu_{31}\nu_{23})\Upsilon \\ C_{13} &= E_1(\nu_{31} + \nu_{21}\nu_{32})\Upsilon \\ C_{23} &= E_2(\nu_{32} + \nu_{12}\nu_{31})\Upsilon \\ C_{44} &= G_{12} \\ C_{55} &= G_{13} \\ C_{66} &= G_{23} \\ \Upsilon &= \frac{1}{1 - \nu_{12}\nu_{21} - \nu_{23}\nu_{32} - \nu_{31}\nu_{13} - 2\nu_{21}\nu_{32}\nu_{13}} \end{aligned} \tag{4.47}$$

To derive the transversely isotropic stiffness matrix $C_{44} = C_{55} = G_{12} = G_{13}$ is set.

The lamina properties calculated by the micromechanics model are used to calculate the stiffness matrix constituents.

## 4.5 Constitutive equations

### 4.5.1 Thermal constitutive equation

The energy balance Eq.(2.2) together with the heat conduction which is assumed to be governed by the Fourier law Eq.(2.3) is the governing equation for the heat transfer model (Eq.(4.48)):

$$\rho_c c_{p_c} \frac{\partial T}{\partial t} = \nabla \cdot (\boldsymbol{k_c} \cdot \nabla T) + \dot{Q} \tag{4.48}$$

where $\boldsymbol{k_c}$ is the conductivity tensor of the composite (Eq.(4.31)) and $\dot{Q}$ is the exothermic heat reaction of the matrix (Eq.(4.49)).

$$\dot{Q} = \rho_m (1 - V_f) H_m \dot{\alpha} \tag{4.49}$$

In Eq.(4.49), $H_m$ $(J/kg)$ is the matrix heat of reaction and $\dot{\alpha}$ is the curing rate (Eq.(4.1)). For the AS4/8552 prepreg $H_m = 540\, kJ/kg$ which is within 20% range of the value measured for the resin system under investigation.

### 4.5.2 Mechanical constitutive equations

#### 4.5.2.1 Modified CHILE material model

The constitutive equation of the CHILE material model is the generalised Hooke's law constitutive equation Eq.(4.50) [99]. These are a set of analytical equations that relate the stress tensor of the material point ($\boldsymbol{\sigma}_{ij}$), with the corresponding mechanical strain tensor ($\boldsymbol{\varepsilon}_{kl}^{Mech}$), with the use of the elastic stiffness matrix ($\boldsymbol{C}_{ijkl}^{\circ}$).

$$\boldsymbol{\sigma}_{ij} = \sum_k \sum_l \boldsymbol{C}_{ijkl}^{\circ} \boldsymbol{\varepsilon}_{kl}^{Mech} \tag{4.50}$$

The CTO to be used by the iterative solution process is set in the CHILE material model equal to the material point stiffness matrix ($\boldsymbol{C}_{ijkl}^{\circ}$).

#### 4.5.2.2 Linear viscoelastic material model

The constitutive update scheme proposed by Poon *et al.* for simulating anisotropic, thermo rheologically simple, viscoelastic solids is presented in Eq.(4.51,4.52,4.53) [111]. Eq.(4.51) is used to calculate the stress tensor of the next time increment.

$$\boldsymbol{\sigma}_{ij}^{n+1}(t) = \sum_{k}\sum_{l}\left(\boldsymbol{C}_{ijkl}^{\circ}\boldsymbol{\varepsilon}_{kl}^{Mech^{n+1}} - \boldsymbol{D}_{ijkl}^{n+1}\right) \tag{4.51}$$

The state variable $\boldsymbol{D}_{ijkl}^{n+1}$ is the fictitious creep stress, being defined as the difference between the purely elastic stress based on instantaneous moduli and the actual stress of the material. It is calculated using Eq.(4.52).

$$\boldsymbol{D}_{ijkl}^{n+1} = \left[\frac{1}{\Delta t} + \frac{1}{\tau_i a_{T_x}^{n+1}}\right]^{-1}\left[\frac{\boldsymbol{D}_{ijkl}^{n}}{\Delta t} + \frac{\tilde{\boldsymbol{C}}_{ijkl}\boldsymbol{\varepsilon}_{kl}^{Mech^{n+1}}}{\tau_i a_{T_x}^{n+1}}\right] \tag{4.52}$$

The CTO is calculated using Eq.(4.53).

$$\frac{\partial\boldsymbol{\sigma}_{ij}^{n+1}}{\partial\Delta\boldsymbol{\varepsilon}_{ab}} = \boldsymbol{C}_{ijab}^{\circ} - \frac{\Delta t}{\Delta t + \tau_i a_{T_x}^{n+1}}\tilde{\boldsymbol{C}}_{ijab} \tag{4.53}$$

In equations Eq.(4.51), (4.52), (4.53) :

- $\boldsymbol{C}_{ijkl}^{\circ}$ : Elastic (glassy) stiffness matrix
- $\boldsymbol{\varepsilon}_{kl}^{Mech^{n+1}}$ : Mechanical strain tensor
- $\tau_i$ : Relaxation time of the $i^{th}$ Maxwell element
- $a_{T_x}^{n+1}$ : Degree of cure - temperature shift factor
- $\Delta t$ : Time increment
- $\tilde{\boldsymbol{C}}_{ijkl}$ : Relaxation stiffness matrix calculated using as input the transient decay of the Prony series Eq.(4.14)

For the calculation of the mechanical strain tensor ($\boldsymbol{\varepsilon}_{kl}^{Mech}$) and elastic stiffness matrix ($\boldsymbol{C}_{ijkl}^{\circ}$) of the material models, the calculation process depicted in Fig. 4.3 with the use of the equations presented in the previous sections is followed. Further information on the implementation of the material models can be found in [30, 111].

Chapter

# 5

# Model Validation

The simulation framework presented in Chapter 4 was used to simulate the experiment of Chapter 3. Therefore, here a comparison between simulation, experimental and the results of an analytical equation for the prediction of the spring-in angle of the specimens is made.

## 5.1 Analytical formula

Radford *et al.* extended the model presented in Section 2.4.1 for the calculation of spring-in angle of angled sections, in order to take into account the CSC of the structure [83]. Therefore, Eq. (5.1) was used as a benchmark of the spring-in angles measured in the experiment.

$$\Delta\theta = \theta \left[ \frac{(CTE_L - CTE_T)\Delta T}{1 + CTE_T \Delta T} + \frac{CSC_L - CSC_T}{1 + CSC_T} \right] \tag{5.1}$$

where $\theta$ is the included angle of the structure, $\Delta\theta$ is the change in included angle, $\Delta T$ is the change in temperature, $CTE_L$, $CSC_L$ and $CTE_T$, $CSC_T$ are the in-plane and through-thickness CTE and CSC, respectively.

Eq. (5.1) assumes that the in-plane properties of the laminate are quasi-isotropic and that the through-thickness properties are uniform throughout the laminate. Eq.

(5.1) takes into account the effect of stacking sequence on the predicted spring-in angle, however, it does not take into account the effect of specimen thickness, corner radius and extrinsic parameters such as tooling effects. Despite its limitation Eq. (5.1) is widely used in the industry and academia, which motivated the use of this formula in this research.

## 5.2 Simulation of the experiment

Depending on the thickness of the specimens, a chemo-mechanical or a sequentially coupled thermo-chemo-mechanical analysis was implemented to model the change of the material properties during the manufacturing process.

According to the work of Chen [78], a thickness threshold of 3 $mm$ was chosen after which a heat transfer analysis should be employed prior to the spring-in analysis in order to identify temperature gradients in the part that lead to significant property gradients affecting its distortion. Parts with a thickness of less than 3 $mm$ are considered to have a homogeneous temperature field, an assumption made to reduce computational cost.

Consequently, for the 8 and 16 ply specimens a chemo-mechanical simulation approach was implemented to calculate the distortion of the parts, since the thickness of the specimens is less than or close to 3 $mm$ (Table 3.6). The temperature used as input in these simulations is assumed to be homogeneous and identical to the temperature measured by the thermocouple placed in the bag (Fig. 5.1). Even though this assumption is not strictly valid, the slow heating and cooling rates suggested by the MRCC contribute to a nearly homogeneous (spatial temperature gradients less than $1°C$) temperature field across the part.

The starting point of the chemo-mechanical simulation is the gelation of the resin as depicted with the red dot in Fig. 5.1. Stresses built up earlier in the curing cycle are assumed to contribute insignificantly to the process induced distortion of the specimens. These stresses are related to the limited chemical contraction of the resin, the thermal expansion of the part and the stresses transmitted to the part from the tool before gelation. The curing history was divided into three steps from the gelation of the resin, one to simulate the heating step to the curing temperature, another step of the isothermal hold of the structure at $180°C$ and a third one for the cool down of the structure to room temperature.

In the case of the 24 ply specimens, a thermo-chemo-mechanical simulation approach was considered as the thickness of the parts is above 3 $mm$ (Table 3.6). The

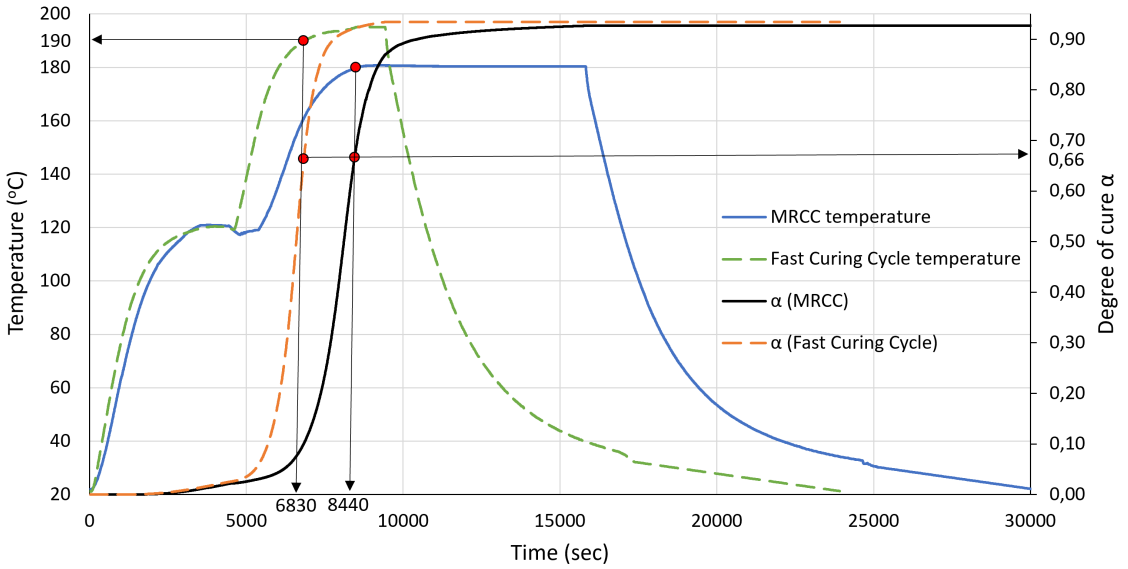


Figure 5.1: The evolution of the degree of cure (Eq.(4.1)) of the two curing cycles is a s-type curve and the red dots depict the gelation of the structure, which is the starting point of the spring-in simulation framework developed. The resin is infused in the preform at 120°$C$ where a slight drop of the laminate temperature is observed.

thermo-chemical analysis depicted in Fig. 4.2 was run first and the resulting temperature field was mapped at each time step to the mechanical analysis for the calculation of the distortion of the structure as depicted in Fig. 4.1. In any case, the temperature field in the chemo-mechanical analysis was introduced as a pre-defined (i.e. not solution dependent) field that exists over the spatial domain of the model. The time increments used in the simulations was 5 *sec* to match the sampling rate of the data recorder of the experiment.

Finally, to simulate the machining operations after demoulding the Model Change functionality of ABAQUS was used in a separate simulation step after the curing cycle was finished. In this step a number of elements were subtracted from the FE mesh of the L-shape specimen representing the area of the specimen which is going to be trimmed (10 *mm* from each side of the part).

To perform this operation prior to the removal step, ABAQUS stores the forces/fluxes that the region to be removed is exerting on the remaining part of the model at the nodes on the boundary between them. These forces are ramped down to zero during the removal step. Therefore, the effect of the removed region on the rest of the model is completely absent only at the end of the removal step. The forces are ramped down gradually to ensure that element removal has a smooth effect on the model. No further element calculations are performed for elements being removed, starting from the beginning of the step in which they are removed.

After the FEA analysis is run the deformed mesh of the part is imported into the GOM Inspect suite. Then, the same process as the one followed for the calculation of the spring-in angle of the manufactured specimens was followed i.e. Gaussian best fit of planes to the flanges of the part and calculation of the spring-in angle based on the angle that the normal vectors of the two planes create (Section 3.3).

### 5.2.1 Mesh

Fig. 5.2 shows the FE mesh for the 8 plies, 16 plies tool-part interaction and 24 plies specimens that was used to simulate the process induced distortion of the L-shape structures. The mesh in the chemo-mechanical analysis consists of C3D8I solid elements, which have incompatible modes to improve their bending behaviour [143]. Each ply is modelled with the use of one element in the thickness direction with the use of three integration points. An element length of approximately 5 $mm$ was chosen in the longitudinal and transverse direction. The corner of the L-shaped structure was discretised using half the element length in the longitudinal direction as the one used for the flanges (2.5 $mm$). The angle of the L-shape parts simulated was exactly 90°.

The biaxial NCF was modeled as two UD plies at the respective orientations by ignoring the stitching of the fabric. Consequently, the total number of integration points of a specimen consisting of UD and NCF in the thickness direction is equal to the number of the resulting plies multiplied by three.

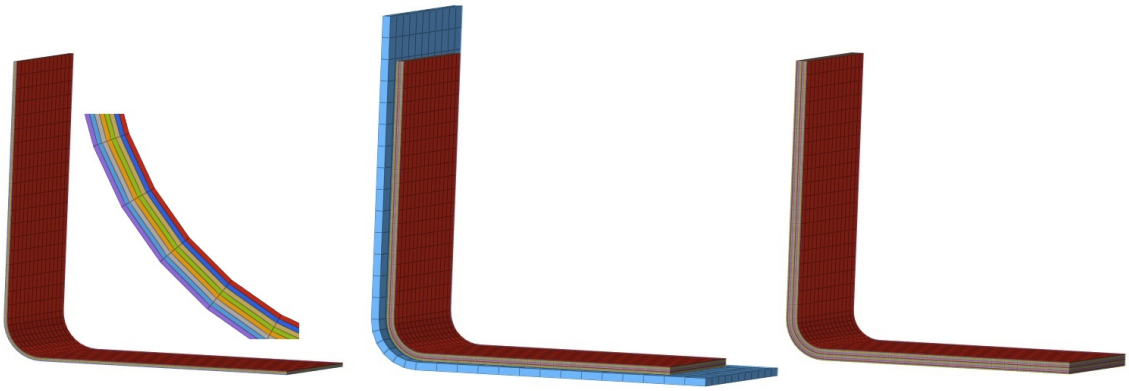

Figure 5.2: The finite element mesh used to model the L-shape structures. Each composite ply is modelled with one element in its thickness direction. From left to right, the 8 plies, 16 plies tool-part interaction and 24 plies mesh.

The number of elements used for the 8, 16 and 24 plies specimens is 5264, 10304 and 15792, respectively. In the tool-part interaction simulation, the tool was modelled with fewer elements compared to the L-shape specimen as shown in Fig. 5.2.

The mesh in the thermal analysis consists of DC3D8 elements which is an 8-node linear heat transfer brick element. Each ply is modelled with the use of one element in the thickness direction and the element size was equal to the one selected for the chemo-mechanical analysis in order to facilitate the mapping process of the temperature field to the spring-in analysis. To account for the ply orientation, the orientation of the elements belonging to a ply was modified accordingly.

## 5.2.2 Boundary Conditions

### 5.2.2.1 Mechanical BCs

Regarding mechanical BCs, "freestanding" and "fixed" BCs were investigated. "Freestanding" BC implies that three nodes are used to suppress rigid body motion of the part during all simulation steps as shown in Fig. 5.3 and Table 5.1. On the other hand, the "fixed" mechanical BC implies that all the translational DoFs of all nodes of the FE mesh are set to zero displacement until the cool down step is over. Then, a demoulding step is added to the simulation in which the fixed mechanical BC is deactivated and three nodes are used to suppress rigid body motion of the part as shown in Fig. 5.3. At this step, the internal stresses of the part are released and the part deforms.

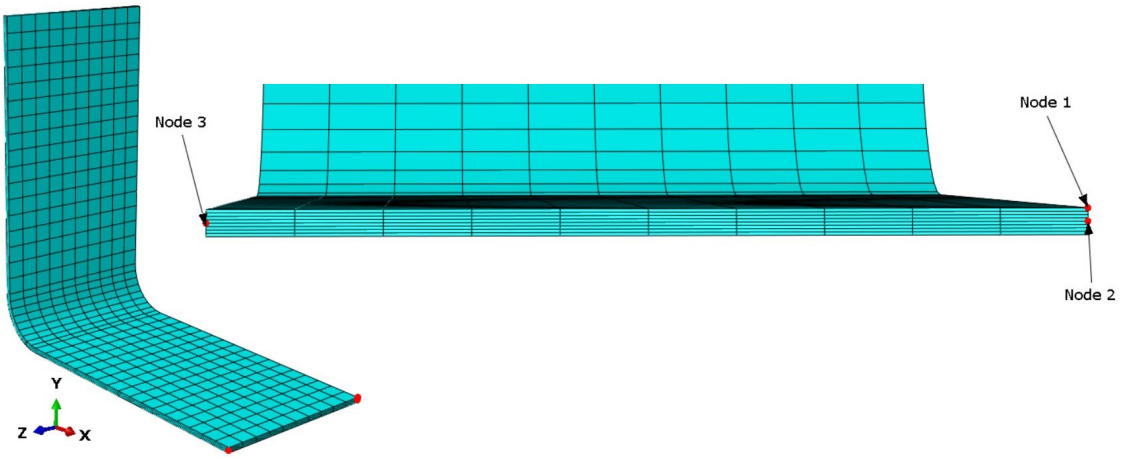


Figure 5.3: The three nodes used to suppress rigid body motion of an 8-ply specimen at the freestanding boundary condition.

Table 5.1: Degrees of freedom constrained per boundary condition type. The nodes numbering refer to Fig. 5.3.

| BC type | Nodes | DOFs constrained |
|---|---|---|
| Freestanding | Node 1 | x |
| | Node 2 | x, y |
| | Node 3 | x, y, z |
| Fixed | All FE nodes | x, y, z |

A more physically representative tool-part interaction approach was also employed to assess its ability to accurately predict the deformed shape of the part. The effect of tool-part interaction was evaluated by modelling the tool and using Coulomb's friction approach to model the stick/slip behaviour and transfer of shear forces at the interfaces. For the tangential directions, an isotropic CoF was used with a shear stress limit of $\tau_{max} = 0.14\ MPa$ after which sliding of the interfaces occurs [46]. Both fixed and cure-dependent CoF in the tangential direction were examined. A typical value for the fixed CoF for modelling the tool-part interaction is $\mu_{fixed} = 0.3$ [46, 54].

The linear function Eq.(5.2) derived from the work of Zeng [57] is adopted, to describe the evolution of the CoF, $\mu(\alpha)$, from the gelation of the structure to cool down. The degree of cure was calculated at every time step of the simulation and was used as input to the contact algorithm in the form of User Defined Field in ABAQUS.

$$\mu(\alpha) = 1.05\alpha - 0.53 \tag{5.2}$$

A hard contact was employed in the normal direction of the tool-part interfaces to prevent the parts penetrating each other. At the faces of the composite part in contact with the vacuum bag, a pressure field equal to atmospheric pressure was applied. Finally, three nodes are used to suppress rigid body motion of the tool during the curing cycle, similar to those shown in Fig. 5.3 for the composite part.

#### 5.2.2.2 Thermal BCs

The tool and the composite part inside the oven are both heated or cooled through convection of the air. The convective boundary condition can be formulated as:

$$(\boldsymbol{k_c} \cdot \nabla T) \cdot \vec{\boldsymbol{n}} = h(T_s - T_{f_\infty}) \tag{5.3}$$

where $\vec{\boldsymbol{n}}$ is the unit vector normal to the surface, $h$ is the heat transfer coefficient, $T_s$ is the surface temperature of the part and $T_{f_\infty}$ is the oven air temperature.

In the thermo-chemical analysis employed in this study, a heat transfer coefficient was used to simulate the heat flow from the vacuum bag to the composite part at the faces of the part in contact with the bagging set-up (peel ply, resin flow mesh, vacuum bag) and another one to simulate the heat flow to the composite part from the tool surface. To avoid costly CFD simulations or indirect measurements of the heat

transfer coefficients, the values used in the simulations were approximated. As input to the simulations, values of the heat transfer coefficients as measured by Premium AEROTEC GmbH in one of their ovens, for manufacturing U-shaped composite aerospace frames on an INVAR tool were used [144]. The bagging materials (vacuum bag, resin flow mesh, peel ply fabric) used in this study are similar to the bagging set up of the measurement. Even though identical conditions cannot be replicated as the oven and geometry of tools differ, it was assumed in this study that $h_{bag} = 8\frac{W}{m^2K}$ represents the heat flow from the bag to the composite part and $h_{mould} = 17\frac{W}{m^2K}$ the heat flow from the tool to the part. Therefore, the part starts to cure from the tool side and the curing front advances towards the side of the bag. The oven air temperature $T_{f_\infty}$ is set equal to the temperature recorded by the thermocouple placed on top of the vacuum bag.

## 5.3 Simulation and analytical results

Tables 5.2-5.5 contain simulation and analytical (Eq. (5.1)) results. As shown in Tables 5.2,5.3,5.5, Eq. (5.1) cannot take into account the effect of thickness on the predicted spring-in angle of the part. It predicts the same spring-in angle for the BS and BF laminates irrespective of the number of plies.

Table 5.2: Predicted spring-in angle (degrees) of the 8 plies specimens manufactured from the INVAR tool with the MRCC and "Fast" curing cycle.

| Laminate | | $BS_8$ | | $BF_8$ | | $AS_8$ | |
|---|---|---|---|---|---|---|---|
| Curing cycle | | MRCC | "Fast" | MRCC | "Fast" | MRCC | "Fast" |
| CHILE | Free | 1.43 | 1.48 | 1.42 | 1.47 | 1.45 | 1.51 |
| | Fixed | 1.09 | 1.11 | 1.08 | 1.10 | 1.14 | 1.16 |
| | Tool | 1.33 | 1.33 | 1.24 | 1.29 | 1.25 | 1.29 |
| Viscoel. | Free | 1.28 | 1.31 | 1.29 | 1.32 | 1.44 | 1.51 |
| | Fixed | 1.07 | 1.05 | 1.06 | 1.05 | 1.08 | 1.09 |
| | Tool | 1.26 | 1.30 | 1.10 | 1.18 | 1.08 | 1.15 |
| Radford Eq. (5.1) | | 1.40 | 1.44 | 1.40 | 1.44 | 1.39 | 1.44 |

The evolution of the degree of cure $\alpha$ of the resin for the MRCC and "Fast" curing cycles is presented in Fig. 5.1. It can be seen that the gelation of the structure is reached earlier compared to the MRCC and the final degree of cure is approximately the same for the two curing cycles and equal to $\alpha_{MRCC} = 0.926$ and $\alpha_{Fast} = 0.934$, respectively.

The evolution of the matrix CTE along with $T^*$ and $T_g$ calculated according to Eq.(4.3), (4.4) and (4.2) respectively is shown in Fig. 5.4. As shown the $T_g$ of the

Table 5.3: Predicted spring-in angle (degrees) of the 16 plies specimens manufactured with the MRCC and INVAR tool.

| Laminate | | $BS_{16}$ | $BC_{16}$ | $SK_{16}$ | $FR_{16}$ | $ST_{16}$ | $SP_{16}$ | $AS_{16}$ | $UB_{16}$ |
|---|---|---|---|---|---|---|---|---|---|
| CHILE | Free | 1.43 | 1.43 | 1.44 | 1.44 | 1.42 | 1.42 | 1.70 | 1.33 |
| | Fixed | 1.09 | 1.09 | 1.11 | 1.12 | 1.09 | 1.09 | 1.49 | 0.97 |
| | Tool | 1.25 | 1.19 | 1.21 | 1.27 | 1.25 | 1.11 | 1.52 | 1.12 |
| Viscoel. | Free | 1.29 | 1.30 | 1.33 | 1.35 | 1.29 | 1.29 | 1.54 | 1.28 |
| | Fixed | 1.07 | 1.03 | 1.04 | 1.10 | 1.07 | 1.02 | 1.41 | 0.92 |
| | Tool | 1.13 | 1.04 | 1.06 | 1.11 | 1.11 | 0.95 | 1.22 | 1.08 |
| Radford Eq. (5.1) | | 1.40 | 1.40 | 1.46 | 1.44 | 1.48 | 1.40 | 1.34 | 1.30 |

Table 5.4: Predicted spring-in angle (degrees) of the laminate groups manufactured also with the steel and aluminium tools. The parts were manufactured with the MRCC.

| Laminate | CHILE | | Viscoel. | |
|---|---|---|---|---|
| Tool | Steel | Aluminium | Steel | Aluminium |
| $BS_{16}$ | 1.25 | 1.25 | 1.13 | 1.13 |
| $ST_{16}$ | 1.25 | 1.25 | 1.11 | 1.11 |
| $SP_{16}$ | 1.12 | 1.11 | 0.95 | 0.95 |
| $AS_8$ | 1.25 | 1.25 | 1.08 | 1.08 |

Table 5.5: Predicted spring-in angle (degrees) of the 24 plies specimens manufactured with the MRCC and INVAR tool.

| Laminate | | $BS_{24}$ | $BC_{24}$ |
|---|---|---|---|
| CHILE | Free | 1.35 | 1.35 |
| | Fixed | 1.05 | 1.05 |
| | Tool | 1.17 | 1.08 |
| Viscoel. | Free | 1.22 | 1.22 |
| | Fixed | 0.99 | 0.98 |
| | Tool | 0.99 | 0.93 |
| Radford Eq. (5.1) | | 1.40 | 1.40 |

matrix at the end of the curing cycle is around $208°C$ and the CTE of the matrix is one third of the value at the beginning of the curing cycle.

The temperature, cure and the combined cure-temperature shift factor of the resin from the gelation to demoulding the structure calculated with the use of Eq.(4.10-4.12) respectively are presented in Fig. 5.5 for the MRCC and "Fast" curing cycle. As depicted for both curing cycles the curves of the shift factors follows the curing cycle profile.

Since the reference temperature in the WLF equation is chosen to be the glass transition temperature of the specimens investigated in the DMA, the degree of cure of which was measured to be 0.94 and considered as the reference degree of cure in

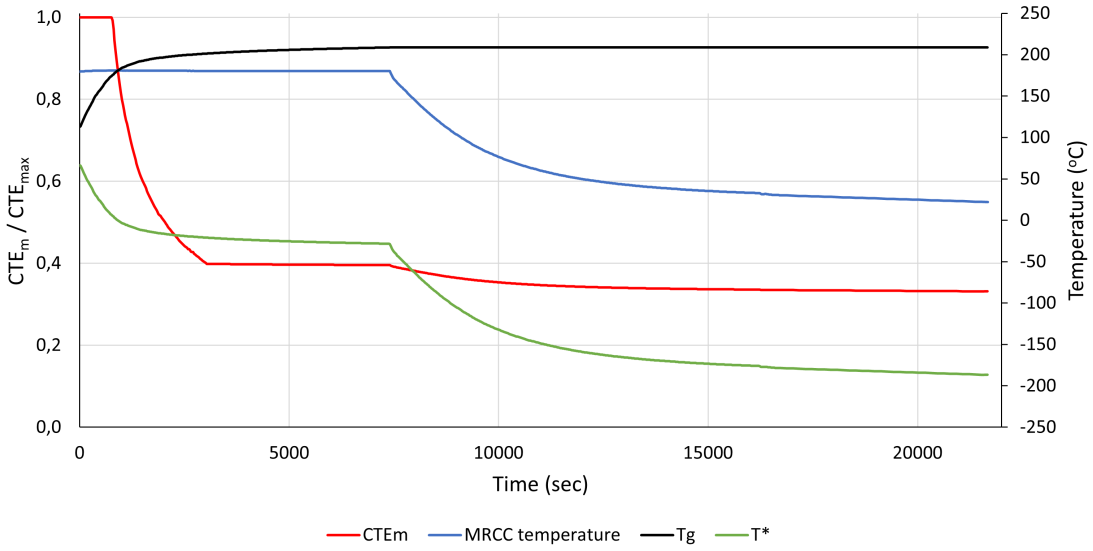


Figure 5.4: Evolution of matrix CTE along with $T^*$ and $T_g$ for the MRCC from gelation to cool down.

the modeling ($T_{ref} = T_g(a_{ref}) = T_g(0.94) = 214.91°C$) the temperature shift factor is positive during the curing cycles (as $T_{cycle} \leq 214.91°C$) as depicted in Fig. 5.5, in contrast to the cure shift factor which is negative for both cycles (as $\alpha_{cycle} \leq 0.94$). The combined cure-temperature shift factor is the sum of the temperature and cure shift factors.

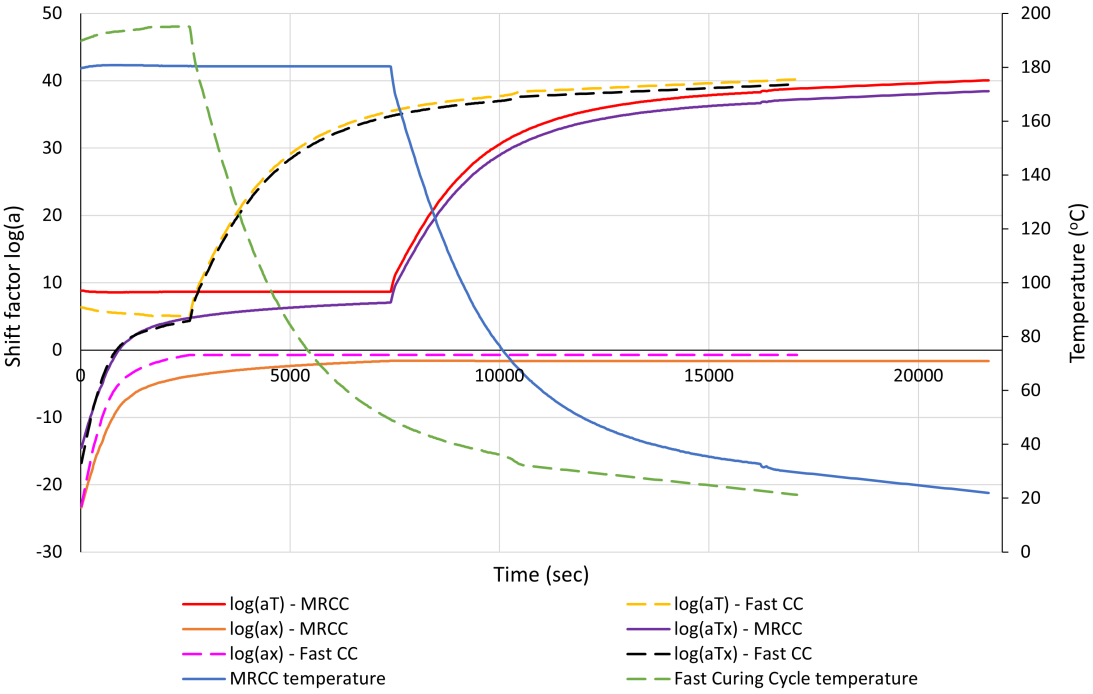


Figure 5.5: The temperature, cure and the combined cure-temperature shift factor from gelation to demoulding the structure.

Fig. 5.6 shows the evolution of the Young's modulus of the resin, according to the CHILE and the viscoelastic material characterisation for the two curing cycles investigated. The "Fast" curing cycle produces a part with higher modulus compare to the MRCC which can be attributed to the slightly higher final degree of cure that the part attains and the earlier gelation of the structure as depicted in Fig. 5.1. Furthermore, the instantaneous modulus predicted by the viscoelastic model is lower compared to the CHILE model for both curing cycles investigated which is due to different modelling approaches used. In the case of the CHILE model, a modified CHILE equation was fitted to DMA data whereas in the linear viscoelastic model a number of Maxwell elements were fitted to DMA data. The resulting shear modulus of the resin calculated according to Eq. (4.16) is shown in Fig. 5.7. As depicted the evolution of $G_m$ is similar to $E_m$ but its magnitude is approximately one third of it.

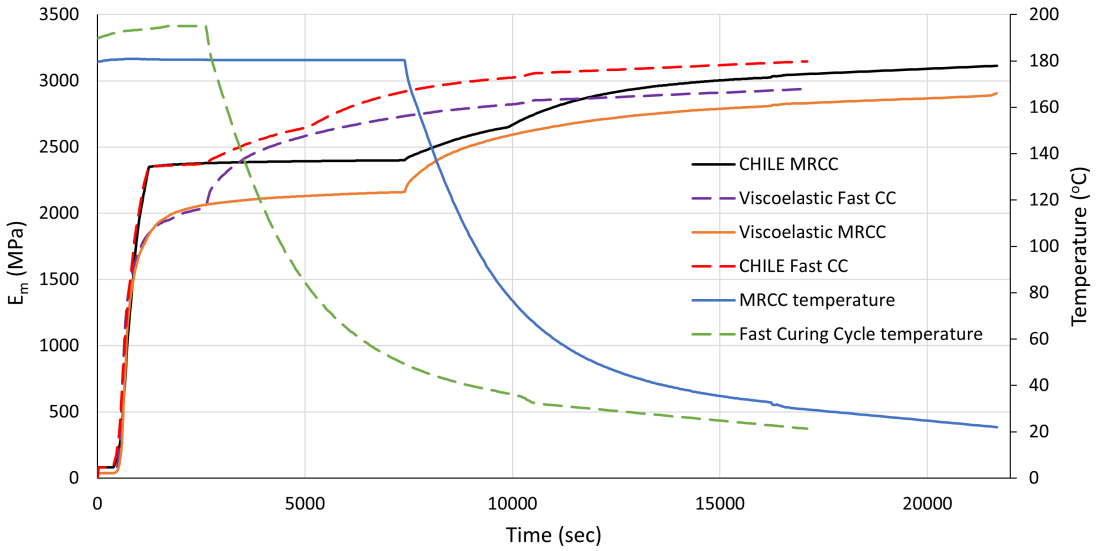


Figure 5.6: Young's modulus development of the resin from the gelation to demoulding the structure, according to the CHILE and the viscoelastic material characterisation for the MRCC and "Fast" curing cycle.

Fig. 5.8 presents the evolution of the fibre volume fraction of the specimens during the curing cycle. As depicted for both curing cycles the curves of the fibre volume fraction follows the curing cycle profile. A small reduction of the fibre volume fraction of the "Fast" curing cycle after its increase due to chemical contraction, is attributed to the slight increase of the temperature of the cycle to reach $195°C$. The fibre volume fraction is reduced in this segment because thermal expansion of the material takes place. In addition, Fig. 5.9 depicts the composite density calculated according to Eq.(4.29). Due to resin chemical shrinkage the composite density increases until the end of the dwell and then it further increases due to thermal contraction until room temperature is reached. Fig. 5.10 depicts the specific

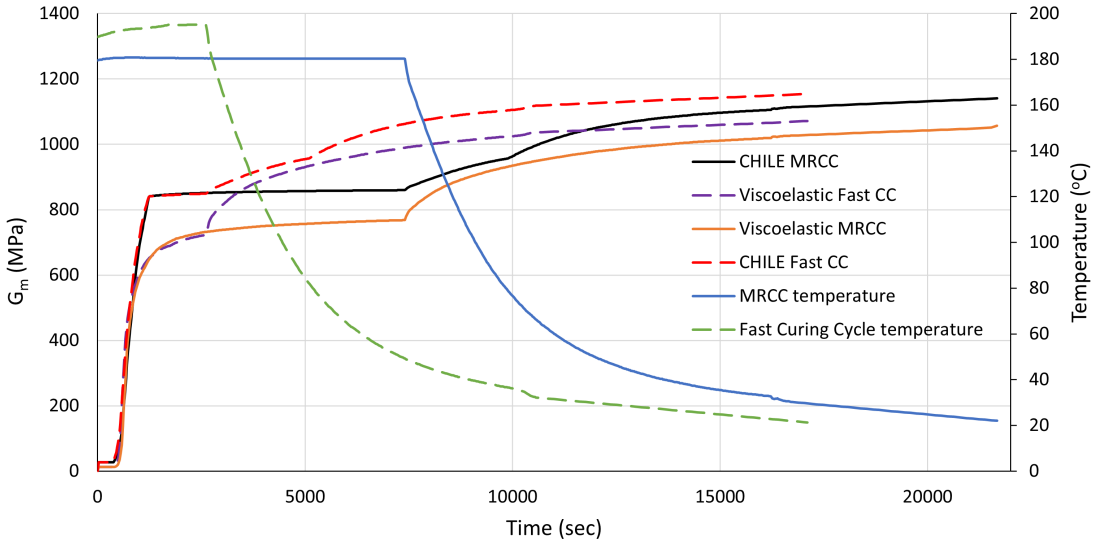


Figure 5.7: Shear modulus development of the resin from the gelation to demoulding the structure, according to the CHILE and the viscoelastic material characterisation for the MRCC and "Fast" curing cycle.

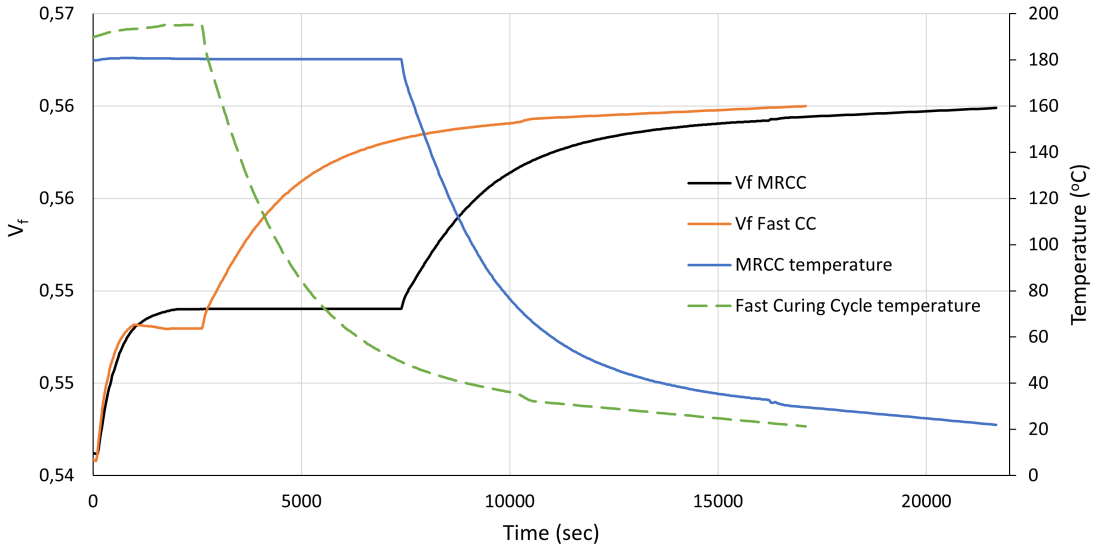


Figure 5.8: The fibre volume fraction for the MRCC and "Fast" curing cycle. It was assumed the final part has $V_f = 0.56$.

heat capacity of the resin, fibre and composite calculated according to Eq.(4.19), Eq.(4.22) and Eq.(4.30) respectively. The specific heat capacity sharply decreases shortly after gelation of the resin and its transformation from the liquid to solid state.

The conductivity of the resin, fibre and composite calculated according to Eq.(4.17), Eq.(4.21) and Eq.(4.31) respectively, are shown in Fig. 5.11. The conductivity of the fibre in the longitudinal direction is approximately three times greater than in

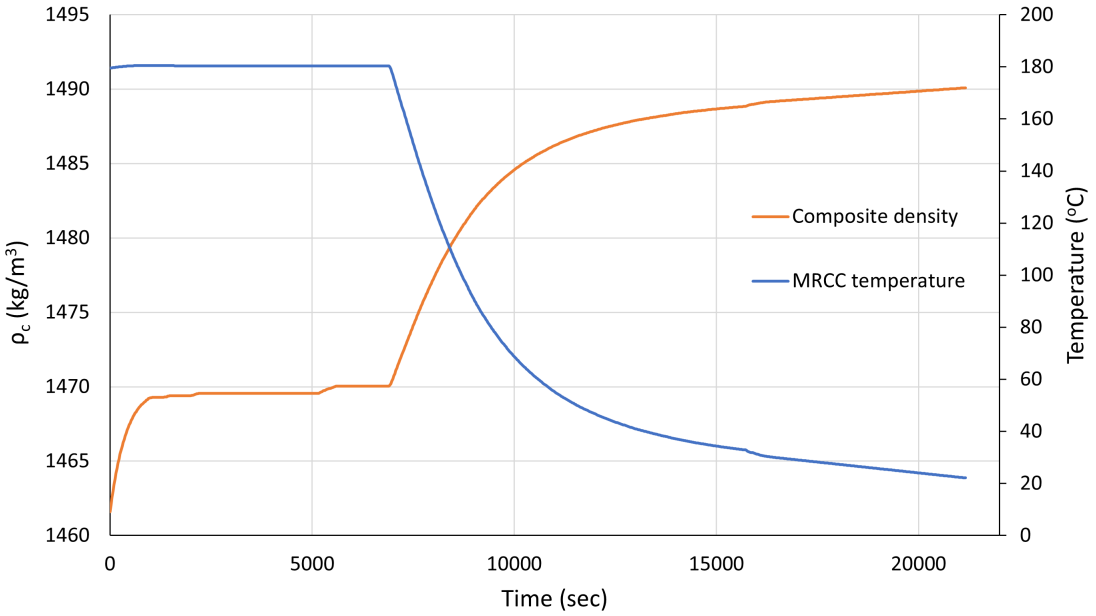


Figure 5.9: The density of the composite from the gelation to demoulding the structure.

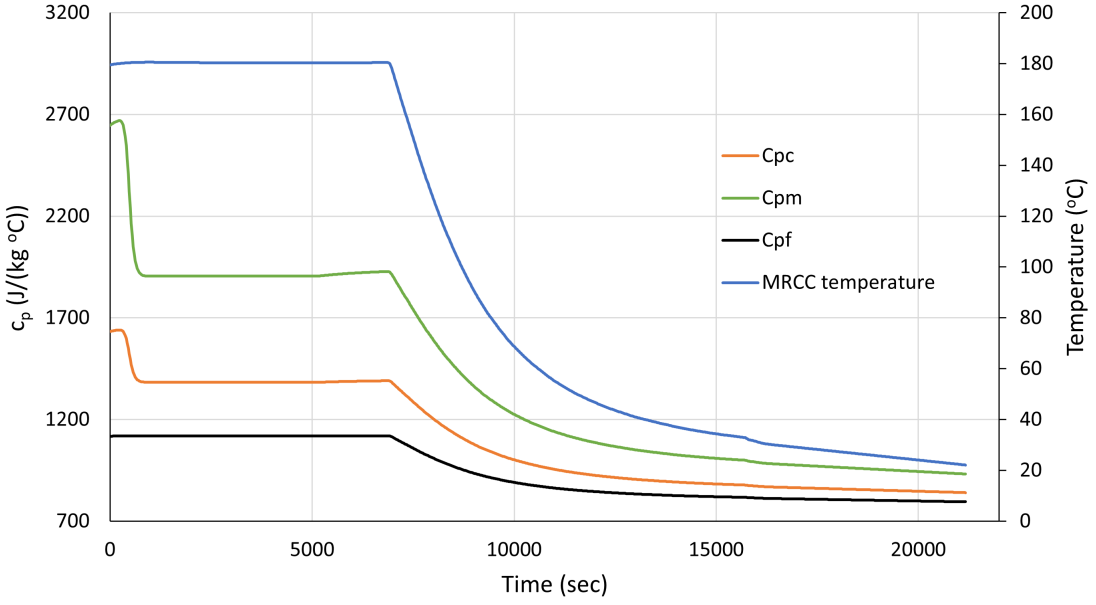


Figure 5.10: The specific heat capacity of the resin, fibre and composite from gelation to demoulding the structure.

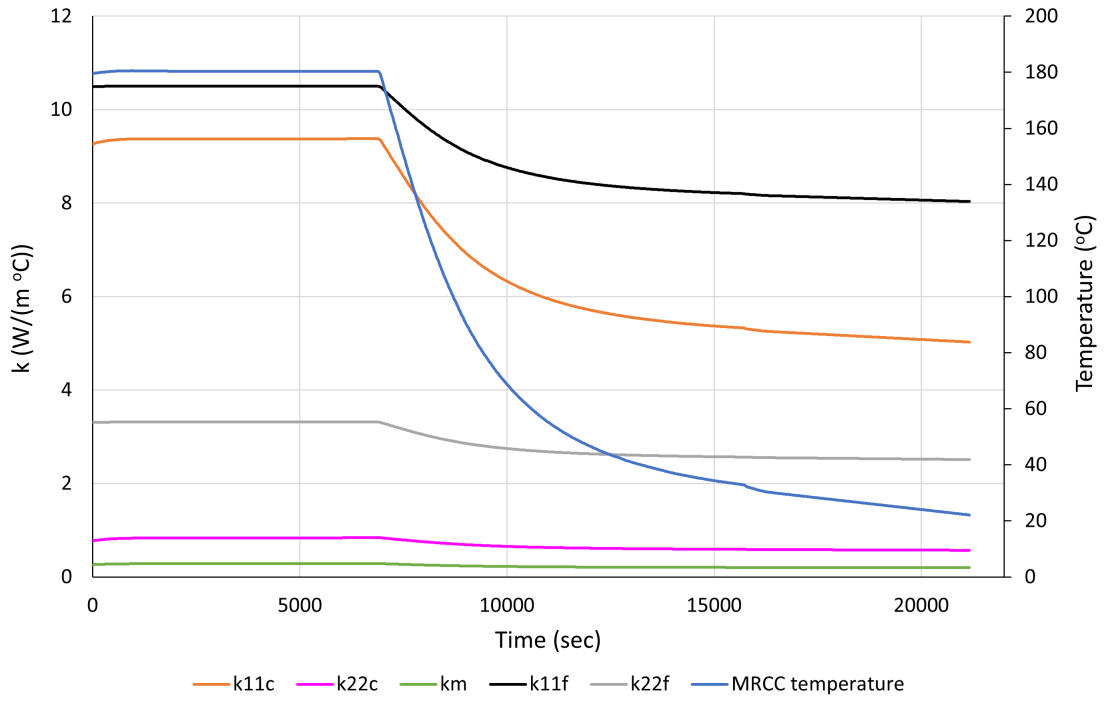


Figure 5.11: The conductivity of the resin, fibre and composite from gelation to demoulding the structure.

transverse. The matrix conductivity is an order of magnitude lower than the fibre conductivity. As a result, the effective conductivity of the composite is between the bounds set by the fibre and matrix values. Since the property is a function of temperature, a reduction of the conductivity is observed during cool down.

The distortion field of the first ply (from the tool side) of the $BS_{16}$ laminate design along the x-axis after the trimming step, as predicted by the CHILE and viscoelastic model with the use of the "freestanding" BC is depicted in Fig. 5.12. The distortion field is scaled by a factor of five in order for the distortions to be visible. The undeformed shape of the part is shown with the black mesh lines in the background. The distortion field for this laminate group is uniform and there is no significant twist or warpage of the part, as expected since its laminate design is symmetric, balanced and quasi-isotropic. From the simulation it was also found that the trimming process releases residual stresses and the part springs back to its nominal shape to some extent (depending on the part $0.01° - 0.05°$).

Fig. 5.13 shows the first layer (OML side) of the $BS_8$ laminate group after trimming the specimen. The material orientations of the layer are presented at various locations across the ply. A node was selected in the middle of the top flange to monitor the development of residual stresses during the curing cycle.

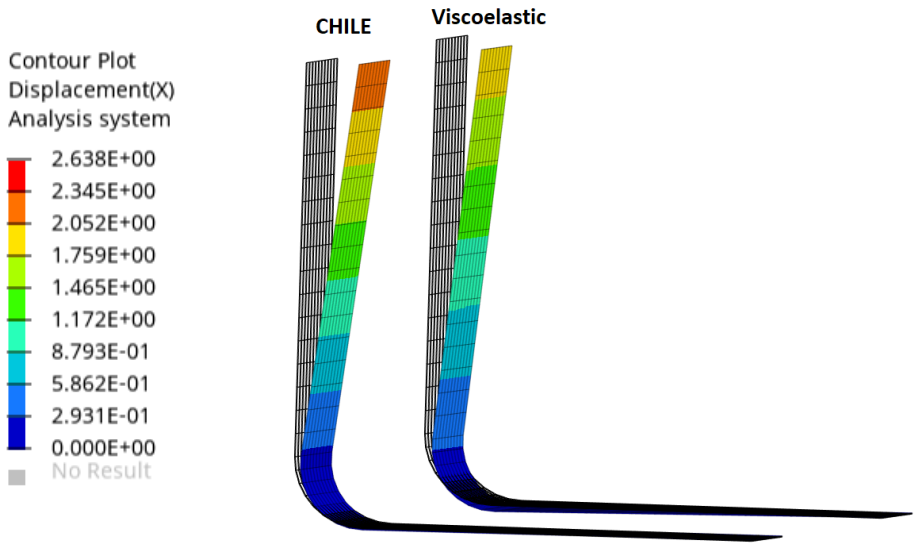


Figure 5.12: Distortion field of the first ply of the $BS_{16}$ group along the x-axis (Fig. 5.3) in $mm$ as predicted by the CHILE (left) and viscoelastic (right) model with the use of the "freestanding" BC after the trimming step. The distortion field is multiplied by a factor of five and the undeformed shape of the part is shown with the black mesh lines.

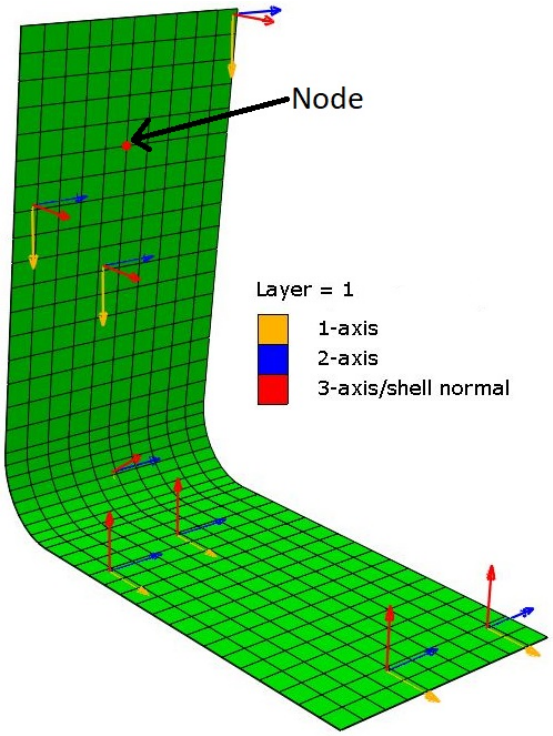


Figure 5.13: Material orientations of the specimens.

The residual stresses predicted by the CHILE model for the "freestanding" and "fixed" BCs during the MRCC are shown in Fig. 5.14. As shown the "freestanding" BC predicts tensile $\sigma_{11}$ stresses (having negative sign due to the material orientation shown in Fig. 5.13) from gelation to cool down. The $\sigma_{22}$ stresses are positive throughout the curing cycle and the same stresses are applied to the last ply of the part (not shown here), while the $\sigma_{33}$ stresses are zero. In contrast, the "fixed" BC predicts a more complex stress state in the part. The ply is subjected to large compressive $\sigma_{11}$ stresses, and positive $\sigma_{22}$ and $\sigma_{33}$ stresses. At the demoulding step the stresses are sharply released. The $\sigma_{11}$ become tensile and the $\sigma_{33}$ zero as the part springs-in. However, at the end of the curing cycle the residual stresses predicted by the "fixed" BC are greater in magnitude compared to those predicted by the "freestanding" BC. This is related to the fact that the "fixed" BC predicts lower spring-in angle compared to the "freestanding" BC. Greater residual stresses in magnitude predicted by the "fixed" BC were also found in [119].

Fig. 5.15 shows the distribution of $\sigma_{11}$ stresses in the first layer (OML side) at the end of the MRCC of the $BS_8$ and $BS_{24}$ laminate predicted by the CHILE model with the "freestanding" BC. Even though the two specimens have a great difference in their bending stiffness $D_{11}$ as shown in Fig. 3.32, the predicted $\sigma_{11}$ stresses are approximately the same. The predicted stresses are tensile for both laminate groups, given the material orientation shown in Fig. 5.13.

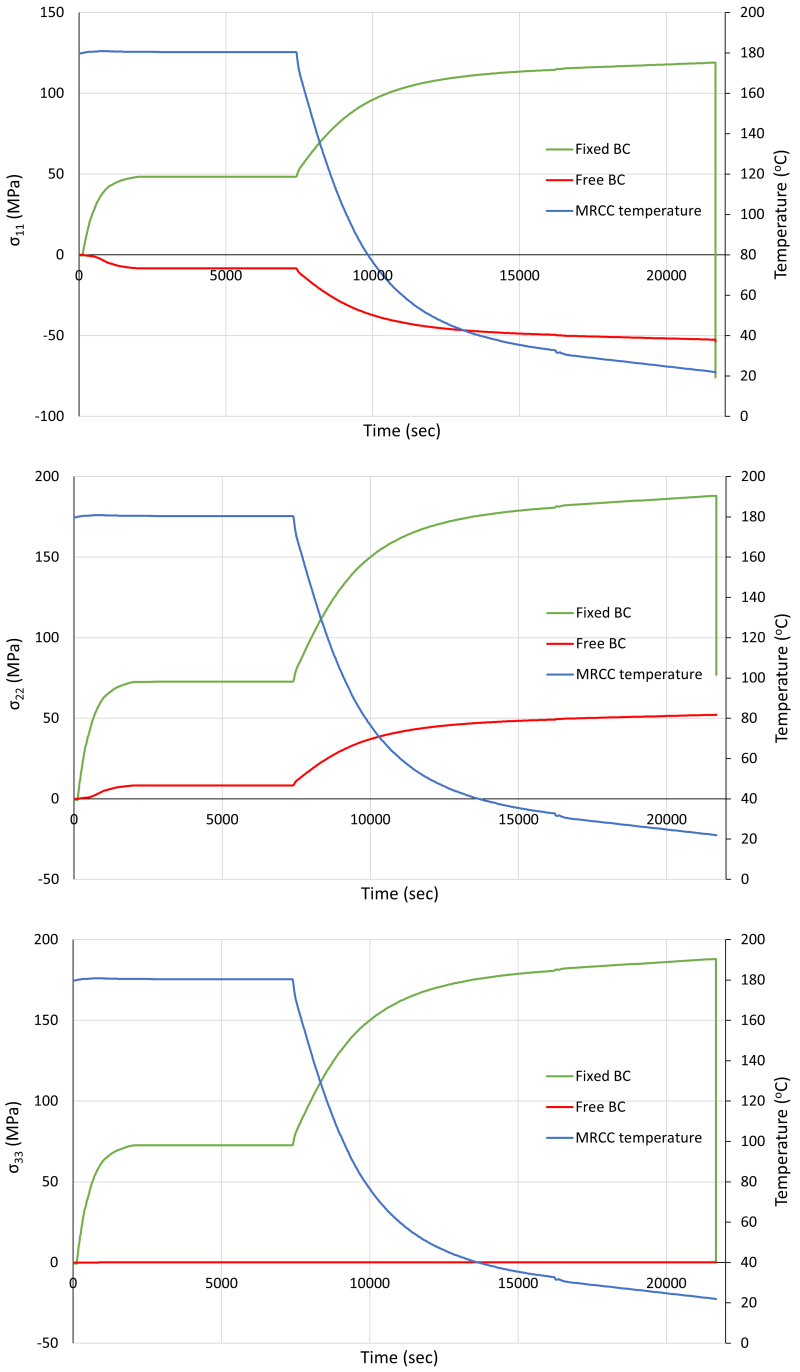


Figure 5.14: Development of residual stresses in the first layer of the $BS_8$ specimen during the MRCC according to the CHILE model.

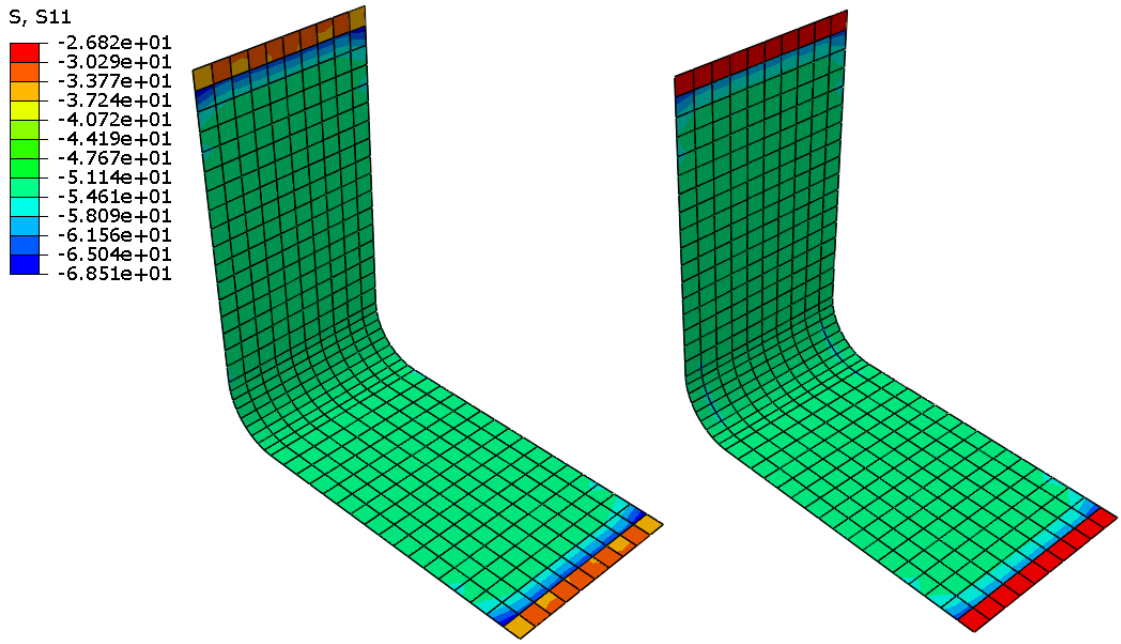


Figure 5.15: Residual stresses $\sigma_{11}$ $(MPa)$ in the first layer (OML side) at the end of the MRCC predicted by the CHILE model with the "freestanding" BC. Left: $BS_8$ Right: $BS_{24}$ laminate group.

## 5.4 Comparison of results

Figs. 5.16-5.19 depict a comparison between experimental results (specimen 1,2 and 3) and the predicted spring-in angle with the use of Eq. (5.1) and the CHILE and viscoelastic material model in relation to the three BCs investigated ("freestanding", "fixed" and tool-part interaction). The results refer to the spring-in angle of the specimens in degrees after demoulding. For the comparison the results acquired from the $3D$ scanner were used for the 8 plies laminates and the CMM results for the rest laminates.

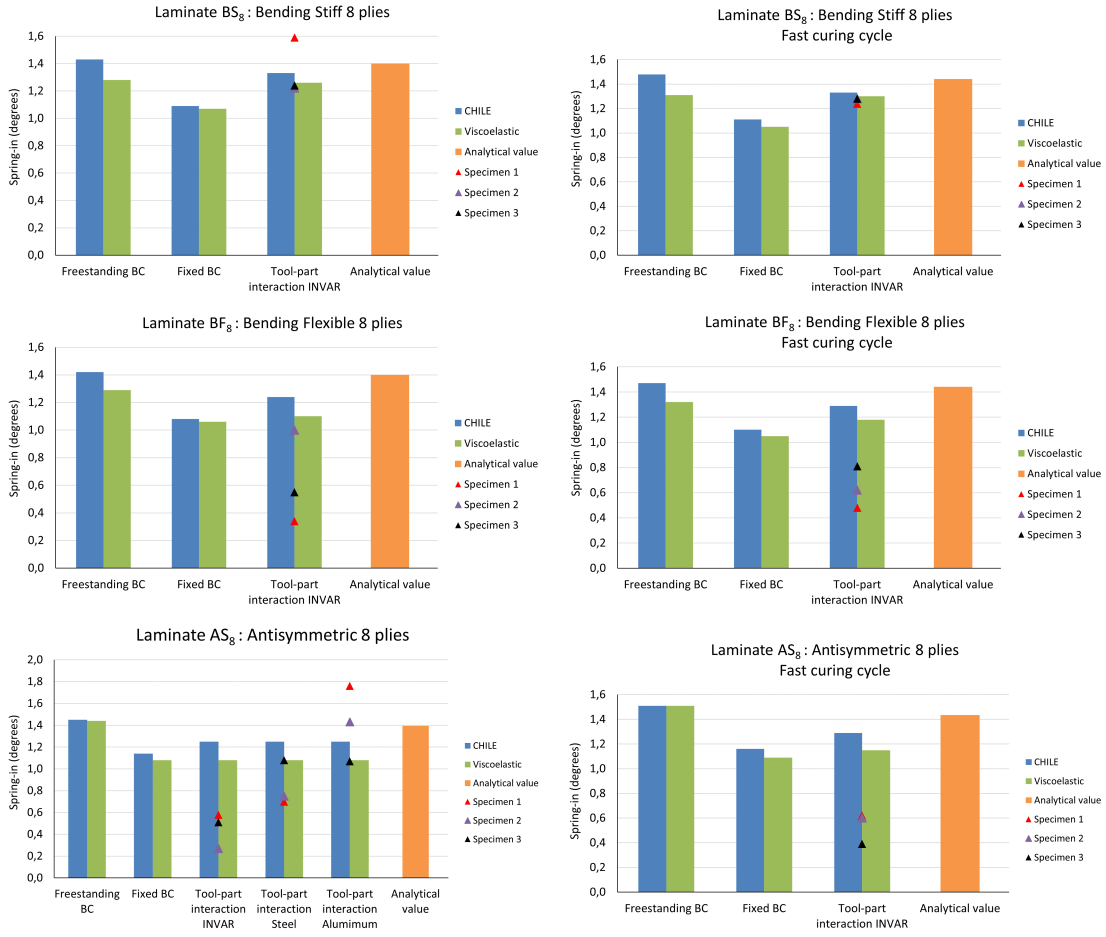


Figure 5.16: Experimentally measured (specimen 1-3) and predicted spring-in angle of the 8 plies specimens.

### 5.4.1 Effect of the Boundary Conditions (BCs)

Regarding the ability of the various BCs to predict the deformed shape of the part, it was found for the CHILE model, that the agreement of the tool-part interaction simulation to the average spring-in angle is the best for 7 out of 16 cases presented in Fig. 5.16-5.19 while for the rest cases the "fixed" BC has the best agreement with the experimental data. The "freestanding" BC proved to overestimate the spring-in

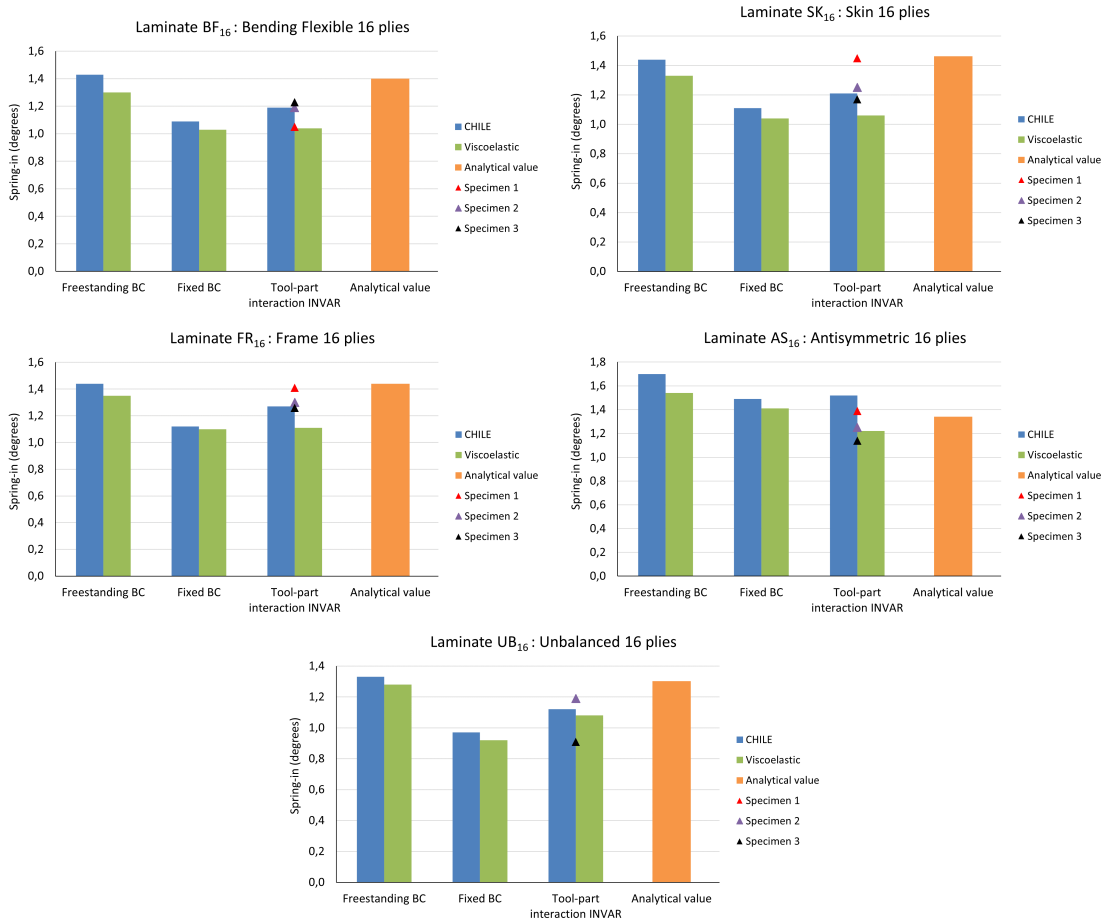


Figure 5.17: Experimentally measured (specimen 1-3) and predicted spring-in angle of the 16 plies specimens manufactured with the INVAR tool and MRCC.

angle of all the parts with the use of the CHILE material model. Concerning the viscoelastic material model each of the "fixed" BC and tool-part interaction simulation predict more accurately the average spring-in angle of 6 out of 16 cases investigated, while for the rest four cases the "freestanding" BC is the most accurate one.

Furthermore, for most of the cases the values for the tool-part interaction prediction lie between the "fixed" and "freestanding" BC cases. The "fixed" BC can be regarded as the case where the part is totally constrained by the tool which does not change its dimensions during the cycle. Therefore, the minimum spring-in should be expected from this case. On the contrary, at the "freestanding" BC the part can expand and contract freely and this case accounts for the upper limit of the expected distortions. This was also observed by Svanberg, who concluded that the most accurate BC to be employed is the tool-part interaction [21]. Moreover, it was found that the dependence of the CoF on degree of cure does not affect the simulation results. A number of cases were also run having a fixed CoF $\mu = 0.3$ and the results were

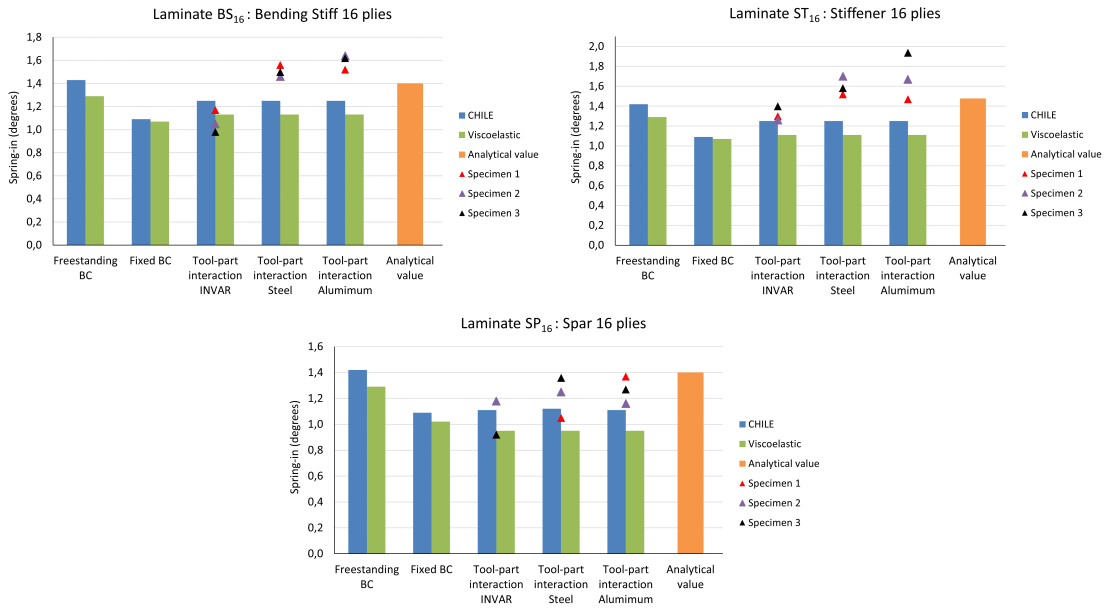


Figure 5.18: Experimentally measured (specimen 1-3) and predicted spring-in angle of the 16 plies specimens manufactured with the INVAR, steel and aluminium tools.

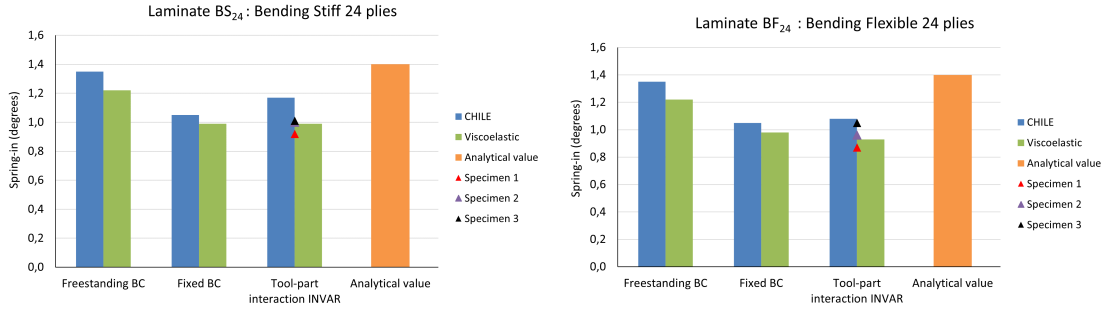


Figure 5.19: Experimentally measured (specimen 1-3) and predicted spring-in angle of the 24 plies specimens manufactured.

almost identical to the tool-part simulations employing Eq.(5.2). Thus, it can be assumed that the CoF is constant during the analysis without reducing simulation accuracy [46, 54].

However, as depicted in Fig. 5.18 and Table 5.4 the tool part-simulation employed here cannot capture the effect of the tool material on spring-in sufficiently for the case of the steel and aluminium tool. It is believed, this is due to the fact that the welding of the tools (position of the weldings and welding material) was not included in the modeling. The weldings affect the distortion of the tool during the curing cycle as they induce inhomogeneous thermal strains to the bent plate, which effect becomes significant when the CTE of the tool is large as in the case of the steel and aluminium tool.

### 5.4.2 Effect of the material models

Comparing the two material models for a given laminate design regarding their ability to predict the deformed shape of the part, the viscoelastic model is the most accurate as with the right combination of BC its prediction is closer to the average spring-in angle measured for most of the cases studied (14 out of 16). Regardless of the laminate design the viscoelastic model is the most accurate material model when the freestanding BC (in all cases studied) and the tool-part interaction (11 out of 16) is employed. Similarly, when the fixed BC is used, the viscoelastic model predicts more accurately the majority of the cases investigated. Overall it can be stated, that the CHILE material model overestimates the spring-in angle in the majority of the cases studied, which is in agreement with the work presented in the literature [104, 145].

As depicted in Fig. 5.16-5.19 the viscoelastic material model predicts a lower spring-in angle compared to the CHILE material model for the same BCs. This can be attributed to the difference in the instantaneous modulus of the two material models as presented in Fig. 5.6 and to the inability of the CHILE material model to account for the time dependent factors, such as stress relaxation, that affect the distortion of the parts from gelation of the structure to cool down.

However, the computational time required by the viscoelastic material model is approximately two times greater than the CHILE material model mainly because of the large number of small time increments required to complete the simulations. In addition, the computational time is increased by the increased number of state variables that have to be read from the memory, updated by the material constitutive equation and stored back in memory at every time increment. The total CPU time of the 24 plies specimens is presented in Table 5.2. The total CPU time on multi-processor machines refers to the sum of CPU time consumed by all of the CPUs utilized by the computer program. The simulations were run in Intel Xeon Gold 6138 2.0GHz CPUs with the use of 24 CPUs.

Table 5.6: Total CPU time (hours) of the 24 plies specimens.

| Laminate | | $BS_{24}$ | $BC_{24}$ |
|---|---|---|---|
| CHILE | Free | 16.99 | 17.75 |
| | Fixed | 15.64 | 15.63 |
| | Tool | 35.88 | 36.73 |
| Viscoel. | Free | 41.57 | 41.43 |
| | Fixed | 35.25 | 36.66 |
| | Tool | 59.23 | 61.03 |

Furthermore, it was found that the result of Eq. (5.1) is greater than the average

spring-in angle for most of the cases investigated and its result is close to the prediction of the CHILE material model with the use of the "freestanding" BC. This is expected as Eq. (5.1) cannot take into account the effect of extrinsic parameters on PID [21, 83].

### 5.4.3 Effect of the curing cycle

Both material models for the majority of the BCs investigated and Eq. (5.1) predict slightly higher spring-in angle for the "Fast" curing cycle compared to the MRCC (Table 5.2). This is expected when considering Eq. (5.1) and its dependence on $\Delta T$, as a greater difference of the curing temperature to room temperature will increase the induced spring-in angle (as $CTE_T$ is small). Therefore taking into account the findings of Section 3.4.3, it can be concluded that the "Fast" curing cycle which has an elevated curing temperature compared to the MRCC ($195°C$ vs. $180°C$) induces higher spring-in angle to the parts.

Moreover, by employing a heat transfer analysis prior to the spring-in analysis it was found for the 24 plies laminates that the non-uniform temperature field mapped to the spring-in analysis (Fig. 4.1) increases the agreement of the predicted spring-in angle in the range of 0.04° to 0.08° compared to the assumption of a homogeneous temperature field across the part. The greatest difference of temperature across the part predicted by the heat transfer analysis for the MRCC is below $1°C$, which is expected due to low heating and cool down rates of the MRCC. However, the impact of employing a heat transfer analysis prior to the spring-in analysis would be greater for thicker parts (spar, wing root etc.) where the exothermic heat reaction generated by the resin is significant and for parts manufactured by curing cycles with high heating and cool down rates ($> 3°C$).

## 5.5 Potential sources of error

The deviation of the simulation results from the experimental measurements can be attributed both to the experimental uncertainties presented in Section 3.5 and to the modeling assumptions made to simulate the experiment.

Regarding the modeling assumptions, the simulation framework developed was applied from the gelation of the structure. Therefore, fabric compaction, permeability and resin flow were not considered in the modelling approach. This leads to the assumption of homogeneous fibre volume fraction and void content in the part during the cure. However, the distribution of the resin in the part at the end

of the infusion process is inhomogeneous to some extent depending among other factors on the local part radius, stacking sequence, positioning of the resin flow medium across the part, fibre bridging, wrinkling and reorientation etc. [13]. These factors cause resin rich and resin starved areas resulting in property gradients in the consolidated laminate affecting PID and residual stresses. While the assumption of stress-free laminate having homogeneous fibre volume fraction before the gelation of the structure ($\alpha = 0.66$) reduces the complexity of the simulation making it also faster to run, it also reduces its accuracy as a small amount of residual stresses might also be developed before that point, slightly affecting the distortion of the structure.

In the absence of specific material data at the application of the simulation framework, material constants published in the literature were used. The Poisson's coefficients, the shear modulus and transverse modulus of AS4 fibre were used as shown in Table 4.1. This might impair the accuracy of the simulation and be responsible for some of the discrepancy between the calculations and the experiment, the exact magnitude of which is not known but is considered small (Appendix B).

Additionally, to calculate the conductivity of the EPIKOTE$^{TM}$ System 600 at every time increment the material constants of the EPON 862/EPIKURE 3300 epoxy system were used. The two resin systems should have approximately the same thermal conductivity in the liquid state. However, the thermal conductivity of the two systems increasingly deviates as the degree of cure increases due to the difference in the crosslinking of the two systems, which is represented by the different recommended cure cycles of the two systems (2 hours at $180°C$ for the EPIKOTE$^{TM}$ System 600, 90 *min* at $82°C$ + 90 *min* at $150°C$ for the EPON 862/EPIKURE 3300 epoxy system). In addition, the material constants of the thermal conductivity and specific heat capacity of AS4 fibre were used.

Nevertheless, the effect of using these material constants in the heat transfer simulation is considered to be small. As was observed in the experiment and in the simulation the difference in the spring-in angle of the specimens manufactured with the MRCC and "Fast" curing cycle is small, despite the fact that these curing cycles were substantially different. Consequently, it is postulated that a difference in the conductivity would result in a temperature field difference in the part which would not substantially affect the spring-in angle of the specimens.

Also, the effective properties of the lamina were calculated with a micromechanics model having as input fibre and resin properties and were not experimentally measured. As shown by Vignoli *et al.* the error of the micromechanical models

compared to the experimentally measured values is larger for the matrix dominated properties (more than 10% for $E_{2c}, G_{12c}, G_{23c}, v_{12c}$) than the fibre dominated properties (approximately 5% for $E_{1c}$) [146]. As a result, the use of the micromechanics model contributes significantly to the discrepancy between the calculations and the experiment.

Moreover, for the 8 and 16 plies specimens, a homogeneous temperature field was considered across the parts due to the small wall thickness of the specimens and the low heating and cool down rates. However, small temperature gradients exist in the structure due to the positioning of the tool in the oven and the exothermic heat reaction of the resin, resulting in property gradients which slightly affect the distortion of the structure. For the 24 ply specimens even though a heat transfer analysis was performed prior to the spring-in analysis the heat transfer coefficient was approximated and not measured or calculated.

Furthermore, the viscoelastic model was based on the assumption of thermo-rheological simplicity, which is considered by Simon *et al.* [123] a good approximation for modelling the evolution of viscoelastic properties after the gelation of the structure. This implies that the shape of the retardation spectrum is assumed to not vary with temperature or degree of cure but is simply shifted along the time axis. Plazek *et al.* suggest this is valid for the time-temperature superposition, but it is not strictly valid for the time-cure superposition [134]. However, consideration of thermo-rheologically complex material behaviour would require further material characterisation.

In addition, all simulations were run from the nominal geometry (having an angle of 90°) so the pre-existing distortion of the tools is not included. This may induce some error to simulation results as different geometries produce different amounts of spring-in, known as non-linearity in the tool compensation process [20]. Moreover, the biaxial NCF was modelled as two UD plies, neglecting the effect of stitching of the fabric and bundle-bundle nesting effects. The corner and part thickening observed in the experiment (Section 3.2) was also not taken into account in the simulation. Finally, similar to the calculation of the spring-in angles of the experiment, the data reduction method used to calculate the spring-in angle of the parts for the simulation (Gaussian best fit of planes to the distorted mesh data) is a potential source of error.

Chapter

# 6

# Industrial Demonstrator

## 6.1 Aerospace test frame

The composite structure that was studied here is shown in Fig. 6.1. It is a demonstrator frame from the door surround structure of the Airbus $A350$ aircraft. It is made from the EPIKOTE$^{TM}$ resin system 600 by VARTM [124]. The frame is composed of UD as well as biax $(45/-45)$ and triax $(45/90/-45)$ NCF of IMS65 fibres. The fibre properties are presented in Table 4.1.

The composite frame was manufactured with the use of an inner and outer tool. The female outer tool was made from INVAR alloy and the inner male tool was made from aluminium as shown in Fig. 6.2. Fig. 6.3 shows the manufacturing process that was followed. The preform was created as shown in Fig. 6.4 and then placed in the female tool. It was manufactured larger than the final part to allow the machining operations to produce the final geometry of the structure. The aluminium caul was then placed on top of the preform and the whole assembly was put in a vacuum bag.

The curing cycle that was used is depicted in Fig. 6.5. It is similar to the one used for the manufacturing of the L-shape specimens of Chapter 3 (Fig. 3.12). The difference in this case is that the cycle depicted in Fig. 6.5 is the product of manufacturing experience given as input from the manufacturing department of Premium AEROTEC GmbH. It is similar to the temperature cycles presented by


Figure 6.1: The composite test frame studied.

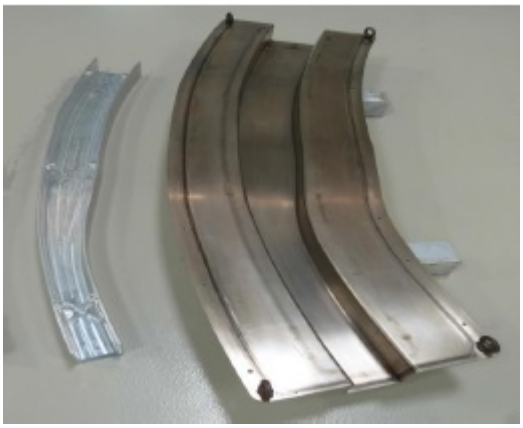

Figure 6.2: The aluminium caul plate (left) and the INVAR tool (right) used.

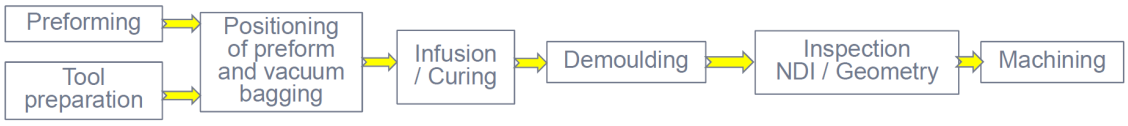


Figure 6.3: The manufacturing process which was followed.

Svanberg [21], who placed thermocouples at specific locations on the laminate and recorded the temperatures during the curing cycle. This approach was employed as no thermocouples were used in the manufacturing of the frame to monitor the temperatures of the tools, as was done in the case of the L-shape specimens of Chapter 3.

Prior to resin infusion, the assembly is preheated with a heating rate of $2°C/min$

Figure 6.4: The preform made from NCF.

to 120°$C$ in the oven. In the meantime, the resin is also heated from its storage temperature of $-18°C$ to 80°$C$. During this phase, the resin transforms from a solid to a liquid phase and its viscosity reduces. When the assembly in the oven reaches 120°$C$ the resin infusion starts and the resin's viscosity drops further. After the resin infusion is finished, a heat-up phase follows where the assembly is heated to the curing temperature of 180°$C$ with a heating rate of $1°C/min$. When the curing process is over, the temperature in the oven drops with a rate of $-2°C/min$ until room temperature is reached.

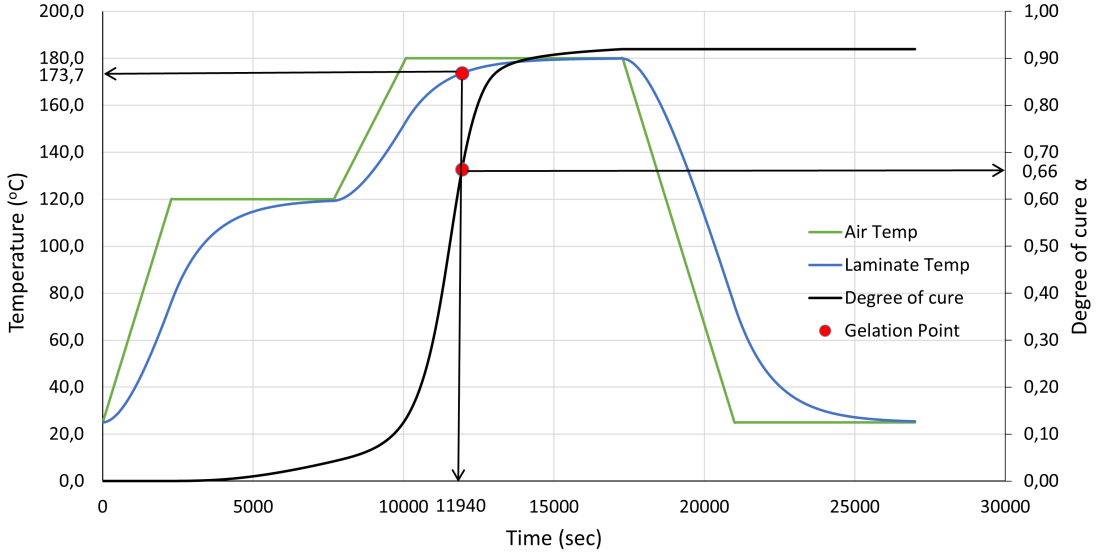


Figure 6.5: The curing cycle used consisting of two dwells until 180°$C$ is reached. The resulting laminate temperature is depicted with blue colour. The gelation point of the structure which is the starting point of the modelling effort is depicted as a red dot in the curing cycle as well as in the evolution of the degree of cure as predicted by Eq.(4.1).

After the curing process was finished, the part was taken out of the tool and was checked for manufacturing defects (void distribution etc). Following its inspection, the composite frame was machined to its final dimensions. The length of the composite frame is around 1769 $mm$ its maximum width is 190 $mm$ and its minimum width 127 $mm$. The height of the inner flange varies from 30 $mm$ to 40 $mm$ and the height of the outer flange from 75 $mm$ to 30 $mm$. The wall thickness of the composite frame ranges from 3.43 $mm$ to 5.76 $mm$.

After machining, the part was scanned with the use of a $3D$ scanner and an *.stl* file was created containing the information of the scanned geometry. This was used as reference for comparing the results of the simulation framework developed (Chapter 4). The manufacturing and the $3D$ scanning of the composite frame took place at the premises of Premium AEROTEC GmbH by the company's technicians.

## 6.2 Simulation of the frame PID

For simplicity, the chemo-mechanical module presented in Section 4.1.2 was used to model the PID of the frame instead of employing a sequentially coupled thermo-chemo-mechanical analysis. Both the CHILE and the viscoelastic model were investigated as to their ability to accurately model the PID of the frame. Again, the simulation starts just before the gelation point of the matrix and stresses built up earlier in the curing cycle are assumed to contribute insignificantly to the PID of the structure.

### 6.2.1 Mesh

Fig. 6.6 depicts the FE mesh that was used to simulate the PID of the composite frame. It consists of 26433 C3D8I solid elements [143]. An element length of approximately 5 $mm$ was chosen in the longitudinal and transverse direction, which is typically used in the industry to model parts of this size with no abrupt changes of curvature. Six elements were used to model the corner between the flanges and the web of the frame. In the thickness direction, the composite frame was modelled with one element consisting of multiple integration points according to the stacking sequence of the zone it belongs in order to reduce the computational time. A mesh sensitivity study was carried out with the use of five elements in the thickness direction and the difference in the calculated PID of the part was less than 1% compared to the adopted mesh density.

The frame consists of six zones as depicted in Fig. 6.6. The ply drops offs from one zone to another is 1:20. The biax and triax NCF fabric was modelled with an

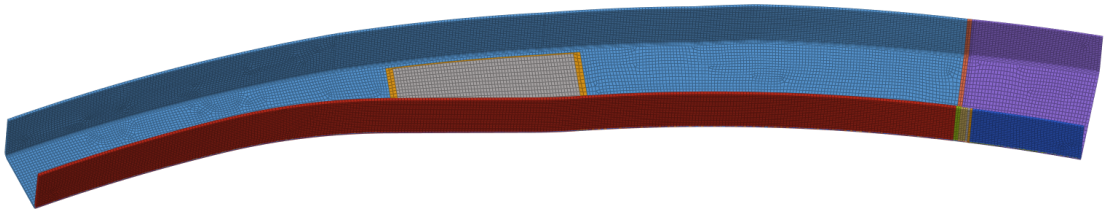

Figure 6.6: The FE mesh used to model the frame, consisting of 26433 C3D8I solid elements.

equivalent number of UD plies at the respective directions by ignoring the stitching of the fabric. Each resulting ply is modelled with the use of three integration points in its thickness direction. Consequently, the total number of integration points of a zone in the thickness direction is equal to the number of the resulting plies multiplied by three.

### 6.2.2 Boundary Conditions

The curing history was divided into five steps from the gelation point of the resin. Tool-part interaction was not considered in this case in order to reduce simulation complexity and runtime. Therefore, the "fixed" mechanical BC was used here as it is considered a better alternative to the use of the "freestanding" BC during the curing cycle (Section 5.4). The simulation steps used along with their imposed BCs are depicted in Table 6.1.

Table 6.1: Simulation steps

| Step | Description | Temperature ($°C$) | Degree of cure | Boundary Condition |
|---|---|---|---|---|
| 1 | Heating | 180 | $\alpha(T(t), \alpha_{t-1})$ | Fixed |
| 2 | Hold | 180 | $\alpha(T(t), \alpha_{t-1})$ | Fixed |
| 3 | Cool down | 25 | $\alpha_\infty$ | Fixed |
| 4 | Demoulding | 25 | $\alpha_\infty$ | Freestanding |
| 5 | Trimming | 25 | $\alpha_\infty$ | Freestanding |

In Table 6.1 the temperature refers to the temperature at the end of the step. In the demoulding and the trimming step all DoFs of all nodes are released except three nodes located at the centerline of the frame, which were used to suppress rigid body motion. Finally, the trimming step refers to the subtraction of a number of elements from the FE mesh to simulate the machining operations which occur after demoulding the part.

## 6.3 Simulation results

Given the curing cycle depicted in Fig. 6.5, the degree of cure $\alpha$ and the glass transition temperature $T_g$ of the matrix are calculated from the gelation to demoulding the structure with the use of Eq.(4.1),(4.2) respectively and are presented in Fig. 6.7.

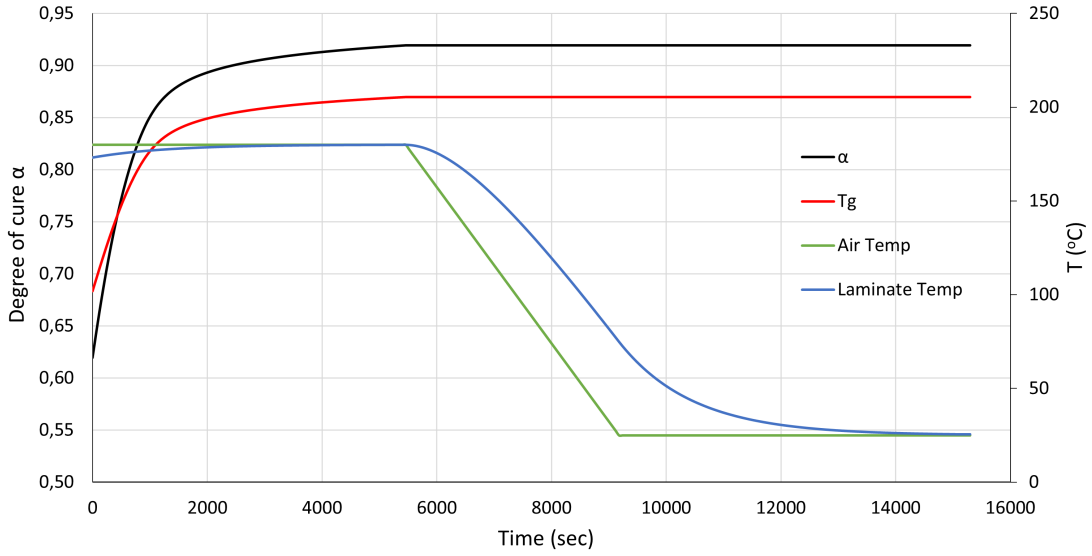


Figure 6.7: The degree of cure $\alpha$ and the glass transition temperature $T_g$ of the resin from the gelation to demoulding the structure.

The thermal and chemical strain of the resin (Eq.(4.7),(4.8)) from the gelation to demoulding the structure is depicted in Fig. 6.8. Since the simulation starts at the gelation point, the thermal strain slightly increases to a positive value following the laminate temperature profile and then thermal shrinkage occurs as the structure cool down to room temperature. As depicted in Fig. 6.8, the chemical strain is negative indicating that chemical shrinkage occurs. The sum of the thermal and chemical strain at any point is the non-mechanical strain experienced by the laminate in through-thickness direction ($\varepsilon_{33}$).

The resulting temperature, cure and the combined cure-temperature shift factor of the resin calculated with the use of Eq.(4.10),(4.11),(4.12) respectively are presented in Fig. 6.9. During the cure the temperature shift factor $a_T$ is positive as the $T_{ref} = T_g(a_{ref}) = T_g(0.94) = 214.91°C$ shifting the material response to higher frequencies, resembling elastic material behaviour, as the temperature during the cure is less than than $T_{ref}$. In contrast the cure shift factor is negative as the degree of cure during the cycle is always less than the reference one $a_{ref} = 0.94$, thus shifting the material response to lower frequencies.

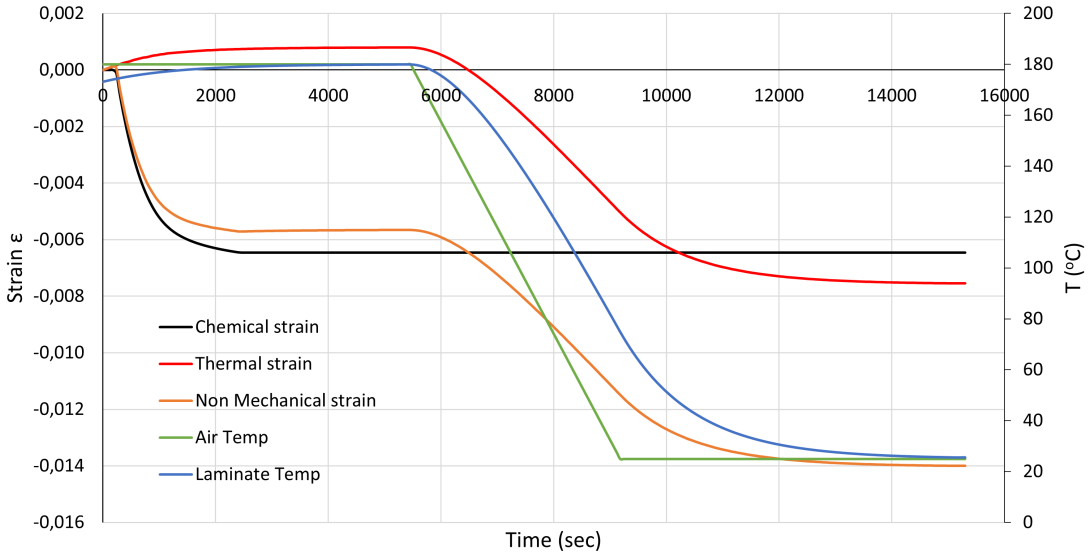


Figure 6.8: Thermal and chemical strain of the resin from the gelation to demoulding the structure. The sum of the thermal and chemical strain equals at any point the non-mechanical strain.

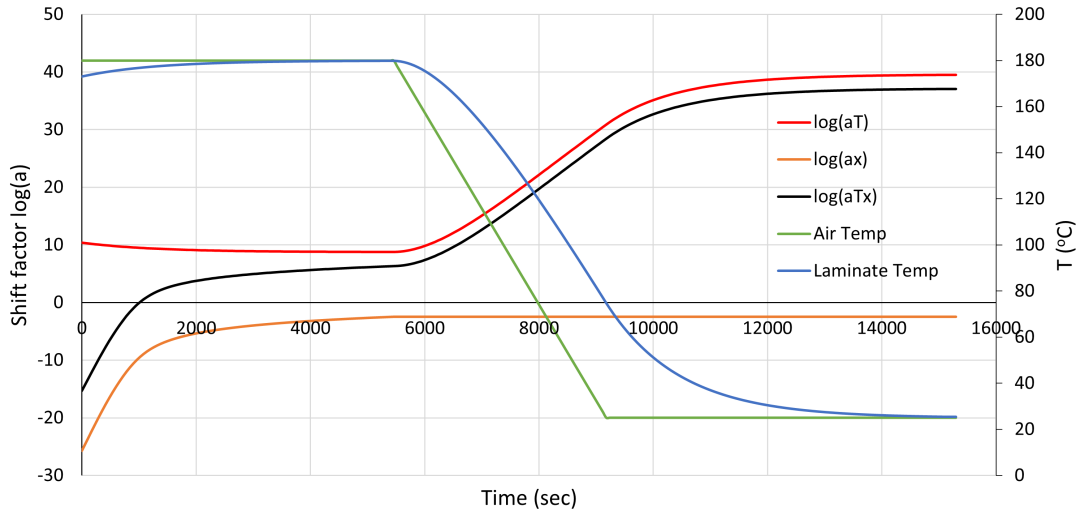


Figure 6.9: The temperature, cure and the combined cure-temperature shift factor of the resin from the gelation to demoulding the structure.

Fig. 6.10 depicts the Young's modulus of the resin, according to the CHILE and the viscoelastic material characterisation. As shown the Young's modulus of the resin for both material models is almost zero before gelation. At the gel point, a sharp increase of the modulus take place both for the CHILE and the viscoelastic model. However, as the cure progresses the modulus predicted by the viscoelastic material model is lower compared to the prediction of the modified CHILE model, which is due to relaxation occurring after gelation. Therefore, at the end of the cure, the

CHILE model predicts greater resin modulus compared to the viscoelastic model. Consequently, the Poisson's coefficient of the resin can be calculated according to Eq.(4.15) and is presented in Fig. 6.11 for the case of the viscoelastic material model.

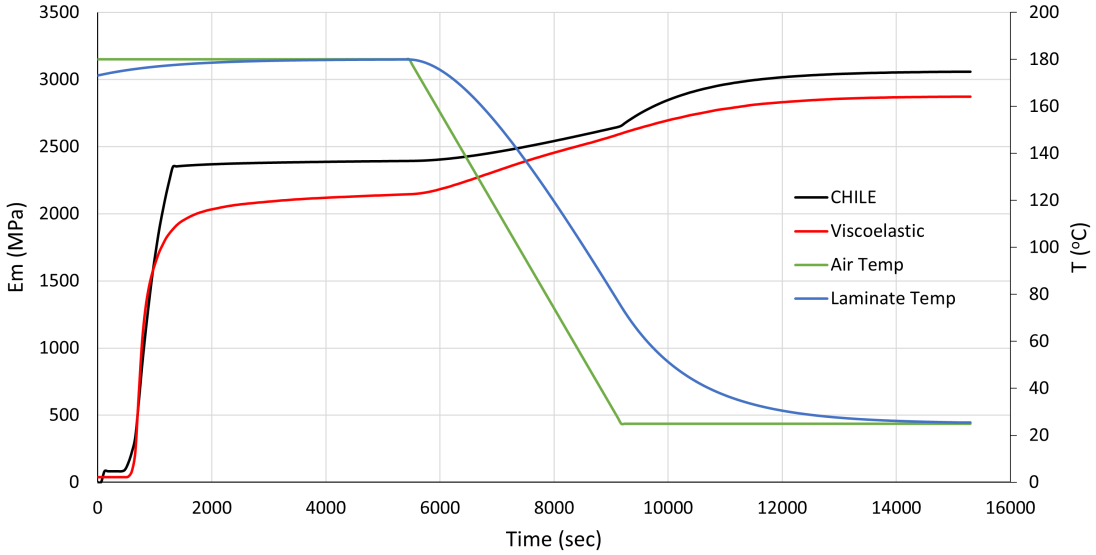


Figure 6.10: The Young's modulus of the resin from the gelation to demoulding the structure, according to the CHILE and the viscoelastic material characterisation.

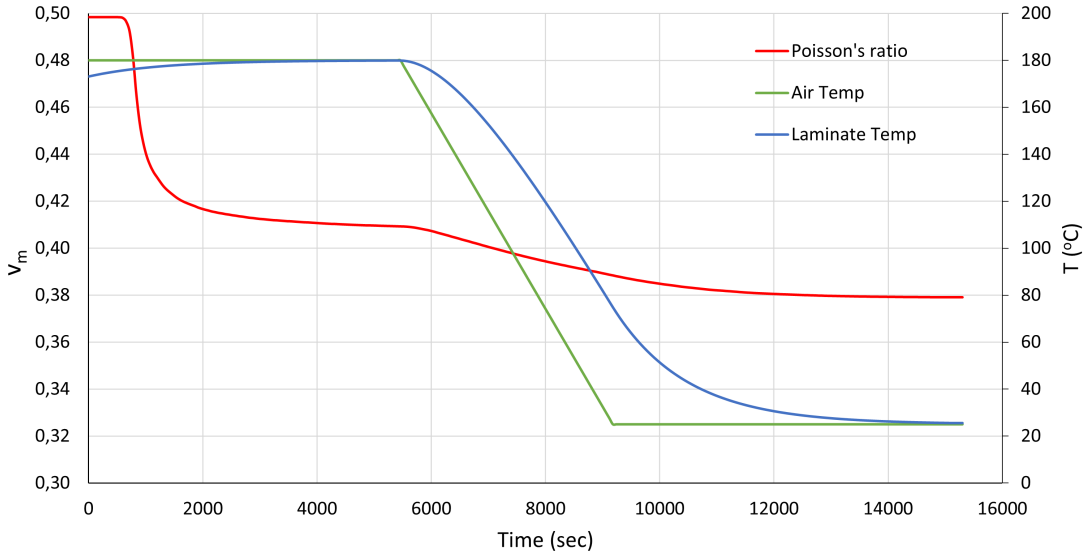


Figure 6.11: Poisson's coefficient of the resin from the gelation to demoulding the structure according to the viscoelastic material model.

Fig. 6.12 depicts the distortions induced in the frame after demoulding, with the use of the CHILE and linear viscoelastic material model respectively. The undeformed shape of the frame is shown with the black feature edges surrounding it. The distortion field is multiplied by a factor of 10 in order for the distortions to be visible.

As expected, the distortion field increases in magnitude from the web to the flanges. The distance between the flanges is reduced an effect caused by the reduction of the angles between the web and the inner and outer flanges. The viscoelastic material model predicts lower distortions compared to the CHILE material model. The maximum displacement value for the CHILE material model is 1.212 *mm* whereas for the viscoelastic material model it is 0.975 *mm*. The simulations also predict that the frame is subjected to warpage. The frame is twisted clockwise while simultaneously it suffers from a downward bending. The greater level of distortion predicted by the CHILE material model can be attributed to its inability to account for stress relaxation from the gelation point of the structure to cool down and to the difference of the Young's modulus of the two material models (Fig. 6.10).

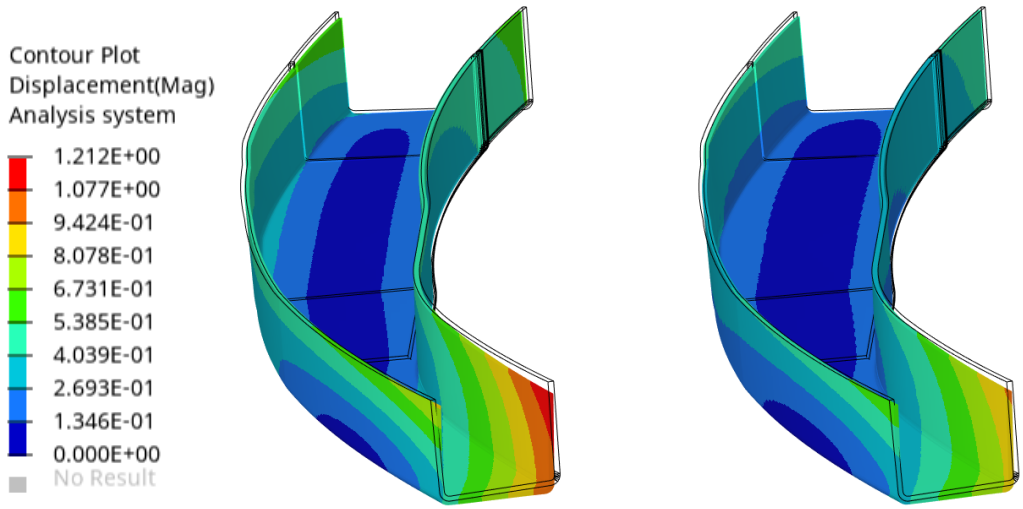


Figure 6.12: Distortion fields (*mm*) after demoulding the frame (CHILE left, viscoelastic right).

Fig. 6.13 depicts the distortion field of the frame after the trimming process. The trimming process releases residual stresses and the frame springs back to its nominal shape to some extent. The maximum displacement value after trimming for the CHILE material model is now 1.117 *mm* whereas for the viscoelastic material model it is 0.923 *mm*. Thus, the maximum displacement predicted by the viscoelastic model is around 17% smaller than the value predicted by the CHILE material model. The trimming operation also slightly alters the distribution of distortions in the frame. Therefore, a tool geometry compensation approach based on the shape of the part after demoulding but before trimming, will produce inaccurate results. However, because the tool compensation is a non linear process, in other words different geometries produce different amounts of spring-in [20] and the discontinuous distortion field between the trimmed and the untrimmed part, a second verification

PID analysis is proposed to verify that the compensated geometry will produce the desired structure.

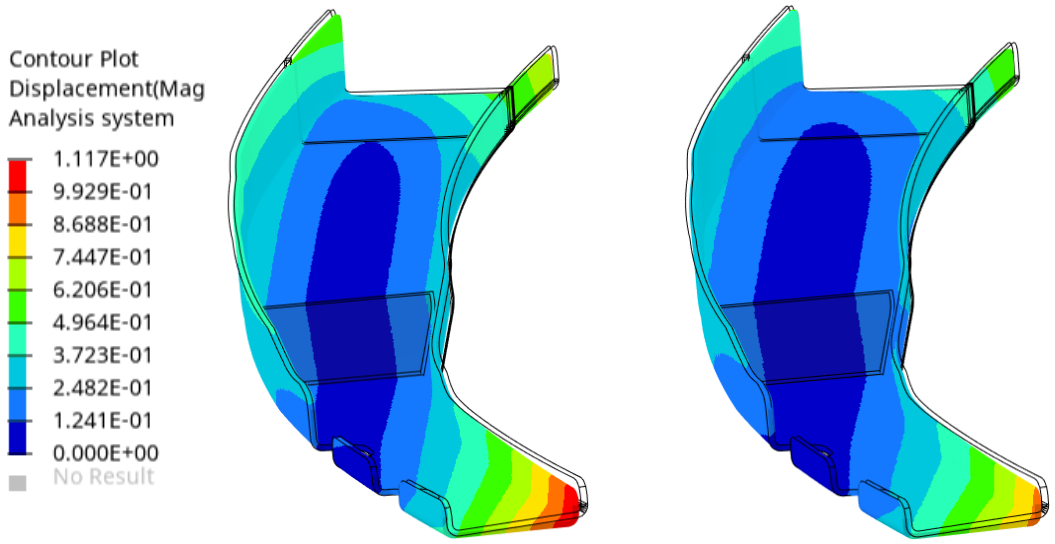


Figure 6.13: Distortion fields ($mm$) after trimming the frame (CHILE left, viscoelastic right).

The difference between the predictions of the two material models is depicted in Fig. 6.14. The CHILE material model predicts greater distortions compared to the viscoelastic material model. Red colour indicates outward displacement for the CHILE model to reach the predictions of the viscoelastic material model, whereas blue colour indicates inward displacement.

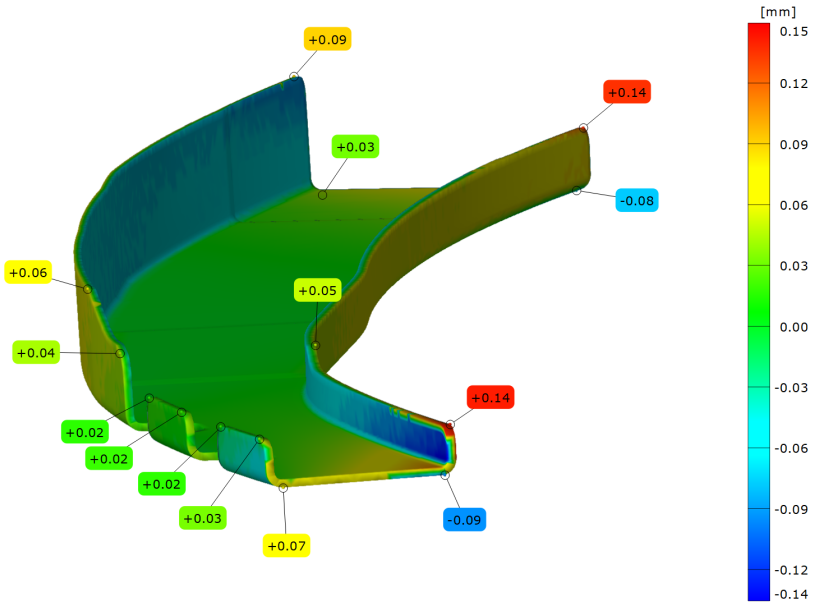


Figure 6.14: The difference in the predicted distortion fields between the two material models.

Here, it is important to note that the viscoelastic material model requires around twice the computational effort compared to the CHILE material model mainly because of the small time steps needed and the increased number of state variables that have to be read from the memory, updated by the material constitutive equation (4.51) and stored back in memory at every time increment. The number of state variables required is equal to the number of the Maxwell elements multiplied by the five independent constants of the transversely isotropic elasticity tensor, plus one which is the degree for cure ($56 \times 5 + 1 = 281$ in total in our case).

Fig. 6.15 depicts the distribution of $\sigma_{11}$ residual stresses predicted by the CHILE and the viscoelastic material model respectively, in the first layer (OML side) after trimming the frame. As it can be seen residual stresses on the magnitude of 10 *MPa* are predicted by the CHILE model. In comparison the residual stresses predicted by the viscoelastic material model are 5.6 *MPa* in magnitude for the first layer of the frame. This can be attributed to some extent to the stress relaxation that the model is able to predict during the curing cycle and to the different modelling approaches of the storage modulus used (modified CHILE model vs. linear viscoelastic model). Reduced residuals stresses with the use of a viscoelastic material model were also predicted by Nielsen [119]. However, while the residual stresses predicted by the CHILE material model are tensile for the first layer, the viscoelastic material model predicts compressive stresses for a significant area of the ply. This fact indicates that a change in the distortion field also results in the redistribution of the internal residuals stresses in the laminate. In any case the residual stresses predicted should be taken into account in the calculation of the safety factors of the structure.

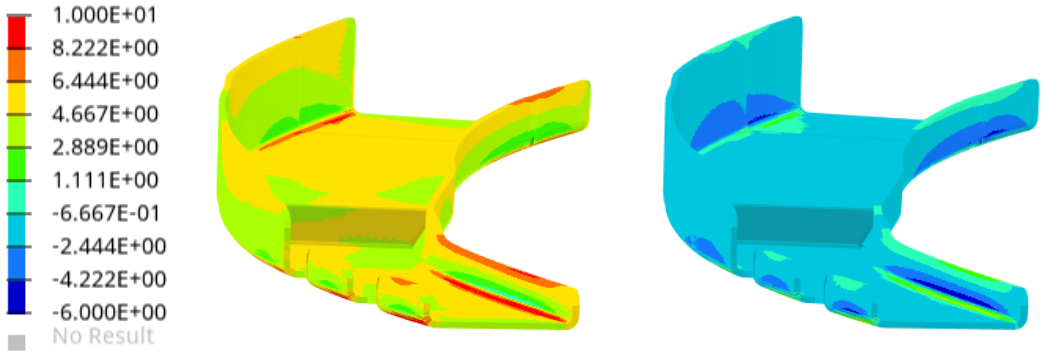


Figure 6.15: The predicted residual stresses $\sigma_{11}$ (*MPa*) in the first layer (CHILE left, viscoelastic right).

## 6.4 Comparison of simulation and experimental results

Before comparing the PID predictions of the two material models with the shape of the manufactured frame, a direct comparison between nominal and manufactured geometry is made as depicted in Fig. 6.16.

To enable the comparison between $3D$ measurements and the CAD geometry or simulation results, the GOM Inspect suite was used [125]. Since the two databases use different coordinate system an alignment step is necessary in order to perform any comparison. For that purpose the best fit algorithm was used. Since the outer flange of the frame is the one to be fitted to the skin of the aircraft a best fit alignment based on the outer flange and web of the frame was used. For this comparison red colour indicates outward displacement for the nominal geometry to meet the manufactured shape, whereas blue colour indicates inward displacement.

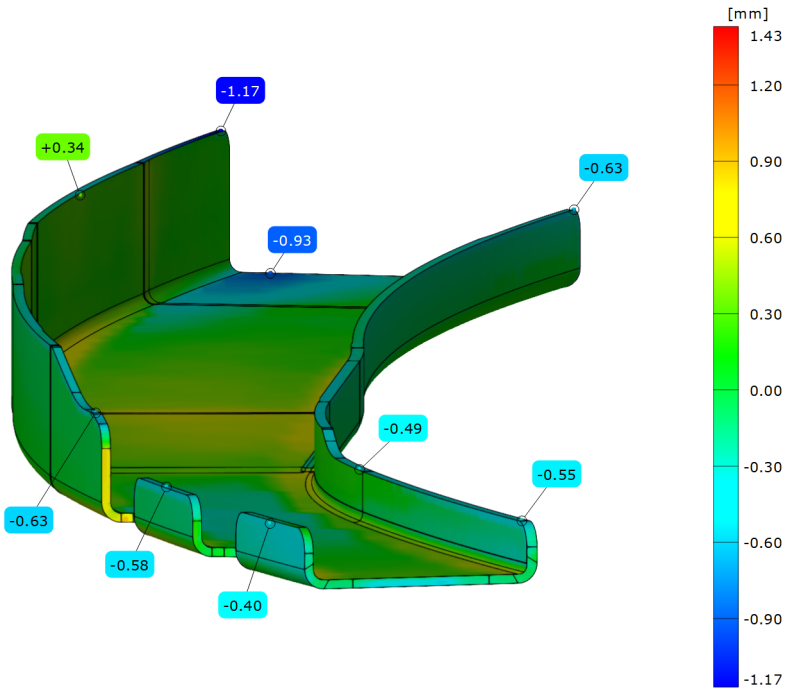


Figure 6.16: PID of the frame.

By comparing the nominal shape of the frame with the manufactured one (Fig. 6.16), it can be concluded that the flanges of the frame are subjected mainly to spring-in. The magnitude of spring-in of the flanges depends on the position of the cross section along the frame. Nine points were placed on the surface of the frame and their deviation to the manufactured frame is depicted in Fig. 6.16. The frame also experiences warpage since the web deviates from its nominal position up to 0.93 $mm$ at the back of the frame.

Moreover, as is depicted in Fig. 6.13 and Fig. 6.16, the measured and calculated

distortions of the composite frame in some areas are more than 0.5 *mm*, which is a typical threshold value used in the industry [20, 41]. Therefore, manufacturing the composite frame without any compensation will produce a product not meeting its manufacturing specifications.

Fig. 6.17 depicts the deviations of the two material models tested from the manufactured part. Red colour indicates outward displacement for the simulation results to reach measurements, whereas blue colour indicates inward displacement.

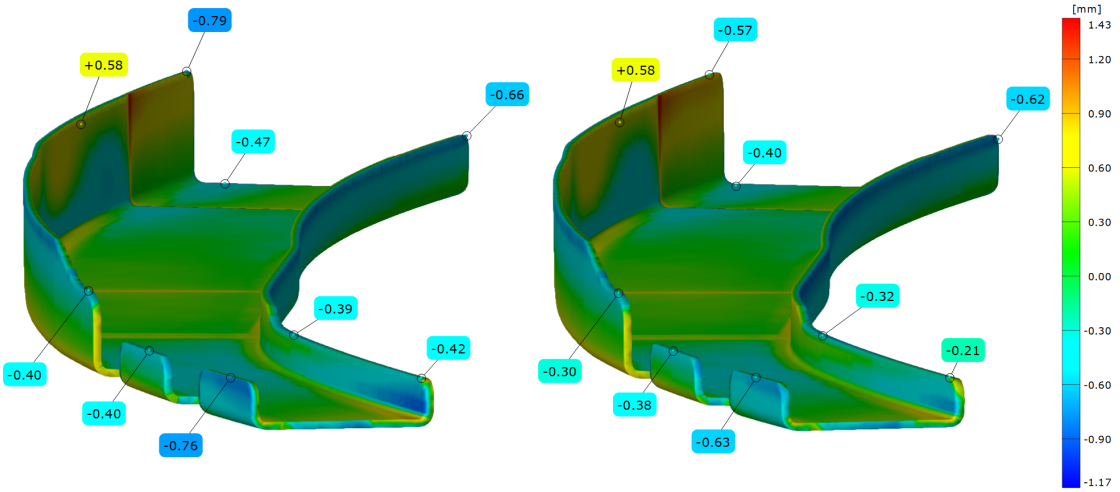


Figure 6.17: Deviation between the measured distortions and the calculated ones (CHILE left, viscoelastic right).

As shown in Fig. 6.17 the viscoelastic material model predicts more accurately the manufactured shape compared to the CHILE material model, which overestimates the PID of the frame. This is in agreement with the work presented in the literature [46, 104, 145]. However, in some areas of the frame (areas in Fig. 6.17 that are not green) both the CHILE and the viscoelastic model predict greater distortions compared to those experimentally observed.

## 6.5 Automation of the mirroring step

The typical process in the industry to perform the "mirroring" step shown in Fig. 2.4, would be the manufacturing engineer to reverse the distortion of the part to the opposite direction with the use of a FE mesh post-processing software (e.g *HyperView*, *μETA* etc.), export the file of the nodes coordinates and send it to the CAD department. Based on the position of the nodes the CAD department would fit surfaces to the point cloud and send them back to the manufacturing engineers for further evaluation.

Fig. 6.18 shows the steps needed to perform the mirroring of PID. The U-section shown is part of the composite frame of Fig. 6.6. The PIDs of the section of the frame were multiplied by a factor of five for visualization purposes. Green colour is the final geometry of the part, whereas the yellow FE are those which are removed during the analysis to simulate the trimming of the part.

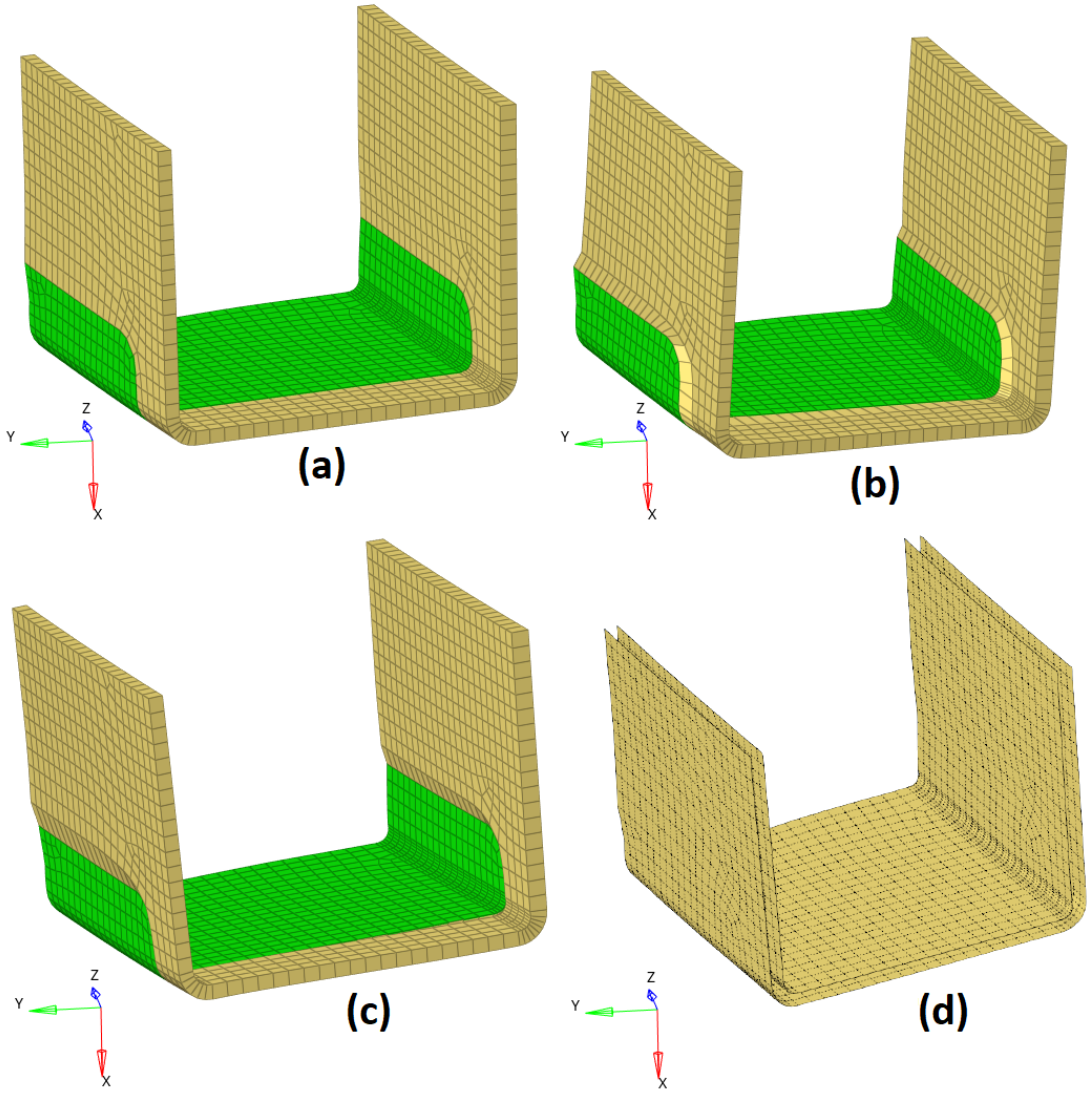


Figure 6.18: The steps needed to perform the mirroring process of the distortions of a spring-in analysis. a) Nominal geometry b) Result of the first PID analysis c) Mirroring of the distortions to the opposite direction d) Smoothing of mesh and creation of CAD surfaces (inner and outer). Green colour is the final trimmed geometry, whereas the yellow FE of a), b) and c) are the elements that are removed during the analysis.

The fitting of surfaces to the point cloud is an automatic process but the set-up of the algorithm is not. A problem that the CAD engineer needs to deal with a part subjected to trimming or machining processes, is that there are two node

groups with discontinuous distortion fields (Fig. 6.18). The two groups represent the untrimmed and final (trimmed) geometry. The discontinuous distortion field is created when a number of elements is subtracted during the analysis from the FE mesh to resemble the area of the structure being trimmed after demolding the part. The group of elements subtracted remain at their original position at the time when the "trimming" took place whereas the final geometry further distorts to simulate the effect of the machining operations.

Therefore, what the CAD engineer tries to achieve is to smooth this discontinuity before fitting any surfaces to the point cloud, usually by translating the points of the untrimmed element group close to the final (trimmed) point group. Then the fitting algorithm is used having as its input a selection of points to create the surfaces.

The drawback of this process for large enterprises is that due to exchange of information between departments, this could be a time consuming and costly process. Furthermore, as parts of the process are done manually, it was observed that two CAD engineers could provide slightly different surfaces given the same input file.

Here, an alternative solution has been investigated by developing three scripts in the pre-processing software *HyperMesh* to automate the "mirroring" step and demonstrate that for the scope of a spring-in analysis the CAD engineer may only be needed before sending the tool geometry for manufacturing. The scripts were developed to handle first order *3D* solid elements and can be used to structures modeled with one element in the through thickness direction. However, the scripts can be easily modified to handle other types of elements or multiple elements in the through thickness direction.

The scripts follow the rationale of the workflow performed by the CAD engineer and should be used sequentially. The first script translates the yellow element set (trimmed geometry) to match the surface which is formed by the green element set (final geometry). It ensures that the mesh will be smooth at the area where the two element sets meet and eliminates the characteristic step shown in Fig. 6.18 (b) & (c).

To achieve this the elements of the part need to be separated into two element sets before the use of the script and the normal vectors of the elements should point the same direction. One element set should contain the "trimming" elements and the other one should contain the elements of the "final" geometry. The coordinates of the elements of the "final" geometry are considered fixed and an iterative process starts to adjust the coordinates of the "trimming" elements. While there are still elements

in the "trimming" element set, the script identifies the neighbouring elements of the two sets based on the fact that they share common nodes. The nodes of each neighbouring element pair found are separated into node lists according to the element face they belong. In ABAQUS the nodes having the index 1 to 4 belong to the same element face, whereas the opposite element face is declared by indices 5 to 8 (Fig. 2.8). Then for each "fixed" element face a surface is created from the nodes of the face. The surface is scaled up and the shortest distance between the surface and the nodes of the "trimming" element of the corresponding face is calculated. The coordinates of the nodes of the "trimming" element are modified and the surfaces created are deleted. Finally, the elements which nodes coordinates have been modified are subtracted from the "trimming" element set and are considered fixed for the next iteration.

The second script is used to smooth areas of the mesh after the use of the first script. It slightly modifies the coordinates of the nodes to reduce the angle between the normal vectors of two adjacent elements. This script affects only the elements of the "trimming" element set. For every element in this set an iterative process is executed. First, the neighbouring elements of a "trimming" element are found. The angle between the normal vectors of the "trimming" element with a neighbouring one is found and in case this is a greater than 1 *rad* (less than 1 *rad* is considered smooth change of curvature) the element pair is considered as a possible distorted one. For the possible distorted element pairs the neighbouring elements are found and the angle between the normal vectors of the neighbouring elements are found. In case there is an angle less than 3 *rad* (a value chosen after testing the script in various geometries) the element pair is considered distorted. If the angles are greater that 3 *rad* the area is considered a geometrical feature such as a fillet. The nodes of each distorted element pair are separated according to the element face they belong (*face 1* or *face 2* Fig. 2.8). For each face, the common nodes of the two elements are identified and the remaining node pair per element face is used to create a line. Therefore, two lines are created one per element. The two lines are used to create a skin surface upon which every node of the element faces is projected. Finally, the surfaces created are deleted before the next interaction.

The job of the third script is to create the inner and outer surface of the tool based on the FE as processed by the two previous scripts. It separates the nodes of the FE mesh into two node lists which contain the nodes of the inner and outer tool surface. Then from the nodes of each list, element surfaces are created. To create the inner or outer tool surface the element surfaces created previously are merged into a single one. Finally, an auto-cleanup function follows to delete any unnecessary fixed points

or lines of the final surface, created at the merging of the element surfaces. However, in complex surfaces the auto-cleanup function may fail to fix all the geometrical inconsistencies. Consequently, after the use of the script, it may be necessary to manually cleanup the geometry created with the pre-processing tools of *HyperMesh* but the extent of these manual operations are usually limited.

Fig. 6.18 (d) shows the results of using the three scripts developed to produce the inner and outer surface of this U-section. With black dashed lines it is shown the information used to construct the surface, which in this case are the element faces. This surface can then be re-meshed to increase mesh quality for a subsequent PID analysis or be sent to the CAD department to produce the final drawings for tool manufacture.

## 6.6 Simulation of the mirrored geometry

After the calculation of the PID of the part, the next step in the design process of new tools for composites, as shown in Fig. 2.4, is the mirroring of distortions to the opposite direction. This serves as the compensated tool geometry. For that purpose the respective functionality of *HyperView* software was used and the mirrored (deformed) geometry was exported as an ABAQUS input file. Then, the files were imported in *HyperMesh* software, where the first two scripts presented in Section 6.5 were used to translate and smooth the mesh between the two element sets (trimmed and final geometry). As a result, the geometric inconsistencies between the two element sets were mitigated.

Afterwards, PIDs analysis on the mirrored geometries were run. The BCs of the analysis, material properties, curing cycle etc. were the same as of the first PID analysis and the two input files differ only by the position of the nodes. A comparison between the nominal CAD geometry of the part and the expected geometry after demoulding the part from the compensated tool is presented in Fig. 6.19 according to the two material models investigated. Here red colour indicates outward displacement for the CAD geometry to meet the predicted geometry.

As shown in Fig. 6.19 for most of the points placed across the frame, the expected deviation of the frame from the CAD geometry is reduced compared to the PID of the frame presented in Fig. 6.16. The deviation of the geometry from the CAD is minimized for the case of the viscoelastic model. The warpage of the frame is greatly reduced as the web deviates from its nominal position less than 0.5 $mm$. Also, the position of the inner flange is within the tolerances set. However, there

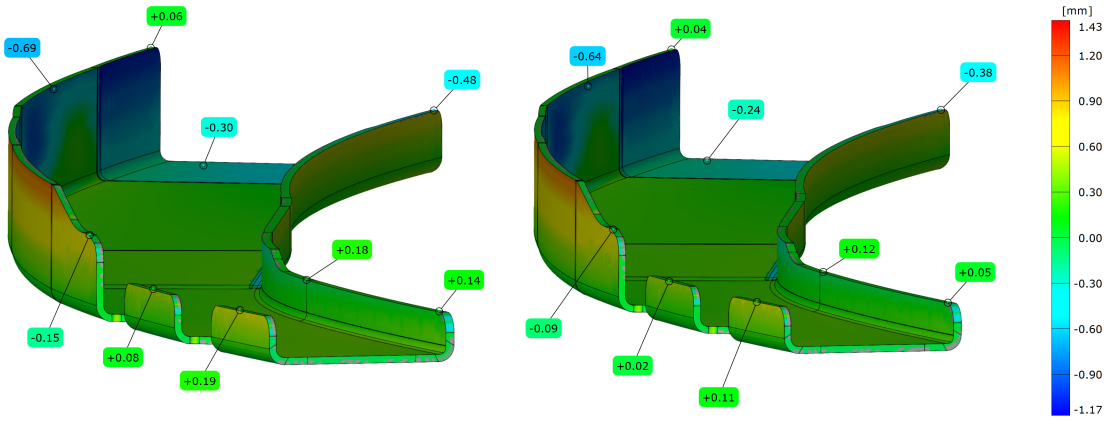


Figure 6.19: Deviation between the CAD and the expected geometry after demoulding the part from the compensated tool geometry (CHILE left, viscoelastic right).

are areas of the outer flange that do not meet this condition. The assumption of linear tool compensation as discussed in Section 2.2 contributes in this discrepancy along with the potential sources of error presented afterwards.

## 6.7 Potential sources of error

The deviation of the simulation results from the manufactured shape can be attributed to a number of assumptions made to simulate PID of the frame.

To begin with, fabric compaction, permeability and resin flow were also not considered in this case study. This leads to the assumption of homogeneous fiber volume fraction and void content in the part during the cure. In order to calculate the inhomogeneous resin distribution in the part at the end of the infusion process, a resin flow simulation needs to be employed. For that purpose, the resin viscosity as a function of temperature and degree of cure needs to be experimentally measured and modelled. Moreover, the biax and triax NCF fabric was modelled as a number of UD plies, neglecting the effect of stitching of the fabric.

Furthermore, a homogeneous temperature field was considered throughout the part, taken as input from manufacturing experience. This assumption was made due to the small wall thickness of the part, the low heating and cool down rates and to reduce the computational cost of the simulation. However, small temperature gradients develop in the structure during cure. These can be attributed to the exothermic heat reaction of the resin, the positioning of the tool in the oven, the part shape and the relative motion of the tool–part interfaces during cure. These temperature gradients result in property gradients and affect the distortion of the

structure.

In addition, tool-part interaction was not taken into account in this study and could play a significant role as it was observed in Chapter 3 for the case of the L-shape structures. The caul plate (Fig. 6.2) was made from aluminium to reduce the cost of the experiment. However, due to the great difference of the CTE between the preform and the caul plate stresses are induced to the frame due to the constrained deformation of the caul plate, which were not taken into account in the simulation.

Also, the light projection method used to measure the distortion field of the frame and the creation of the stereolithography file used to make the comparisons is a potential source of error. More importantly, the tool and the caul plate that produced the frame were not $3D$ scanned and their deviation from the nominal CAD geometry is not known.

Finally, another source of error could be the mesh of the frame which is based on de-featured geometry with many geometric details (e.g. chamfer edges, fillets etc.) deliberately removed from the CAD geometry to facilitate the meshing operation. This is assumed to be the reason for the characteristic red step observed in the contour plot in Fig. 6.17 at the back of the frame, as in front of the ply drop off area a geometric detail shown with black feature lines in Fig. 6.16 was removed before meshing. Also, this error contributes to the characteristic blue area (indicating that the predicted geometry is inwards of the CAD geometry) presented in Fig. 6.19 for both the CHILE and viscoelastic model at the back of the frame.

Chapter

# 7

# Conclusions

## 7.1 Summary and conclusions

In this research, PID of composites structures is investigated experimentally and numerically. The material system studied in this work is the EPIKOTE$^{TM}$ resin system 600 with IMS65 fibres in the form of NCF.

An experimental investigation was performed to investigate the effect of stacking sequence, tool material, curing cycle and specimen thickness on PID of L-shaped composite structures. Seventy-two specimens were manufactured with VARTM and their distortion was measured with the use of a $3D$ scanner and a CMM. The parts were manufactured by 13 stacking sequences, including representative stacking sequences used in the aerospace (SK,SP etc.) and academic ones (AS, UB etc.). The specimens were manufactured from INVAR, steel and aluminium tools and were separated into three groups by their nominal thickness (1.5 $mm$, 3.0 $mm$ and 4.5 $mm$). The effect of the MRCC and a "Fast" curing cycle, which has an elevated curing temperature, on PID of the parts was also investigated.

From the experiment, it was found that the material of the tool has a significant effect on the spring-in angle of the parts. The parts manufactured with the INVAR tool experience on average less deformation compared to the parts manufactured with the steel or aluminium tools. Therefore, tool-part interaction plays an important role

even in the manufacturing of simple L-shape structures. Its effect is more evident when there is a large difference between the CTE of the laminate and the tool.

Furthermore, it was found, that the spring-in angle on the parts reduces as the bending stiffness, $D_{11}$, of the laminate increases, as the 24 plies specimens experience the least average spring-in angle compared to the other laminate groups. Moreover, symmetric and balanced laminates are recommended to avoid the coupling of the bending and twisting distortions of the laminate, which were observed in the case of the $AS_{16}$ laminate group.

Also the "Fast" curing cycle which has an elevated curing temperature compared to the MRCC ($195°C$ vs. $180°C$) induces higher spring-in angle of the parts. However, the increase of the spring-in angle of the parts due to the "Fast" curing cycle is considered small compared to the manufacturing time saved by the use of this curing cycle.

Following the experiments, a simulation framework was developed to predict PID of composites structures. It consists of two modules the thermo-chemical module and the chemo-mechanical one. The two modules can be used independently or can be combined to increase the accuracy of the simulation. In this case, the thermo-chemical module runs first and the calculated temperature field is mapped to the spring-in analysis. The material modelling was implemented in ABAQUS software with the use of material subroutines.

The thermo-chemical module is able to calculate the temperature distribution across the part at every time increment of the curing history. This is achieved with the calculation of the effective thermal properties of the lamina based on the thermal properties of its constituents, as a function of the degree of cure and temperature.

The chemo-mechanical module is able to update the stress tensor and CTO of the material integration point at every time increment. In order to do so, the instantaneous matrix properties (matrix CTE,CSC etc.) are calculated at every time increment and are used by the micromechanics model to calculate the effective lamina properties. Then, the effective lamina properties are used by the material constitutive equation. In this research, two material models were investigated, the CHILE and a linear viscoelastic material model.

The software developed was used to simulate the experiment. Both material models were investigated regarding their accuracy to predict the deformed shape of the specimens. For the thick 24 plies laminates ($4.5\ mm$), where significant temperature

gradients are expected through the thickness of the parts, a heat transfer analysis was performed before the spring-in analysis. This was found to increase the accuracy of the predicted spring-in angle in the range of 0.04° to 0.08° compared to the assumption of a homogeneous temperature field across the part. Furthermore, the increase of the spring-in angle of the parts due to the higher curing temperature of the "Fast" curing cycle was predicted by the simulation and the analytical equation (Eq. (5.1)).

Two BCs were investigated in each case, the "freestanding" and "fixed" BCs. Tool-part interaction was studied by employing a cure dependent CoF during the cycle. The aim was to investigate which material model and BCs can better predict the experimental findings as well as validate the simulation framework developed.

The spring-in angles predicted by the tool-part interaction model were usually between the bounds defined by the use of the "fixed" (lower bound) and "freestanding" (upper bound) BC. A model that includes tool-part interaction was found to be more accurate in predicting PID of composites than the models employing the "fixed" and "freestanding" BCs. The use of the cure-dependent CoF was found to have negligible effect on the results while adding significant computational costs.

It was found that the CHILE material model overestimates the spring-in angle for the majority of the cases studied. The analytical equation (Eq.(5.1)) also overestimates the average spring-in angle of most of the cases and its result is close to the prediction of the CHILE material model with the use of the "freestanding" BCs. The viscoelastic material model is proposed to be employed for an accurate prediction of PID of composites with tight tolerances (e.g. less than 0.5 $mm$), as it can take into account the time dependent factors, such as stress relaxation, that affect the distortion of the parts from gelation of the structure through to cool down.

Then, the chemo-mechanical module was applied to predict PID of a composite test frame. Both material models were investigated and "fixed" BCs were assumed in this case. After manufacturing, the frame was $3D$ scanned and the shape of it was compared with the CAD nominal one.

The predictions of the two material models were compared against each other and was found that the CHILE material model predicts greater distortions in magnitude compared to the viscoelastic model. By comparing the shape predicted from the two material models with the manufactured shape, it was found that the viscoelastic model more accurately predicts the manufactured shape. However, it needs approximately twice the computational time compared to the CHILE model

to run. In addition, an increased material characterisation effort is required to derive the viscoelastic material properties needed as input for the material model.

Furthermore, since the calculated and measured distortions of the frame in some areas were more than *0.5 mm*, which is a typical threshold value used in the industry, manufacturing the product without any compensation will produce a part not meeting its manufacturing specifications.

Moreover, it was found that a tool geometry compensation approach based on the shape of the part after demoulding will produce inaccurate results as the trimming operations which usually take place in the industry, release stresses that affect the distortion field of the structure, depending on the extent of these operations. Also, residual stresses exist in the final product and should be taken into account in the calculation of the reserve factors of the structure.

Finally, three scripts were developed to automate the mirroring step in the design process of new tools. Their purpose is to translate and smooth the mesh before attaching to it surfaces in order for the second PID simulation loop to run. The use of the scripts enables the manufacturing engineer to design new tools seamlessly without interfacing with the CAD department, thus reducing design time and costs.

To summarise, to address the challenges presented in Section 1.7, this work contributed the following:

1. A literature review was performed, to identify the factors contributing to PID of composites and the methods used to predict PID.
2. An experimental investigation was performed to evaluate the influence of the driving factors contributing to PID of L-shape structures made from the EPIKOTE$^{TM}$ System 600 and IMS65 fibres.
3. A modular simulation framework was developed to predict PID of composites.
4. The proposed simulation framework was validated against experimental measurements and analytical results.
5. The proposed simulation framework was applied to predict PID of an aerospace test frame.
6. Three post-processing scripts were developed to automate the "mirroring" step as defined by the industry.

## 7.2 Future work

The work presented in this thesis contributes towards a Right First Time (RFT) approach in the design of new tools for composite structures. However, a better understanding of the tool-part interaction is needed, to substitute the expensive INVAR tools used in the manufacturing of primary structures.

More specifically, research should be conducted towards an accurate modelling of the tool, to identify potential geometric and material non-linearities induced to the tools from their manufacturing (welding of the tool, bending of substructures etc.). For that purpose the geometry of the tool as manufactured should be used instead the CAD nominal one. The areas of the welding should be modelled in detail along with the properties of the welded material. It is believed that the manufacturing of the tool significantly affect its shape and expansional behaviour during the curing cycle, thus contributing to PID of the final product.

Regarding the simulation framework developed, potential areas of future research include the study and use of draping, fabric compaction and resin flow simulation prior to the thermo-chemical or chemo-mechanical module. This is expected to increase the accuracy of the simulation framework for the calculation of PID.

A draping simulation enables the calculation of fibre reorientation at the manufacturing of the preform. The mapping of this field to the spring-in analysis will increase the validity of the model. Furthermore, a fabric compaction simulation results in a nonuniform thickness distribution across the part and the identification of areas where fibre bridging or wrinkles might occur. These are resin rich areas where increased local distortions are expected due to the increased CTE of the area. A permeability modelling and resin flow simulation enables the calculation of inhomogeneous fibre volume fraction and void content in the part during the cure. Moreover, the effect of fabric weaving or stitching on the mechanical properties of the fabric should be considered (instead of assuming an equivalent cross ply laminate) to increase PID simulation accuracy.

While most of these simulation capabilities already exist to some extent in the manufacturing simulation of composites, the challenge is to combine all these phenomena for the calculation of PID of large scale structures without significantly increasing calculation time and modeling complexity. Therefore, the driving factors of each discipline should be identified and used in the context of PID simulations and the added value that the increased simulation complexity brings should be quantified. Also, more research should be conducted towards the training and evaluation of

machine learning models for the calculation of PID of composite structures.

In addition, the use of experimentally measured effective lamina properties, instead the use of micromechanics models will increase the accuracy of the simulation framework. Furthermore, the experimental measurement of the permeability of the laminate and viscosity of resin during the curing cycle is proposed to be carried out for a resin flow simulation. Moreover, it would be interesting to investigate the effect of tool release agent on the PID of the parts. A number of specimens could be manufactured from various release agents or even without any applied on the tool surface and monitor the differences on the PID of the parts under the same manufacturing conditions (curing cycle, tool material, bagging set up etc.). Finally, more than one tools could be manufactured from the same material but with different manufacturing processes e.g. milling or additive manufacturing and monitor the differences on the PID of the parts.

Appendix

# A

# Plane fit metrics

Table A.1: Standard deviation ($\sigma$(mm)) and maximum absolute deviation (max $|d_i|$ (mm)) of points from the fitting plane of the 8 ply specimens manufactured with MRCC.

| Laminate | | | $3D$ scanner | | | | CMM | | | |
|---|---|---|---|---|---|---|---|---|---|---|
| | | | Plane 1 | | Plane 2 | | Plane 1 | | Plane 2 | |
| | | | $\sigma$ | max $\lvert d_i \rvert$ | $\sigma$ | max $\lvert d_i \rvert$ | $\sigma$ | max $\lvert d_i \rvert$ | $\sigma$ | max $\lvert d_i \rvert$ |
| $AS_8$ | INVAR | Spec.1 | 0.065 | 0.286 | 0.067 | 0.260 | 0.056 | 0.163 | 0.048 | 0.153 |
| | | Spec.2 | 0.052 | 0.244 | 0.064 | 0.283 | 0.071 | 0.206 | 0.035 | 0.108 |
| | | Spec.3 | 0.078 | 0.291 | 0.064 | 0.291 | 0.054 | 0.151 | 0.053 | 0.134 |
| | Steel | Spec.1 | 0.093 | 0.352 | 0.091 | 0.352 | 0.076 | 0.193 | 0.076 | 0.226 |
| | | Spec.2 | 0.077 | 0.294 | 0.073 | 0.280 | 0.051 | 0.129 | 0.046 | 0.149 |
| | | Spec.3 | 0.069 | 0.282 | 0.089 | 0.342 | 0.065 | 0.178 | 0.046 | 0.122 |
| | Alum. | Spec.1 | 0.073 | 0.319 | 0.073 | 0.294 | 0.043 | 0.125 | 0.047 | 0.144 |
| | | Spec.2 | 0.076 | 0.288 | 0.077 | 0.319 | 0.048 | 0.137 | 0.053 | 0.145 |
| | | Spec.3 | 0.066 | 0.240 | 0.076 | 0.292 | 0.047 | 0.137 | 0.047 | 0.125 |
| $BS_8$ | INVAR | Spec.1 | 0.045 | 0.231 | 0.039 | 0.221 | 0.029 | 0.076 | 0.035 | 0.084 |
| | | Spec.2 | 0.043 | 0.221 | 0.057 | 0.228 | 0.029 | 0.079 | 0.043 | 0.091 |
| | | Spec.3 | 0.052 | 0.256 | 0.030 | 0.253 | 0.029 | 0.066 | 0.045 | 0.096 |
| $BF_8$ | INVAR | Spec.1 | 0.051 | 0.207 | 0.035 | 0.148 | 0.023 | 0.064 | 0.035 | 0.075 |
| | | Spec.2 | 0.052 | 0.224 | 0.052 | 0.224 | 0.038 | 0.087 | 0.047 | 0.101 |
| | | Spec.3 | 0.050 | 0.214 | 0.048 | 0.230 | 0.033 | 0.086 | 0.042 | 0.101 |

Appendix

# B

# Sensitivity analysis

In order to assess the sensitivity of the results of the simulation framework developed in Chapter 4 on the material constants used, the values of the resin and fibre properties were changed by ±10%. Table B.1 presents the result of the analysis conducted for a number of material properties. For the analysis the $BS_8$ laminate group was used, manufactured with the MRCC and simulated with the CHILE model and the use of the "freestanding" BC. As shown in Table 5.2, the spring-in angle in this case is 1.43°. This was used as a reference for calculating the % change of the predicted spring-in angle due to the change of the material property. As shown in Table B.1 the result of the simulation framework developed is more sensitive to the change of the resin properties than to the change of the fibre properties. An increase of the CSC and the CTE of the resin results in an increased spring-in angle, as further strains (chemical and thermal) are induced to the structure. On the contrary an increase in the resin modulus results in a reduced spring-in angle as the part gains stiffness. The CTE of the fiber do not seem to affect the end result, as it is at least an order of magnitude lower compared to the CTE of the resin (Fibre: Table 4.1, Matrix: Table 4.4). Furthermore, a ±10% change on the mechanical properties of the fibre does not significantly affect the spring-in angle of the part.

Table B.1: Effect of the material property change by 10% on the spring-in angle of the $BS_8$ part manufactured with the MRCC and simulated with the CHILE model and the use of the "freestanding" BC.

| Property | Spring-in angle | | Change % | |
|---|---|---|---|---|
| | +10% | −10% | +10% | −10% |
| $CSC_m$ | 1.50 | 1.35 | 4.90 | 5.59 |
| $CTE_m$ | 1.49 | 1.36 | 4.20 | 4.90 |
| $E_m$ | 1.40 | 1.45 | 2.10 | 1.40 |
| $CTE_{11f}$ | 1.43 | 1.43 | 0.00 | 0.00 |
| $CTE_{22f}$ | 1.43 | 1.42 | 0.00 | 0.70 |
| $E_{11f}$ | 1.43 | 1.42 | 0.00 | 0.70 |
| $E_{22f}$ | 1.43 | 1.43 | 0.00 | 0.00 |
| $G_{12f}$ | 1.43 | 1.43 | 0.00 | 0.00 |
| $G_{23f}$ | 1.42 | 1.43 | 0.70 | 0.00 |
| $\nu_{12f}$ | 1.42 | 1.43 | 0.70 | 0.00 |

Appendix

# C

# Publications

Parts of this research have been presented in various scientific conferences and published in leading peer reviewed journals. Below is a list of the articles and conferences associated with this work.

## C.1 Articles published in scientific journals

[1] **N. Traiforos**, T. Turner, P. Runeberg, F. Daoud, D. Chronopoulos, F. Glock, G. Schuhmacher, D. Hartung, A simulation framework for predicting process-induced distortions for precise manufacturing of aerospace thermoset composites, Composite Structures 275 (2021) 114465.

[2] G. Corrado, G. Ntourmas, M. Sferza, **N. Traiforos**, A. Arteiro, L. Brown, D. Chronopoulos, F. Daoud, F. Glock, J. Ninic, E. Ozcan, J. Reinoso, G. Schuhmacher, T. Turner, Recent progress, challenges and outlook for multidiscipli nary structural optimization of aircraft and aerial vehicles, Progress in Aerospace Sciences 135 (2022) 100861.

[3] **N. Traiforos**, M. Matveev, D. Chronopoulos, T. Turner, Spring-in of composite L-shape specimens: An experimental and numerical investigation, Composite Structures 310 (2023) 116772

## C.2 International conferences

[1] **N. Traiforos**, D. Hartung, P. Runeberg, T. Turner, D. Chronopoulos, G. Schuhmacher, F. Daoud, F. Glock, On the investigation of a simulation framework to predict process-induced shape distortions suitable for manufacturing aerospace thermoset composites, 7$^{th}$ Aircraft Structural Design Conference by RAeS, 2020.

[2] **N. Traiforos**, T. Turner, P. Runeberg, F. Daoud, D. Chronopoulos, F. Glock, G. Schuhmacher, An Updated Simulation Framework for the Prediction of Process Induced Shape Distortion in Thermoset Composites, 8$^{th}$ ECCOMAS Thematic Conference on the Mechanical Response of Composites (Composites 2021), 2021.

[3] **N. Traiforos**, T. Turner, P. Runeberg, F. Daoud, D. Chronopoulos, F. Glock, G. Schuhmacher, D. Hartung, On the investigation of a simulation framework to predict process-induced shape distortions suitable for manufacturing aerospace thermoset composites, International Conference on Manufacturing of Advanced Composites 2021 (ICMAC), 2021.

[4] **N. Traiforos**, T.Turner, P. Runeberg, F. Daoud, D. Chronopoulos, F. Glock, G. Schuhmacher, An Updated Simulation Framework for the Prediction of Process Induced Shape Distortion in Thermoset Composites, NAFEMS World Congress (NWC21), 2021.

[5] **N. Traiforos**, T. Turner, M. Matveev, An experimental investigation and modelling of the factors contributing to spring-in of composite L-shape structures, International Conference on Manufacturing of Advanced Composites 2022 (ICMAC), 2022.

# Bibliography


[1] K. Elssel, Ö. Petersson, CA-AeroStruct - Multidisziplinäre Optimierung und Simulation zukünftiger Hochleistungsplattformen Schlussbericht, a ed., Airbus Defence and Space GmbH, Manching, 2016.

[2] G. Corrado, G. Ntourmas, M. Sferza, N. Traiforos, A. Arteiro, L. Brown, D. Chronopoulos, F. Daoud, F. Glock, J. Ninic, E. Ozcan, J. Reinoso, G. Schuhmacher, T. Turner, Recent progress, challenges and outlook for multidisciplinary structural optimization of aircraft and aerial vehicles, Progress in Aerospace Sciences 135 (2022) 100861.

[3] S. Kumar, N. P. Padture, Materials in the Aircraft Industry, Springer International Publishing, Cham, 2018, pp. 271–346.

[4] Guide to composites, Gurit, 2022.

[5] https://store.acpcomposites.com/woven-fabric-style-guide.

[6] V. Schrank, M. Beer, M. Beckers, T. Gries, 10 - polymer-optical fibre (pof) integration into textile fabric structures, in: C.-A. Bunge, T. Gries, M. Beckers (Eds.), Polymer Optical Fibres, Woodhead Publishing, 2017, pp. 337–348.

[7] Prepreg vacuum bagging user guide, Airtech Global, 2022.

[8] R. J. H. Wanhill, Carbon Fibre Polymer Matrix Structural Composites, Springer Singapore, Singapore, 2017, pp. 309–341.

[9] J. P.-H. Belnoue, T. Mesogitis, O. J. Nixon-Pearson, J. Kratz, D. S. Ivanov, I. K. Partridge, K. D. Potter, S. R. Hallett, Understanding and predicting defect formation in automated fibre placement pre-preg laminates, Composites Part A: Applied Science and Manufacturing 102 (2017) 196–206.

[10] H. Ning, S. Pillay, K. B. Thattaiparthasarathy, U. K. Vaidya, Design and manufacturing of long fiber thermoplastic composite helmet insert, Composite Structures 168 (2017) 792–797.

[11] https://composite-integration.co.uk/resin-transfer-moulding/.

[12] D. Rout, R. K. Nayak, S. Praharaj, Chapter 13 - aerospace and vehicle industry, in: C. M. Hussain (Ed.), Handbook of Polymer Nanocomposites for Industrial Applications, Micro and Nano Technologies, Elsevier, 2021, pp. 399–417.

[13] I. Baran, K. Cinar, N. Ersoy, R. Akkerman, J. H. Hattel, A review on the mechanical modeling of composite manufacturing processes., Arch Computat Methods Eng 24 (2017) 365–395.

[14] F. Heinecke, C. Willberg, Manufacturing-induced imperfections in composite parts manufactured via automated fiber placement, Journal of Composites Science 3 (2019).

[15] A. Kitselis, N. Traiforos, D. Manolakos, The effect of resonance on the void content in cfrp tubes, Composites Part B: Engineering 106 (2016) 164–171.

[16] M. Fiorina, A. Seman, B. Castanie, K. Ali, C. Schwob, L. Mezeix, Spring-in prediction for carbon/epoxy aerospace composite structure, Composite Structures 168 (2017) 739–745.

[17] T. Hirche, Curing simulation with ansys, in: Carbon Composites Colloquium Presentations, 2019, pp. 2–10.

[18] G. T. Göran Fernlund, Anoush Poursartip, C. Albert, Residual stress, spring-in and warpage in autoclaved composite parts, Department of Metals and Materials Engineering, The University of British Columbia, 2003.

[19] G. Fernlund, A. Osooly, A. Poursartip, R. Vaziri, R. Courdji, K. Nelson, P. George, L. Hendrickson, J. Griffith, Finite element based prediction of process-induced deformation of autoclaved composite structures using 2d process analysis and 3d structural analysis, Composite Structures 62 (2003) 223–234.

[20] E. Kappel, Compensating process-induced distortions of composite structures: A short communication, Composite Structures 192 (2018) 67–71.

[21] J. M. Svanberg, Predictions of manufacturing induced shape distortions, Lulea University of Technology, 2002.

[22] https://classes.engineering.wustl.edu/2009/spring/mase5513/abaqus/docs/v6.6/books/stm/default.htm.

[23] https://www.mitutoyo.com/webfoo/wp-content/uploads/CRYSTA_ApexS-_2202.pdf.

[24] D. Roylance, Engineering viscoelasticity, Massachusetts Institute of Technology, 2001.

[25] G. Ntourmas, F. Glock, F. Daoud, G. Schuhmacher, D. Chronopoulos, E. Özcan, Mixed integer linear programming formulations of the stacking sequence and blending optimisation of composite structures, Composite Structures 264 (2021) 113660.

[26] G. Ntourmas, F. Glock, F. Daoud, G. Schuhmacher, D. Chronopoulos, E. Özcan, Generic stacks and application of composite rules for the detailed sizing of laminated structures, Composite Structures 276 (2021) 114487.

[27] G. Ntourmas, F. Glock, S. Deinert, F. Daoud, G. Schuhmacher, D. Chronopoulos, E. Özcan, J. Ninić, Stacking sequence optimisation of an aircraft wing skin, Structural and Multidisciplinary Optimization 66 (2023).

[28] G. Corrado, A. Arteiro, A. Marques, J. Reinoso, F. Daoud, F. Glock, An extended invariant approach to laminate failure of fibre-reinforced polymer structures, The Aeronautical Journal 126 (2022) 1045–1068.

[29] M. Sferza, J. Ninić, D. Chronopoulos, F. Glock, F. Daoud, Multidisciplinary optimisation of aircraft structures with critical non-regular areas: Current practice and challenges, Aerospace 8 (2021) 223.

[30] N. Traiforos, T. Turner, P. Runeberg, D. Fernass, D. Chronopoulos, F. Glock, G. Schuhmacher, D. Hartung, A simulation framework for predicting process-induced distortions for precise manufacturing of aerospace thermoset composites, Composite Structures 275 (2021) 114465.

[31] N. Traiforos, M. Matveev, D. Chronopoulos, T. Turner, Spring-in of composite l-shape specimens: An experimental and numerical investigation, Composite Structures 310 (2023) 116772.

[32] https://ec.europa.eu/clima/eu-action/transport-emissions/reducing-emissions-aviation_en.

[33] J. Bold, P. F. Rodriguez, O. Chevillard, S. Tucker, C. Ruckert, J. Bergerat, Materials, in: Transnational Composite Training, Materials and Processes, Airbus France S.A.S, 2008, pp. 1–53.

[34] S. Tucker, C. Ruckert, J. Bold, P. F. Rodriguez, B. Malsallez, O. Chevillard, J. Bergerat, Prepreg processes, in: Transnational Composite Training, Materials and Processes, Airbus France S.A.S, 2009, pp. 1–67.

[35] G. Schuhmacher, Multidisziplinare, fertigungsgerechte Optimierung von Faserverbund-Flachentragwerken, Ph.D. thesis, 1995.

[36] O. Chevillard, J. Bergerat, C. Ruckert, S. Pansart, Liquid composite molding, in: Transnational Composite Training, Materials and Processes, Airbus France S.A.S, 2009, pp. 1–52.

[37] J. Lowe, 11 - aerospace applications, in: A. Long (Ed.), Design and Manufacture of Textile Composites, Woodhead Publishing Series in Textiles, Woodhead Publishing, 2005, pp. 405–423.

[38] A. Brasington, C. Sacco, J. Halbritter, R. Wehbe, R. Harik, Automated fiber placement: A review of history, current technologies, and future paths forward, Composites Part C: Open Access 6 (2021) 100182.

[39] S. Chen, O. McGregor, A. Endruweit, M. Elsmore, D. De Focatiis, L. Harper, N. Warrior, Double diaphragm forming simulation for complex composite structures, Composites Part A: Applied Science and Manufacturing 95 (2017) 346–358.

[40] A. Smith, A. Endruweit, G. Choong, D. De Focatiis, P. Hubert, Adaptation of material deposition parameters to account for out-time effects on prepreg tack, Composites Part A: Applied Science and Manufacturing 133 (2020) 105835.

[41] E. Kappel, A zone-based approach to predict process-induced distortions of composite structures based on a 'spring-in reference curve', Composite Structures 209 (2019) 143–149.

[42] C. Albert, G. Fernlund, Spring-in and warpage of angled composite laminates, Composites Science and Technology 62 (2002) 1895–1912.

[43] M. Abouhamzeh, J. Sinke, K. Jansen, R. Benedictus, Closed form expression for residual stresses and warpage during cure of composite laminates, Composite Structures 133 (2015) 902–910.

[44] G. Twigg, A. Poursartip, G. Fernlund, Tool–part interaction in composites processing. part i: experimental investigation and analytical model, Composites Part A: Applied Science and Manufacturing 35 (2004) 121–133.

[45] E. Kappel, D. Stefaniak, C. Hühne, Process distortions in prepreg manufacturing – an experimental study on cfrp l-profiles, Composite Structures 106 (2013) 615–625.

[46] L. Khoun, R. de Oliveira, V. Michaud, P. Hubert, Investigation of process-induced strains development by fibre bragg grating sensors in resin transfer moulded composites, Composites Part A: Applied Science and Manufacturing 42 (2011) 274–282.

[47] G. Fernlund, N. Rahman, R. Courdji, M. Bresslauer, A. Poursartip, K. Willden, K. Nelson, Experimental and numerical study of the effect of cure cycle, tool surface, geometry, and lay-up on the dimensional fidelity of autoclave-processed composite parts, Composites Part A: Applied Science and Manufacturing 33 (2002) 341–351.

[48] M. Wisnom, M. Gigliotti, N. Ersoy, M. Campbell, K. Potter, Mechanisms generating residual stresses and distortion during manufacture of polymer–matrix composite structures, Composites Part A: Applied Science and Manufacturing 37 (2006) 522–529.

[49] E. Hörberg, T. Nyman, M. Åkermo, S. Hallström, Thickness effect on spring-in of prepreg composite l-profiles – an experimental study, Composite Structures 209 (2019) 499–507.

[50] A. Ding, S. Fang, X. Li, L. Sun, J. Wang, H. Chen, Experimental and numerical investigation of tool-part interaction on the process-induced distortions in composite structures, Composite Structures 279 (2022) 114871.

[51] C. Bellini, L. Sorrentino, Analysis of cure induced deformation of cfrp u-shaped laminates, Composite Structures 197 (2018) 1–9.

[52] C. Bellini, L. Sorrentino, W. Polini, A. Corrado, Spring-in analysis of cfrp thin laminates: numerical and experimental results, Composite Structures 173 (2017) 17–24.

[53] L. Mezeix, A. Seman, M. Nasir, Y. Aminanda, A. Rivai, B. Castanié, P. Olivier, K. Ali, Spring-back simulation of unidirectional carbon/epoxy flat laminate composite manufactured through autoclave process, Composite Structures 124 (2015) 196–205.

[54] K. Çınar, N. Ersoy, 3d finite element model for predicting manufacturing distortions of composite parts, Journal of Composite Materials 50 (2016) 3791–3807.

[55] G. Twigg, A. Poursartip, G. Fernlund, Tool–part interaction in composites processing. part ii: numerical modelling, Composites Part A: Applied Science and Manufacturing 35 (2004) 135–141.

[56] E. Kappel, Forced-interaction and spring-in – relevant initiators of process-induced distortions in composite manufacturing, Composite Structures 140 (2016) 217–229.

[57] X. Zeng, J. Raghavan, Role of tool-part interaction in process-induced warpage of autoclave-manufactured composite structures, Composites Part A: Applied Science and Manufacturing 41 (2010) 1174–1183.

[58] R. de Oliveira, S. Lavanchy, R. Chatton, D. Costantini, V. Michaud, R. Salathé, J.-A. Månson, Experimental investigation of the effect of the mould thermal expansion on the development of internal stresses during carbon fibre composite processing, Composites Part A: Applied Science and Manufacturing 39 (2008) 1083–1090.

[59] K.-T. Hsiao, S. Gangireddy, Investigation on the spring-in phenomenon of carbon nanofiber-glass fiber/polyester composites manufactured with vacuum assisted resin transfer molding, Composites Part A: Applied Science and Manufacturing 39 (2008) 834–842.

[60] A. Ghasemi, M. Mohammadi, M. Mohandes, The role of carbon nanofibers on thermo-mechanical properties of polymer matrix composites and their effect on reduction of residual stresses, Composites Part B: Engineering 77 (2015) 519–527.

[61] M. Shokrieh, A. Daneshvar, S. Akbari, M. Chitsazzadeh, The use of carbon nanofibers for thermal residual stress reduction in carbon fiber/epoxy laminated composites, Carbon 59 (2013) 255–263.

[62] D. Stefaniak, E. Kappel, T. Spröwitz, C. Hühne, Experimental identification of process parameters inducing warpage of autoclave-processed cfrp parts, Composites Part A: Applied Science and Manufacturing 43 (2012) 1081–1091.

[63] L. Sun, J. Wang, A. Ni, S. Li, A. Ding, Modelling and experiment of process-induced distortions in unsymmetrical laminate plates, Composite Structures 182 (2017) 524–532.

[64] G. Twigg, A. Poursartip, G. Fernlund, An experimental method for quantifying tool–part shear interaction during composites processing, Composites Science and Technology 63 (2003) 1985–2002.

[65] N. Ersoy, K. Potter, M. R. Wisnom, M. J. Clegg, An experimental method to study the frictional processes during composites manufacturing, Composites Part A: Applied Science and Manufacturing 36 (2005) 1536–1544.

[66] N. Ersoy, K. Potter, M. R. Wisnom, M. J. Clegg, Development of spring-in angle during cure of a thermosetting composite, Composites Part A: Applied Science and Manufacturing 36 (2005) 1700–1706.

[67] T. Garstka, N. Ersoy, K. Potter, M. Wisnom, In situ measurements of through-the-thickness strains during processing of as4/8552 composite, Composites Part A: Applied Science and Manufacturing 38 (2007) 2517–2526.

[68] E. Kappel, R. Prussak, On abnormal thermal-expansion properties of more orthotropic m21e/ima carbon-fiber-epoxy laminates, Composites Communications 17 (2020) 129–133.

[69] C. Dong, Process-induced deformation of composite t-stiffener structures, Composite Structures 92 (2010) 1614–1619.

[70] E. Kappel, Spring-in of curved cfrp/foam-core sandwich structures, Composite Structures 128 (2015) 155–164.

[71] M. Al-Dhaheri, K. Khan, R. Umer, F. van Liempt, W. Cantwell, Process induced deformations in composite sandwich panels using an in-homogeneous layup design, Composites Part A: Applied Science and Manufacturing 137 (2020) 106020.

[72] Y. Mahadik, K.Potter, Experimental investigation into the thermoelastic spring-in ofcurved sandwich panels, Composites Part A: Applied Science and Manufacturing 49 (2013) 68–80.

[73] M. Al-Dhaheri, K. Khan, R. Umer, F. van Liempt, W. Cantwell, Process-induced deformation in u-shaped honeycomb aerospace composite structures, Composite Structures 248 (2020) 112503.

[74] M. R. Wisnom, K. D. Potter, N. Ersoy, Shear-lag analysis of the effect of thickness on spring-in of curved composites, Journal of Composite Materials 41 (2007) 1311–1324.

[75] Z. Yuan, Y. Wang, X. Peng, J. Wang, S. Wei, An analytical model on through-thickness stresses and warpage of composite laminates due to tool–part interaction, Composites Part B: Engineering 91 (2016) 408–413.

[76] C. Dong, Modeling the process-induced dimensional variations of general curved composite components and assemblies, Composites Part A: Applied Science and Manufacturing 40 (2009) 1210–1216.

[77] E. Kappel, D. Stefaniak, G. Fernlund, Predicting process-induced distortions in composite manufacturing – a pheno-numerical simulation strategy, Composite Structures 120 (2015) 98–106.

[78] W. Chen, D. Zhang, A micromechanics-based processing model for predicting residual stress in fiber-reinforced polymer matrix composites, Composite Structures 204 (2018) 153–166.

[79] A. Ding, S. Li, J. Wang, A. Ni, L. Zu, A new path-dependent constitutive model predicting cure-induced distortions in composite structures, Composites Part A: Applied Science and Manufacturing 95 (2017) 183–196.

[80] M. Abouhamzeh, J. Sinke, K. Jansen, R. Benedictus, A new procedure for thermo-viscoelastic modelling of composites with general orthotropy and geometry, Composite Structures 133 (2015) 871–877.

[81] A. R. A. Arafath, R. Vaziri, A. Poursartip, Closed-form solution for process-induced stresses and deformation of a composite part cured on a solid tool: Part i – flat geometries, Composites Part A: Applied Science and Manufacturing 39 (2008) 1106–1117.

[82] A. R. A. Arafath, R. Vaziri, A. Poursartip, Closed-form solution for process-induced stresses and deformation of a composite part cured on a solid tool: Part ii – curved geometries, Composites Part A: Applied Science and Manufacturing 40 (2009) 1545–1557.

[83] D. W. Radford, T. S. Rennick, Separating sources of manufacturing distortion in laminated composites, Journal of Reinforced Plastics and Composites 19 (2000) 621–641.

[84] J. Chen, J. Wang, S. Li, C. Wang, A. Ding, Analytical solutions for process-induced spring-in of u-shaped composite parts, Thin-Walled Structures 169 (2021) 108425.

[85] A. Ding, S. Li, J. Wang, A. Ni, A new analytical solution for spring-in of curved composite parts, Composites Science and Technology 142 (2017) 30–40.

[86] A. Ding, J. Wang, S. Li, Understanding process-induced spring-in of l-shaped composite parts using analytical solution, Composite Structures 250 (2020) 112629.

[87] E. Kappel, D. Stefaniak, T. Spröwitz, C. Hühne, A semi-analytical simulation strategy and its application to warpage of autoclave-processed cfrp parts, Composites Part A: Applied Science and Manufacturing 42 (2011) 1985–1994.

[88] P. Hubert, A. Poursartip, A review of flow and compaction modelling relevant to thermoset matrix laminate processing, Journal of Reinforced Plastics and Composites 17 (1998) 286–318.

[89] J. Lightfoot, M. Wisnom, K. Potter, A new mechanism for the formation of ply wrinkles due to shear between plies, Composites Part A-applied Science and Manufacturing 49 (2013) 139–147.

[90] K. Potter, C. Langer, B. Hodgkiss, S. Lamb, Sources of variability in uncured aerospace grade unidirectional carbon fibre epoxy preimpregnate, Composites Part A: Applied Science and Manufacturing 38 (2007) 905 – 916.

[91] E. Lamers, Shape distortions in fabric reinforced composite products due to processing induced fibre reorientation, Ph.D. thesis, Netherlands, 2004.

[92] M. Benavente, L. Marcin, A. Courtois, M. Lévesque, E. Ruiz, Numerical analysis of viscoelastic process-induced residual distortions during manufacturing and post-curing, Composites Part A: Applied Science and Manufacturing 107 (2018) 205–216.

[93] W. Chen, D. Zhang, A micromechanics-based processing model for predicting residual stress in fiber-reinforced polymer matrix composites, Composite Structures 204 (2018) 153–166.

[94] B. Tavakol, P. Roozbehjavan, A. Ahmed, R. Das, R. Joven, H. Koushyar, A. Rodriguez, B. Minaie, Prediction of residual stresses and distortion in carbon fiber-epoxy composite parts due to curing process using finite element analysis, Journal of Applied Polymer Science 128 (2013) 941–950.

[95] J. Zhang, M. Zhang, S. Li, M. Pavier, D. Smith, Residual stresses created during curing of a polymer matrix composite using a viscoelastic model, Composites Science and Technology 130 (2016) 20–27.

[96] A. Ding, S. Li, J. Wang, L. Zu, A three-dimensional thermo-viscoelastic analysis of process-induced residual stress in composite laminates, Composite Structures 129 (2015) 60–69.

[97] A. Ding, S. Li, J. Sun, J. Wanga, L. Zu, A thermo-viscoelastic model of process-induced residual stresses in composite structures with considering thermal dependence, Composite Structures 136 (2016) 34–43.

[98] T. A. Bogetti, J. W. Gillespie, Process-induced stress and deformation in thick-section thermoset composite laminates, Journal of Composite Materials 26 (1992) 626–660.

[99] A. A. Johnston, An integrated model of the development of process-induced deformation in autoclave processing of composite structures, Ph.D. thesis, University of British Columbia, 1997.

[100] Q. Wang, T. Li, X. Yang, K. Wang, B. Wang, M. Ren, Prediction and compensation of process-induced distortions for l-shaped 3d woven composites, Composites Part A: Applied Science and Manufacturing 141 (2021) 106211.

[101] E. Zappino, N. Zobeiry, M. Petrolo, R. Vaziri, E. Carrera, A. Poursartip, Analysis of process-induced deformations and residual stresses in curved composite parts considering transverse shear stress and thickness stretching, Composite Structures 241 (2020) 112057.

[102] O. G. Kravchenko, S. G. Kravchenko, R. B. Pipes, Cure history dependence of residual deformation in a thermosetting laminate, Composites Part A: Applied Science and Manufacturing 99 (2017) 186–197.

[103] L. Moretti, B. Castanié, G. Bernhart, P. Olivier, Characterization and modelling of cure-dependent properties and strains during composites manufacturing, Journal of Composite Materials 54 (2020) 3109–3124.

[104] W. Chen, D. Zhang, Improved prediction of residual stress induced warpage in thermoset composites using a multiscale thermo-viscoelastic processing model, Composites Part A: Applied Science and Manufacturing 126 (2019) 105575.

[105] N. Ersoy, T. Garstka, K. Potter, M. R. Wisnom, D. Porter, G. Stringer, Modelling of the spring-in phenomenon in curved parts made of a thermosetting composite, Composites Part A: Applied Science and Manufacturing 41 (2010) 410–418.

[106] C. Liu, Y. Shi, A thermo-viscoelastic analytical model for residual stresses and spring-in angles of multilayered thin-walled curved composite parts, Thin-Walled Structures 152 (2020) 106758.

[107] X. Liu, Z. Guan, X. Wang, T. Jiang, K. Geng, Z. Li, Study on cure-induced residual stresses and spring-in deformation of l-shaped composite laminates using a simplified constitutive model considering stress relaxation, Composite Structures 272 (2021) 114203.

[108] N. Zobeiry, A. Forghani, C. Li, K. Gordnian, R. Thorpe, R. Vaziri, G. Fernlund, A. Poursartip, Multiscale characterization and representation of composite materials during processing, Philosophical Transactions of the Royal Society A: Mathematical, Physical and Engineering Sciences 374 (2016) 20150278.

[109] G. Zhang, J. Wang, A. Ni, H. Hu, A. Ding, S. Li, Process-induced deformation of l - shaped variable-stiffness composite structures during cure, Composite Structures 230 (2019).

[110] M. A. Zocher, S. E. Groves, A three dimentional finite element formulation for thermoviscoelastic orthotropic media, International Journal for Numerical Methods in Engineering 40 (1997) 2267–2288.

[111] H. Poon, M. F. Ahmad, A material point time integration procedure for anisotropic, thermo rheologically simple, viscoelastic solids, Computational Mechanics 21 (1998) 236–242.

[112] H. Poon, M. F. Ahmad, A finite element constitutive update scheme for anisotropic, viscoelastic solids exhibiting non-linearity of the schapery type, International Journal for Numerical Methods in Engineering 46 (1999) 2027–2041.

[113] R. Schapery, On the characterization of nonlinear viscoelastic materials, Polymer Engineering and Science 9 (1969) 295–310.

[114] Y. Eom, L. Boogh, V. Michaud, P. Sunderland, J.-A. Manson, Time-cure-temperature superposition for the prediction of instantaneous viscoelastic properties during cure, Polymer Engineering and Science 40 (2000) 1281–1292.

[115] D. J. O'Brien, P. T. Mather, S. R. White, Viscoelastic properties of an epoxy resin during cure, Journal of Composite Materials 35 (2001) 883–904.

[116] E. I. Avgoulas, D. M. Mulvihill, A. Endruweit, M. P. Sutcliffe, N. A. Warrior, D. S. De Focatiis, A. C. Long, Frictional behaviour of non-crimp fabrics (ncfs) in contact with a forming tool, Tribology International 121 (2018) 71–77.

[117] A. Das, G. Y. Choong, D. A. Dillard, D. S. De Focatiis, M. J. Bortner, Characterizing friction for fiber reinforced composites manufacturing: Method development and effect of process parameters, Composites Part B: Engineering 236 (2022) 109777.

[118] V. Kaushik, J. Raghavan, Experimental study of tool–part interaction during autoclave processing of thermoset polymer composite structures, Composites Part A: Applied Science and Manufacturing 41 (2010) 1210–1218.

[119] M. Nielsen, Prediction of process induced shape distortions and residual stresses in large fibre reinforced composite laminates: With application to Wind Turbine Blades, Ph.D. thesis, 2013.

[120] E. Kappel, D. Stefaniak, D. Holzhüter, C. Hühne, M. Sinapius, Manufacturing distortions of a cfrp box-structure – a semi-numerical prediction approach, Composites Part A: Applied Science and Manufacturing 51 (2013) 89–98.

[121] B. Wucher, F. Lani, T. Pardoen, C. Bailly, P. Martiny, Tooling geometry optimization for compensation of cure-induced distortions of a curved carbon/epoxy c-spar, Composites Part A: Applied Science and Manufacturing 56 (2014) 27–35.

[122] M. Benavente, L. Marcin, A. Courtois, M. Lévesque, E. Ruiz, Viscoelastic distortion in asymmetric plates during post curing, Composites Part A: Applied Science and Manufacturing 103 (2017) 122–130.

[123] O. S. Sindee L. Simon, Gregory B. Mckenna, Modeling the evolution of the dynamic mechanical properties of a commercial epoxy during cure after gelation, Journal of Applied Polymer Science 76 (2000) 495–508.

[124] Epikote system 600 and mixing services for high performance composite structures, in: Product Bulletin, HEXION, 2019.

[125] https://www.gom.com/en/products/gom-inspect-suite.

[126] D. Kalpić, N. Hlupić, M. Lovrić, Student's t-Tests, Springer Berlin Heidelberg, Berlin, Heidelberg, 2011, pp. 1559–1563.

[127] A. Nettles, Basic mechanics of laminated composite plates, NASA, 1994.

[128] Delivery programme and characteristics for tenax® ims65 filament yarn, Toho Tenax, 2010.

[129] H.-C. Lahne, D. Gerling, D. Staton, Y. C. Chong, Design of a 50000 rpm high-speed high-power six-phase pmsm for use in aircraft applications, in: 2016 Eleventh International Conference on Ecological Vehicles and Renewable Energies (EVER), 2016, pp. 1–11.

[130] S.-N. Lee, M.-T. Chiu, H.-S. Lin, Kinetic model for the curing reaction of a tetraglycidyl diamino diphenyl methane/diamino diphenyl sulfone (tgddm/dds) epoxy resin system, Polymer Engineering & Science 32 (1992) 1037–1046.

[131] K. C. Cole, J. J. Hechler, D. Noel, A new approach to modeling the cure kinetics of epoxy/amine thermosetting resins. 2. application to a typical system based on bis[4-(diglycidylamino)phenyl]methane and bis(4-aminophenyl) sulfone, Macromolecules 24 (1991) 3098–3110.

[132] J. Weiland, Eps600 charakterisierung: Abschlussbericht, TUM Lehrstuhl fur Carbon Composites, 2017.

[133] T. B. Loredana Kehrer, Sebastian Reimann, Dynamisch mechanische analyse an eps600, Kalsruher Institut fur Technologie, Institut fur Technische Mechanik, 2019.

[134] D. J. Plazek, I.-C. Chay, The evolution of the viscoelastic retardation spectrum during the development of an epoxy resin network, Journal of Polymer Science Part B: Polymer Physics 29 (1991) 17–29.

[135] A. Lee, G. B. McKenna, Effect of crosslink density on physical ageing of epoxy networks, Polymer 29 (1988) 1812–1817.

[136] M. L. Williams, R. F. Landel, J. D. Ferry, The temperature dependence of relaxation mechanisms in amorphous polymers and other glass-forming liquids, Journal of the American Chemical Society 77 (1955) 3701–3707.

[137] https://www.maplesoft.com/support/help/maple/view.aspx?path=Statistics%2FNonlinearFit.

[138] D. Dykeman, Minimizing uncertainty in cure modeling for composites manufacturing, Ph.D. thesis, University of British Columbia, 2008.

[139] J. Torres, M. Simmons, F. Sket, C. González, An analysis of void formation mechanisms in out-of-autoclave prepregs by means of x-ray computed tomography, Composites Part A: Applied Science and Manufacturing 117 (2019) 230–242.

[140] N. Ersoy, T. Garstka, K. Potter, M. R. Wisnom, D. Porter, M. Clegg, G. Stringer, Development of the properties of a carbon fibre reinforced thermosetting composite through cure, Composites Part A: Applied Science and Manufacturing 41 (2010) 401–409.

[141] Y. Benveniste, A new approach to the application of mori-tanaka's theory in composite materials, Mechanics of Materials 6 (1987) 147–157.

[142] S. White, Y. Kim, Process-induced residual stress analysis of as4/3501-6 composite material, Mechanics of Advanced Materials and Structures 5 (1998) 153–186.

[143] Abaqus analysis user's guide version 6.14, Dassault Systemes Simulia Corp, 2014.

[144] C. Wolm, Thermo-mechanische simulation von vap - prozessen.

[145] M. W. Nielsen, J. W. Schmidt, J. H. Hattel, T. L. Andersen, C. M. Markussen, In situ measurement using fbgs of process-induced strains during curing of thick glass/epoxy laminate plate: experimental results and numerical modelling, Wind Energy 16 (2013) 1241–1257.

[146] L. L. Vignoli, M. A. Savi, P. M. Pacheco, A. L. Kalamkarov, Comparative analysis of micromechanical models for the elastic composite laminae, Composites Part B: Engineering 174 (2019) 106961.